

Dynamic Responses of Networks under Perturbations: Solutions, Patterns and Predictions

Dissertation

for the award of the degree
"Doctor rerum naturalium"
of the Georg-August-Universität Göttingen

within the doctoral program
Physics of Biological and Complex Systems
of the Georg-August University School of Science (GAUSS)

submitted by
Xiaozhu Zhang
from
Shanghai, China

Göttingen 2017

Thesis Committee

Prof. Dr. Marc Timme (1st Referee)

Network Dynamics, Max Planck Institute for Dynamics and Self-organization

Prof. Dr. Reiner Kree (2nd Referee)

Institute for Theoretical Physics, Georg-August-University Göttingen

Prof. Dr. Ulrich Parlitz

Biomedical Physics, Max Planck Institute for Dynamics and Self-organization

Extended Members of the Examination Board

Prof. Dr. Chenchang Zhu

Mathematics Institute, Georg-August-University Göttingen

Prof. Dr. Theo Geisel

Nonlinear Dynamics, Max Planck Institute for Dynamics and Self-organization

Prof. Dr. Michael Wilczek

Theory of Turbulent Flows, Max Planck Institute for Dynamics and Self-organization

Date of Oral Examination

January 2018

献给我的外婆和母亲。
是你们的理想主义，坚韧和爱永远励我前行。

*To my beloved grandma and mother.
Your idealism, fortitude and love is my
constant source of courage.*

Declaration

I hereby declare that the contents of this dissertation are original except where specific reference is made to the work of others.

Xiaozhu Zhang
October 2017

List of Publications

- [1] **X. Zhang**, D. Witthaut, and M. Timme. *Transient Responses in Oscillatory Networks*. in preparation, 2017.
- [2] **X. Zhang**, S. Hallerberg, M. Matthiae, D. Witthaut, and M. Timme. *Dynamic Response Patterns of Complex Oscillator Networks*. submitted, 2017.
- [3] J. Casadiego, **X. Zhang**, and M. Timme. *Locating Perturbation Sources and Monitoring Unmeasured Units from Collective Dynamics*. in preparation, 2017.
- [4] Zhiyi Lv, Jan Rosenbaum, **X. Zhang**, Timo Aspelmeier, Jörg Großhans. *Collective Dynamics in Drosophila Embryo*. in preparation, 2017.
- [5] D. Manik, M. Rohden, H. Ronellenfitsch, **X. Zhang**, S. Hallerberg, D. Witthaut, and M. Timme. *Network Susceptibilities: Theory and Applications*. Phys. Rev. E 95, 012319, 2017.
- [6] D. Witthaut, M. Rohden, **X. Zhang**, S. Hallerberg, and M. Timme. *Critical Links and Nonlocal Rerouting in Complex Supply Networks*. Phys. Rev. Lett. 116(13):138701, 2016.
- [7] M. Matthiae, B. Schäfer, **X. Zhang**, M. Rohden, M. Timme, and D. Witthaut. *Escape Routes, Weak Links, and Desynchronization in Fluctuation-driven Networks*. Phys. Rev. E 95: 060203(R), 2016.
- [8] **X. Zhang**, C. Kuehn, and S. Hallerberg. *Predictability of Critical Transitions*. Phys. Rev. E 92(5):052905, 2015

Contents

Nomenclature	xiii
Introduction	1
I. Fundamentals	9
1 Networks as Dynamical Systems	11
1.1 Networks	11
1.2 Dynamical systems	16
1.3 Dynamical systems on networks	18
2 Dynamics of Network Responses	21
2.1 Time evolution of small perturbations	21
2.2 Network responses to external driving	26
2.3 Summary	28
3 Phase Oscillator Networks and Power Grids	31
3.1 Synchronization and phase oscillator networks	31
3.2 The oscillator model of power grids	33
II. Dynamic Patterns in Steady Network Responses	43
4 Steady Network Responses to External Driving Signals	45
4.1 Total network response to a sinusoidal signal	45
4.2 Steady nodal responses to a sinusoidal signal	47
4.3 Steady responses to a step-function signal	52

4.4	Conclusion	55
5	Three Frequency Regimes of Steady Response Patterns	59
5.1	Frequency: key parameter for pattern formation	59
5.2	Eigenfrequencies and the resonance regime	61
5.3	Lower frequencies: the bulk regime	64
5.4	Higher frequencies: the localized regime	65
5.5	Conclusion	69
6	Response Patterns at High- and Low-damping Limits	73
6.1	High-damping limit: Kuramoto oscillator networks	73
6.2	Low-damping limit: a Hamiltonian system	81
6.3	Conclusion	83
7	Predicting Network Responses to Irregular and Distributed Signals	87
7.1	An approach to predict network responses	87
7.2	Predicting dynamic responses of power grids to fluctuations	90
7.3	Prediction error and limit of validity	95
7.4	Conclusion	101
III.	Transient Dynamics of Network Responses	103
8	Transient Network Responses to Perturbations	105
8.1	Full nodal response to external driving	105
8.2	Approximation of transient nodal response	108
8.3	First insights into perturbation spreading	112
8.4	Conclusion	114
9	Characterizing Perturbation Spreading in Networks	117
9.1	Asymptotic spreading behavior of perturbation	117
9.2	The topological factor	124
9.3	Predicting perturbation arrival time	126
9.4	Conclusion	129

10 Towards a Theory of Perturbation Spreading in Networks	131
10.1 Universality of perturbation spreading behavior	131
10.2 Two conjectures on bounds of asymptotic spreading speed	137
10.3 Conclusion	140
 Conclusion	 143
 Appendix A Proof of Proposition 2	 147
 Appendix B Proof of Proposition 3	 153
 References	 157
 Acknowledgement	 169

Nomenclature

Roman Symbols

\mathcal{J}	Jacobian matrix
\mathcal{L}	graph Laplacian, or Laplacian matrix
$\mathcal{P}_{i \rightarrow j}^{(r)}$	a path from vertex i to j with length r
\mathbf{A}	adjacency matrix
\mathbf{D}	degree matrix
\mathbf{K}	weighted adjacency matrix, or connectivity matrix
\mathbf{V}	the square matrix with the Laplacian eigenvectors as its columns
$\tilde{T}_i^{(k)}$	general topological factor
$A_i^{(k)}$	response strength at node i to a perturbation at node k
$A_i^{*(k)}$	normalized frequency response strength at node i to a perturbation at node k
$C^{(k)}(d)$	the instantaneous spreading speed of a perturbation from node k at distance d
C_∞	the asymptotic spreading speed at $d \rightarrow \infty$
$d(i, j)$	the geodesic distance between vertex i and j
$G(d)$	general spreading function
$H(t)$	a heaviside function of t
$M(d)$	master curve of perturbation spreading
$T_i^{(k)}$	topological factor for homogeneously coupled networks

Greek Symbols

$\Delta_i^{(k)}$	response phase delay at node i to a perturbation at node k
$\dot{\theta}_i$	phase velocity, or frequency of oscillator i
ϵ_{th}	the threshold of nodal response for determining perturbation arrival time $\tau_i^{(k)}$
$\lambda^{[\ell]}$	the ℓ -th eigenvalue of the Laplacian matrix
$\mu^{[\ell]}$	the ℓ -th eigenvalue of the Jacobian matrix
Ω_0	the nominal frequency of power grids
Λ	the diagonal matrix with the Laplacian eigenvalues as its diagonal elements
$\tau_i^{(k)}$	threshold-crossing arrival time of a perturbation from node k at node i
θ_i^*	fixed point of oscillator i
θ_i	phase of oscillator i
$\Theta_i^{(k)}$	phase response of oscillator i to a perturbation at oscillator k

Other Symbols

(i, j)	an edge between vertex i and j
$\#[\cdot]$	the total number of $[\cdot]$
$\deg(i)$	the degree of vertex i
\imath	the imaginary unit

Acronyms / Abbreviations

LRT	Linear Response Theory
ODE	Ordinary Differential Equation
PSD	Power Spectral Density

萬物並作，吾以觀復。
夫物芸芸，各復歸其根。

老子《道德經》

*The myriad things rise and fall,
I thereby observe and contemplate the Law.
All things bloom and flourish,
then return to their roots, each by each.*

Laozi “*”
(400 BC)*

Introduction

It makes me so happy. To be at the beginning again, knowing almost nothing... The ordinary-sized stuff which is our lives, the things people write poetry about—clouds—daffodils—waterfalls... these things are full of mystery, as mysterious to us as the heavens were to the Greeks... It's the best possible time to be alive, when almost everything you thought you knew is wrong.

— Tom Stoppard, *Arcadia*

Reductionism has been the basis of scientific methodology since the age of enlightenment. In *Discourse on the Method*, René Descartes described his scientific method as “to divide all the difficulties under examination into as many parts as possible, and as many as were required to solve them in the best way” [1]. For centuries, under a belief that “a whole can be understood completely if you understand its parts, and the nature of their ‘sum’ ” [2], scientists have been pursuing a reductionist explanation of all phenomena in nature. While great successes have been made through scientific reductionism in explaining both the microscopic and the macroscopic world, the phenomena at human-scale, which are of most concern to our daily life, have been left mysterious and unexplained.

By the mid-twentieth century, the reductionist dream was broken when more and more scientists realized that many *complex* phenomena *cannot* be explained by simply summing the understanding of their parts [3]: the knowledge on fluid dynamics does not lead to the full predictability of the weather and the climate; the knowledge on chemistry and biology does not enable us to understand how life arises from non-living matter; and the knowledge on the behavior of a single starling does not ensure the comprehension of their flocking behavior. Fascinating phenomena such as the weather, life, and the flocking of birds arise from large collections of simpler components, but are much more than the sum of them: the dynamical *interaction* between the parts gives rise to the complexity of the whole.

Complex networks: *interaction* matters

A *network*, essentially a collection of nodes connected by edges, is thus an ideal construct for describing how a group of discrete objects interact with each other [4, 5]. In this light, almost all complex systems can be represented as networks: the human brain is a network of more than 80 billion of interconnected neurons sending each other synapses [6, 7]; an ecosystem can be seen as a network of living organisms and the supporting components of their environment linked by nutrient cycles and energy flows [8]; and ultimately, the entire universe is a grand network of interacting planets, stars, galaxies and all of space, time, matter, and energy [9]. Studying complex systems as networks, i.e. focusing on the interaction between the components, can be a shortcut leading to the source of complexity in complex systems.

Most real-world networks are *complex networks*, where the patterns of connection between the elements are nontrivial: neither purely regular nor purely random [10]. Although complex networks are inherently difficult to understand, due to the possible diversities in their components and connections, among other complications [11], even networks with identical nodes obeying simple rules of interaction can exhibit rich and complex behaviors such as synchronization, chimera states and pattern formation [12–19], as a consequence of the interplay between the network structure and the nonlinear dynamics within and among the components.

The spontaneous emergence of such phenomena are signatures of *self-organization*: order is created out of disorder, which seemingly defies the second-law of thermodynamics stating that entropy, or disorder, always wins out over time. Self-organized network dynamics underlies almost all aspects of the natural and the civilized world, from the neural networks [20–22] and the gene regulatory circuits [23] in living organisms to man-made communication networks [24, 25] and AC power grids [26, 14, 15] in human industry. If these self-organized network systems were to stop functioning even for a second, the world as we know it would cease to exist.

Network robustness and pattern formation

A robust function of these networked systems essentially relies on how their self-organizing dynamics respond to external perturbations. In the real world, nothing is left alone: systems that are perfectly isolated from the environment without being disturbed simply

do not exist. Evolving over eons of time, the self-organized networks in nature manage to respond stably and reliably against environmental perturbations and even to acquire new functions to adapt to new environments. The gene-regulatory network provide a specific example. They exhibit robustness against mutations and the stochastic nature of the production of individual protein molecules even in the absence of natural selection, which was proved to be an emergent property of evolution [27, 28]. Operating close to a critical regime of the average network connectivity, maximum robustness and evolvability occur simultaneously [29]. However, how does the functional robustness arise from the collective dynamic behavior of the components? How does self-organization work to counteract the undermining of external noises while allowing novel features to emerge? The first step towards answering these questions is to understand how complex networks respond to external perturbations, i.e. the *dynamic response patterns* of complex networks.

Fundamental aspects of the formation of spatiotemporal patterns was originally established for systems far from equilibrium in continuous space of a restricted dimension of one or two [30, 31]. In the comprehensive review on pattern formation in systems ranging from thermal convection in fluids to nonlinear optics [31], Cross et al. proposed a theoretical framework where nonequilibrium spatiotemporal patterns are classified according to the linear instabilities of the deterministic systems. The *characteristic wave vector* and/or the *characteristic frequency* associated with the largest-real-part eigenvalue of the linearized system dynamics at the instability threshold indicate the periodicity in time and space of the formed pattern. Beyond the instability threshold, the dynamics of the emerging patterns characterized by these wave vectors and/or frequencies may be accurately described by simple equations called *amplitude equations* derived from *perturbation theory* [32, 33].

The attention on pattern formation mechanism was soon extended to high-dimensional networked dynamical systems. Although Othmer and Scriven pointed out that Turing patterns observed in continuous reaction-diffusion systems can also occur in networks as early as in 1971 [18], concrete evidences of the theory were limited to small networks [17] and regular lattices [18, 19]. In 2010, Nakao and Mikhailov revealed through extensive numerical simulation that Turing patterns exhibit strikingly different behavior in large random networks, in contrast to classical diffusion in continuous or regular media [34]. Novel classes of patterns emerge if the underlying network architecture is further generalized. Patterns such as travelling waves and quasi-stationary patterns can be induced in directed, hence non-symmetric networks [35] and distinct heterogeneous patterns occur in multiplex networks [36].

However, all the above mentioned works focused on patterns caused by the instability of the system. Studies on the emerging dynamic patterns as a consequence of time-dependent driving signals are limited. Besides Kaneko's early work on the clustering effect of external forcing on globally coupled chaotic systems [37], Coullet and Emilsson reported strong resonant patterns in a continuous system of coupled oscillators [38]. For regular sparse networks of phase oscillators, Zanette related the response pattern to a sinusoidal driving with the underlying interaction network structure [39, 40].

A general theory about how dynamic patterns form in complex networks as a response to time-dependent perturbations is still missing to date. To understand the pattern formation mechanism and to predict network-wide responses to a given but arbitrary perturbation signal remains to be an unfinished task. Its non-triviality lies in (i) the high-dimensionality of the complex networked system, and (ii) the temporally irregular and spatially distributed form of the perturbation signals as well as the responses.

Network sensitivity and perturbation spreading

While some network systems, such as gene regulatory networks and neural networks, demonstrate high robustness in their steady reliable function against random disturbances, other networks show high *sensitivity* to perturbations. That is, even a slight, highly localized deviation from normal state can rapidly spread across the entire network and significantly affect the overall performance, sometimes even lead to catastrophic consequences. Examples range from the outbreak of a worldwide pandemic of a new disease [41–44] to the nontrivial propagation of tsunami waves [45] in natural systems, and internet collapses caused by subsequent congestions [46] and power blackouts triggered by the failure of a single element [47–49] in artificial networks. On 4 November 2006, a huge power outage hit Europe, leaving about 15 million households without electricity for about two hours. All of this started with a manual disconnection of a power transmission line in Northern Germany, triggering a sequence of tripping of high-voltage lines and inducing a severe frequency drop in the Western European power grid [50]. How does a seemingly harmless mild disturbance escalate by spreading across the network? How fast does a perturbation signal propagate through the complex interaction between nodes, which propagation paths are dominating, and how strongly does it hit other nodes? To answer these questions, it is essential to understand how a complex network *transiently* responds to a single perturbation.

An intensively studied topic in the field of perturbation spreading is the impact of a single structural failure on supply networks, including the redistribution of load [51, 52] and the loss of dynamical stability [47, 48]. The investigations of the resulting cascading failure are mostly based on *static* models where the static load distribution before and after a failure of infrastructure is computed separately [49, 53–55]. The effect of dynamical load redistribution in a cascading failure is considered only recently [56, 57].

Important insights into the dynamical process of perturbation spreading in networks has been gained in the study of epidemic outbreaks [41–44, 58–60]. Theoretical approaches provide estimations of key quantities in epidemic spreading such as the epidemic threshold and the size of epidemic outbreaks [41], however, few of them are exact. Most explicit results are based on strong assumptions and rely on a mean-field approach [58]. Meanwhile, significant progresses have been made on data-driven microsimulation models [60], which are capable of providing quantitative analyses supporting policy-making in public-health domain. These models reveal interesting and nontrivial patterns in epidemic spreading processes, which however still require theoretical understanding.

Theoretical efforts for quantitatively describing the transient process of perturbation spreading have been made for specific systems with *stochastic* nature [43, 44, 59, 61–63]. By replacing the geographic distance with a *effective distance* involving the transport probability on edges, Brockmann and Helbing demonstrated that complex spatiotemporal epidemic spreading patterns can be reduced to simple wave propagation patterns [43]. This measure of effective distance was recently justified by random walk theory and generalized by including all paths connecting the source and target instead of only the shortest one [44]. Specifically, the arrival times or the most efficient routing paths of a spreading disease or information in networks of stochastic systems was quantified using the effective distance and other analytical approaches [44, 59, 61, 62].

Thus, we can discern that, despite the importance and ubiquity of the problem of perturbation spreading, general answers to simple questions like “When and how will a perturbation affect a given node?” are still missing to date. Even for networks of linear deterministic dynamical systems, the questions remain open [64].

Synopsis of the thesis

In this thesis, we develop a theory of dynamic response patterns for complex networks under the influence of fluctuating perturbations. Motivated by the functional robustness

and sensitivity against perturbations demonstrated by natural and artificial complex networks, we aim at understanding how a normally functioning network of dynamical systems reacts to external disturbances, which are fluctuating in time and distributed in space. For the first time, we reveal novel spatiotemporal patterns in the response of networks with nontrivial connectivity structures, employing methods from graph theory, dynamical system theory and linear response theory. In addition to the derivation of the main results from the second-order Kuramoto oscillator networks, we generalize the theory by discussing the results in different regimes of the high-dimensional parameter space.

The thesis is organized as follows. This [introduction](#) is followed by the main content of the thesis which splits into three parts.

Part I In the first three chapters, we provide the theoretical foundations for the derivation of the main results of the thesis. In [Chap. 1](#) we briefly review the basic concepts and tools to describe networks and dynamical systems. Especially, we highlight the relation between the Laplacian matrix and the shortest paths in [Prop. 1](#) and the linear stability analysis of networked dynamical systems. In [Chap. 2](#) we present the established results on the dynamics of network responses and indicate their limitations. Particularly, for networks of first-order dynamical systems with diffusive couplings, we establish the relation between the Jacobian matrix of the system and the Laplacian matrix of the underlying network architecture. In [Chap. 3](#) we introduce a model class of phase oscillator networks, based on the paradigmatic Kuramoto oscillator model [65]. Especially, we focus on the most general case in the model class, the second-order Kuramoto-like oscillator model: its relation to the collective dynamics of AC power grids and its dynamical features such as the existence, the linear stability of a fixed point and its relation to a saddle-node bifurcation.

Part II In the four chapters in Part II, we present our theory of the long-term dynamic response patterns rising in networks driven by fluctuating and distributed signals. In [Chap. 4](#), we derive in detail the analytical solutions of the steady network responses to a time-dependent driving signal, including to a sinusoidal signal with frequency $\omega > 0$ and to a step-function signal. Based on the explicit solutions, we identify distinct spatiotemporal response patterns in three frequency regimes in [Chap. 5](#). Specifically, we analytically derive the characteristic responsive behaviors in the respective regimes from the solutions via asymptotic analysis. In [Chap. 6](#) we generalize our theory by discussing the response patterns at the high- and low-damping limits of the second-order Kuramoto-like oscillator model. In [Chap. 7](#), based on the derived theory, we propose

an approach to accurately predict the dynamic responses of a network to fluctuating and distributed signals. The application of the approach is demonstrated in predicting the frequency response of a sample power grid to real-world power fluctuations. At the end of this part, we discuss the validity of the theory at the limit of strong perturbations and heavy initial network loads.

Part III In the last three chapters of the thesis, we focus on the patterns in the transient spreading of a single perturbation signal in networks. In **Chap. 8**, we derive the analytical solution describing the full evolution of the network response to a driving signal, and then focus on the transient response and derive a one-term approximation of the response characterizing the first impact of the perturbation on the target node. In **Chap. 9**, we quantitatively characterize and analyze the perturbation spreading behavior based on the one-term approximation of network response. We demonstrate the asymptotic spreading behavior in homogeneous networks and its explicit dependence on the network topology. Based on these results, we propose an approach to accurately predict a perturbation's arrival time at each node in an arbitrary network under the construction of a topology-independent *master curve* of perturbation spreading. In **Chap. 10**, we demonstrate the generality of our results by considering different scenarios of perturbation spreading. Furthermore, we propose two conjectures on the lower- and upper-bound of the asymptotic speed of perturbation spreading in homogeneous networks of second-order dynamical systems.

Finally, we [summarize](#) and discuss our results achieved in this thesis and give a brief outlook to future research.

Part I. Fundamentals

In Part I of the thesis, we provide the theoretical foundations which are relevant to the concepts and findings presented in the later parts.

In Chap. 1, we begin with the basic concepts and the quantitative tools to describe and to analyze networks, dynamical systems, and, as a combination of both, dynamical processes on networks. Most of the content of this chapter is a subset of two branches of mathematics, namely graph theory and dynamical systems theory.

In Chap. 2, we present the basic theory on the dynamics of networks' responses to small perturbations given that the system is close to a steady state, i.e. on the linearization of system's dynamics at a fixed point. In particular, we derive a general form of networks' linear responses to perturbations on the state variable and to external driving signals.

In the last chapter of this part, Chap. 3, we introduce the dynamics of an important type of networks which are made up of coupled phase oscillators. Additionally, we pay special attention on a practical aspect of the second-order Kuramoto-like phase oscillator network model. With a simple parameter mapping, it is directly related to the oscillator model of AC power grids.

Chapter 1

Networks as Dynamical Systems

As the beginning of the thesis, we present the most fundamental concepts underlying the study of dynamic network responses in this thesis. We start with basic and relevant concepts in graph theory, such as graphs, paths and distances (Sec. 1.1). Particularly, we highlight the relation between the distance between a pair of nodes and the element of the power of Laplacian matrices associated to the node pair. In Sec. 1.2, we move on to another branch of mathematics, i.e. dynamical system theory. We present the definition of dynamical systems and focus on the linear stability analysis at fixed points. In the last section of the chapter, Sec. 1.3, we combine the aforementioned concepts from the two branches and present basic considerations about the dynamics of a networked system, i.e. a system of coupled dynamical systems. We especially focus on the linearization of the dynamics of a general network system with pair-wise coupling at the fixed point.

1.1 Networks

Networks are closely related to the concept *graph* in mathematical literature, which is defined as a collection of *vertices* connected by *edges*, representing how a set of objects are related to each other (Fig. 1.1). Vertices and edges are sometimes also called *nodes* and *links*, or *sites* and *bonds* [4]. The three terms “vertices”, “nodes” and “sites” referring to the same notion are interchangeable in this thesis, as well as “edges”, “links”, and “bonds”.

1.1.1 The matrix representation of graphs

Mathematically, a graph $G(V, E)$ consists of a non-empty finite set V of vertices and a finite family E of edges, which are unordered pairs of vertices [5]. In this thesis we consider only *simple graphs*, where two special kinds of edges are not allowed: (i) *multiedges*, meaning more than one edge joining the same pair of vertices, and (ii) *loops* that join a

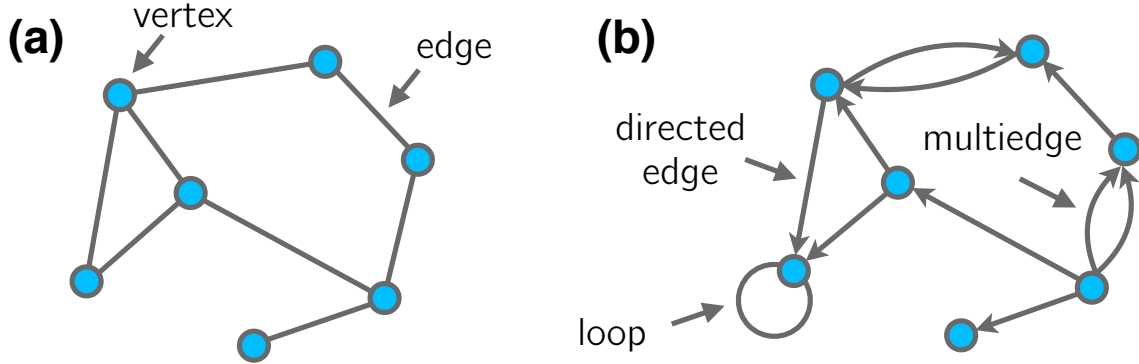


Fig. 1.1 Sketch of two small graphs. (a) a simple graph with seven vertices and eight edges. (b) a directed graph with ten edges, eight directed edges, one multiedge and one loop. In directed graphs, the edges connecting the same source vertex and the same target vertex are referred to as one multiedge.

vertex to itself [4]. In *undirected graphs*, an edge joining the vertices u and v is denoted as $(u, v) = (v, u)$; in *directed graphs*, the involved *directed edges* with particular orientations are associated with $(u, v) \neq (v, u)$. Fig. 1.1 shows examples of (a) a simple graph and (b) a directed general graph with multiedges, loops and directed edges.

A representation of a simple graph is the *adjacency matrix*. For a simple graph $G(V, E)$ with N vertices, the adjacency matrix \mathbf{A} is an $N \times N$ square matrix. The element of the adjacency matrix A_{ij} is binary and defined as

$$A_{ij} := \begin{cases} 1 & \text{if there is an edge between node } i \text{ and node } j, \\ 0 & \text{otherwise.} \end{cases} \quad (1.1)$$

For directed graphs $A_{ij} = 1$ if there is an edge from j to i . Thus the adjacency matrix is symmetric for undirected graphs and asymmetric for directed graphs. If each edge (i, j) is assigned with a weight, the graph is called a *weighted graph*. The connectivity information of a weighted graph is encoded in a *weighted adjacency matrix*, or *connectivity matrix* \mathbf{K} which is defined as

$$K_{ij} := \begin{cases} \text{the weight of } (i, j) & \text{if there is an edge between node } i \text{ and node } j, \\ 0 & \text{otherwise.} \end{cases} \quad (1.2)$$

The *degree* $\deg(i)$ of a vertex i is the number of edges connected to the vertex:

$$\deg(i) := \sum_{j=1}^N A_{ij} \quad (1.3)$$

For weighted graphs we define the vertex degree as the sum of the weight of the edges connected to vertex i .

Another important matrix representation of a graph is the *graph Laplacian*, or the *Laplacian matrix*. For a simple graph $G(V, E)$ with $|V| = N$ vertices, its Laplacian matrix \mathcal{L} is defined as [4]

$$\mathcal{L} := \mathbf{D} - \mathbf{A}, \quad (1.4)$$

where \mathbf{D} is the *degree matrix* of G , a diagonal matrix with $D_{ij} = \delta_{ij} \deg(i)$. The Laplacian matrix can be interpreted as the discrete version of the negative Laplace operator $-\nabla^2$. This can be easily shown as follows. Suppose we have a quantity ψ_i , e.g. concentration of some substance, assigned to each vertex i in a network. Multiplying the vector of the quantity $\boldsymbol{\psi} = \{\psi_1, \dots, \psi_N\}$ by the Laplacian matrix, we can write the i -th element of the resulting vector as

$$(\mathcal{L}\boldsymbol{\psi})_i = \sum_j \mathcal{L}_{ij} \psi_j = \sum_j -A_{ij} \psi_j + \sum_j A_{ij} \psi_i = -\sum_j A_{ij} (\psi_j - \psi_i). \quad (1.5)$$

Recall that the second derivative of a one-dimensional continuous function $\Psi(x)$ over x is

$$\Psi''(x) = \lim_{h \rightarrow 0} \frac{\Psi(x+h) + \Psi(x-h) - 2\Psi(x)}{h^2}. \quad (1.6)$$

Comparing Eq. 1.5 and Eq. 1.6, we find that $-(\mathcal{L}\boldsymbol{\psi})_i$ is in fact a $\deg(i)$ -dimensional difference quotient at vertex i if we take a finite difference $h = 1$. This analog provides important intuition about the graph Laplacian, which helps the analysis in the later parts of the thesis.

For weighted graphs, we define the *weighted graph Laplacian* by replacing the binary entries of the adjacency matrix by the respective weight of the edges:

$$\mathcal{L}_{ij} := \begin{cases} -K_{ij} & \text{if } i \neq j, \\ \sum_{\ell=1}^N K_{i\ell} & \text{if } i = j. \end{cases} \quad (1.7)$$

1.1.2 Paths and distances

Intuitively a path between two vertices in a network is a route that runs from vertex to vertex along the edges. In the language of mathematics, a *path*¹ between vertex i and j

¹In this thesis we adopt Newman's terminology in [4]. We allow the repetition of vertices and edges in a *path*. In some books such repetitions are not allowed for *paths* but allowed for *walks*.

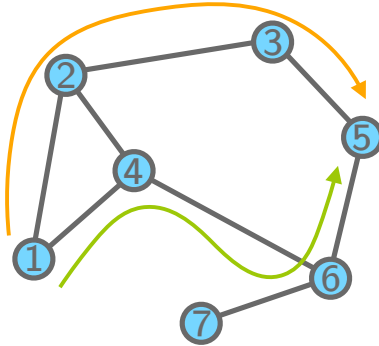


Fig. 1.2 Non-uniqueness of the shortest paths. There are two distinct shortest paths between node 1 and node 5, $1 \rightarrow 2 \rightarrow 3 \rightarrow 5$ and $1 \rightarrow 4 \rightarrow 6 \rightarrow 5$, indicated by the orange and the green arrow respectively. The geodesic distance $d(1, 5) = 3$.

in graph $G(E, V)$, denoted as $\mathcal{P}_{i \rightarrow j}$, is defined as a sequence of adjacent edges in E which connect a sequence of vertices in V with the initial vertex i and the final vertex j [4, 5]. The number of edges traversed along the path is called the *length* of the path.

For unweighted simple graphs, the total number of $\mathcal{P}_{i \rightarrow j}$ of length r , denoted as $\#\mathcal{P}_{i \rightarrow j}^{(r)}$, can be expressed in terms of the adjacency matrix \mathbf{A} [4]:

$$\#\mathcal{P}_{i \rightarrow j}^{(r)} = \sum_{k_1, \dots, k_{r-1}=1}^N A_{ik_1} A_{k_1 k_2} \cdots A_{k_{r-1} j} = (\mathbf{A}^r)_{ij}. \quad (1.8)$$

Because the product $A_{ik_1} A_{k_1 k_2} \cdots A_{k_{r-1} j}$ is 1 only if there exists a path of length r between i and j , otherwise it is 0. For weighted simple graphs the element of the adjacency matrix gives the edge weights, therefore $(\mathbf{A}^r)_{ij}$ gives the sum of the product of the coupling strength of the edges along the path over all paths between i and j :

$$(\mathbf{A}^r)_{ij} = \sum_{\mathcal{P}_{i \rightarrow j}^{(r)}} \prod_{(u,v) \in \mathcal{P}_{i \rightarrow j}^{(r)}} A_{uv}. \quad (1.9)$$

As the name suggests, a *shortest path*, or a *geodesic path* between two vertices i and j is the path with the smallest length among all $\mathcal{P}_{i \rightarrow j}$. Shortest paths are not necessarily unique, meaning there can be multiple paths with the same shortest length between a vertex pair (Fig. 1.2). The length of the shortest path is called the *geodesic distance* or simply the *distance* between the vertices in question. Mathematically the distance between the vertices i and j , $d(i, j)$, is the smallest value of r such that $(\mathbf{A}^r)_{ij} > 0$. The length of the longest geodesic path between any pair of vertices in a graph, if a path exists, is called the *diameter* of the graph.

Proposition 1. Let i and j be two distinct vertices in graph $G(V, E)$ with distance $d(i, j) = r$, and \mathcal{L} the graph Laplacian of G . Then for $d \in \mathbb{N}^+$,

$$(\mathcal{L}^d)_{ij} = \begin{cases} 0 & \text{for } d < r \\ \sum_{\mathcal{P}_{i \rightarrow j}^{(r)}} \prod_{(u,v) \in \mathcal{P}_{i \rightarrow j}^{(r)}} \mathcal{L}_{uv} & \text{for } d = r. \end{cases} \quad (1.10)$$

Proof. According to the definition of matrix multiplication, we have

$$(\mathcal{L}^d)_{ij} = \sum_{k_1, \dots, k_{d-1}=1}^N \mathcal{L}_{ik_1} \mathcal{L}_{k_1 k_2} \cdots \mathcal{L}_{k_{d-1} j}.$$

By the definition of graph Laplacian (Eq. 1.4), $\mathcal{L}_{uv} = -A_{uv}$ for all $u \neq v$. In the vertex sequence of any shortest paths between i and j , the vertices must be distinct, so there are no diagonal elements of \mathcal{L} that enter the product $\mathcal{L}_{ik_1} \mathcal{L}_{k_1 k_2} \cdots \mathcal{L}_{k_{d-1} j}$. Therefore

$$(\mathcal{L}^r)_{ij} = (-1)^r (\mathbf{A}^r)_{ij} = \sum_{\mathcal{P}_{i \rightarrow j}^{(r)}} \prod_{(u,v) \in \mathcal{P}_{i \rightarrow j}^{(r)}} (-A_{uv}) = \sum_{\mathcal{P}_{i \rightarrow j}^{(r)}} \prod_{(u,v) \in \mathcal{P}_{i \rightarrow j}^{(r)}} \mathcal{L}_{uv}. \quad (1.11)$$

For $d < r$, we have $(\mathbf{A}^r)_{ij} = 0$, since there are no paths from i to j with a length smaller than r . Hence $(\mathcal{L}^d)_{ij} = 0$. \square

In this thesis, we consider *connected* networks, meaning there should be at least one path between every pair of vertices in the graph. Or equivalently, the adjacency matrix of the graph should be *irreducible*. The topic of the thesis is the dynamical response of networks, therefore we naturally require that an initial local perturbation *can* actually reach every node of the network through at least one path. The irreducibility of the adjacency matrix is a direct result of graph connectivity [66]. Assume the adjacency matrix of graph $G(V, E)$ is reducible, then the vertices V can be partitioned into two nonempty sets V_1 and V_2 such that there is no edge between any vertex in V_1 and any vertex in V_2 . That means there are no paths between any node pairs with one node in V_1 and the other in V_2 . Hence graph G is not connected. For directed networks, we require them to be *strongly connected*, meaning there should be at least one directed path from every vertex to every other vertex.

1.2 Dynamical systems

While networks, or graphs, provide us a mathematical structure to represent the relationships between a collection of objects, whose properties are fixed in time, the theory of dynamical systems deals with *change*, with the state of systems that evolves in time.

In this thesis, we consider dynamical systems with continuous time and follow the definition in [67–69], where a *dynamical system* is defined as a tuple (S, T, Φ) :

- $S = \mathbb{R}^d$ is the *state space*. The state of the system is given by a d -dimensional vector $\mathbf{x} = (x_1, x_2, \dots, x_d) \in S$, and the state space is a collection of all possible states of the system. Here $d \in \mathbb{N}$ is the *order* of the dynamical system.
- $T = \mathbb{R}$ is the set of *time* t , or the so-called *evolution parameter*.
- $\Phi : S \times T \rightarrow S$ is the *evolution function* that dictates the temporal evolution of the system, and also known as a *flow* which obeys
 - i. $\Phi(\mathbf{x}, 0) = \mathbf{x}$;
 - ii. $\Phi(\Phi(\mathbf{x}, s), t) = \Phi(\mathbf{x}, s + t)$ for $s, t \in T$;
 - iii. $\dot{\Phi}(\mathbf{x}, \tau) = \mathbf{f}(\mathbf{x}, \tau)$ for all $\tau \in T$, with $\mathbf{f} : S \times T \rightarrow S$ is called the *vector field* of the flow Φ .

In the last property $\dot{\Phi}$ denotes the time derivative of Φ , $\dot{\Phi} := \frac{d\Phi}{dt}$. Property (iii) is known as the differentiability of flow, which is required since $T = \mathbb{R}$. The combination of the three properties associates the evolution function $\Phi(\mathbf{x}, t)$ with a system of d ordinary differential equations (ODEs)

$$\dot{\mathbf{x}} = \mathbf{f}(\mathbf{x}, t). \quad (1.12)$$

If \mathbf{f} does not depend explicitly on t , that is,

$$\dot{\mathbf{x}} = \mathbf{f}(\mathbf{x}), \quad (1.13)$$

then the dynamical system is called an *autonomous* system. Given the initial condition of the system $\mathbf{x}(t = 0) = \mathbf{x}_0$, the solution of the ODE system (Eq. 1.12) is the flow Φ with one of the variables being constant \mathbf{x}_0 :

$$\mathbf{x}(t) = \Phi(\mathbf{x}_0, t). \quad (1.14)$$

The solution $\mathbf{x}(t)$ is also referred to as the *trajectory* of the dynamical system with initial condition \mathbf{x}_0 .

1.2.1 Fixed Points and Linear Stability Analysis

In this thesis, we focus on autonomous systems² (Eq. 1.13). If a state $\mathbf{x}^* \in S$ satisfies $\Phi(\mathbf{x}^*, t) = \mathbf{x}^*$, or equivalently $\mathbf{f}(\mathbf{x}^*) = 0$ for all $t \in T$, then \mathbf{x}^* is referred to as a *fixed point* of the dynamical system. Fixed points can be classified as stable or unstable, according to the behavior of the trajectory of points in their vicinity [70, 69]. A fixed point \mathbf{x}^* is said to be *stable* or *Liapunov stable* if the trajectories that start near to \mathbf{x}^* remain near to it for all positive time, that is, for each $\varepsilon > 0$, there is a $\delta > 0$ such that if $\|\mathbf{x}(0) - \mathbf{x}^*\| < \delta$ then $\|\mathbf{x}(t) - \mathbf{x}^*\| < \varepsilon$ for all $t \geq 0$. Here $\|\cdot\|$ denotes some norm in the state space S . Furthermore, we say \mathbf{x}^* is *attracting* if all trajectories that start near to \mathbf{x}^* are guaranteed to arrive at \mathbf{x}^* eventually, that is, there is a $\delta > 0$ such that if $\|\mathbf{x}(0) - \mathbf{x}^*\| < \delta$ then $\lim_{t \rightarrow \infty} \mathbf{x}(t) = \mathbf{x}^*$. If a fixed point is both stable and attracting, we call it *asymptotically stable*. When a fixed point is Liapunov stable but not attracting, it is said to be *neutrally stable* or *marginally stable*. Finally, fixed points that are neither Liapunov stable nor attracting are *unstable*.

Moreover, the local behavior of a dynamical system $\dot{\mathbf{x}} = \mathbf{f}(\mathbf{x})$ near a fixed point \mathbf{x}^* can be assessed by the *linearization* of $\dot{\mathbf{x}} = \mathbf{f}(\mathbf{x})$ at $\mathbf{x} = \mathbf{x}^*$ if [71]:

$$\dot{\mathbf{X}} = \mathcal{J}\mathbf{X}, \quad (1.15)$$

where $\mathbf{X} := \mathbf{x} - \mathbf{x}^*$ is a small deviation away from the fixed point and $\mathcal{J} := D\mathbf{f}(\mathbf{x})|_{\mathbf{x}=\mathbf{x}^*}$ is the *Jacobian matrix* of function \mathbf{f} with respect to \mathbf{x} , namely

$$\mathcal{J}_{ij} := \left. \frac{\partial f_i}{\partial x_j} \right|_{\mathbf{x}=\mathbf{x}^*}. \quad (1.16)$$

For square matrix $\mathcal{J} \in \mathbb{R}^{d \times d}$ there exists a basis such that \mathcal{J} can be represented as a *Jordan canonical form* [72]:

$$\mathcal{J} = \begin{pmatrix} \mathcal{J}_1 & & & \mathbf{0} \\ & \mathcal{J}_2 & & \\ & & \ddots & \\ \mathbf{0} & & & \mathcal{J}_k \end{pmatrix} \quad (1.17)$$

²Here we refer to dynamical systems prior to perturbations. Yet we allow external perturbations that drives the system to be time-dependent, which makes the perturbed system non-autonomous.

where \mathcal{J}_j are *Jordan blocks*

$$\mathcal{J}_j = \begin{pmatrix} \mathbf{R}^{[j]} & \mathbf{I} & & \mathbf{0} \\ & \mathbf{R}^{[j]} & \mathbf{I} & \\ & & \ddots & \mathbf{I} \\ \mathbf{0} & & & \mathbf{R}^{[j]} \end{pmatrix} \quad (1.18)$$

with

$$\mathbf{R}^{[j]} = \begin{pmatrix} a^{[j]} & -b^{[j]} \\ b^{[j]} & a^{[j]} \end{pmatrix}, \text{ and } \mathbf{I} = \begin{pmatrix} 1 & 0 \\ 0 & 1 \end{pmatrix}, \quad (1.19)$$

$\sum_{j=1}^k \dim \mathcal{J}_j = d$. Each Jordan block \mathcal{J}_j is uniquely associated with an eigenvalue $\mu^{[j]} = a^{[j]} + i b^{[j]}$ and the corresponding (general) eigenvectors of the Jacobian matrix $\mathbf{w}^{[j]} = \mathbf{u}^{[j]} + i \mathbf{v}^{[j]}$ [69]. Then

$$E^s = \text{span} \left\{ \mathbf{u}^{[j]}, \mathbf{v}^{[j]} \mid a^{[j]} < 0 \right\}, \quad (1.20)$$

$$E^c = \text{span} \left\{ \mathbf{u}^{[j]}, \mathbf{v}^{[j]} \mid a^{[j]} = 0 \right\}, \quad (1.21)$$

$$\text{and } E^u = \text{span} \left\{ \mathbf{u}^{[j]}, \mathbf{v}^{[j]} \mid a^{[j]} > 0 \right\} \quad (1.22)$$

are called the *stable*, the *center* and the *unstable* subspace corresponding to eigenvalues $\mu^{[j]}$ with negative, zero and positive real parts respectively. All solutions in E^s approach the fixed point \mathbf{x}^* as $t \rightarrow \infty$ and all solutions in E^u approach the fixed point \mathbf{x}^* as $t \rightarrow -\infty$. The *Center Manifold Theorem* [71, 73] ensures that, there exist *stable*, *center* and *unstable* manifolds, W^s , W^c and W^u that are tangent to E^s , E^c and E^u at \mathbf{x}^* respectively, and they are all *invariant manifolds* under the flow Φ .

1.3 Dynamical systems on networks

Based on the theory introduced in the last two sections, we are now in the position to present a mathematical tool to describe and to analyze *dynamical processes on networks*, or *networks as dynamical systems*, in short, *network dynamics*. That is, the dynamics that occur on not only one, but a set of discrete entities, which interact with each other. As a whole, the set of connected dynamical systems can be viewed as a new, more complex dynamical system, whose behavior relies on the underlying nontrivial connectivity within the system.

Importantly, we should not confuse the term *network dynamics* with *dynamical networks*. The latter refers to the networks whose structure, i.e. the underlying graph, is changing with time. It is true not only that the topological structure of a network system can

affect the dynamics occurring on the network, e.g. Braess Paradox which postulates the addition of connectivity can lower the network performance, but also that the dynamical processes can affect the network structure. For example, in a power grid network, power generating units and power consuming units are nodes and the power transmission lines connecting them are edges. One of the state variables of the networked dynamical system is the AC power frequency at each node. When the power frequency, i.e. the rotation speed, of a power generator surpasses the designed speed limit, the generator would be shut down for protecting it from overheating and damage. Thus the node is considered to be “removed” from the network, which affects the collective dynamics of the power grid. Sometimes, the change in the dynamics such as the redistribution of flows again causes changes in network structure, thus triggers a *cascading failure*. The structure-changing networks are sometimes also called *adaptive networks* [74]. In this thesis, we assume the underlying network topologies are time-independent and thus focus on how dynamical processes occurring on networks are affected by network structure.

We consider a dynamical process on top of a network consisting of N vertices. The state $\mathbf{x}_i(t)$ of vertex $i \in \{1, 2, \dots, N\}$ at time $t \in \mathbb{R}$ is described by d variables: $\mathbf{x}_i(t) = [x_{i,1}(t), x_{i,2}(t), \dots, x_{i,d}(t)] \in \mathbb{R}^d$. The evolution of $\mathbf{x}_i(t)$ is governed partially by the local intrinsic dynamics at node i , $\mathbf{f}_i(\mathbf{x}_i) : \mathbb{R}^d \rightarrow \mathbb{R}^d$, and partially by the pair-wise interactions $\mathbf{g}_{ij}(\mathbf{x}_i, \mathbf{x}_j) : \mathbb{R}^d \times \mathbb{R}^d \rightarrow \mathbb{R}^d$ with the directly neighboring vertices j satisfying $A_{ij} \neq 0$:

$$\dot{\mathbf{x}}_i(t) = \mathbf{f}_i(\mathbf{x}_i) + \sum_{j=1}^N A_{ij} \mathbf{g}_{ij}(\mathbf{x}_i, \mathbf{x}_j). \quad (1.23)$$

For weighted graphs, the network dynamics is the same as (1.23) except A_{ij} is replaced by edge weight K_{ij} . Thus the dynamics of the whole network is described by Nd coupled equations: d equations for each of the N nodes.

A fixed point $\mathbf{x}^* = (\mathbf{x}_1^*, \mathbf{x}_2^*, \dots, \mathbf{x}_N^*) \in \mathbb{R}^{d \times N}$ of the network system (1.23) is given by the constraints $\dot{\mathbf{x}}_i(t) = 0$ for all $i \in \{1, 2, \dots, N\}$, thus by the solution of the set of Nd equations

$$\mathbf{f}_i(\mathbf{x}_i) + \sum_{j=1}^N A_{ij} \mathbf{g}_{ij}(\mathbf{x}_i, \mathbf{x}_j) = \mathbf{0} \quad (i = 1, \dots, N). \quad (1.24)$$

The linear stability of the system at $\mathbf{x} = \mathbf{x}^*$ is determined by the Jacobian matrix \mathcal{J} of (1.24) with

$$\begin{aligned}\mathcal{J}_{ij} &= \frac{\partial}{\partial \mathbf{x}_j} \left(\mathbf{f}_i(\mathbf{x}_i) + \sum_{\ell=1}^N A_{i\ell} \mathbf{g}_{i\ell}(\mathbf{x}_i, \mathbf{x}_\ell) \right) \Big|_{\mathbf{x}=\mathbf{x}^*} \\ &= \delta_{ij} \left(\frac{\partial \mathbf{f}_i}{\partial \mathbf{x}_i}(\mathbf{x}_i) \Big|_{\mathbf{x}=\mathbf{x}^*} + \sum_{\ell=1}^N A_{i\ell} \frac{\partial \mathbf{g}_{i\ell}}{\partial \mathbf{x}_i}(\mathbf{x}_i, \mathbf{x}_\ell) \Big|_{\mathbf{x}=\mathbf{x}^*} \right) + A_{ij} \frac{\partial \mathbf{g}_{ij}}{\partial \mathbf{x}_j}(\mathbf{x}_i, \mathbf{x}_j) \Big|_{\mathbf{x}=\mathbf{x}^*}. \quad (1.25)\end{aligned}$$

Technically, the Jacobian matrix \mathcal{J} for Eq. 1.23 is a tensor of rank 4. For brevity, here we express it as “a matrix with matrices as elements”: each element \mathcal{J}_{ij} of the Jacobian matrix is furthermore a matrix (Eq. 1.25). Alternatively, we can treat the state of the network system as a vector $\mathbf{x} \in \mathbb{R}^{Nd}$ and thus write the Jacobian matrix as a Nd by Nd square matrix. In the following chapters we adopt the latter approach for simplicity.

Chapter 2

Dynamics of Network Responses

In this chapter we present some general considerations about the dynamics of the collective responses of a high dimensional autonomous system under perturbations. As a starting point, we consider a general dynamical system at its fixed point and ask how it responds to small disturbances, including small shifts in the system's state and small external time-dependent driving signals. We start from the mathematical framework of linearizing dynamical systems introduced in the last chapter and derive solutions for dynamical system responses. As a special example, for *diffusively* coupled first-order dynamical systems, we establish a relation between the dynamical network responses and the network structures.

The first section is devoted to dynamical systems without external driving signals. Given small perturbations around a system's fixed point as the initial condition, we assume linear network responses to the perturbation and derive the time evolution of network responses in terms of the spectrum of the network's Jacobian matrix. In particular we focus on networks of first-order diffusively coupled systems, where we reveal the direct relation between the Jacobian matrix and the graph Laplacian. In the second section we discuss networks' linear responses to external driving signals, especially to weak sinusoidal signals. In the last section we give a summary of the network response dynamics in different scenarios: with symmetric or asymmetric Jacobians, and perturbations as deviations in initial conditions or as external driving signals.

2.1 Time evolution of small perturbations

Suppose $\mathbf{x}^* \in \mathbb{R}^N$ is a fixed point of an N dimensional autonomous dynamical system $\dot{\mathbf{x}} = \mathbf{f}(\mathbf{x})$. By definition, at the fixed point, the system stays at the fixed point if there are no perturbations i.e. $\dot{\mathbf{x}} = \mathbf{f}(\mathbf{x}^*) = 0$.

Now we consider the scenario where the system's state is perturbed, i.e. is close to but not exactly at the fixed point. We write the system's state as $\mathbf{x} = \mathbf{x}^* + \mathbf{X}$, where

$\mathbf{X} \in \mathbb{R}^N$ denotes a small deviation from the fixed point \mathbf{x}^* . Thus the system's dynamics $\dot{\mathbf{x}} = \dot{\mathbf{x}}^* + \dot{\mathbf{X}} = \dot{\mathbf{X}} = \mathbf{f}(\mathbf{x}^* + \mathbf{X})$ is essentially the dynamics of the small deviation $\mathbf{X}(t)$. Taylor expanding the function $\mathbf{f}(\mathbf{x}^* + \mathbf{X})$ on the right hand side to the first order of \mathbf{X} , we obtain the linearization (Eq. 1.15) of the system introduced in Sec. 1.2.1:

$$\dot{\mathbf{X}} = D\mathbf{f}(\mathbf{x})|_{\mathbf{x}=\mathbf{x}^*} = \mathcal{J}\mathbf{X}. \quad (2.1)$$

The Jacobian matrix in the linearized system 2.1 provides information about the stability of the fixed point through its eigenvalues, and moreover, Eq. 2.1 is solvable thus gives information about how small perturbations evolve in terms of linear approximation. The solution reads

$$\mathbf{X}(t) = e^{\mathcal{J}t}\mathbf{X}_0 = \left(\sum_{n=0}^{\infty} \frac{\mathcal{J}^n}{n!} t^n \right) \mathbf{X}_0 \quad (2.2)$$

with $\mathbf{X}_0 \in \mathbb{R}^N$ being the initial perturbation vector at $t = 0$. Particularly, if only one variable x_k is perturbed initially, $x_k(0) = x_k^* + \varepsilon$, i.e. there is only one non-zero element in \mathbf{X}_0 :

$$\mathbf{X}_0 = (0, \dots, \underbrace{\varepsilon}_{X_{0,k}}, \dots, 0), \quad (2.3)$$

then the small deviation at the i -th state variable is determined by the ik -th element of the powers of the Jacobian matrix:

$$X_i(t) = \varepsilon \sum_{n=0}^{\infty} \frac{(\mathcal{J}^n)_{ik}}{n!} t^n. \quad (2.4)$$

As discussed in Sec. 1.2.1, Jacobian matrix $\mathcal{J} \in \mathbb{R}^{N \times N}$ can be written in Jordan canonical form with respect to a basis of general eigenvectors in \mathbb{C} . The eigenvectors of Jacobian are linearly independent, but not necessarily orthogonal in general. In particular, when Jacobian \mathcal{J} is symmetric, its N eigenvectors are orthogonal if the eigenvalues are non-degenerate. Even if there are degenerate eigenvalues, it is always possible to find an orthogonal basis of \mathbb{R}^N based on the eigenvectors using Gram–Schmidt orthogonalization [75]. We can thus write the time evolution of the small perturbations in terms of the eigenvectors $\{\mathbf{w}^{[1]}, \dots, \mathbf{w}^{[N]}\}$ of the Jacobian matrix

$$\mathbf{X}(t) = \sum_{\ell=1}^N c^{[\ell]}(t) \mathbf{w}^{[\ell]}, \quad (2.5)$$

where $c^{[\ell]}(t)$ is the time-dependent coefficient associated to the eigenvector $\mathbf{w}^{[\ell]}$. Inserting this expression Eq. 2.5 into the linearized dynamics Eq. 2.8, we obtain the equation

for the coefficients

$$\sum_{\ell=1}^N \dot{c}^{[\ell]}(t) \mathbf{w}^{[\ell]} = \sum_{\ell=1}^N c^{[\ell]}(t) \mu^{[\ell]} \mathbf{w}^{[\ell]}. \quad (2.6)$$

If the eigenvectors are orthonormal to each other, $\mathbf{w}^{[i]} \cdot \mathbf{w}^{[j]} = \delta_{ij}$, we determine the coefficients by multiplying both sides of Eq. 2.6 with the N eigenvectors one by one. The coefficient $\dot{c}^{[\ell]}(t)$ obeys the dynamics $\dot{c}^{[\ell]}(t) = \mu^{[\ell]} c^{[\ell]}(t)$ with solution

$$c^{[\ell]}(t) = c_0^{[\ell]} e^{\mu^{[\ell]} t}, \quad (2.7)$$

where $c_0^{[\ell]}$ denotes the initial value of the coefficient at $t = 0$, i.e. the projection of the initial perturbation vector \mathbf{X}_0 on the respective eigenvector $\mathbf{w}^{[\ell]}$ such that $c_0^{[\ell]} = \mathbf{X}_0 \cdot \mathbf{w}^{[\ell]}$. Thus we have the solution

$$\mathbf{X}(t) = \sum_{\ell=1}^N (\mathbf{X}_0 \cdot \mathbf{w}^{[\ell]}) e^{\mu^{[\ell]} t} \mathbf{w}^{[\ell]}. \quad (2.8)$$

For a single-variable initial perturbation (Eq. 2.3), the perturbation evolves as

$$\mathbf{X}(t) = \varepsilon \sum_{\ell=1}^N (w_k^{[\ell]}) e^{\mu^{[\ell]} t} \mathbf{w}^{[\ell]}. \quad (2.9)$$

The solution of the system's small deviations (2.8) describes how an arbitrary-dimensional dynamical system behaves if it is slightly disturbed at a fixed point. In this sense, we call the small deviation \mathbf{X} as the *linear response*, or in short, the *response* of a dynamical system to perturbations in this thesis. Expressing the linear response of a high dimensional nonlinear dynamical system in terms of the Jacobian spectrum, i.e. (2.8), is a well-proven method and has been applied e.g. in identifying coherent generators in perturbed power grids [76].

2.1.1 Linear response in networks of first-order dynamical systems

Next we discuss the linear response to a perturbation in networks of diffusively coupled first-order dynamical systems. As we will show in the following, it is an interesting example since there is a direct relation between the Jacobian matrix of the dynamical system and the Laplacian matrix of the underlying graph. The analysis in this section lays foundation for the main results for networks of second-order oscillator to be presented in the later parts of the thesis.

We assume *diffusive* coupling function $g_{ij}(x_j - x_i)$ between node pair x_i and x_j . Every node i in a network is coupled to its nearest neighbor j (i.e. $A_{ij} \neq 0$) via a coupling function g_{ij} depending on the state difference of the node pair $(x_j - x_i)$ [77, 78]. This kind of coupling function appear in a variety of network models describing the dynamics of physiological and chemical systems [79–83], among which the most famous one is the Kuramoto model [65, 84] and its variations [26, 85–87].

As an illustrative example, we consider a network of N identical first-order dynamical systems with identical couplings. Each node follows the dynamics

$$\dot{x}_i = f(x_i) + \sum_{j=1}^N K_{ij} g(x_j - x_i) \quad \text{for } i \in \{1, \dots, N\}, \quad (2.10)$$

where x_i is the state variable of node i . The function $f : \mathbb{R} \rightarrow \mathbb{R}$ describes the intrinsic dynamics and the coupling function $g : \mathbb{R} \rightarrow \mathbb{R}$ describes the diffusive coupling between node pairs. The matrix $\mathbf{K} = (K_{ij})$ is the connectivity matrix (1.2) describing the interaction structure of the network, i.e. its element measures the coupling strength between nodes i and j . The solution of the equation system

$$f(x_i) + \sum_{j=1}^N K_{ij} g(x_j - x_i) = 0 \quad \text{for } i \in \{1, \dots, N\} \quad (2.11)$$

gives a fixed point $\mathbf{x}^* = (x_1^*, \dots, x_N^*)$ of the system. The dynamics of network's linear response and the stability of the fixed point is determined by the Jacobian matrix with

$$\mathcal{J}_{ij} = \delta_{ij} \left(\frac{df}{dx_i}(x_i) \Big|_{x_i=x_i^*} - \sum_{\ell=1}^N K_{i\ell} \frac{dg}{d(x_\ell - x_i)} \Big|_{x_{i,\ell}=x_{i,\ell}^*} \right) + K_{ij} \frac{dg}{d(x_j - x_i)} \Big|_{x_{i,j}=x_{i,j}^*} \quad (2.12)$$

If $\beta_i := -\frac{df}{dx_i}(x_i) \Big|_{x_i=x_i^*} \geq 0$, $\alpha_{ij} := \frac{dg}{d(x_j - x_i)} \Big|_{x_{i,j}=x_{i,j}^*} > 0$, and $K_{ij} > 0$ if there is an edge between i and j , then the fixed point of the network system is ensured to be at least neutrally stable. The Jacobian matrix

$$\mathcal{J}_{ij} = \begin{cases} -\beta_i - \sum_{\ell=1}^N K_{i\ell} \alpha_{i\ell} & \text{if } i = j, \\ K_{ij} \alpha_{ij} & \text{otherwise,} \end{cases} \quad (2.13)$$

is symmetric if the network is undirected ($K_{ij} = K_{ji}$), the derivative of the coupling function is even ($\alpha_{ij} = \alpha_{ji}$). Additionally \mathcal{J} is diagonally dominant:

$$|\mathcal{J}_{ii}| = \left| -\beta_i - \sum_{\ell=1}^N K_{i\ell} \alpha_{i\ell} \right| = \beta_i + \sum_{\ell=1}^N K_{i\ell} \alpha_{i\ell} \geq \sum_{\ell=1}^N K_{i\ell} \alpha_{i\ell} = \sum_{\ell=1}^N |K_{i\ell} \alpha_{i\ell}| = \sum_{j=1}^N |K_{ij} \alpha_{ij}|.$$

The *Gershgorin circle theorem* states that every eigenvalue of a square matrix $B = (b_{ij}) \in \mathbb{C}^{N \times N}$ is contained in some disk $D_j = \{z : |z - a_{jj}| \leq r_j, z \in \mathbb{C}\}$ with $r_j = \sum_{k=1, k \neq j}^N |a_{jk}|$ in the complex plane [88]. For the Jacobian matrix (Eq. 2.13) all the discs lie on the left side of the imaginary axis, i.e. in $\{z \mid \operatorname{Re}(z) \leq 0\}$. In addition, the Jacobian eigenvalues and eigenvectors are real since the Jacobian is Hermitian. Therefore, all eigenvalues are non-positive real numbers, and the eigenvalues can be zero only when there exists some $\beta_i = 0$. Consequently, the fixed point is stable, and has center subspace, i.e. is neutrally stable only when there are $\beta_i = 0$ for some i .

Since the Jacobian matrix is symmetric, its eigenvectors form an orthonormal basis and hence the linear response of first-order networks (Eq. 2.10) can be written as Eq. 2.8. Especially, if $\beta_i = 0$ for all i , then the Jacobian is exactly the negative of the Laplacian matrix of the underlying graph: $\mathcal{J} = -\mathcal{L}$, if we view $K_{ij} \alpha_{ij}$ as the weight of edge (i, j) . Thus, the Jacobian eigenvectors are identical to the Laplacian eigenvectors with the respective eigenvalues being opposite. Thus the linear response can also be expressed as

$$\mathbf{X}(t) = \sum_{\ell=1}^N (\mathbf{X}_0 \cdot \mathbf{v}^{[\ell]}) e^{-\lambda^{[\ell]} t} \mathbf{v}^{[\ell]}, \quad (2.14)$$

where $\mathbf{v}^{[\ell]}$ denotes the ℓ -th eigenvector of the graph Laplacian and $\lambda^{[\ell]} \geq 0$ the corresponding eigenvalue. For notational simplicity we sort the Laplacian eigenvalues as $0 = \lambda^{[0]} \leq \lambda^{[1]} \leq \dots \leq \lambda^{[N-1]}$. The eigenvalue 0 and its corresponding eigenvector $(1, 1, \dots, 1)$ is a consequence of the construction of the Laplacian matrix.

If only one node k is initially perturbed with $\varepsilon > 0$, the linear response reads

$$\mathbf{X}(t) = \varepsilon \sum_{\ell=1}^N (v_k^{[\ell]}) e^{-\lambda^{[\ell]} t} \mathbf{v}^{[\ell]}. \quad (2.15)$$

For networks of m -order dynamical systems with $m \geq 2$, the state of the network system can be written as $\mathbf{x} = (\mathbf{x}^{(0)}, \dots, \mathbf{x}^{(m)})$ with $\mathbf{x}^{(i)} = (x_1^{(i)}, \dots, x_N^{(i)})$ being the vector of the i -th time derivative of (x_1, \dots, x_N) . The corresponding Jacobian is almost always asymmetric, thus its eigenvectors are not orthonormal and the solution for linear response Eq. 2.8 is not valid. In Part II and Part III where we consider the linear response of networks of second-order phase oscillators, we will present a new way to find the solution,

i.e. exploiting the Hermitian-ness of other matrices occurring in the equation, such as the graph Laplacian.

2.2 Network responses to external driving

In last section we have discussed how a small deviation in state variables from a fixed point evolves under linear approximation. However, in many natural and artificial network systems, not only small kicks in systems' state, but also temporal fluctuations in input signals are present due to the environmental influence. How networks self-organized respond to those external driving signals essentially underlie the robust functioning of these network systems.

The classical linear response theory (LRT) in statistical mechanics, first formulated by R. Kubo in 1957 [89], is devoted to reveal the relation between the time-dependent linear response of a system to a weak external field and the dynamical properties of the system at equilibrium. Furthermore, LRT was also generalized to nonequilibrium steady states with necessary modifications [90]. However, the linear response function in LRT usually characterizes the dependence of an macroscopic observable on an macroscopic field which influences the whole system.

In this thesis, we solve for the linear response of networked dynamical systems to local driving signals in the spirit of the LRT in statistical mechanics: we assume the nodal response in networks is proportional to the driving signal and look for the relation between the responses and the external signal. However, important differences lie in the nature of the system in question and in the range of the external influence. We focus on networked systems where each node can be seen as a discrete entity and the specific connectivity topology essentially determines the system's dynamical behavior, unlike the continuous system where only the averaged quantity, i.e. the observable, is relevant and interesting. Furthermore, we investigate the system's response to a local signal and ask how signals at the different positions generate qualitatively different network responses, which is a nontrivial question in networked system. In this section we make first discussions on the linear response of networks to external driving signals. As we will see in a few moments, a general and explicit answer is extremely difficult to find. In the later parts of the thesis, we will give answer for a specific model class.

We consider a general dynamical system at a fixed point \mathbf{x}^* , perturbed by a time-dependent *driving vector* $\mathbf{D}(t)$. The linear response of the system $\mathbf{X}(t)$ follows

$$\dot{\mathbf{X}} = \mathcal{J}\mathbf{X} + \mathbf{D}(t). \quad (2.16)$$

Given the initial condition \mathbf{X}_0 , the solution of the inhomogeneous matrix ODE reads

$$\mathbf{X}(t) = e^{\mathcal{J}t} \left(\mathbf{X}_0 + \int e^{-\mathcal{J}t} \mathbf{D}(t) dt - \int \mathbf{D}(t) dt \right). \quad (2.17)$$

However, for a general $\mathbf{D}(t)$ it is not easy to compute the integrals.

In the following we focus on the case where the perturbation has the form of a sinusoidal function, which serves as a basis for the characterization of more complicated signals through Fourier analysis. Let the system be perturbed by a single small sinusoidal signal at node k with magnitude $\varepsilon > 0$, frequency ω and phase φ , i.e.

$$\mathbf{D}(t) = (0, \dots, \underbrace{\varepsilon e^{i(\omega t+\varphi)}}_{D_k}, \dots, 0). \quad (2.18)$$

To further simplify the problem and obtain an explicit analytical solution for the linear response $\mathbf{X}(t)$, we assume the Jacobian matrix to be symmetric, as in the case where the network is undirected and diffusively coupled. Thus we can express the linear response in terms of the eigensystem of the Jacobian. Again writing the linear response as a linear combination of the orthogonal Jacobian eigenvectors with time-dependent coefficients as in Eq. 2.5, we have

$$\sum_{\ell=1}^N \dot{c}^{[\ell]}(t) \mathbf{w}^{[\ell]} = \sum_{\ell=1}^N c^{[\ell]}(t) \mu^{[\ell]} \mathbf{w}^{[\ell]} + \mathbf{D}(t). \quad (2.19)$$

Exploiting the orthogonality of the Jacobian eigenvectors, we determine the coefficients as the solution of

$$\dot{c}^{[\ell]}(t) = c^{[\ell]}(t) \mu^{[\ell]} + \varepsilon w_k^{[\ell]} e^{i(\omega t+\varphi)}, \quad \text{for } \mu^{[\ell]} \neq 0. \quad (2.20)$$

The general solution of Eq. 2.20 is of the form of the complementary solution to the homogeneous differential equation $Ae^{\mu^{[\ell]}t}$ plus a particular solution of the inhomogeneous solution $\frac{\varepsilon w_k^{[\ell]}}{-\mu^{[\ell]} + i\omega} e^{i(\omega t+\varphi)}$. The initial condition of the coefficients $c_0^{[\ell]} = \mathbf{X}_0 \cdot \mathbf{w}^{[\ell]}$. Thus, the solution for the coefficients reads

$$c^{[\ell]}(t) = (\mathbf{X}_0 \cdot \mathbf{w}^{[\ell]}) e^{\mu^{[\ell]}t} + \frac{\varepsilon w_k^{[\ell]} e^{i\varphi}}{-\mu^{[\ell]} + i\omega} (-e^{\mu^{[\ell]}t} + e^{i\omega t}) \quad (2.21)$$

Especially, for $\mu^{[\ell]} = 0$, the dynamics of the corresponding coefficient follows the dynamics

$$\dot{c}^{[\ell]}(t) = \varepsilon w_k^{[\ell]} e^{i(\omega t+\varphi)}, \quad (2.22)$$

which gives the solution

$$c^{[\ell]}(t) = (\mathbf{X}_0 \cdot \mathbf{w}^{[\ell]}) + \frac{\varepsilon w_k^{[\ell]} e^{i\varphi}}{i\omega} (-1 + e^{i\omega t}). \quad (2.23)$$

This solution (2.23) coincides with the solution (2.21) with $\mu^{[\ell]} = 0$. Therefore the linear response of the network system to an sinusoidal signal can be written unitedly as

$$\mathbf{X}(t) = \sum_{\ell=1}^N \left[(\mathbf{X}_0 \cdot \mathbf{w}^{[\ell]}) e^{\mu^{[\ell]} t} + \frac{\varepsilon w_k^{[\ell]} e^{i\varphi}}{-\mu^{[\ell]} + i\omega} (-e^{\mu^{[\ell]} t} + e^{i\omega t}) \right] \mathbf{w}^{[\ell]}. \quad (2.24)$$

2.3 Summary

In this chapter we discussed the dynamics of network responses to perturbations in the linearized regime near a fixed point. Specifically, apart from the solutions for a general dynamical system, analytical expressions of network linear responses are derived also for networks with symmetric Jacobians. We established the relation $\mathcal{J} = -\mathcal{L}$ between the Jacobian and the graph Laplacian of the underlying network structure for those networks. A tabular list of the solutions and the corresponding constraints is shown in Tab. 2.1.

	no external driving $\dot{\mathbf{X}} = \mathcal{J}\mathbf{X}$	with external driving $\dot{\mathbf{X}} = \mathcal{J}\mathbf{X} + \mathbf{D}(t)$
general	$\mathbf{X}(t) = e^{\mathcal{J}t} \mathbf{X}_0$	$\mathbf{X}(t) = e^{\mathcal{J}t} \left(\mathbf{X}_0 + \int e^{-\mathcal{J}t} \mathbf{D}(t) dt - \int \mathbf{D}(t) dt \right)$
first-order	if \mathcal{J} symmetric, eigenvectors $\{\mathbf{w}^{[1]}, \dots, \mathbf{w}^{[N]}\}$ orthogonal	
	$\mathbf{X}(t) = \sum_{\ell=1}^N (\mathbf{X}_0 \cdot \mathbf{w}^{[\ell]}) e^{\mu^{[\ell]} t} \mathbf{w}^{[\ell]}$	sinusoidal driving: $D_i(t) = \delta_{ik} e^{i(\omega t + \varphi)}$ $\mathbf{X}(t) = \sum_{\ell=1}^N \left[(\mathbf{X}_0 \cdot \mathbf{w}^{[\ell]}) e^{\mu^{[\ell]} t} + \frac{\varepsilon w_k^{[\ell]} e^{i\varphi}}{-\mu^{[\ell]} + i\omega} (-e^{\mu^{[\ell]} t} + e^{i\omega t}) \right] \mathbf{w}^{[\ell]}$
second-order	if networks <i>diffusively</i> coupled, $\mathcal{J} = -\mathcal{L}$	\mathcal{J} almost always asymmetric
	see Part III	see Part II, Part III

Table 2.1 **Solutions of networks' linear responses to perturbations.** Listed are solutions of a network system's linear responses near a fixed point under different conditions.

We considered the time evolution of a initial small deviation \mathbf{X}_0 in an arbitrary dimensional dynamical system with and without external driving $\mathbf{D}(t)$. For both cases it is

possible to write down the general solution (see the first row of Tab. 2.1). However, computing the linear responses explicitly is not easy since both solutions contain matrix exponential which implies infinite power series of matrices. Furthermore, the solution for linear responses under external driving is even more complicated to compute since it involves also the integral $\int e^{-\mathcal{J}t} \mathbf{D}(t) dt$.

In particular, the solutions are more tractable if the system's Jacobian is symmetric. In this case the Jacobian eigenvectors form an orthonormal basis, thus we can project the system's linear response to the eigenmodes of the Jacobian and determine the projections using the orthogonality of the eigenvectors. Observing the solutions in terms of the Jacobian eigensystem (the second row of Tab. 2.1), we see both solutions contain the term describing the exponential decay of the initial deviation in respective eigenmodes. The solution for systems with an external sinusoidal driving contains an additional term describing a sinusoidal response with the same frequency as the driving signal and with a shift in amplitude and in phase (see Eq. 2.24).

A symmetric Jacobian is a natural result for networks of first-order dynamical systems with diffusive and undirected coupling. In such networks, it differs from the graph Laplacian only by a sign, $\mathcal{J} = -\mathcal{L}$, thus both matrices share the same set of eigenvectors and opposite corresponding eigenvalues. As a result, there is a direct relation between the system's dynamics and its underlying network topology.

However, for networks of higher-order dynamical systems, the Jacobian matrix is typically not symmetric. Hence the Jacobian eigenvectors do not consist an orthogonal basis on which the linear responses can be projected. In Part II and Part III of the thesis, we will discuss the linear responses of the network of second-order phase oscillators with diffusive and undirected coupling. The graph Laplacian of this type of networks are symmetric, and enter naturally into the dynamics of networks' linear response. Thus the orthogonality of the Laplacian eigenvectors can be exploited to obtain tractable solutions of networks' linear responses. They are related to the structural features of the network through Laplacian eigenvalues and eigenvectors.

Chapter 3

Phase Oscillator Networks and Power Grids

In the first two chapters we introduced the basic concepts of the networks of dynamical systems, and discussed the general aspects of network systems' linear responses to perturbations. However, as concluded in last chapter, networks' dynamical responses are not trivial to compute explicitly for systems with non-symmetric Jacobians, which is typically the case for networks of dynamical systems with order greater than one. From this chapter on, we focus on an important class of network systems, namely the second-order phase oscillator networks with diffusive and undirected coupling, and investigate the linear responses of such network systems.

In this chapter, we first introduce in Sec. 3.1 the basics of phase oscillator networks and the most important feature of such networks, i.e., synchronization. In particular, we introduce the oscillator model of power grids in Sec. 3.2 as an important application of the second-order Kuramoto model with inertia.

3.1 Synchronization and phase oscillator networks

Synchronization is one of the most fascinating cooperative phenomena observed in nature. Systems across biology, chemistry, physics and social life exhibit the tendency to operate in synchrony, that is, the rhythmical behavior of individual elements in the system tend to act coherently [91, 92]. Such synchronizable systems require *self-sustained oscillatory*¹ elements with *interactions*. The state of each element is determined by both the internal processes and the external forcing, from other elements or from signals outside the system. Despite the very different and complex biological or technological origin of the internal processes, one hopes to find a few basic principles which capture the essence of synchronization.

¹Here “self-sustained oscillation” means the oscillator has a stable closed isolated trajectory, i.e. a limit cycle, even without external forcing.

Since first observed in 1665 by Christiaan Huygens, synchronization has been studied intensively for centuries. Within the framework of modern nonlinear dynamics, mathematical models of synchronizable systems include *relaxation oscillator* networks and *phase oscillator* networks. The dynamics of a relaxation oscillator is characterized by a slow growth of some quantity, i.e. a “relaxation period”, and a fast resetting when the quantity reaches a threshold. The reset of one oscillator produces a pulse, which alters the current state of the neighboring oscillators by shifting their phases, i.e. the so-called *pulse-coupling*. This mechanism is abundant in nature so that the relaxation oscillator network successfully models e.g. the firing of a neuron [93, 94], the heartbeat [95, 96] and the flashing of fireflies [12].

Another model class exhibiting synchronization phenomena, the phase oscillator networks, deals with a population of nonlinearly coupled oscillators moving coherently in the attracting limit cycle of constant amplitude. The state of a phase oscillator is only described by the phase and its time derivatives. In 1967, Winfree pioneered a phase oscillator model based on the mean-field assumption of oscillators’ interactions. For the first time it revealed that synchronization is related to a threshold in coupling strength: oscillators synchronize when the coupling is strong enough [97]. This threshold, i.e., the minimal coupling strength required to achieve synchronization is called the *critical coupling*. Not long after, in 1975, motivated by the behavior of chemical and biological oscillators, Kuramoto proposed a simple functional form of the coupling of oscillators: the sine of the oscillator pair’s phase difference [65, 84]. Kuramoto’s model is mathematically tractable due to its simplicity, yet is complex enough to exhibit a variety of nontrivial self-organizing behavior [98–100, 16, 85]. Over several decades, the Kuramoto model and its variations found widespread applications such as neural networks [101, 102], Josephson junctions arrays [103] and charge-density waves [104, 105].

Due to the ubiquity and the importance of phase oscillator networks, in this thesis, we focus on the network dynamics of a phase oscillator model class closely related to the paradigmatic Kuramoto model. We consider a network of N coupled phase oscillators $i \in \{1, \dots, N\}$ with dynamics

$$\alpha_i \dot{\theta}_i + \beta_i \ddot{\theta}_i = \Omega_i + \sum_{j=1}^N K_{ij} g(\theta_j - \theta_i) + \varepsilon_i D_i(t). \quad (3.1)$$

The state of oscillator i at time t is described by its phase angle $\theta_i(t) \in [0, 2\pi)$ and phase velocity $\dot{\theta}_i(t)$. $\Omega_i \in \mathbb{R}$ denotes the intrinsic frequency or acceleration of oscillator i , depending on the order of the dynamics². The coupling between oscillators adopts a diffusive form (see Sec. 2.1.1): the interaction between oscillator i and j is described by a function $g(\cdot)$ depending on only the phase difference $\theta_j - \theta_i$ of the node pair with a

²If $\beta_i \neq 0$, the dynamics is of order 2, Ω_i acts as an intrinsic angular acceleration. If $\beta_i = 0$, $\alpha_i > 0$, then the dynamics is of order 1 and Ω_i is the intrinsic frequency of the oscillator, i.e. the oscillator rotates with this frequency when it is not connected to other oscillators.

coupling strength $K_{ij} > 0$. The matrix $\mathbf{K} = (K_{ij})$ encodes the weighted connectivity of the underlying network structure, as defined in Eq. 1.2. Core parameters α_i and β_i in this model class set the relative influences of the rates of change of the phase angles and those of the phase velocities:

- For $\alpha_i \neq 0$, $\beta_i \equiv 0$ for all i and $g(\cdot) = \sin(\cdot)$, the famous Kuramoto type models arise, characterizing synchronization, phase locking, desynchronization, chimera states and other patterns across systems in biology, engineering and physics [65, 98–100, 16, 85].
- For $\alpha_i \equiv 0$ and $\beta_i \neq 0$ we obtain an oscillator network system without damping, i.e. a Hamiltonian system [106]. As we will see later, the dynamics of the network response of such systems follows the discrete version of the wave equation.
- Taking generically both $\alpha_i, \beta_i \neq 0$ and $g(\cdot) = \sin(\cdot)$ yields a characteristic AC power grid model, the swing equation on networks [26, 107], on which we pay special attention in this thesis. The details of the model will be introduced in Sec. 3.2.

The functions $D_i(t)$ represent the driving signal with strength ε_i at oscillator i and collectively constitute a high-dimensional, distributed dynamic driving signal to the network. The core question we try to answer in the thesis is, how does a network collectively respond to such dynamic signals?

The analysis and computation we present in Part II and Part III of the thesis are based on taking $g(\theta_j - \theta_i) = \sin(\theta_j - \theta_i)$. However, as we will see, the results can be easily translated to network systems with an arbitrary diffusive coupling function $g(\theta_j - \theta_i)$ with its first order derivative $\frac{dg}{d(\theta_j - \theta_i)}$ is even, so that the graph Laplacian is symmetric.

3.2 The oscillator model of power grids

In this section we focus on an important realistic aspect of the second-order Kuramoto networks with inertia, i.e. model class 3.1 with $\alpha_i, \beta_i > 0$ and $g(\cdot) = \sin(\cdot)$. With these settings, this model captures a simplified dynamics of the alternating current (AC) power grids [26, 107].

3.2.1 Modeling power grid dynamics

Modern power grids typically consist of thousands of generators linked across thousands of kilometers [108]. Hence they are probably the largest man-made infrastructure network ever existed. The stable operation of power grids affects almost every aspect of the modern life, while it relies on the collective dynamical behavior of the numerous

elements in the networks. Modeling the dynamics of power grids is thus a task with both great significance and complexity.

Available power grid models range from the simplest single-node model where the whole power grid is modeled as a copper plate [109, 110] to detailed component-level models such as [111] which are typically used by engineers for specific simulations. The so-called *oscillator model* of AC power grids proposed by Filatrella et al. [26] captures the essential dynamical features of power grids, but is still mathematically simple enough to allow for analytical analysis and hence understanding of the collective power grid dynamics on a large scale. Fruitful research on power grid dynamics has been stimulated by this model, e.g. [107, 112, 113, 47]. Filatrella's power grid model essentially combines the *swing equation* of a synchronous machine, which is the standard equation describing rotor dynamics in engineering, with a few simplifications for AC power transmission in high-voltage transmission networks, and establishes a relation between the synchronization of coupled Kuramoto-type oscillators and the stability of AC power grids. In the following we briefly demonstrate this connection.

The swing equation of synchronous machines *Synchronous machines* are the most widely used AC power units. It converts mechanical power to electric power as a generator, or vice versa, converts electric power from the grid to mechanical power as a motor. Its functioning is due to the interaction of the electromagnetic fields of its two parts, the stator and the rotor (see Fig. 3.1). When operated as a generator, the rotor is driven by e.g. a turbine and its rotation induces an alternating current voltage in the stator with a frequency synchronous to the rotation. The process is reversed when a synchronous machine is operated as a motor.

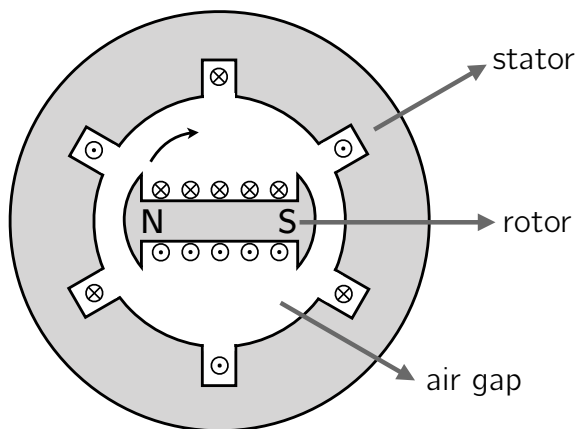


Fig. 3.1 A schematic diagram of a six-pole three-phase synchronous machine. Figure reproduced based on [114].

At steady state, a synchronous machine rotates with a fixed frequency Ω_0^m corresponding to the nominal operation frequency of the connected power grid $\Omega_0 = 2\pi \times 50$ or $2\pi \times$

60 Hz.³ Any acceleration or deceleration of the rotation is a result of the imbalance of the torque acting on the rotor, which is governed by Newton's second law [115, 114]

$$I\ddot{\theta}^m + D^m\dot{\theta}^m = T^{\text{mech}} - T^{\text{el}}, \quad (3.2)$$

where $\theta^m(t)$ [rad] is the rotor angle deviated from the rotating reference frame $\Omega_0^m t$, I [kg m²] is the moment of inertia of the turbine and the rotor, D^m [N m s] is the coefficient of the damping torque caused by the velocity-dependent friction at the air gap. T^{mech} [N m] denotes the net mechanical torque, i.e. the torque produced by the turbine less the damping torque at the reference frequency $D^m\Omega_0^m$ and T^{el} [N m] denotes the counteracting electromagnetic torque.

Expressing the torque on the right hand side of the equation in terms of power and noticing the rotation speed deviation during a disturbance is usually small such that $(\dot{\theta}^m + \Omega_0^m)^{-1} \approx (\Omega_0^m)^{-1}$, we rewrite equation of motion as

$$I\ddot{\theta}^m + D^m\dot{\theta}^m = \frac{1}{\Omega_0^m} (P^{\text{mech}} - P^{\text{el}}), \quad (3.3)$$

where P^{mech} [W] and P^{el} [W] are the net injected mechanical power and the transmitted electrical power respectively. If the machine is operated as a generator, P^{mech} is positive, and if operated as a motor, P^{mech} is negative. For a synchronous machine with p poles per phase, the relation of the mechanical rotor angle θ^m and the mechanical reference angular velocity Ω_0^m with their electrical counterparts reads

$$\theta^m(t) = \frac{\theta(t)}{p/2}, \quad \Omega_0^m = \frac{\Omega_0}{p/2}. \quad (3.4)$$

Inserting this relation to the equation of motion, we obtain the *swing equation* describing the dynamics of the synchronous machine in terms of the electrical *load angle* θ and the input- and output-power

$$M\ddot{\theta} + D\dot{\theta} = P^{\text{mech}} - P^{\text{el}}, \quad (3.5)$$

where $M = (p/2)^2\Omega_0 I$ is the angular momentum of the rotor at the synchronous speed and $D = (p/2)^2\Omega_0 D^m$ is the *damping coefficient* of the machine. In practice the swing equation is usually written in per unit form, so that the dynamics of synchronous machines with diverse sizes become comparable via the normalized parameters of the moment of inertia and the damping, which we will discuss in detail in Sec. 7.2.

From swing equation to Kuramoto-like oscillators The swing equation of a synchronous machine (Eq. 3.5) relates the dynamics of the load angle θ to the power flowing

³The grid operation frequency $\Omega_0 = 2\pi \times 50$ Hz for power grids in Europe and $\Omega_0 = 2\pi \times 60$ Hz for power grids in USA [106].

into and out of the machine. Thus a direct analogy between the power grids and the phase oscillator networks can be made: every synchronous machine, generator or consumer, can be viewed as a oscillator, whose state is described by its load angle θ and its frequency deviation $\dot{\theta}$, while the electrical power transmission lines between the connected machines are viewed as edges. With the following assumptions, we can find an explicit correspondence between the swing equation and the dynamics of a second-order Kuramoto oscillator.

The time-dependent voltage at node i of an AC power grid has the form $\tilde{U}_i = U_i \sin(\Omega_0 t + \theta_i)$ with amplitude U_i , frequency Ω_0 and phase angle θ_i . The effective voltage at this node, i.e. the voltage value in a direct current circuit that would produce the same power over a resistive load, is $\bar{U}_i = \frac{1}{\sqrt{2}} U_i e^{i\theta_i}$. The *complex power transmission* S_{ij} between two three-phase synchronous machines i and j is conventionally defined as three times the effective voltage at node i multiplied by the complex conjugate of the effective current on the transmission line \bar{I}_{ij} , i.e. $S_{ij} := 3\bar{U}_i \bar{I}_{ij}^*$. In the calculation of the power transmission, we make the following assumptions:

Assumption 1. *The voltage amplitude at each node is identical and constant: $U_i \equiv U, \forall i$.*

Assumption 2. *All transmission lines are without Ohmic loss: $Y_{ij} \equiv iB_{ij}, \forall (i, j)$, with Y_{ij} being the admittance of the line connecting node pair and B_{ij} being the susceptance.*

Assumption 3. *Only the active power transmission $P_{ij} := \text{Re}[S_{ij}]$ is considered.⁴*

Incorporating these assumptions, the (active) power transmission from node i to node j reads

$$P_{ij} = \text{Re}[S_{ij}] = \text{Re}[3\bar{U}_i \bar{I}_{ij}^*] = \frac{3}{2} U^2 B_{ij} \sin(\theta_i - \theta_j). \quad (3.6)$$

Thus, a Kuramoto-type diffusive coupling $\sin(\theta_i - \theta_j)$ arises. Inserting the expression of the electrical power transmission term Eq. 3.6 into the swing equation (Eq. 3.5), we obtain the dynamics for node i as

$$M_i \ddot{\theta}_i + D_i \dot{\theta}_i = P_i^{\text{mech}} - \sum_{j=1}^N \frac{3}{2} U^2 B_{ij} \sin(\theta_i - \theta_j). \quad (3.7)$$

⁴The imaginary part of S_{ij} , the *reactive power*, is not consumed by the load but converted back and forth between the energy source and the reactive loads, i.e. inductors and capacitors. Although the reactive power does no work but only heats up the grid, it is necessary for sustaining the voltage level.

The simplified oscillatory dynamics of synchronous machines in AC power grids Eq. 3.7 has exactly the same form of the second-order phase oscillator model Eq. 3.1 with $\alpha_i, \beta_i > 0$ and $g(\cdot) = \sin(\cdot)$. We thus obtain the *oscillator model of AC power grids*

$$\ddot{\theta}_i = P_i - \alpha_i \dot{\theta}_i + \sum_{j=1}^N K_{ij} \sin(\theta_j - \theta_i), \quad (i = 1, \dots, N) \quad (3.8)$$

with parameter mappings

$$\alpha_i = \frac{D_i}{M_i}, \quad P_i = \frac{P_i^{\text{mech}}}{M_i}, \quad K_{ij} = \frac{3}{2} \frac{U^2 B_{ij}}{M_i}. \quad (3.9)$$

The coupling strength $K_{ij} = K_{ji} > 0$ represents the maximal power that can be transmitted between node pair (i, j) , we thus alternatively call it the *transmission capacity* of line (i, j) . Furthermore, we define the *power flow* from node j to node i as the active power transmission

$$F_{ji} := K_{ij} \sin(\theta_j - \theta_i). \quad (3.10)$$

See Fig. 3.2 for an illustrative sketch of the oscillator model of a seven-node power grid network.

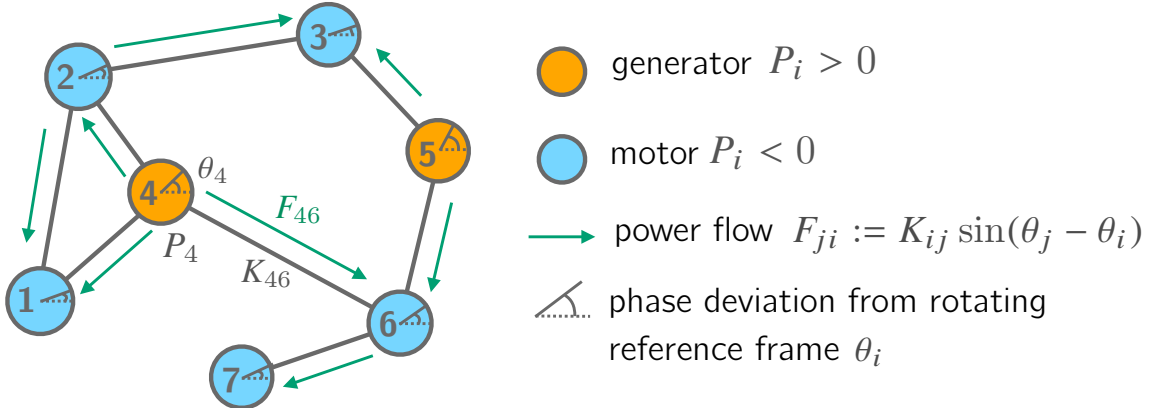


Fig. 3.2 A sketch of the oscillator model of a small AC power grid. The power flow from a generator, node 4, to a motor, node 6, is labeled: $F_{46} = K_{46} \sin(\theta_6 - \theta_4)$. The green arrows represent the direction of the positive power flows, e.g. $F_{46} > 0$. It does not mean the edges are directed in the oscillator model.

So far we derived the oscillator model of AC power grid based on the swing equation of synchronous machines and a few simplifying assumptions on power transmission. More technical details of the model derivation can be found in e.g. [116].

3.2.2 The steady states of the oscillator model

The normal operation state of a power grid corresponds to a stable fixed point of the oscillator model (Eq. 3.8): all synchronous machines run with the same nominal grid frequency Ω_0 , but with fixed relative phases between each other, i.e. the oscillator network system is in a *phase-locked* state [91]. The dynamical properties of such fixed points essentially determine the stability of the normal operation of power grids. Thus we briefly review the bifurcation nature and the stability of the fixed points, which lay the foundation for the further analysis on the network responses of the oscillator model to perturbations.

The existence of fixed points A fixed point of the oscillator model of power grids (Eqs. 3.8) $\boldsymbol{\theta}^* = (\theta_1^*, \dots, \theta_N^*)$ is a solution of the transcendental equations

$$P_i + \sum_{j=1}^N K_{ij} \sin(\theta_j - \theta_i) = 0, \quad (i = 1, \dots, N), \quad (3.11)$$

which come from the oscillator model with $\ddot{\boldsymbol{\theta}} = \mathbf{0}$ and $\dot{\boldsymbol{\theta}} = \mathbf{0}$. It is shown that the existence of such fixed points is equivalent to the existence of local extrema or saddle points of the potential function

$$V(\boldsymbol{\theta}) = - \sum_{j=1}^N P_j \theta_j - \frac{1}{2} \sum_{i,j=1}^N K_{ij} \cos(\theta_j - \theta_i), \quad (3.12)$$

where $\frac{\partial V}{\partial \theta_i} = 0$ for all $i \in \{1, \dots, N\}$ [106, 117]. In fact, if the damping is zero $\alpha_i = 0$ for all i , the network system defined by Eqs. 3.8 becomes a Hamiltonian system with the kinetic energy

$$T(\dot{\boldsymbol{\theta}}) = \frac{1}{2} \sum_{j=1}^N \dot{\theta}_j^2 \quad (3.13)$$

and the potential energy defined in Eq. 3.12 [106]. The set of all fixed points of the oscillator model are identical to the set of fixed points of the corresponding Hamiltonian system, since the solution of Eq. 3.11 is independent of the damping α_i . Furthermore, the fixed points are also the same as those of the Kuramoto model, which can be viewed as the over-damped limit of the oscillator model of power grids.

As an illustrative example, we consider an elementary system consisting of two oscillators, one generator and one motor (consumer) with the same damping α , opposite injected power $P_1 = P = -P_2$ and coupling strength K . For the two-element system, the potential function $V(\boldsymbol{\theta}) = -\frac{1}{2}\Delta P \Delta \theta - \frac{1}{2}K \cos(\Delta \theta)$ with $\Delta P = P_1 - P_2$ and $\Delta \theta = \theta_1 - \theta_2$ has a tilted washboard-like shape [116, 106]. When the coupling strength is greater than the critical

coupling $K > K_c = P$, two fixed points exist: $\Delta\theta^*_1 = \arcsin \frac{\Delta P}{2K}$ and $\Delta\theta^*_2 = \pi - \arcsin \frac{\Delta P}{2K}$. At $K = K_c = P$, the two fixed points merge to one. Naturally one would ask, what are the stability properties of the fixed points? And how do they change when the parameters P , K and α are varied? We discuss these questions in the following subsections.

Linear stability of steady states The linear stability of a specific fixed point $\boldsymbol{\theta}^*$ is determined by the Jacobian eigenvalues of the system at $\boldsymbol{\theta} = \boldsymbol{\theta}^*$ (see Sec. 1.2.1). A small deviation of the phase angles from the fixed point under observation $\boldsymbol{\Theta} := \boldsymbol{\theta} - \boldsymbol{\theta}^*$ follows the linearized dynamics

$$\frac{d}{dt} \begin{pmatrix} \boldsymbol{\Theta} \\ \dot{\boldsymbol{\Theta}} \end{pmatrix} = \mathcal{J} \begin{pmatrix} \boldsymbol{\Theta} \\ \dot{\boldsymbol{\Theta}} \end{pmatrix}, \quad (3.14)$$

where the Jacobian matrix is given by

$$\mathcal{J} = \begin{pmatrix} \mathbf{0}_N & \mathbf{I}_N \\ -\mathcal{L} & -\mathcal{A} \end{pmatrix} \quad (3.15)$$

with $\mathbf{0}_N$ being an $N \times N$ zero matrix, \mathbf{I}_N an $N \times N$ identity matrix and \mathcal{A} an $N \times N$ diagonal matrix with $\mathcal{A}_{ii} = \alpha_i$. The matrix \mathcal{L} is the Hesse matrix of the potential function $V(\boldsymbol{\theta})$ (Eq. 3.12):

$$\mathcal{L}_{ij} = \frac{\partial^2 V}{\partial \theta_i \partial \theta_j} = \begin{cases} -K_{ij} \cos(\theta_j^* - \theta_i^*) & \text{if } i \neq j, \\ \sum_{\ell=1}^N K_{i\ell} \cos(\theta_\ell^* - \theta_i^*) & \text{if } i = j. \end{cases} \quad (3.16)$$

Remarkably, this Hesse matrix can be interpreted as the weighted graph Laplacian of the underlying network structure of the system (cf. Eq. 1.7) if we let $K_{ij} \cos(\theta_j^* - \theta_i^*)$ be the weight of edge (i, j) . We thus denote the matrix with the symbol of the graph Laplacian \mathcal{L} ⁵ and its eigenvalues as $0 = |\lambda^{[0]}| \leq |\lambda^{[1]}| \leq \dots \leq |\lambda^{[N-1]}|$.

It is proved that the fixed point $\boldsymbol{\theta}^*$ is at least neutrally stable if all of the Laplacian eigenvalues are non-negative [106]. Let $\mathbf{w} = (\mathbf{w}_1, \mathbf{w}_2) \in \mathbb{C}^{2N}$ with $\mathbf{w}_1, \mathbf{w}_2 \in \mathbb{C}^N$ be an eigenvector of \mathcal{J} with eigenvalue $\mu \in \mathbb{C}$. We then have

$$\mu \mathbf{w}_2 = -\mathcal{L} \mathbf{w}_1 - \mathcal{A} \mathbf{w}_2 \quad \text{and} \quad \mathbf{w}_2 = \mu \mathbf{w}_1, \quad (3.17)$$

which combinedly lead to

$$\mu^2 \mathbf{w}_1 + \mu \mathcal{A} \mathbf{w}_1 + \mathcal{L} \mathbf{w}_1 = 0. \quad (3.18)$$

⁵The Laplacian eigenvalues are real since \mathcal{L} is Hermitian: $K_{ij} \cos(\theta_j^* - \theta_i^*) = K_{ji} \cos(\theta_i^* - \theta_j^*)$.

Multiplying both sides with \mathbf{w}_1^\dagger , the conjugate transpose of \mathbf{w}_1 , we thus obtain an expression of μ

$$\mu = \frac{-\chi_2 \pm \sqrt{\chi_2^2 - 4\chi_1\chi_3}}{2\chi_1}, \quad (3.19)$$

where $\chi_1 = \mathbf{w}_1^\dagger \mathbf{w}_1 \geq 0$, $\chi_2 = \mathbf{w}_1^\dagger \mathcal{A} \mathbf{w}_1 \geq 0$ and $\chi_3 = \mathbf{w}_1^\dagger \mathcal{L} \mathbf{w}_1 \geq 0$. χ_2 and χ_3 are non-negative since $\mathcal{A}_{ii} = \alpha_i > 0$ and \mathcal{L} is positive semi-definite. Therefore, we always have $\text{Re}(\mu) \leq 0$. Additionally, $\mu = 0$ only when $\mathcal{L}\mathbf{w}_1 = 0$, where \mathbf{w}_1 has to lie in the linear span of the Laplacian eigenvector $\mathbf{v}^{[0]} = (1, 1, \dots, 1)$ corresponding to $\lambda^{[0]} = 0$. Thus, the fixed point is neutrally stable only for small deviation vectors $\Theta \in \text{span}(\{\mathbf{v}^{[0]}\})$, and is asymptotically stable for any other perturbations. In fact, a perturbation $\Theta \in \text{span}(\{\mathbf{v}^{[0]}\})$ means a uniform global phase shift in the oscillator network, which leads the network system to a new fixed point $\tilde{\theta}^* = \theta^* + a\mathbf{v}^{[0]}$ with $a \in \mathbb{R}$ and stay there if no further perturbation is present.

Stability, overload and bifurcation As discussed, a fixed point of the oscillator model is ensured to be stable by the non-negativity of the Laplacian eigenvalues. It is a well-known result [4] and can be easily shown by applying the Gershgorin circle theorem that the non-negativity of the Laplacian eigenvalues is in fact a consequence of the non-negativity of the edge weights, i.e.

$$\cos(\theta_j^* - \theta_i^*) \geq 0 \quad \text{for all } (i, j). \quad (3.20)$$

If a power grid is weakly loaded, which is usually the case in real-world power grids for safety reasons, the phase difference between connected oscillators are typically small $|\theta_i^* - \theta_j^*| \leq \pi/2$, so the condition (3.20) is always satisfied. In further analysis we assume (3.20) is true for the fixed point under consideration.

We have seen from the example of the two-element toy model that the existence of fixed points is closely related to the critical coupling $K_c = P$: a stable operation is possible only when the transmission capacity of transmission lines is large enough to carry the power must to be transmitted, i.e. K_c . If the transmission capacity in a grid is greater than K_c , there are fixed points such that $|\theta_i^* - \theta_j^*| < \pi/2$ for all (i, j) and thus the fixed points are stable. If smoothly decreasing the coupling strengths K_{ij} or cranking up the power injections P_i , at least one pair of stable fixed points approach to each other and vanish in a saddle-node bifurcation [116, 106]. At the bifurcation point the grid is critically coupled, meaning at least one of transmission line becomes fully-loaded: the flow $F_{ij} = K_{ij} = K_c$, i.e. $|\theta_i - \theta_j| = \pi/2$ and thus $\mathcal{L}_{ij} = \mathcal{L}_{ji} = 0$. Beyond the point the stable fixed point is lost and the grid becomes desynchronized. However, as reported in [106], another scenario can occur where the loss of stability is not related to overload: if at the fixed point the condition (3.20) is not satisfied, then the edge weights can be negative thus the above

results do not apply. In this case the desynchronization of the grid is a collective effect of the interacting components with no transmission line is overloaded.

Part II. Dynamic Patterns in Steady Network Responses

In Part II of the thesis, we investigate the long-term dynamic patterns emerging in the collective network responses to external driving signals. In comparison to previous studies which focus on *instability*-induced long-term patterns [17–19, 30–36], we study the dynamic response patterns induced by persistent spatiotemporal driving signals. Especially, we focus on a model class of Kuramoto-like oscillator networks (3.1) introduced in Chap. 3.

In Chap. 4, we first derive the analytical solutions of the linear network responses close to a fixed point in the spirit of the linear response theory.

Based on the solutions, in Chap. 5, we identify three frequency regimes of dynamic response patterns, which show distinct spatiotemporal features depending on the frequency of the external driving signal.

Furthermore, in Chap. 6 we explore how the dynamic responses change at the high- and low-damping limits, where the model approaches the classical Kuramoto model and a Hamiltonian system respectively.

In the last chapter of Part II, Chap. 7, we turn our attention towards a practical aspect: we develop a method to accurately predict the dynamic network responses to irregular and distributed signals. In particular, we discuss the application of the predictive method in estimating the frequency response in AC power grids to fluctuations in power production and consumption. Last but not least, we investigate the limit of validity of our theory.

Chapter 4

Steady Network Responses to External Driving Signals

Starting from this chapter, we present the main results of this thesis. In this chapter, we present an analytical analysis of the linear dynamic responses to an external driving signal in second-order Kuramoto-like oscillator networks. In particular, we focus on the scenario where a single node in the network is driven by a small sinusoidal signal, since sinusoidal functions are the building blocks of signals with more complex forms in Fourier analysis. By observing the solution of the total network phase, i.e. the sum of the oscillator phases over all nodes in the network, we distinguish the *transient* and the *steady*, or *long-term* ($t \rightarrow \infty$) network responses (Sec. 4.1), and then focus on the latter for investigating the formation of the dynamic pattern across network under perturbation (Sec. 4.2 and Sec. 4.3). Specifically, we explicitly derive the solution of networks' nodal steady responses to a sinusoidal signal (Sec. 4.2) and to a step-function signal as a special case with the driving frequency being zero (Sec. 4.3). These analytical solutions allow for theoretical insights into the dynamic network responses near a fixed point, and lay a solid foundation for the investigation of the dynamic pattern formation in networks, which will be elaborated in next chapter.

4.1 Total network response to a sinusoidal signal

From now on we focus on the networks of N coupled Kuramoto-like oscillators following the dynamics

$$\alpha_i \dot{\theta}_i + \beta_i \ddot{\theta}_i = \Omega_i + \sum_{j=1}^N K_{ij} \sin(\theta_j - \theta_i) + \varepsilon D_i(t), \quad \text{for } i \in \{1, \dots, N\}, \quad (4.1)$$

which is essentially the model class introduced in Sec. 3.1 plus setting $g(\cdot) = \sin(\cdot)$. We first investigate how such a network as a whole responds to a sinusoidal driving signal at node k starting from $t = 0$, $D_i = H(t)\delta_{ik}e^{i(\omega t+\varphi)}$. Here $H(t)$ is a heaviside function with value 0 for $t < 0$ and 1 for $t \geq 0$. Throughout the thesis, we assume both the driving signals and thus the responses start from $t = 0$, i.e. equal to zero for $t < 0$, therefore for notational brevity we drop the heaviside function $H(t)$ for the signals and the responses in the rest of the thesis. The initial conditions at $t = 0$ are specified *ad hoc*. First intuition about the response can be gained by observing the trajectory of the sum of the phases of all units, $\theta^{\text{tot}} := \sum_{i=1}^N \theta_i$, which is rigorously solvable. For simplicity we assume $\alpha_i \equiv \alpha \neq 0$, $\beta_i \equiv \beta \neq 0$ for all i , and thus obtain an equation for θ^{tot} by summing the N equations for each node:

$$\alpha\dot{\theta}^{\text{tot}} + \beta\ddot{\theta}^{\text{tot}} = \sum_{i=1}^N \Omega_i + \sum_{i=1}^N \sum_{j=1}^N K_{ij} \sin(\theta_j - \theta_i) + \varepsilon e^{i(\omega t+\varphi)}. \quad (4.2)$$

Due to the assumption that the considered network system has at least one stable fixed point, the sum of the natural frequencies/accelerations must add up to zero: $\sum_{i=1}^N \Omega_i = 0$. At the fixed point $\boldsymbol{\theta} = \boldsymbol{\theta}^*$, the time derivatives vanish by definition, we thus have

$$\sum_{i=1}^N \Omega_i = - \sum_{i=1}^N \sum_{j=1}^N K_{ij} \sin(\theta_j^* - \theta_i^*) = 0. \quad (4.3)$$

The double summation $\sum_{i=1}^N \sum_{j=1}^N K_{ij} \sin(\theta_j - \theta_i)$ is zero since $\sin(-x) = -\sin(x)$ for $x \in \mathbb{R}$ and $K_{ij} = K_{ji}$ for all (i, j) . In the context of power grids, Eq. 4.3 implies that the power generation and power consumption must be balanced to ensure a steady state. The total network phase θ^{tot} thus follows

$$\alpha\dot{\theta}^{\text{tot}} + \beta\ddot{\theta}^{\text{tot}} = \varepsilon e^{i(\omega t+\varphi)}, \quad (4.4)$$

which is analytically solvable for θ^{tot} . In the most general case where $\beta > 0$ and $\alpha > 0$, Eq. 4.4 is a second order inhomogeneous ODE, which has the solution

$$\theta^{\text{tot}}(t) = C_1 + C_2 e^{-\frac{\alpha}{\beta}t} + \frac{\varepsilon}{-\beta\omega^2 + i\alpha\omega} e^{i(\omega t+\varphi)} \quad (4.5)$$

with the constants being

$$\begin{aligned} C_1 &= \theta_0^{\text{tot}} + \frac{\beta}{\alpha}\dot{\theta}_0^{\text{tot}} - \frac{\varepsilon e^{i\varphi}}{-\beta\omega^2 + i\alpha\omega} \left(\frac{i\beta\omega}{\alpha} + 1 \right) \\ C_2 &= -\frac{\beta}{\alpha}\dot{\theta}_0^{\text{tot}} + \frac{\beta}{\alpha} \frac{i\varepsilon e^{i\varphi}}{-\beta\omega + i\alpha}. \end{aligned}$$

Here $\theta_0^{\text{tot}} := \theta^{\text{tot}}(0)$ and $\dot{\theta}_0^{\text{tot}} := \dot{\theta}^{\text{tot}}(0)$ are the initial conditions of θ^{tot} and $\dot{\theta}^{\text{tot}}$ at $t = 0$. Please note that the solution Eq. 4.5 is general in the sense that it is valid as long as the parameters Ω_i and K_i are chosen such as the system has at least a fixed point. The validity of the solution does not require the system to be in the neighborhood of the fixed point. Additionally, we notice that the initial conditions of the system appear only in the coefficients of the first and the second term, which is respectively a constant and a term decaying with time. The third term, a sinusoidal response, is independent of the initial conditions.

In the thesis we focus on a network system's response near its steady state, thus we let the initial conditions be a fixed point $\boldsymbol{\theta}^*$, i.e. $\theta_0^{\text{tot}} = \sum_{i=1}^N \theta_i^* \equiv \theta^{*,\text{tot}}$ and $\dot{\theta}_0^{\text{tot}} = 0$. In this case, the evolution of the total network phase reads

$$\theta^{\text{tot}}(t) = \theta^{*,\text{tot}} + \frac{i\varepsilon}{\alpha\omega} e^{i\varphi} + \frac{\varepsilon\beta}{\alpha^2 + i\alpha\beta\omega} e^{i\varphi} e^{-\frac{\alpha}{\beta}t} + \frac{\varepsilon}{-\beta\omega^2 + i\alpha\omega} e^{i(\omega t + \varphi)}. \quad (4.6)$$

The solution Eq. 4.6 implies that, as a whole, the network responds to a sinusoidal driving signal with (i) a constant total phase shift $\frac{i\varepsilon}{\alpha\omega} e^{i\varphi}$ from the fixed point, (ii) an exponentially decaying transient response with a time constant $\frac{\beta}{\alpha}$, and (iii) a persistent sinusoidal response with the same frequency as the driving signal and a complex amplitude $\frac{\varepsilon}{-\beta\omega^2 + i\alpha\omega}$ (See Fig. 4.1 for an example). Interestingly, the complex amplitude is independent of the initial condition of the system. It also implies a phase shift $\arctan\left(\frac{\alpha}{\beta\omega}\right)$ between the periodic behavior of the total network response and the external driving signal.

The scenarios where $\alpha \neq 0, \beta = 0$ and $\alpha = 0, \beta \neq 0$, which are respectively associated to the high- and low-damping limit of the second-order oscillator networks, will be discussed in Chap. 6.

4.2 Steady nodal responses to a sinusoidal signal

As revealed by the solution of the total network response (Eq. 4.6), the long-term impact of a sinusoidal driving ($t \rightarrow \infty$) is embodied in a constant total phase shift and a sinusoidal total response with a complex amplitude. We notice that the strength of both effects are proportional to the amplitude of the driving signal ε , which suggests a *linear* response function. This is noticeable since it means that, the network as a whole responds to external driving linearly even far from a fixed point.

However, a more intriguing question is, how is the total network response is distributed across the network, i.e. what are the dynamic network response patterns evoked by a sinusoidal signal? Taking the hints from the solution of the total phase response (4.6), which (i) includes *linear response*, i.e. the response up to the first order of the perturbation strength, and (ii) contains a phase shift and a sinusoidal function, we assume the phase of

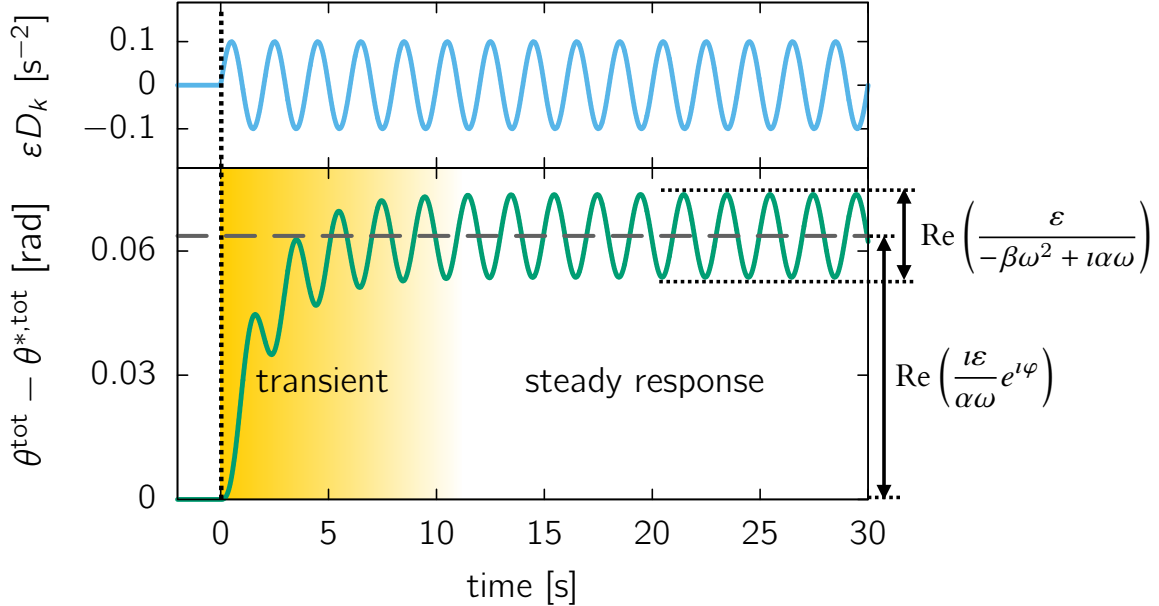


Fig. 4.1 Total network response to a sinusoidal driving signal. An Illustration for the transient and the steady response in the total network response given in Eq. 4.6. The transient stage characterized by an exponential decay is shaded in yellow. The steady response contains a phase shift (grey dashed line) and a sinusoidal oscillation. The magnitude of the phase shift and the amplitude of the sinusoidal response is labeled. The sinusoidal driving signal is plotted in the upper panel and its onset is indicated by a dotted line. Parameters: $\alpha = 0.5 \text{ s}^{-1}$, $\beta = 1$, $\omega = 0.5 \times 2\pi \text{ Hz}$, $\varphi = -\frac{\pi}{2}$, $\varepsilon = 0.1 \text{ s}^{-2}$.

node i responding to a driving signal at node k has a similar form:

$$\theta_i^{(k)}(t) = \theta_i^* + \varepsilon \eta_i^{(k)} + \varepsilon \Theta_i^{(k)}(t), \quad (4.7)$$

where the nodal phase shift $\eta_i^{(k)}$ satisfies

$$\sum_{i=1}^N \eta_i^{(k)} = \frac{i e^{i\varphi}}{\alpha \omega} \quad (4.8)$$

and the nodal sinusoidal response has a harmonic form

$$\Theta_i^{(k)}(t) = A_i^{(k)} e^{i(\omega t + \Delta_i^{(k)})}. \quad (4.9)$$

The amplitude $A_i^{(k)}$ of the nodal sinusoidal response and the response phase shift $\Delta_i^{(k)}$ with respect to the sinusoidal signal generally depend on the site k of perturbation and the site i of response.

Interestingly, the nodal phase shift is identical for each node, i.e. $\eta_i^{(k)} = \eta$. To show this, we insert Eq. 4.7 into the dynamics of the sinusoidally driven network system (Eq. 4.1), and Taylor-expand the nonlinear coupling function up to the first order of small phase deviation $\theta_i - \theta_i^*$, we obtain

$$-\beta\omega^2\Theta_i^{(k)} + i\alpha\omega\Theta_i^{(k)} = \sum_{j=1}^N K_{ij} \cos(\theta_j^* - \theta_i^*) (\eta_j^{(k)} - \eta_i^{(k)} + \Theta_j^{(k)} - \Theta_i^{(k)}) + \delta_{ik}e^{i(\omega t+\varphi)}. \quad (4.10)$$

By defining the *response vector* $\Theta^{(k)} := (\Theta_1^{(k)}, \Theta_2^{(k)}, \dots, \Theta_N^{(k)})$, the *normalized driving vector* $\mathbf{D}^{(k)}$ with $D_i^{(k)} = \delta_{ik}e^{i(\omega t+\varphi)}$, the *shift vector* $\mathbf{H}^{(k)} := (\eta_1^{(k)}, \eta_2^{(k)}, \dots, \eta_N^{(k)})$, we write the linearized dynamics in a matrix form

$$(-\beta\omega^2 + i\alpha\omega + \mathcal{L})\Theta^{(k)} - \mathbf{D}^{(k)} = -\mathcal{L}\mathbf{H}^{(k)}, \quad (4.11)$$

where the Laplacian matrix \mathcal{L} as defined in 3.16 arises. If integrated over a period $[0, \frac{2\pi}{\omega}]$, the left hand side of Eq. 4.13 vanishes since both $\Theta^{(k)}$ and $\mathbf{D}^{(k)}$ are sinusoidal. Thus on the right hand side $\mathcal{L}\mathbf{H}^{(k)} = \mathbf{0}$. As discussed in Sec. 3.2.2, the weighted graph Laplacian has only one zero eigenvalue $\lambda^{[0]}$ with corresponding eigenvector $\mathbf{v}^{[0]} = (1, 1, \dots, 1)$ for connected networks. This implies that the shift vector $\mathbf{H}^{(k)} \in \text{span}(\{\mathbf{v}^{[0]}\})$, meaning the shift of each node is identical:

$$\eta_i^{(k)} = \eta = \frac{ie^{i\varphi}}{\alpha\omega N}. \quad (4.12)$$

This result can be understood as, for a network system close to the fixed point, the constant phase shift evoked by a single sinusoidal signal (Eq. 4.5) is distributed homogeneously across the network as $t \rightarrow \infty$.

Hence the dynamics of the steady linear network responses (Eq. 4.11) is essentially

$$(-\beta\omega^2 + i\alpha\omega + \mathcal{L})\Theta^{(k)} = \mathbf{D}^{(k)}. \quad (4.13)$$

The solution of the steady linear responses $\Theta^{(k)}$ can be obtained by utilizing the orthogonality of the Laplacian eigenvectors. \mathcal{L} is real and symmetric, so that its eigenvectors $\{\mathbf{v}^{[0]}, \dots, \mathbf{v}^{[N-1]}\}$ form an orthogonal basis. Expressing the response vector $\Theta^{(k)}$ in this basis, i.e. $\Theta^{(k)} = \sum_{\ell=0}^{N-1} c^{[\ell]} \mathbf{v}^{[\ell]}$, we obtain

$$-\omega^2\beta \sum_{\ell=0}^{N-1} c^{[\ell]} \mathbf{v}^{[\ell]} + i\omega\alpha \sum_{\ell=0}^{N-1} c^{[\ell]} \mathbf{v}^{[\ell]} + \sum_{\ell=0}^{N-1} \lambda^{[\ell]} c^{[\ell]} \mathbf{v}^{[\ell]} = \mathbf{D}^{(k)}. \quad (4.14)$$

The coefficient of projection $c^{[m]}$ for the m -th eigenspace is given by multiplying both sides of the equation by Laplacian eigenvector $\mathbf{v}^{[m]}$:

$$c^{[m]} = \frac{v_k^{[m]} e^{i(\omega t + \varphi)} v_k^{[m]}}{-\omega^2 \beta + i\omega\alpha + \lambda^{[m]}}. \quad (4.15)$$

Thus the solution of the steady linear sinusoidal response vector $\Theta^{(k)}$ reads

$$\Theta^{(k)} = e^{i(\omega t + \varphi)} \sum_{\ell=0}^{N-1} \frac{v_k^{[\ell]} v_i^{[\ell]}}{-\beta\omega^2 + i\alpha\omega + \lambda^{[\ell]}} \mathbf{v}^{[\ell]}. \quad (4.16)$$

Thus, close to a fixed point, the steady nodal response at node i to a sinusoidal signal at node k is written as

$$\theta_i^{(k)}(t) = \theta_i^* + \frac{i\varepsilon e^{i\varphi}}{\alpha\omega N} + \sum_{\ell=0}^{N-1} \frac{\varepsilon e^{i(\omega t + \varphi)} v_k^{[\ell]} v_i^{[\ell]}}{-\beta\omega^2 + i\alpha\omega + \lambda^{[\ell]}}. \quad (4.17)$$

Here all Laplacian eigenvalues are non-negative since in the normal operation state the phase difference between neighboring units satisfies $\theta_j^* - \theta_i^* \leq \pi/2$ for all edges (i, j) (see Sec. 3.2.2). Thus the eigenvalues and the corresponding eigenvectors $v^{[0]}, v^{[1]}, \dots, v^{[N-1]}$ of \mathcal{L} are indexed as $0 = \lambda^{[0]} < \lambda^{[1]} < \dots < \lambda^{[N-1]}$.

Since each node shares the same phase shift, $\frac{i\varepsilon e^{i\varphi}}{\alpha\omega N}$, interesting and nontrivial dynamic response patterns are essentially encoded in the steady sinusoidal response (Eq. 4.16): in long term, every node in the network responds sinusoidally, with the same frequency as the driving signal but with a characteristic complex amplitude, depending on the parameters α, β , the driving frequency ω and its position in the network. It implies a change in amplitude and in phase between the sinusoidal driving signal and the sinusoidal response. Therefore we define the complex amplitude characterizing the nodal response as the *nodal response factor* of node i to a sinusoidal perturbation at node k

$$R_i^{(k)} := \sum_{\ell=0}^{N-1} \frac{v_k^{[\ell]} v_i^{[\ell]}}{-\beta\omega^2 + i\alpha\omega + \lambda^{[\ell]}}. \quad (4.18)$$

The change in amplitude and the phase shift in the nodal response can be expressed as the absolute value and the complex argument of $R_i^{(k)}$:

$$A_i^{(k)} = |R_i^{(k)}| = \sqrt{(\operatorname{Re} R_i^{(k)})^2 + (\operatorname{Im} R_i^{(k)})^2}, \quad (4.19)$$

$$\Delta_i^{(k)} - \varphi = \arg(R_i^{(k)}) = \operatorname{atan2}(\operatorname{Im} R_i^{(k)}, \operatorname{Re} R_i^{(k)}) \quad (4.20)$$

with

$$\operatorname{Re}(R_i^{(k)}) = \sum_{\ell=0}^{N-1} \frac{v_k^{[\ell]} v_i^{[\ell]} (-\beta\omega^2 + \lambda^{[\ell]})}{(-\beta\omega^2 + \lambda^{[\ell]})^2 + \alpha^2\omega^2} \quad (4.21)$$

$$\operatorname{Im}(R_i^{(k)}) = \sum_{\ell=0}^{N-1} \frac{v_k^{[\ell]} v_i^{[\ell]} (-\alpha\omega)}{(-\beta\omega^2 + \lambda^{[\ell]})^2 + \alpha^2\omega^2}. \quad (4.22)$$

We call the amplitude of the sinusoidal response $A_i^{(k)}$ as the *nodal response strength* and the phase difference $\Delta_i^{(k)} - \varphi$ as the *nodal response phase delay*. Here the function $\operatorname{atan2}(y, x)$ gives the principle value of the function $\arctan(y/x)$ in the range $(-\pi, \pi]$, i.e. the argument of the complex number $x + iy$.

Remarkably, the nodal response factor is symmetric: $R_i^{(k)} = R_k^{(i)}$. That means the effect of a sinusoidal signal at node k on another node i is identical to the effect of a sinusoidal signal at node i on node k .

In general, the parameters α_i and β_i can be heterogeneous across the network. For such systems, the steady nodal response can be estimated by again linearizing the impact of the heterogeneity. Without loss of generality, we assume $\beta_i \equiv 1$ for all i , which is equivalent to rescaling the dynamics of each node by dividing both sides of the equation with β_i . In this way, the heterogeneity in the relation between the change rates of θ_i in the nodal dynamics is concentrated in the (rescaled) parameter α_i . Treating α_i as a quantity fluctuating around the network average $\alpha_0 := \frac{1}{N} \sum_i \alpha_i$, i.e. $\alpha_i = \alpha_0 + \alpha'_i$ with small α'_i , we assume the steady nodal response as

$$\Theta_i^{(k)} = \Theta_{0,i}^{(k)} + \Theta_i'^{(k)}, \quad (4.23)$$

that is, the sum of two parts: the response to the average parameter, $\Theta_{0,i}^{(k)}$, and the small correction of response caused by the parameter heterogeneity $\Theta_i'^{(k)}$. The dynamics of the network response for heterogeneous α_i reads

$$-\omega^2 \Theta^{(k)} + \imath\omega \boldsymbol{\alpha} \circ \Theta^{(k)} + \mathcal{L}\Theta^{(k)} = \mathbf{D}^{(k)}, \quad (4.24)$$

where “ \circ ” denotes the element-wise (Schur) product of two vectors. Inserting the assumptions for $\boldsymbol{\alpha}$ and $\Theta^{(k)}$ to the dynamics (4.24), and neglecting the term to the second order of smallness, we arrive at the matrix equation for the correction response vector

$$-\omega^2 \Theta'^{(k)} + i\omega \alpha_0 \Theta'^{(k)} + \mathcal{L} \Theta'^{(k)} = -i\omega \boldsymbol{\alpha}' \circ \Theta_0^{(k)}. \quad (4.25)$$

Thus $\Theta'^{(k)}$ is solved as

$$\Theta'^{(k)} = \sum_{\ell=0}^{N-1} \frac{-i\omega (\boldsymbol{\alpha}' \circ \Theta_0^{(k)}) \cdot \mathbf{v}^{[\ell]}}{-\omega^2 + i\omega \alpha_0 + \lambda^{[\ell]}} \mathbf{v}^{[\ell]}, \quad (4.26)$$

which gives the linear estimate of the steady response vector for a heterogeneous dissipation parameter

$$\Theta^{(k)} = \sum_{\ell=0}^{N-1} \frac{(\mathbf{D}^{(k)} - i\omega \boldsymbol{\alpha}' \circ \Theta_0^{(k)}) \cdot \mathbf{v}^{[\ell]}}{-\omega^2 + i\omega \alpha_0 + \lambda^{[\ell]}} \mathbf{v}^{[\ell]}. \quad (4.27)$$

4.3 Steady responses to a step-function signal

In this section we discuss the network responses to a step-function signal, which can be viewed as a special case of sinusoidal signals with $\omega = 0$. Similarly, we first solve for the total network response which gives us hints for reasonable assumptions of the form of the nodal responses, then we compute the nodal responses in terms of the Laplacian eigensystem.

Total response The total phase $\theta^{\text{tot}}(t) = \sum_i^N \theta_i(t)$ of a network system (Eq. 4.1) driven by a step-function signal $\varepsilon \mathbf{D}^{(k)}$ with $D_i = \delta_{ik}$ follows the dynamics

$$\alpha \dot{\theta}^{\text{tot}} + \beta \ddot{\theta}^{\text{tot}} = \varepsilon, \quad (4.28)$$

where we again let $\alpha_i \equiv \alpha > 0$ and $\beta_i \equiv \beta > 0$. Given initial conditions $\theta^{\text{tot}}(0) = \theta_0^{\text{tot}}$ and $\dot{\theta}^{\text{tot}}(0) = \dot{\theta}_0^{\text{tot}}$, the solution of the total network phase reads

$$\theta^{\text{tot}}(t) = C_1 + C_2 e^{-\frac{\alpha}{\beta} t} + \frac{\varepsilon}{\alpha} t \quad (4.29)$$

with

$$\begin{aligned} C_1 &= \theta_0^{\text{tot}} + \frac{\beta}{\alpha} \left(\dot{\theta}_0^{\text{tot}} - \frac{\varepsilon}{\alpha} \right) \\ C_2 &= -\frac{\beta}{\alpha} \left(\dot{\theta}_0^{\text{tot}} - \frac{\varepsilon}{\alpha} \right). \end{aligned}$$

Like in the total network response to a sinusoidal signal (Eq. 4.5), the initial condition of the system appears only the constant phase shift and the transient response, but not the third term, a drift with a constant speed. If the system is perturbed at a fixed point, i.e. $\theta^{\text{tot}}(0) = 0$ and $\dot{\theta}^{\text{tot}}(0) = 0$, the total phase responds to a step-function signal as

$$\theta^{\text{tot}}(t) = \theta^{*,\text{tot}} - \frac{\varepsilon\beta}{\alpha^2} + \frac{\varepsilon\beta}{\alpha^2}e^{-\frac{\alpha}{\beta}t} + \frac{\varepsilon}{\alpha}t, \quad (4.30)$$

which suggests (i) a negative time-independent phase shift $-\frac{\varepsilon\beta}{\alpha^2}$, (ii) a transient response exponentially decaying with time constant $\frac{\beta}{\alpha}$, and (iii) a drift away from the original fixed point with a constant speed $\frac{\varepsilon}{\alpha}$. The phase shift, the strength of the transient response and the drift speed are proportional to the signal magnitude ε . An illustration of the total response is shown in Fig. 4.2.

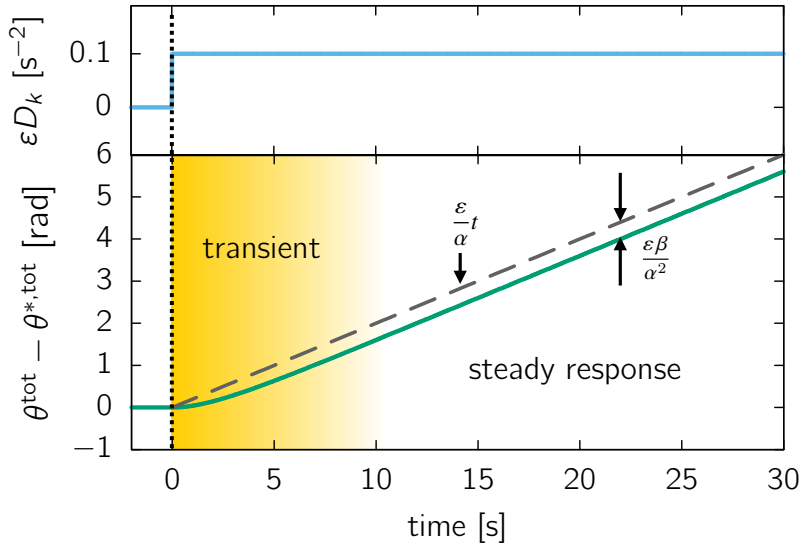


Fig. 4.2 Total network response to a step-function driving signal. An Illustration for the transient and the steady response in the total network response given in Eq. 4.30. The transient stage characterized by an exponential decay is shaded in yellow. The steady response contains a phase shift and a drift with a constant speed $\frac{\varepsilon}{\alpha}$ (grey dashed line). The step-function driving signal is plotted in the upper panel. Parameters: $\alpha = 0.5 \text{ s}^{-1}$, $\beta = 1$, $\varepsilon = 0.1 \text{ s}^{-2}$.

Steady nodal response As before, we take the hints given by the total phase response (4.30), which contains a phase shift and a uniform drift, both are linear with respect to the perturbation strength, thus assume the *nodal* linear response contains a nodal phase shift $\eta_i^{(k)}$ and a nodal drift with speed $u_i^{(k)}$. The solution for the steady nodal response thus reads

$$\theta_i^{(k)} = \theta_i^* + \varepsilon\eta_i^{(k)} + \varepsilon u_i^{(k)}t, \quad (4.31)$$

with $\eta_i^{(k)}$ and $u_i^{(k)}$ satisfying $\sum_{i=1}^N \eta_i^{(k)} = -\frac{\beta}{\alpha^2}$ and $\sum_{i=1}^N u_i^{(k)} = \frac{1}{\alpha}$.

Remarkably, in the response to a step-function perturbation, the nodal drift speed is *identical* for each node, but the nodal phase shift is not (see Fig. 4.3), which implies a redistribution of flow in the network. Inserting the ansatz of the nodal response (Eq. 4.31) to the driven network dynamics (Eq. 4.1) and linearizing the dynamics yields

$$-\mathbf{D}^{(k)} + \alpha \mathbf{U}^{(k)} + \mathcal{L} \mathbf{H}^{(k)} = -\mathcal{L} \mathbf{U}^{(k)} t, \quad (4.32)$$

where $\mathbf{U}^{(k)} := (u_1^{(k)}, u_2^{(k)}, \dots, u_N^{(k)})$ is the vector of the drift speed. The left hand side of the equation is time independent, hence the right hand side must be too. We thus have $\mathcal{L} \mathbf{U}^{(k)} = \mathbf{0}$, which implies an identical nodal drift speed for every node: $u_i^{(k)} = u = \frac{1}{N\alpha}$, $\forall i$. The shift vector is then determined by

$$\mathcal{L} \mathbf{H}^{(k)} = \mathbf{D}^{(k)} - \frac{1}{N} \mathbf{1}, \quad (4.33)$$

where $\mathbf{1} = (1, \dots, 1)$. Again, writing the shift vector $\mathbf{H}^{(k)}$ in the basis of the orthonormal Laplacian eigenvectors and computing the coefficients yields

$$\mathbf{H}^{(k)} = \sum_{\ell=1}^{N-1} \frac{1}{\lambda^{[\ell]}} \left(v_k^{[\ell]} - \frac{1}{N} \sum_{i=1}^N v_i^{[\ell]} \right) \mathbf{v}^{[\ell]} + \mathbf{H}'^{(k)}. \quad (4.34)$$

The projection on the eigenvector $\mathbf{v}^{[0]}$ corresponding to the zero eigenvalue $\mathbf{H}'^{(k)} := \eta'^{(k)} \mathbf{1}$, which describes the homogeneous phase shift across the network, is determined such that the constraint $\sum_{i=1}^N \eta_i = -\frac{\beta}{\alpha^2}$ is satisfied:

$$\eta'^{(k)} = \frac{1}{N} \left[-\frac{\beta}{\alpha^2} - \sum_{\ell=1}^{N-1} \frac{1}{\lambda^{[\ell]}} \left(v_k^{[\ell]} \sum_{i=1}^N v_i^{[\ell]} - \frac{1}{N} \left(\sum_{i=1}^N v_i^{[\ell]} \right)^2 \right) \right]. \quad (4.35)$$

In summary, the steady nodal response to a step-function signal is

$$\boldsymbol{\theta}^{(k)}(t) = \boldsymbol{\theta}^* + \varepsilon \mathbf{H}^{(k)} + \frac{\varepsilon}{N\alpha} t \mathbf{1}, \quad (4.36)$$

where the nodal phase shift $\mathbf{H}^{(k)}$ is given by Eq. 4.34 and Eq. 4.35. This solution suggests that, as a steady response to a step-function driving signal, the phase of each node is shifted and drifts away from the initial fixed point. Interestingly, the nodal drift speed $\frac{\varepsilon}{N\alpha}$ is identical for each node, however, the nodal phase shift is not. It is characterized by the site of perturbation, the site of response, the network topology and the steady state prior to perturbation (see Fig. 4.3).

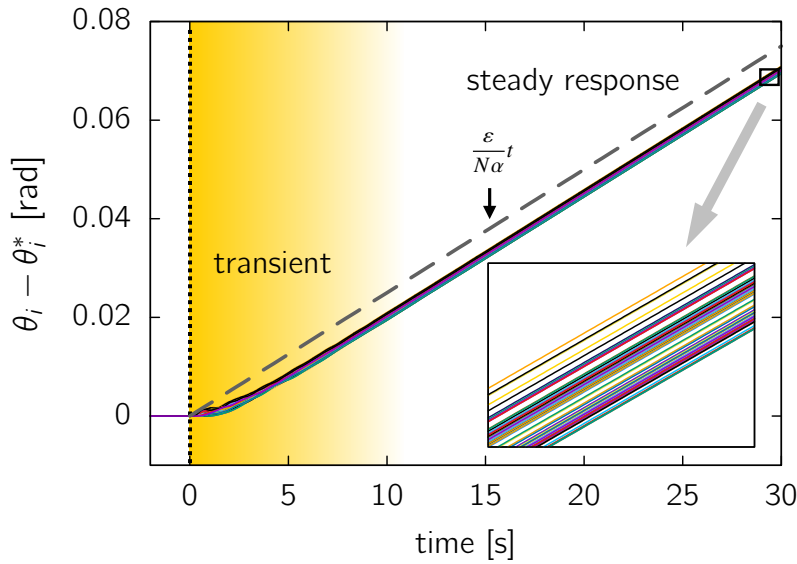


Fig. 4.3 Nodal response to a step-function driving signal. An illustration for the steady nodal response given in Eq. 4.35. The steady response contains a topology-dependent phase shift and a topology-independent drift with a constant speed $\frac{\varepsilon}{N\alpha}$ (grey dashed line). A zoom-in highlighting the topology-dependent phase shift is shown in the inset. The network parameters are the same as in Fig. 4.2.

4.4 Conclusion

In this chapter we derived analytical solutions of the steady response of a second-order Kuramoto-like phase oscillator network to external driving signals.

driving signal ($t > 0$)	total network response ($t > 0$)		
	phase shift	transient response	particular response
$\varepsilon e^{i(\omega t + \varphi)}$ (sinusoidal)	$\frac{\beta}{\alpha} \dot{\theta}_0^{\text{tot}} - \frac{\varepsilon e^{i\varphi}}{-\beta\omega^2 + i\alpha\omega} \left(\frac{i\beta\omega}{\alpha} + 1 \right)$	$\left(-\frac{\beta}{\alpha} \dot{\theta}_0^{\text{tot}} + \frac{\beta}{\alpha} \frac{i\varepsilon e^{i\varphi}}{-\beta\omega + i\alpha} \right) e^{-\frac{\alpha}{\beta}t}$	$\frac{\varepsilon}{-\beta\omega^2 + i\alpha\omega} e^{i(\omega t + \varphi)}$ (sinusoids with complex amplitude)
ε (step-function)	$\frac{\beta}{\alpha} \left(\dot{\theta}_0^{\text{tot}} - \frac{\varepsilon}{\alpha} \right)$	$-\frac{\beta}{\alpha} \left(\dot{\theta}_0^{\text{tot}} - \frac{\varepsilon}{\alpha} \right) e^{-\frac{\alpha}{\beta}t}$	$\frac{\varepsilon}{\alpha} t$ (drift with constant speed)

Table 4.1 Total network responses to an external driving signal.

For balanced networks with $\sum_{i=1}^N \Omega_i = 0$, where the existence of at least one fixed point is ensured, the time evolution of the total network phase $\sum_{i=1}^N \theta_i(t)$ can be solved rigorously. The solution gives information about how the entire network responds to driving signals as one. If driven by a sinusoidal signal, the network responds with (i) a constant phase shift, (ii) an exponentially decaying transient response ($\propto e^{-\frac{\alpha}{\beta}t}$), and (iii) a particular sinusoidal response, with a shift in amplitude and in phase from the driving signal. If driven by a step-function signal, the particular sinusoidal response is replaced by a drift away from the initial condition with a constant speed. A tabular summary of results for the total network response can be found in Tab. 4.1.

For both responses, only the phase shift and the transient response depend on the initial conditions of θ_i and $\dot{\theta}_i$ (the cells shaded in yellow in Tab. 4.1). Remarkably, the particular response that characterizes the form of the driving signal, i.e. the sinusoidal response for a sinusoidal signal and the drift for a constant signal, are *independent* of the initial conditions (the cells shaded in orange in Tab. 4.1). That means, no matter the system is close to the fixed point or not, the sum of the oscillators' phases has always the same particular responses to driving signals, proportional to the driving strength, even though the nodal responses can be dramatically different. This result might be interesting for the studies of the coarse-graining of networks. Particularly, if the network is at a fixed point prior to perturbations, the total response appears to be *linear* to the strength of the driving signal (see Eq. 4.6 and Eq. 4.30). It suggests a linear response theory for network dynamics.

driving signal at node k $(t > 0)$	steady response at node i ($t \rightarrow \infty$)	
	phase shift	particular response
$\varepsilon e^{i(\omega t + \varphi)}$ (sinusoidal)	$\frac{i\varepsilon e^{i\varphi}}{\alpha\omega N}$	$\sum_{\ell=0}^{N-1} \frac{e^{i(\omega t + \varphi)} v_k^{[\ell]}}{-\beta\omega^2 + i\alpha\omega + \lambda^{[\ell]}} v_i^{[\ell]}$ (sinusoids with complex amplitude)
ε (step-function)	$\sum_{\ell=1}^{N-1} \frac{\varepsilon}{\lambda^{[\ell]}} \left(v_k^{[\ell]} - \frac{1}{N} \sum_{i=1}^N v_i^{[\ell]} \right) v_i^{[\ell]} + \varepsilon \eta'^{(k)}$	$\frac{\varepsilon}{N\alpha} t$ (drift with constant speed)

Table 4.2 Steady nodal responses to an external driving signal.

With the hints provided by the analysis of the total network responses, we find solutions for the steady nodal responses in the linearized regime, which encode the steady dynamic response patterns in such networks. We include the constant phase shift and the particular response in the assumptions for the nodal responses while discarding the transient response.

Since the weighted graph Laplacian arises in the linearized dynamics of the system, we express the nodal responses in terms of the projections on the Laplacian eigenvectors and determine the projection coefficients using the orthogonality of the eigenvectors. The solutions are summarized in Tab. 4.2.

Interestingly, for a sinusoidal signal, the network has a homogenous phase shift, while for a step-function signal the drift speed is homogeneous across the network (see the cells shaded in blue in Tab. 4.2). The particular sinusoidal nodal response to a sinusoidal signal and the phase shift evoked by a step-function signal are different for each node, thus characterize the topology of the network (see the cells shaded in orange in Tab. 4.2). Particularly, if we interpret the network dynamics as the operation of power grids, the node-specific phase shift implies a *redistribution* of the power flow caused by the constant external input, which causes the imbalance of the power generation and consumption. However, the sinusoidal response with a node-specific amplitude and phase delay forms a more complex dynamic network response, which exhibit qualitatively different patterns in three frequency regimes. See next chapter for details.

Chapter 5

Three Frequency Regimes of Steady Response Patterns

In this chapter we elaborate the frequency dependence of the steady response pattern induced by a sinusoidal perturbation signal. In particular, based on the analytical solution of the steady nodal responses derived in Sec. 4.2, we identify three frequency regimes of steady response patterns with distinct spatial distributions of response strength.

We start from an illustrative example showing the qualitatively different response patterns in a sample network to the low-, intermediate- and high-frequency Fourier modes of a noisy perturbation signal (Sec. 5.1). In Sec. 5.2, we focus on the eigenfrequencies of a network which lead to resonant responses in network and define the three frequency regimes of steady response patterns in terms of the eigenfrequencies. In Sec. 5.3 and Sec. 5.4, we mathematically analyze the response pattern for perturbation frequencies lower and higher than the eigenfrequencies. At the end of the chapter we give a summary of the features of the steady response patterns in different frequency regimes.

5.1 Frequency: key parameter for pattern formation

The dynamic response of a network described by Eq. 4.1 to a noisy perturbation signal may look arbitrary and confusing at first sight: no clear correlations in time or in space can be identified. A node further away from the perturbation can respond more intensively than a closer node, but not necessarily. However, are there any patterns in the dynamic network responses that are intuitively simple, and also mathematically clear? If so, what is the key parameter that defines the network response pattern? As we will show in this chapter, the perturbation frequency is the key.

An example is shown in Fig. 5.1. At its steady state, a sample network (Fig. 5.1a) is perturbed at node 1 by a Brownian noise with a broad spectrum of frequency components

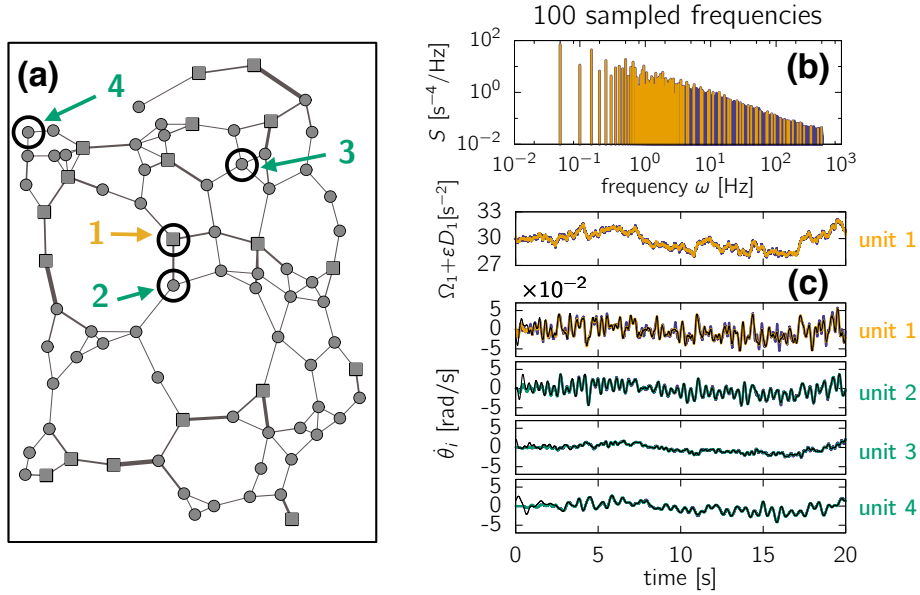


Fig. 5.1 Network response to a Brownian noise. Response time series at 4 nodes (a) are shown for a Brownian noise at node 1. The original noise and responses are shown in purple in (c). The nodal acceleration Ω_i perturbed by different subsets of the Fourier components of the noise and the corresponding responses are shown in yellow (for node 1) and green (for node 2–4) in (c). The selected frequencies are highlighted in yellow in the power spectrum of the original noise (b). The black lines in (c) indicate the linear nodal response given by Eq. 4.16. Parameters: $N = 80$, $K_{ij} \equiv K = 100\text{ s}^{-2}$, $\alpha = 1\text{ s}^{-1}$, $\Omega = 30\text{ s}^{-2}$ for 20 nodes indicated by squares and $\Omega = -10\text{ s}^{-2}$ for the rest 60 nodes indicated by discs in (a).

(Fig. 5.1b). Response time series of $\dot{\theta}_i(t)$ are shown in Fig. 5.1c for three representative nodes, node 2, 3, and 4, with different distances to the perturbed node 1. In Fig. 5.1c, the dependence of response strength on the distance is not clear: the response at node 4 with $d(1, 4) = 6$ is much stronger than that at node 3 with $d(1, 3) = 3$. A clear temporal correlation between responses is not apparent either.

However, if we represent the Brownian noise signal in frequency domain via Fourier transform and look at the nodal responses to its low-, intermediate- and high- frequency components (Fig. 5.2), interesting response patterns in the network arise: for lower frequencies the response at each node look similar (Fig. 5.2a-b), for high frequencies the response seems to dissipate over distance (Fig. 5.2e-f), while for intermediate frequencies the responses collectively exhibit a special pattern which can not be easily interpreted in terms of the distance (Fig. 5.2c-d). How do we mathematically understand the frequency dependence of the qualitatively different response patterns?

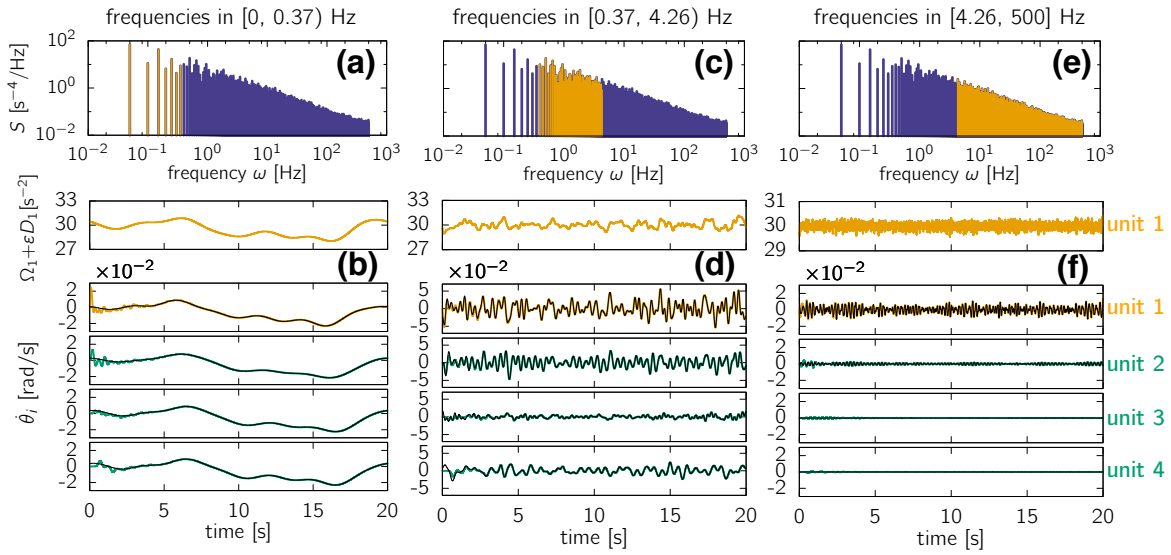


Fig. 5.2 Network response patterns depending on perturbation frequency. Network responses to the low-, intermediate-, and high-frequency components in the Brownian noise are respectively shown in (a-b), (c-d), and (e-f). The color-coding of the lines and the network settings are the same as in Fig. 5.2.

5.2 Eigenfrequencies and the resonance regime

The dynamic response pattern across network is encoded in the linear nodal responses given by Eq. 4.16, which also suggests a frequency dependence. To estimate the response strength, we focus on the rationalized denominator, i.e. $(-\beta\omega^2 + \lambda^{[\ell]})^2 + \alpha^2\omega^2$, in the ℓ -th eigenmode in the nodal response factor $R_i^{(k)}$ (see Eq. 4.18–4.22). We notice that the denominator $(-\beta\omega^2 + \lambda^{[\ell]})^2 + \alpha^2\omega^2$ matches exactly with that of the amplitude of the steady response of a sinusoidally driven damped harmonic oscillator following dynamics $\beta\ddot{x} + \alpha\dot{x} + \lambda^{[\ell]}x = e^{i(\omega t+\varphi)}$. The driven damped harmonic oscillator exhibits resonance when the driving frequency equals to its natural frequency

$$\omega_0 = \sqrt{\frac{\lambda^{[\ell]}}{\beta}}. \quad (5.1)$$

Thus, we can view the network system as a dynamical system with a spectrum of frequencies that induce resonances, which characterize the network topology since they are directly related to the Laplacian eigenvalues. We hence define the *resonance frequencies*

of the network system as

$$\omega_{\text{res}}^{[\ell]} = \sqrt{\frac{\lambda^{[\ell]}}{\beta}}. \quad (5.2)$$

Remarkably, the resonance frequencies are close to the *eigenfrequencies* of the linearized system. For dynamical systems close to a fixed point, the imaginary part of the Jacobian eigenvalues represent the intrinsic frequencies at which the system tends to oscillate. For $\alpha_i \equiv \alpha$ and $\beta_i \equiv \beta$, a relation between the eigenvalues of the Jacobian and the Laplacian matrix can be found. Let \mathbf{w}_1 in Eq. 3.18 be in turn the Laplacian eigenvectors, we obtain the Jacobian eigenvalues $\mu^{[\ell]}$ in terms of the corresponding Laplacian eigenvalues $\lambda^{[\ell]}$:

$$\mu^{[\ell]} = -\frac{\alpha}{2\beta} \pm \sqrt{\frac{\alpha^2}{4\beta^2} - \frac{\lambda^{[\ell]}}{\beta}} \quad (\ell = 0, \dots, N-1). \quad (5.3)$$

In the low dissipation regime, $\frac{\alpha^2}{4\beta^2} - \frac{\lambda^{[\ell]}}{\beta} < 0$ for most of the Laplacian eigenvalues. Thus the *eigenfrequencies* of the linearized network dynamics are given by

$$\omega_{\text{eigen}}^{[\ell]} = \sqrt{\frac{\lambda^{[\ell]}}{\beta} - \frac{\alpha^2}{4\beta^2}}, \quad (5.4)$$

which is very close to the resonance frequency $\omega_{\text{res}}^{[\ell]}$ for $\beta_i \equiv \beta$ in Eq. 5.2.

If the perturbation frequency is close to one of the eigenfrequencies/resonance frequencies, the magnitude of the corresponding ℓ -th eigenmode in the nodal response factor $R_i^{(k)}$ (Eq. 4.18) is maximized, which can be interpreted as the effect of resonance. However, since the contribution of each eigenmode is complex, the maximization of the magnitude of one eigenmode does not necessary lead to a salient resonance peak in the magnitude of the response, especially if the complex contributions from different eigenmodes are not well aligned. The expected resonance peaks can be observed in the direct numerical simulations of networks' frequency response magnitudes for a varying frequency, and also in the plot of the (normalized) nodal frequency response strength¹ as a function of ω (Fig. 5.3), both of which agree with each other quite well².

Furthermore, we find that the eigenfrequencies divide the steady response patterns into three regimes (Fig. 5.3). First, if the frequency of the sinusoidal perturbation signal ω is comparable to the eigenfrequencies, resonant patterns arise, which characterize the

¹The normalized nodal frequency response strength $A_i^{*(k)}$ is essentially the response factor multiplied by the perturbation frequency, $\omega R_i^{(k)}$. The definition will be given in Sec. 5.3.

²The agreement can be seen in e.g. Fig. 5.1 and Fig. 5.2. A systematic discussion on the error of the analytically determined linear responses is presented in Chap. 7.3.

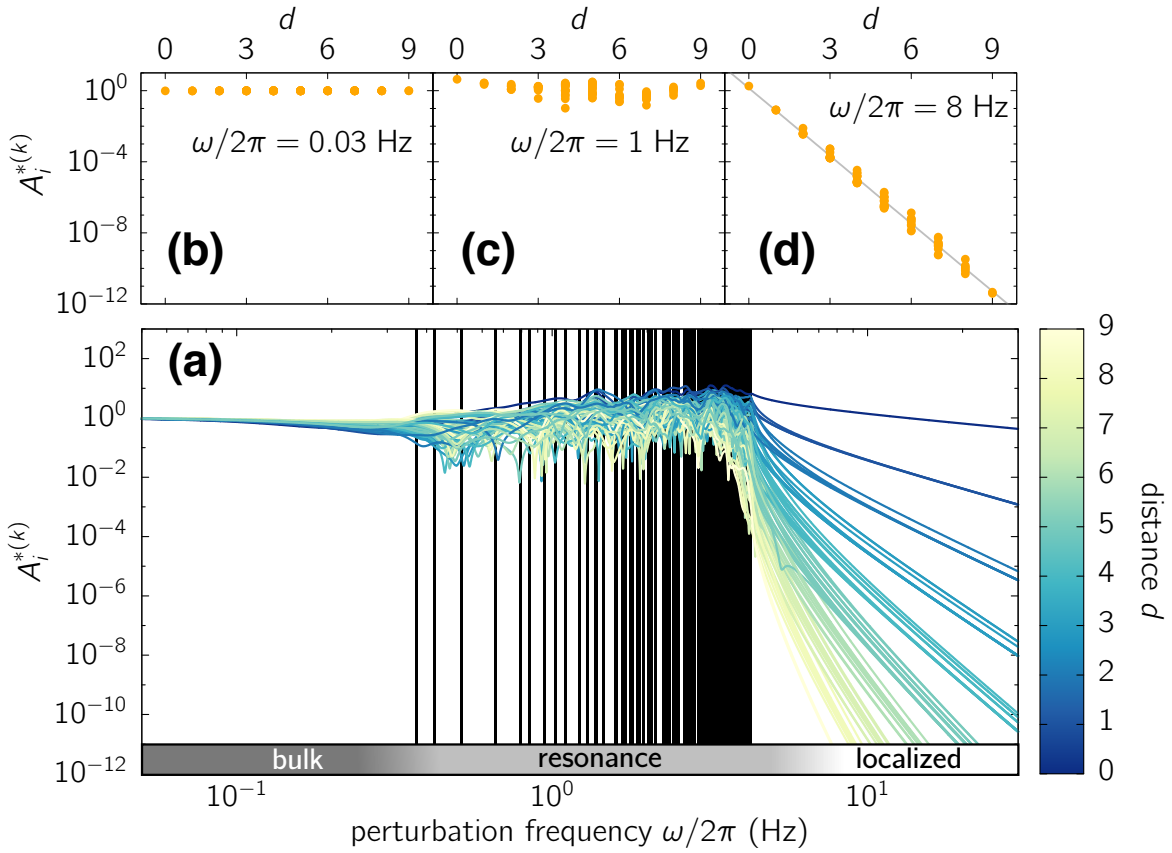


Fig. 5.3 Frequency Response Strengths in three frequency regimes. (a) Normalized nodal frequency response strengths are plotted for a broad range of perturbation frequencies, color-coded by the distance to the perturbation. The dependence of nodal response strengths on distances are plotted for three representative frequencies in (b-d). Black vertical lines in (a) indicate the eigenfrequencies. Network settings are the same as in Fig. 5.1.

network topology via the Laplacian eigenvalues and eigenvectors. Thus we call this regime the *resonance regime*. If ω is lower than the smallest eigenfrequency corresponding to the smallest non-zero Laplacian eigenvalue, i.e. the so-called *algebraic connectivity*, the frequency response strength of every node in the network appear to converge to a same value. It suggests that the network responds to slow-changing signals as a bulk: a homogeneous response pattern arises across the network. We thus name the low-frequency regime as the *bulk regime*. At last, if ω is greater than any of the eigenfrequencies, nodal response strengths decay with increasing ω as a power-law. Moreover, they split into clusters with respect to the distance: the nodes with the same distance share the same exponent in the power-law decay. Specifically, the larger the distance, the faster the decay. That means, for a fixed high-frequency perturbation, the nodes that are further away from the perturbation respond with weaker strengths. The impact of the perturbation seems to be localized around the perturbed node. Thus the

high-frequency regime is referred to as the *localized regime*. In fact, the range of the low-, intermediate-, and high-frequency ranges in Fig. 5.2 are chosen according to the network's eigenfrequencies. In the following sections, we will discuss in detail networks' steady response pattern in the bulk regime and in the localized regime.

5.3 Lower frequencies: the bulk regime

As suggested by Fig. 5.3a-b, when the frequency of the sinusoidal perturbation goes to zero, the steady response strength of each unit in network approaches a same value. This behavior can be confirmed by an asymptotic analysis of the nodal response factor $R_i^{(k)}$ which characterizes the amplitude and the phase of the sinusoidal response of each node. As $\omega \rightarrow 0$, the real part and the imaginary part of the nodal response factor (Eq. 4.18) behave as³

$$\operatorname{Re} (R_i^{(k)}) \xrightarrow{\omega \rightarrow 0} -\frac{1}{N\alpha^2} + \sum_{\ell=1}^{N-1} \frac{v_k^{[\ell]} v_i^{[\ell]}}{\lambda^{[\ell]}} \quad (5.5)$$

$$\operatorname{Im} (R_i^{(k)}) \xrightarrow{\omega \rightarrow 0} -\frac{1}{N\alpha\omega}. \quad (5.6)$$

Consequently, the asymptotic behavior of the nodal response strength as $\omega \rightarrow 0$ is dominated by the imaginary part, and can be written as

$$A_i^{(k)} = |R_i^{(k)}| \xrightarrow{\omega \rightarrow 0} \frac{1}{N\alpha\omega}. \quad (5.7)$$

The relation 5.7 suggests that, no matter which node is perturbed and which node is responding in a network, the response strength always behaves in the same way as long as the perturbation frequency is infinitely small.

In this thesis we mainly focus on the nodal response on the phase velocity $\dot{\theta}_i$ instead of on the phase θ_i due to its relevance in the context of power grids network. The response on the phase velocity is associated with the deviation of the AC frequency which is crucial for the normal operation of synchronous machines and power grids. We thus observe the *nodal frequency response strength*:

$$|\dot{\Theta}_i^{(k)}| = \omega A_i^{(k)} \xrightarrow{\omega \rightarrow 0} \frac{1}{N\alpha}, \quad (5.8)$$

which approaches to a node-independent constant $\frac{1}{N\alpha}$ as the perturbation frequency goes to zero. The limit value is however dependent on the network size N and the global

³Without loss of generality, we let $\beta = 1$ in the following analysis. Replacing α by α/β would trivially reintroduce β .

dissipation α . To compare nodal frequency response strengths among networks, it is thus convenient to define a *normalized* nodal frequency response strength $A_i^{*(k)}$ as

$$A_i^{*(k)} := \frac{\omega A_i^{(k)}}{\lim_{\omega \rightarrow 0} \omega A_i^{(k)}} = N\alpha \omega A_i^{(k)}, \quad (5.9)$$

which goes to 1 for all networks as $\omega \rightarrow 0$.

The steady response pattern is also described by the phase delay of the nodal response with respect to the perturbation: $\Delta_j^{(k)} - \varphi$. Inserting the behavior of the real part and the imaginary part of the nodal response factor (5.5) and (5.6) into the definition of the phase delay (Eq. 4.20), we obtain

$$\begin{aligned} \Delta_j^{(k)} - \varphi &= \arg(R_i^{(k)}) \xrightarrow{\omega \rightarrow 0} \text{atan}2\left(-\alpha, -\omega - \omega\alpha^2 N \sum_{\ell=1}^N \frac{v_k^{[\ell]} v_i^{[\ell]}}{\lambda^{[\ell]}}\right) \\ &\Rightarrow \lim_{\omega \rightarrow 0} (\Delta_j^{(k)} - \varphi) = -\frac{\pi}{2}. \end{aligned} \quad (5.10)$$

The result shows that all nodes in network share the same phase delay in response, $-\pi/2$, with respect to the phase of the sinusoidal perturbation. It is also easy to find that the phase delay in frequency response

$$\Delta_j^{*(k)} - \varphi := \arg(\dot{\Theta}_i^{(k)}) - \varphi = 0, \quad (5.11)$$

which is interesting for power grids since it suggests an almost homogeneous in-phase impact of slow-changing power fluctuations on grid frequency. In short, in the limit of low perturbation frequency, all nodes in a network responds to perturbations as one: they all have the same response strength and the same response phase delay.

5.4 Higher frequencies: the localized regime

For perturbation frequencies higher than the largest eigenfrequency $\omega_{\text{eigen}}^{[N-1]}$ (Eq. 5.4), the network exhibit *localized* response patterns (see Fig. 5.2e-f and Fig. 5.3a,d): the nodal response strength appears to decay with distance exponentially. This pattern results from the fact that the response strength decreases with the perturbation frequency as a power-law, and particularly, the exponent of the power-law decay depends *linearly* on the distance to the perturbation.

In this section we derive the localized response pattern from the complex nodal response factor $R_i^{(k)}$ (Eq. 4.18) with $\omega > \omega_{\text{eigen}}^{[N-1]}$. To see the frequency dependence of the nodal

response strength, i.e. the magnitude of $R_i^{(k)}$, we first reduce $\operatorname{Re}(R_i^{(k)})$ and $\operatorname{Im}(R_i^{(k)})$ to a common denominator:

$$\operatorname{Re}(R_i^{(k)}) = \frac{\sum_{\ell=0}^{N-1} v_k^{[\ell]} v_i^{[\ell]} (-\omega^2 + \lambda^{[\ell]}) \prod_{\substack{\ell'=0, \\ \ell' \neq \ell}}^{N-1} [(-\omega^2 + \lambda^{[\ell']})^2 + \alpha^2 \omega^2]}{\prod_{\ell=0}^{N-1} [(-\omega^2 + \lambda^{[\ell]})^2 + \alpha^2 \omega^2]} \quad (5.12)$$

$$\operatorname{Im}(R_i^{(k)}) = \frac{\sum_{\ell=0}^{N-1} v_k^{[\ell]} v_i^{[\ell]} (-\alpha \omega) \prod_{\substack{\ell'=0, \\ \ell' \neq \ell}}^{N-1} [(-\omega^2 + \lambda^{[\ell']})^2 + \alpha^2 \omega^2]}{\prod_{\ell=0}^{N-1} [(-\omega^2 + \lambda^{[\ell]})^2 + \alpha^2 \omega^2]} \quad (5.13)$$

Both of the numerators and the denominators can be viewed as polynomials of ω . For large enough ω , the behavior of the polynomials is dominated by their leading terms, i.e. their monomials with the highest degree and non-zero coefficients. For the denominators, it is easy to find that the leading term is ω^{4N} , whose coefficient is a constant. However for the numerators, it is more tricky to find the leading term. The numerators sum over N eigenmodes with the ℓ -th summand containing the elements of the corresponding Laplacian eigenvector $\mathbf{v}^{[\ell]}$ and a polynomial of ω with coefficients depending on all Laplacian eigenvalues except $\lambda^{[\ell]}$.

To find the leading term of the numerators, we first focus on the common product in the summand of both numerators:

$$Q(\omega) := \prod_{\substack{\ell'=0, \\ \ell' \neq \ell}}^{N-1} [(-\omega^2 + \lambda^{[\ell']})^2 + \alpha^2 \omega^2]. \quad (5.14)$$

Proposition 2. *The product $Q(\omega)$ defined in (5.14) satisfies*

$$Q(\omega) = \sum_{j=0}^{2N-2} C_\ell^{[j]} \omega^{4N-4-2j},$$

where the coefficients $C_\ell^{[j]}$ can be expressed as a polynomial of $\lambda^{[\ell]}$ with degree j .

This can be shown by considering $C_\ell^{[j]}$ as sums of products of the coefficients of ω in the multiplicand, i.e. 1, $(\alpha^2 - 2\lambda^{[\ell']})$ and $(\lambda^{[\ell']})^2$ with $\ell' \neq \ell$. Expressing $C_\ell^{[j]}$ as combinations of coefficients involving all N eigenvalues minus the ones involving $\lambda^{[\ell']}$ gives the relation between $C_\ell^{[j]}$ and $\lambda^{[\ell']}$. A detailed proof can be found in Appx. A.

Therefore, the numerators N_{ki}^{Re} and N_{ki}^{Im} for the real part and the imaginary part of $R_i^{(k)}$ satisfy

$$N_{ki}^{\text{Re}} = \sum_{\ell=0}^{N-1} v_k^{[\ell]} v_i^{[\ell]} \sum_{j=0}^{2N-1} F_\ell^{[j]} \omega^{4N-2-2j}, \quad N_{ki}^{\text{Im}} = \sum_{\ell=0}^{N-1} v_k^{[\ell]} v_i^{[\ell]} \sum_{j=0}^{2N-2} G_\ell^{[j]} \omega^{4N-3-2j}.$$

The coefficients $F_\ell^{[j]}$ and $G_\ell^{[j]}$ are also polynomials of $\lambda^{[\ell]}$ with degree j like $C_\ell^{[j]}$. Exchanging the order of summation in the numerators and writing them compactly in matrix form, we obtain the numerator matrices

$$\mathbf{N}^{\text{Re}} = \sum_{j=0}^{2N-1} \Phi^{[j]} \omega^{4N-2-2j}, \quad \mathbf{N}^{\text{Im}} = \sum_{j=0}^{2N-2} \Gamma^{[j]} \omega^{4N-3-2j} \quad (5.15)$$

where the coefficient matrices $\Phi^{[j]}$ and $\Gamma^{[j]}$ are defined as

$$\Phi^{[j]} = \mathbf{V} \mathbf{F}^{[j]} \mathbf{V}^T \quad \text{and} \quad \Gamma^{[j]} = \mathbf{V} \mathbf{G}^{[j]} \mathbf{V}^T. \quad (5.16)$$

Here $\mathbf{V} \in \mathbb{R}^{N \times N}$ denotes the square matrix with the Laplacian eigenvectors as its columns, and $\mathbf{F}^{[j]}, \mathbf{G}^{[j]} \in \mathbb{R}^{N \times N}$ are diagonal matrices with $F_\ell^{[j]}$ and $G_\ell^{[j]}$ being the ℓ -th diagonal element respectively. Since $F_\ell^{[j]}$ and $G_\ell^{[j]}$ are polynomials of $\lambda^{[\ell]}$ with degree j , the diagonal matrices $\mathbf{F}^{[j]}$ and $\mathbf{G}^{[j]}$ are also j -degree polynomials of the $N \times N$ diagonal matrices $\mathbf{\Lambda}$ with $\Lambda_{ii} = \lambda^{[i-1]}$. Conveniently, $\mathbf{V} \mathbf{\Lambda} \mathbf{V}^T$ recovers the Laplacian matrix, thus $\Phi^{[j]}$ and $\Gamma^{[j]}$ are in fact polynomials of \mathcal{L} with degree j .

Recall Prop. 1 stating that $(\mathcal{L}^d)_{ij}$ is non-zero for $d \geq d(i, j)$ and is zero otherwise. Therefore, given node pair (k, i) with distance $d(k, i)$, $\Phi_{ki}^{[j]}$ and $\Gamma_{ki}^{[j]}$ are non-zero only for $j \geq d(k, i)$. As a result, the leading term in the numerators are $\Phi_{ki}^{[d(k,i)]} \omega^{4N-2-2d(k,i)}$ and $\Gamma_{ki}^{[d(k,i)]} \omega^{4N-3-2d(k,i)}$, since higher-order terms of ω all have zero coefficients: $\Phi_{ki}^{[j]} = 0$ and $\Gamma_{ki}^{[j]} = 0$ for $j < d(k, i)$.

We thus obtain the asymptotic behavior of $\text{Re}(R_i^{(k)})$ and $\text{Im}(R_i^{(k)})$

$$\begin{aligned}\text{Re}(R_i^{(k)}) &\stackrel{\text{large } \omega}{\sim} \Phi_{ki}^{[d(k,i)]} \omega^{-2-2d(k,i)}, \\ \text{Im}(R_i^{(k)}) &\stackrel{\text{large } \omega}{\sim} \Gamma_{ki}^{[d(k,i)]} \omega^{-3-2d(k,i)},\end{aligned}\quad (5.17)$$

which lead to the asymptotic behavior of the nodal response strength

$$A_i^{(k)} = |R_i^{(k)}| \stackrel{\text{large } \omega}{\sim} |\Phi_{ki}^{[d(k,i)]}| \omega^{-2-2d(k,i)}. \quad (5.18)$$

Derivatively, for the normalized nodal frequency response strength, we have

$$A_i^{*(k)} = N\alpha\omega |R_i^{(k)}| \stackrel{\text{large } \omega}{\sim} N\alpha |\Phi_{ki}^{[d(k,i)]}| \omega^{-1-2d(k,i)}. \quad (5.19)$$

The relation (5.19) reveals the power-law dependence of response strengths on the perturbation frequency in the localized regime (see Fig. 5.4). For a general complex network, the coefficient matrices $\Phi^{[j]}$ and $\Gamma^{[j]}$ can be determined numerically.

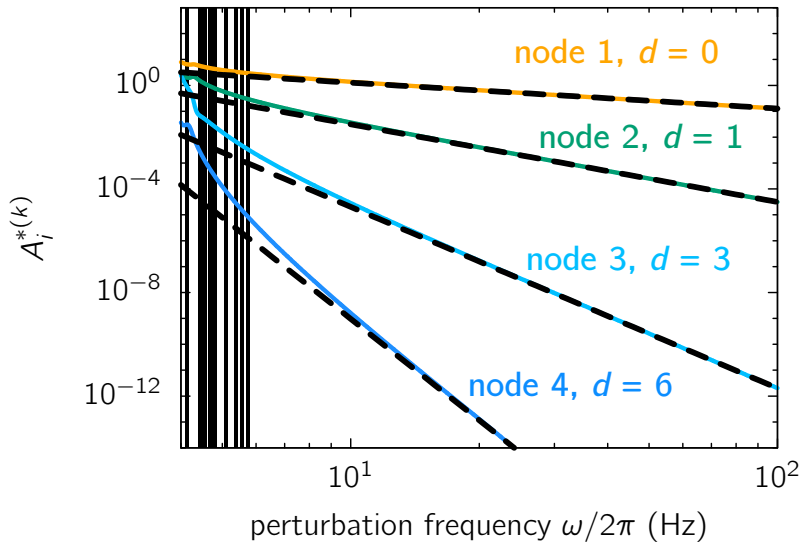


Fig. 5.4 Asymptotic response behavior in the localized regime. The frequency dependence of the normalized nodal frequency response strength is plotted for 4 representative nodes as shown in Fig. 5.1a. The black dashed lines are high-frequency approximations given by Eq. 5.19. The network settings are the same as in Fig. 5.1.

In this regime, the phase delay between the nodal sinusoidal response $\Theta_i^{(k)}$ and the sinusoidal perturbation can be written as:

$$\Delta_i^{(k)} - \varphi = \arg(R_i^{(k)}) \stackrel{\text{large } \omega}{\sim} \text{atan2}(\Gamma_{ki}^{[d(k,i)]}, \Phi_{ki}^{[d(k,i)]}\omega). \quad (5.20)$$

For large ω , the phase delay is close to either 0 or π , depending on the sign of $\Gamma_{ki}^{[d(k,i)]}$ and $\Phi_{ki}^{[d(k,i)]}$. The phase delay in frequency response

$$\Delta_i^{*(k)} - \varphi \xrightarrow{\text{large } \omega} \text{atan2}\left(\Phi_{ki}^{[d(k,i)]}\omega, -\Gamma_{ki}^{[d(k,i)]}\right), \quad (5.21)$$

thus approaches $\pm\frac{\pi}{2}$ for large ω .

In fact, relations (5.19) and (5.20) are valid for $\omega \rightarrow \infty$. If the perturbation frequency ω is much larger than all of the eigenfrequencies ($\omega \gg \omega_{\text{eigen}}^{[N-1]}$), all Laplacian eigenvalues $\lambda^{[\ell]}$ becomes negligible compared to ω^2 , since $\omega \gg \sqrt{\lambda^{N-1}}$ (cf. Eq. 5.4). As $\omega \rightarrow \infty$, $\text{Re}(R_i^{(k)})$ and $\text{Im}(R_i^{(k)})$ behave as

$$\text{Re}(R_i^{(k)}) \xrightarrow{\omega \rightarrow \infty} \sum_{\ell=0}^{N-1} \frac{-v_k^{[\ell]} v_i^{[\ell]}}{\omega^2} = -\delta_{ki} \omega^{-2}, \quad (5.22)$$

$$\text{Im}(R_i^{(k)}) \xrightarrow{\omega \rightarrow \infty} \sum_{\ell=0}^{N-1} \frac{-\alpha v_k^{[\ell]} v_i^{[\ell]}}{\omega^3} = \delta_{ki} \alpha \omega^{-3}. \quad (5.23)$$

The equations in (5.22) and (5.23) come from the orthonormality of the Laplacian eigenvectors:

$$\sum_{\ell=0}^{N-1} v_k^{[\ell]} v_i^{[\ell]} = (\mathbf{V} \mathbf{V}^T)_{ki} = \delta_{ki}. \quad (5.24)$$

Therefore, for the perturbed node k , we have

$$|A_k^{(k)}| \xrightarrow{\omega \rightarrow \infty} \omega^{-2} \quad \text{and} \quad \Delta_k^{(k)} - \varphi \xrightarrow{\omega \rightarrow \infty} \pi, \quad (5.25)$$

which is consistent with the result given by (5.19) and (5.20) for large ω . For other nodes in the network, the limit value of the response factor is exactly zero, thus the behavior of the nodal response at $\omega \rightarrow \infty$ is still described by relations (5.19) and (5.20).

5.5 Conclusion

In this chapter we discussed the three frequency regimes of the steady response patterns induced by a single sinusoidal signal, where the patterns show distinct temporal and spatial features. Illustrative examples of the typical responsive patterns are shown in Fig. 5.5 and a tabular summary of the three regimes is given in Tab. 5.1. Based on the analytical solution of the linear network responses given in last chapter, we derived

the typical response behaviors in three frequency regimes via asymptotic analysis, thus provide mathematical interpretations of the distinct collective responsive behaviors in each regime.

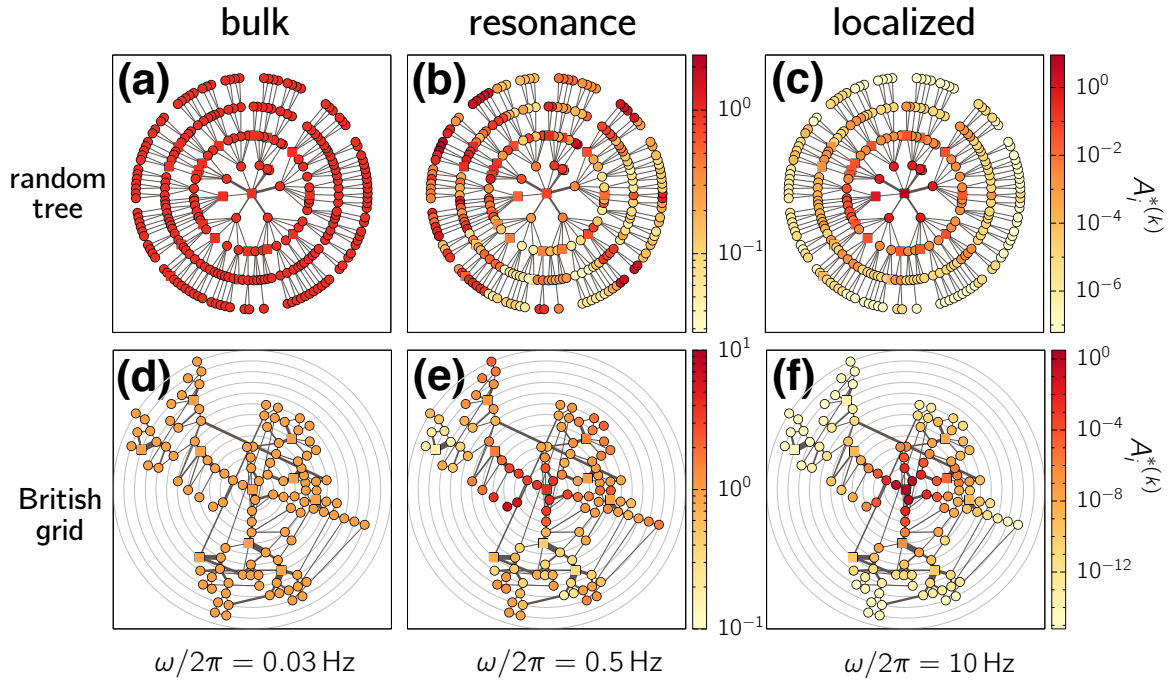


Fig. 5.5 Typical patterns of response strength in three frequency regimes. The steady response patterns of two sample networks, a random tree and the British high-voltage power grid network, are illustrated. The nodes are positioned on concentric circles with the perturbed node at the center and the radii of the circles being proportional to the topological distance to the perturbation signal. The nodes are color-coded by the normalized frequency response strength in logarithmical scale.

Resonance patterns that are specific to network topologies arise if the external driving frequency coincides with one of the eigenfrequencies of the network system. The eigenfrequencies are defined as the imaginary part of the Jacobian eigenvalues, which represent the intrinsic oscillation frequencies of the network system near the fixed point. In the resonance regime, the amplitude and the phase of the nodal sinusoidal response characterize the Laplacian eigensystem of the network, thus depend on the specific network topology and the driving frequency through Eq. 4.18–4.20. Remarkably, *nonlocal* responses can arise in this regime: strong responses can appear at nodes that are faraway from the perturbation due to resonances, while the closer nodes may exhibit weaker responses (Fig. 5.5b, 5.5e).

If the driving frequency is lower than the eigenfrequencies of the system, the responses at every node are similar. The nodal frequency response strengths approach the same value $\frac{1}{N\alpha}$ as $\omega \rightarrow 0$, which only depends on the network size and the damping parameter.

driving signal $\varepsilon e^{i(\omega t+\varphi)}$	perturbation frequency ω	steady response pattern ($t \rightarrow \infty$)		scale of impact
		$A_i^{*(k)}$	$\Delta_i^{*(k)} - \varphi$	
<i>bulk regime</i>	$\omega \rightarrow 0$	1 homogeneous	0 in phase	global
<i>resonance regime</i>	$\omega \sim \omega_{\text{eigen}}$	topology-specific resonances		global
<i>localized regime</i>	$\omega \rightarrow \infty$	$N\alpha \Phi_{ki}^{[d(k,i)]} \omega^{-1-2d(k,i)}$ distance-dependent power-law decay	$\pm \frac{\pi}{2}$ in phase quadrature	local

Table 5.1 Three frequency regimes of steady response patterns.

Normalized by this constant, nodal response strengths become comparable across networks so that the impact of network topology become evident. In this regime, a single sinusoidal perturbation has almost the same effect on each node, thus has a *global* effect. Notably, if $\omega = 0$, the sinusoidal perturbation becomes a step-function thus the nodal response is described by Eq. 4.36, where the responsive drift speed $\frac{1}{N\alpha}$ coincides nicely with the frequency response strength at low frequency limit. The result is reasonable since both quantities describe the rate of change the response.

For high driving frequencies larger than the eigenfrequencies, the steady network response become increasingly localized at the perturbed node as $\omega \rightarrow \infty$. Specifically, the nodal response strength decays with increasing ω as a power-law with its exponent being linear to the distance. As a consequence, the nodal response strength decays exponentially with distance, which leads to a localized response pattern in networks. This result become evident if one notices that the order of the leading term in the response factor as $\omega \rightarrow \infty$ depends on the distance through its coefficient.

In summary, the steady response pattern to a sinusoidal signal depends crucially on the signal's frequency. The pattern for frequencies lower or higher than system's eigenfrequencies does not depend on the specific network topology while the resonance patterns do (shaded in orange in Tab. 5.1). A single perturbation evokes nonlocal responses if its frequency is lower or comparable to the eigenfrequencies, while its impact becomes more and more localized as the frequency goes beyond all eigenfrequencies.

Chapter 6

Response Patterns at High- and Low-damping Limits

In this chapter we discuss the response patterns for two limit cases of the second-order Kuramoto-like oscillator networks (4.1). By extending our previously presented results to high- and low-damping limits, we establish the relations between our theory and the state-of-the-art works in the field of perturbation-induced pattern formation in oscillatory networks, especially Zanette's studies on Kuramoto oscillator networks [39, 40].

If the damping parameter α is much larger than β so that the rates of change of the oscillators' phases $\dot{\theta}$ dominate the dynamics, the network dynamics approaches the dynamics of Kuramoto oscillator networks, where $\beta = 0$. The response patterns of networks at high-damping limits, i.e. with $\alpha \neq 0$ and $\beta = 0$, are presented in Sec. 6.1. If the damping parameter α is much smaller than β , i.e. $\beta \neq 0$ and $\alpha = 0$, the network system becomes a Hamiltonian system as discussed in Sec. 3.2.2. As we show in Sec. 6.2, networks at low-damping limits never reach a stage of steady responses, thus steady response patterns do not exist when $\alpha = 0$. In the last section we summarize the steady response patterns in network class (4.1) by comparing the patterns in three cases of network dynamics: with a general setting $\alpha \neq 0, \beta \neq 0$, at the high-damping limit $\alpha \neq 0, \beta = 0$ and at the low-damping limit $\alpha = 0, \beta \neq 0$.

6.1 High-damping limit: Kuramoto oscillator networks

At the high-damping limit, the network system follows

$$\alpha \dot{\theta}_i = \Omega_i + \sum_{j=1}^N K_{ij} \sin(\theta_j - \theta_i) + \varepsilon D_i(t), \quad (i = 1, \dots, N), \quad (6.1)$$

which are equivalent to the dynamics of a network of Kuramoto oscillators with nodal perturbation signal $\varepsilon D_i(t)$. Without loss of generality, we let $\alpha = 1$ in the following analysis.

6.1.1 Linear network responses

We start with solving for the responses of a network at a fixed point $\boldsymbol{\theta} = \boldsymbol{\theta}^*$, including the total network response θ^{tot} and the nodal response, to a small signal such as a sinusoidal signal $\varepsilon e^{i(\omega t + \varphi)}$ and a step-function signal ε .

Responses to a sinusoidal signal

Total network response The total network response of a Kuramoto oscillator network (6.1) is determined by

$$\dot{\theta}^{\text{tot}} = \varepsilon e^{i(\omega t + \varphi)}, \quad (6.2)$$

where the natural frequencies and the flows sum to zero on the right hand side. This is ensured by the existence of the fixed point as discussed for the general case (see Sec. 4.1). With initial condition $\theta^{\text{tot}}(t = 0) = \theta_0^{\text{tot}}$, Eq. 6.2 gives the solution

$$\theta^{\text{tot}}(t) = \theta_0^{\text{tot}} - \frac{\varepsilon}{i\omega} e^{i\varphi} + \frac{\varepsilon}{i\omega} e^{i(\omega t + \varphi)}, \quad (6.3)$$

which implies a constant phase shift and a sinusoidal response with a complex amplitude, both are proportional to the perturbation strength ε . The total network response at the fixed point is obtained by simply substituting the initial condition with $\theta^{*,\text{tot}}$. The total network response differs from the one for the general case only by a missing transient decay with time constant $\frac{\beta}{\alpha}$ (cf. Fig 4.1 and Fig. 6.1). This is reasonable since $\beta = 0$ leads to the time constant being zero, thus the total network response at the high-damping limit can be interpreted as the transient response phase in the general case is shortened to zero. Remarkably, the phase shift is the same as the general case (cf. Eq. 4.6)

Nodal response Following the same routine as for the general case, we compute the steady nodal response in a Kuramoto oscillator network. The nodal response consists of a constant phase shift $\varepsilon \eta_i$ and a characteristic sinusoidal response $\varepsilon \Theta_i^{(k)} = \varepsilon A_i^{(k)} e^{i(\omega t + \Delta_i^{(k)})}$. The phase shift must be identical for each node, which can be shown with the same argument as in the general case. We thus have $\eta_i \equiv \eta = \frac{i\varepsilon' \varphi}{N\omega}$. The nodal sinusoidal response follows the dynamics

$$(i\omega + \mathcal{L}) \boldsymbol{\Theta}^{(k)} = \mathbf{D}^{(k)}. \quad (6.4)$$

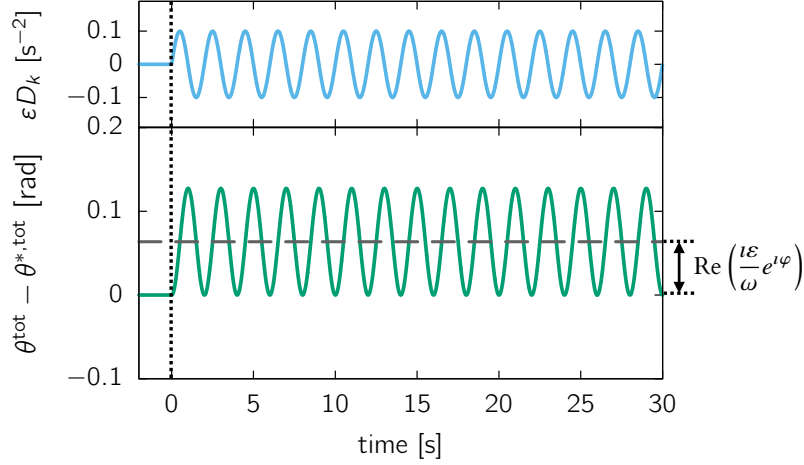


Fig. 6.1 Kuramoto oscillator network's total response to a sinusoidal driving signal. An illustration for the total network response given in Eq. 6.3, which contains a phase shift (grey dashed line) and a sinusoidal oscillation. The sinusoidal driving signal is plotted in the upper panel. The network setting is the same as in Fig. 4.1 except $\beta = 0$.

Writing the response vector in the basis of the orthonormal Laplacian eigenvectors, we obtain

$$\Theta^{(k)} = e^{i(\omega t + \varphi)} \sum_{\ell=0}^{N-1} \frac{v_k^{[\ell]}}{i\omega + \lambda^{[\ell]}} \mathbf{v}^{[\ell]}. \quad (6.5)$$

Thus the steady nodal response to a sinusoidal driving signal reads

$$\theta_i^{(k)}(t) = \theta_i^* + \frac{i\epsilon e^{i\varphi}}{N\omega} + \sum_{\ell=0}^{N-1} \frac{\epsilon e^{i(\omega t + \varphi)} v_k^{[\ell]}}{i\omega + \lambda^{[\ell]}} \mathbf{v}^{[\ell]}. \quad (6.6)$$

Notably, the solution is exactly the same as the one for the general case (Eq. 4.17) with $\beta = 0$ and $\alpha = 1$. Similarly, the nodal response factor for Kuramoto oscillator networks is

$$R_i^{(k)} := \sum_{\ell=0}^{N-1} \frac{v_k^{[\ell]} v_i^{[\ell]}}{i\omega + \lambda^{[\ell]}}, \quad (6.7)$$

with its real part and imaginary part being

$$\operatorname{Re}(R_i^{(k)}) = \sum_{\ell=0}^{N-1} \frac{v_k^{[\ell]} v_i^{[\ell]} \lambda^{[\ell]}}{\omega^2 + (\lambda^{[\ell]})^2}, \quad \text{and} \quad \operatorname{Im}(R_i^{(k)}) = \sum_{\ell=0}^{N-1} \frac{-v_k^{[\ell]} v_i^{[\ell]} \omega}{\omega^2 + (\lambda^{[\ell]})^2}. \quad (6.8)$$

Responses to a step-function signal

Total network response The total network phase of a Kuramoto oscillator network responds to a step-function signal as

$$\theta^{\text{tot}}(t) = \theta_0^{\text{tot}} + \varepsilon t. \quad (6.9)$$

This result implies a simple uniform drift away from the initial condition. Furthermore, the constant drift speed is exactly the perturbed signal strength ε . The solution Eq. 6.9 is in fact the same as the result for the general second-order oscillator network (Eq. 4.29) with $\beta = 0$ and $\alpha = 1$: the phase shift and the transient exponential decay disappear with $\beta = 0$ and the drift speed remains the same (see Fig. 6.2).

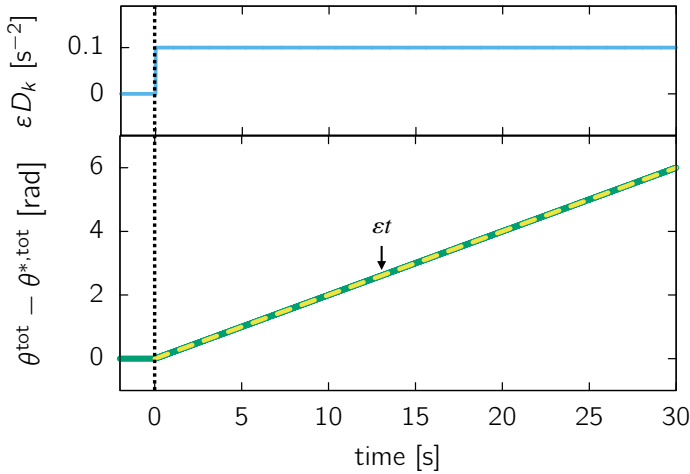


Fig. 6.2 **Total network response to a step-function driving signal.** An illustration for the total network response given in Eq. 6.9, which is essentially a phase drift with a constant speed ε (yellow dashed line). The step-function driving signal is plotted in the upper panel. The network setting is the same as in Fig. 4.2 except $\beta = 0$.

Nodal response The nodal response to a step-function signal in a Kuramoto oscillator network can be determined in the same way as presented in Sec. 4.3. Particularly, the zero phase shift in the total network response does not imply a zero nodal phase shift. Thus we still assume that the nodal response has the form

$$\theta_i^{(k)} = \theta_i^* + \varepsilon \eta_i^{(k)} + \varepsilon u_i^{(k)} t, \quad (6.10)$$

with $\sum_{i=1}^N \eta_i^{(k)} = 0$ and $\sum_{i=1}^N u_i^{(k)} = 1$. With the same argument it can be shown that the nodal drift speed is identical, thus $u_i^{(k)} = u = \frac{1}{N}$, for all i . The shift vector still satisfies Eq. 4.33 hence has the same form as in Eq. 4.34. The only difference is that the contribution of the zeroth eigenmode to the shift vector, $\mathbf{H}'^{(k)}$, is determined such that

the constraint $\sum_{i=1}^N \eta_i^{(k)} = 0$ is satisfied. Thus the homogeneous phase shift is given by

$$\eta'^{(k)} = -\frac{1}{N} \sum_{\ell=1}^{N-1} \frac{1}{\lambda^{[\ell]}} \left(v_k^{[\ell]} \sum_{i=1}^N v_i^{[\ell]} - \frac{1}{N} \left(\sum_{i=1}^N v_i^{[\ell]} \right)^2 \right). \quad (6.11)$$

To summarize, the nodal response is still given by the solution for the general case, i.e. Eq. 4.36, Eq. 4.34 and Eq. 4.35 with $\beta = 0, \alpha = 1$. Each node in a Kuramoto oscillator network responds to a step-function signal with a characteristic phase shift and a uniform drift with a homogeneous drift speed, although the nodal phase shift sums to zero over the network.

6.1.2 Three frequency regimes

The Laplacian eigenvalues and the transition regime The steady response patterns in Kuramoto oscillator networks are also governed by three frequency regimes. For lower and higher frequencies, the response behavior of Kuramoto oscillator networks is very similar to the behavior of the general second-order oscillator networks. However, the resonances which appear when the perturbation frequency coincides with the eigenfrequencies disappear for Kuramoto oscillator networks, and instead, the nodal frequency response strength experiences a smooth transition from the constant and homogeneous value in the bulk regime to the distance-dependent power-law decay in the localized regime.

The reason for this difference lies in the nodal response factor $R_i^{(k)}$ (Eq. 6.7): the rationalized denominators in the ℓ -th eigenmode $\omega^2 + (\lambda^{[\ell]})^2$ increases monotonously with ω for $\omega > 0$, thus no resonances can happen. In fact, for networks of Kuramoto oscillators, eigenfrequencies do not exist either. The Jacobian matrix at the fixed point is essentially the Laplacian matrix: $\mathcal{J} = -\mathcal{L}$, thus all Jacobian eigenvalues are non-positive real numbers, indicating there are no intrinsic oscillations in the neighborhood of the fixed point.

However, the driving frequencies which are comparable to the Laplacian eigenvalues $\omega \sim \lambda^{[\ell]}, (\ell = 1, \dots, N-1)$ indicate a *transition regime* between the bulk regime and the localized regime. For driving frequencies that are much smaller than the Laplacian eigenvalues, the ℓ -th Laplacian eigenvalue dominates the denominator of the ℓ -th eigenmode of the response factor. As the driving frequency increases, it surpasses the non-negative Laplacian eigenvalues one by one and finally takes over and dominates the denominator in the localized regime when it is much larger than all Laplacian eigenvalues.

As the eigenfrequencies for the second-order oscillator networks $\omega_{\text{eigen}[\ell]} \sim \sqrt{\lambda^{[\ell]}}$, the transition regime for the first-order Kuramoto oscillator networks extends much wider than the resonance regime (cf. Fig. 5.3 and Fig. 6.3).

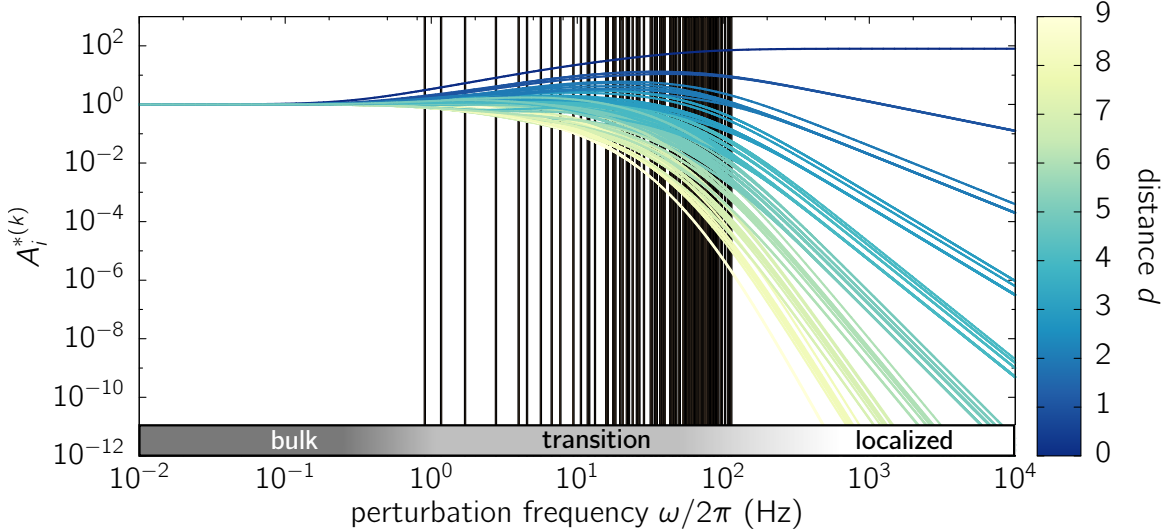


Fig. 6.3 Three frequency regimes of the frequency response patterns in Kuramoto oscillator networks. Normalized nodal frequency response strengths are plotted for a broad range of perturbation frequencies, color-coded by the distance to the perturbation. Black vertical lines indicate the Laplacian eigenvalues. Network settings are the same as in Fig. 5.1.

The bulk regime At very low perturbation frequencies, i.e. $\omega \rightarrow 0$, every node in a Kuramoto oscillator network responds to a small sinusoidal perturbation homogeneously, as in a second-order oscillator network. Again, asymptotic analysis gives the low-frequency limit the common frequency response strength

$$|\dot{\Theta}_i^{(k)}| = \omega A_i^{(k)} = \omega |R_i^{(k)}| \xrightarrow{\omega \rightarrow 0} \frac{1}{N} \quad (6.12)$$

and the phase delay

$$\begin{aligned} \Delta_i^{(k)} - \varphi &= \arg(R_i^{(k)}) \xrightarrow{\omega \rightarrow 0} \text{atan2}\left(-1, N\omega \sum_{\ell=1}^{N-1} \frac{v_k^{[\ell]} v_i^{[\ell]}}{\lambda^{[\ell]}}\right) \\ &\Rightarrow \lim_{\omega \rightarrow 0} (\Delta_i^{(k)} - \varphi) = -\frac{\pi}{2}. \end{aligned} \quad (6.13)$$

The results are consistent with the ones for the second-order oscillator networks (Eq. 5.7 and Eq. 5.10) with $\alpha = 1$.

The localized regime When the perturbation frequency is large enough, the nodal response strengths in the Kuramoto oscillator networks also exhibit a localized pattern: they decay as a power-law as the driving frequency grows, with a distance-dependent exponent. However the power-law decay is slower than for second-order oscillator networks. As before (Sec. 5.4), this behavior is derived from the asymptotic behavior of the complex nodal response factor.

The real part and the imaginary part of the nodal response factor (Eq. 6.7) reduced to a common denominator read

$$\operatorname{Re}(R_i^{(k)}) = \frac{\sum_{\ell=0}^{N-1} v_k^{[\ell]} v_i^{[\ell]} \lambda^{[\ell]} \prod_{\substack{\ell'=0, \\ \ell' \neq \ell}}^{N-1} [\omega^2 + (\lambda^{[\ell']})^2]}{\prod_{\ell=0}^{N-1} [\omega^2 + (\lambda^{[\ell]})^2]}, \quad \text{and} \quad (6.14)$$

$$\operatorname{Im}(R_i^{(k)}) = \frac{\sum_{\ell=0}^{N-1} -v_k^{[\ell]} v_i^{[\ell]} \omega \prod_{\substack{\ell'=0, \\ \ell' \neq \ell}}^{N-1} [\omega^2 + (\lambda^{[\ell']})^2]}{\prod_{\ell=0}^{N-1} [\omega^2 + (\lambda^{[\ell]})^2]}. \quad (6.15)$$

For sufficiently large ω , the leading term of the shared common denominator is ω^{2N} . The shared product in the numerators

$$Q'(\omega) := \prod_{\substack{\ell'=0, \\ \ell' \neq \ell}}^{N-1} [\omega^2 + (\lambda^{[\ell']})^2] \quad (6.16)$$

has the same structure as $Q(\omega)$ (Prop. 2). In fact, Q' is a polynomial with respect to ω

$$Q'(\omega) = \sum_{j=0}^{N-1} C_\ell^{[j]} \omega^{2N-2-2j} \quad (6.17)$$

with the coefficient $C_\ell^{[j]}$ is a polynomial of $\lambda^{[\ell]}$ of degree $2j$, which is proved following a similar idea as in the proof of Prop. 2 (Appx. A): The coefficient $C_\ell^{[j]}$ is in fact the sum of the products of j times $(\lambda^{[\ell']})^2$ over all possible choices of j elements in $S_\ell = \{0, \dots, N-1\} \setminus \ell$:

$$C_\ell^{[j]} = \sum_{s_j \in \binom{S_\ell}{j}} \prod_{p \in s_j} (\lambda^{[p]})^2, \quad (6.18)$$

which is a polynomial of $\lambda^{[\ell]}$ of degree $2j$ as proved in step 2 in Appx. A. Thus, the numerators can be written as elements of the matrices

$$\mathbf{N}^{\text{Re}} = \sum_{j=0}^{N-1} \Phi^{[2j+1]} \omega^{2N-2-2j}, \quad \mathbf{N}^{\text{Im}} = \sum_{j=0}^{N-1} \Gamma^{[2j]} \omega^{2N-1-2j}, \quad (6.19)$$

where the coefficient matrices $\Phi^{[2j+1]}$ and $\Gamma^{[2j]}$ defined similarly as in Sec. 5.4 and are polynomials of the Laplacian matrix \mathcal{L} of degree $2j + 1$ and $2j$. For large enough ω so that the leading term in the numerators are the ones with the highest order of ω and a nonzero coefficient, we obtain the asymptotic behavior of the response strength for large ω as

$$A_i^{(k)} = |R_i^{(k)}| \underset{\text{large } \omega}{\sim} \begin{cases} \Phi_{ki}^{[d(k,i)]} \omega^{-1-d(k,i)} & \text{if } d \text{ odd;} \\ \Gamma_{ki}^{[d(k,i)]} \omega^{-1-d(k,i)} & \text{if } d \text{ even.} \end{cases} \quad (6.20)$$

The normalized frequency response strength behaves as

$$A_i^{*(k)} = N\omega |R_i^{(k)}| \underset{\text{large } \omega}{\sim} \begin{cases} N\Phi_{ki}^{[d(k,i)]} \omega^{-d(k,i)} & \text{if } d \text{ odd;} \\ N\Gamma_{ki}^{[d(k,i)]} \omega^{-d(k,i)} & \text{if } d \text{ even.} \end{cases} \quad (6.21)$$

In the derivation here we use Prop. 1. The above results reveal that, in the localized regime, the nodal response strength of the Kuramoto oscillators decays slower than that of the second-order oscillators: the exponent of the power-law decay is $-d(k,i) - 1$ instead of $-2d(k,i) - 2$, which essentially comes from the order of the dynamics. Particularly, the frequency response strength of the perturbed node in Kuramoto oscillator networks does not decay at all: the exponent is 0 thus it approaches a constant as $\omega \rightarrow \infty$ (see Fig. 6.3).

The phase delay of the steady sinusoidal response $\Theta_i^{(k)}$ approaches 0, π or $\pm\frac{\pi}{2}$ depending on the distance being odd or even, and also on the sign of the leading coefficients $\Phi_{ki}^{[d(k,i)]}$ or $\Gamma_{ki}^{[d(k,i)]}$:

$$\Delta_i^{(k)} - \varphi = \arg(R_i^{(k)}) \underset{\text{large } \omega}{\sim} \begin{cases} \text{atan2}\left(-\Gamma_{ki}^{[d(k,i)+1]}, \Phi_{ki}^{[d(k,i)]} \omega\right) & \text{if } d \text{ odd;} \\ \text{atan2}\left(-\Gamma_{ki}^{[d(k,i)]} \omega, \Phi_{ki}^{[d(k,i)+1]}\right) & \text{if } d \text{ even.} \end{cases} \quad (6.22)$$

As $\omega \rightarrow \infty$, the relations (6.20)–(6.22) still stand. $\text{Re}(R_i^{(k)})$ and $\text{Im}(R_i^{(k)})$ behave asymptotically as

$$\text{Re}(R_i^{(k)}) \underset{\omega \rightarrow \infty}{\sim} \sum_{\ell=0}^{N-1} \frac{v_k^{[\ell]} v_i^{[\ell]} \lambda^{[\ell]}}{\omega^2} = \mathcal{L}_{ki} \omega^{-2}, \quad \text{Im}(R_i^{(k)}) \underset{\omega \rightarrow \infty}{\sim} \sum_{\ell=0}^{N-1} \left(-\frac{v_k^{[\ell]} v_i^{[\ell]}}{\omega} \right) = -\delta_{ki} \omega^{-1}, \quad (6.23)$$

leading to consistent results for the nodes with $d(k, i) = 0$ and $d(k, i) = 1$. For other nodes with larger distances the limit values are zero, thus their behaviors are still described by (6.20)–(6.22).

6.2 Low-damping limit: a Hamiltonian system

When the damping parameter α is much smaller than β , the dynamics of the phase oscillator networks is dominated by the change of rate of the oscillators' phase velocities $\ddot{\theta}$. Without loss of generality, we let $\beta = 1$ and $\alpha = 0$:

$$\ddot{\theta}_i = \Omega_i + \sum_{j=1}^N K_{ij} \sin(\theta_j - \theta_i) + \varepsilon D_i(t), \quad (i = 1, \dots, N). \quad (6.24)$$

This is a Hamiltonian system with the potential energy and the kinetic energy given by Eq. 3.12 and Eq. 3.13 [106], where no energy is dissipated in the network system through damping. That means, if the system is not driven ($\varepsilon = 0$), Liouville's theorem [118] applies: a volume element of the $2N$ -dimensional state space is conserved along every trajectory of the system.

Network responses to a sinusoidal signal

The total network response of such a hamiltonian system is governed by

$$\ddot{\theta}^{\text{tot}} = \varepsilon e^{i(\omega t + \varphi)}, \quad (6.25)$$

which gives the solution

$$\theta^{\text{tot}}(t) = \theta_0^{\text{tot}} + \frac{\varepsilon}{\omega^2} e^{i\varphi} + \left(\dot{\theta}_0^{\text{tot}} + \frac{i\varepsilon}{\omega} e^{i\varphi} \right) t - \frac{\varepsilon}{\omega^2} e^{i(\omega t + \varphi)}. \quad (6.26)$$

With initial conditions being at the fixed point, $\theta_0^{\text{tot}} = \theta^{*,\text{tot}}$ and $\dot{\theta}_0^{\text{tot}} = 0$, the total network response reads

$$\theta^{\text{tot}}(t) = \theta^{*,\text{tot}} + \frac{\varepsilon}{\omega^2} e^{i\varphi} + \frac{i\varepsilon}{\omega} e^{i\varphi} t - \frac{\varepsilon}{\omega^2} e^{i(\omega t + \varphi)}. \quad (6.27)$$

Since the characteristic equation of Eq. 6.25 has a root 0 with multiplicity 2, the solution of the total network response include a linear term with respect to t apart from a constant phase shift and an sinusoidal response (Fig. 6.4). All responses are proportional to the perturbation strength ε . This additional term means a uniform drift away from the initial state, which is particular for the Hamiltonian case. The drift term also implies that, as

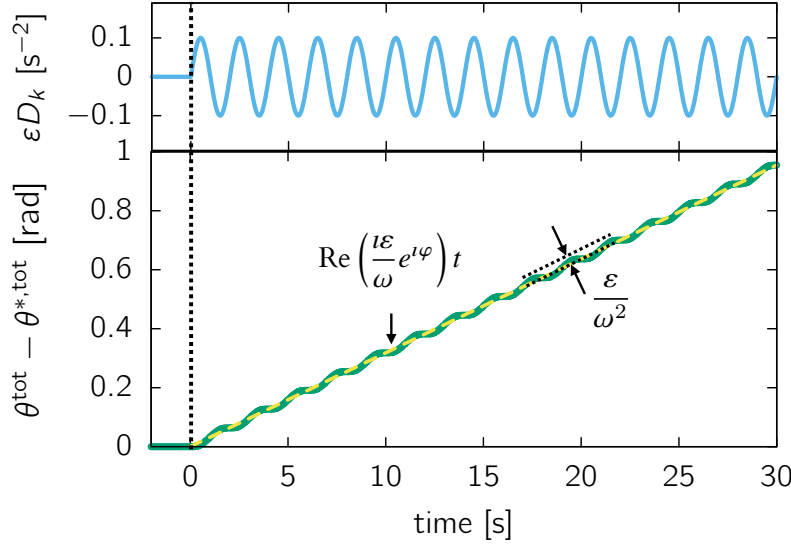


Fig. 6.4 Network's total response to a sinusoidal driving signal at the low-damping limit. An illustration for the total network response given in Eq. 6.27, which contains a phase shift, a sinusoidal oscillation and a uniform drift. The sinusoidal driving signal is plotted in the upper panel. The network setting is the same as in Fig. 4.1 except $\alpha = 0$.

the total network response grows linearly with time, no steady response patterns exist as $t \rightarrow \infty$ in the networks at the low-damping limit.

At the low-damping limit, solving for the nodal responses to a sinusoidal driving is not as straightforward as for the general case in Sec. 4.2 and for the high-damping case in Sec. 6.1. Assuming nodal responses being $\theta_i^{(k)}(t) = \theta_i^* + \varepsilon\eta_i^{(k)} + \varepsilon u_i^{(k)}t + \varepsilon\Theta_i^{(k)}$ leads to a matrix equation

$$-\omega^2\Theta^{(k)} = -\mathcal{L}\mathbf{H}^{(k)} - \mathcal{L}\mathbf{U}t - \mathcal{L}\Theta^{(k)}, \quad (6.28)$$

which has too many variables to be determined. In fact, as we will see in Part III of the thesis, the nodal response has a more complicated form, which can be obtained by expressing the nodal responses as a linear combination of Laplacian eigenvectors with *time-dependent* coefficients.

Network response to a step-function signal

The total network response to a step-function signal at the low-damping limit follows

$$\ddot{\theta}^{\text{tot}} = \varepsilon, \quad (6.29)$$

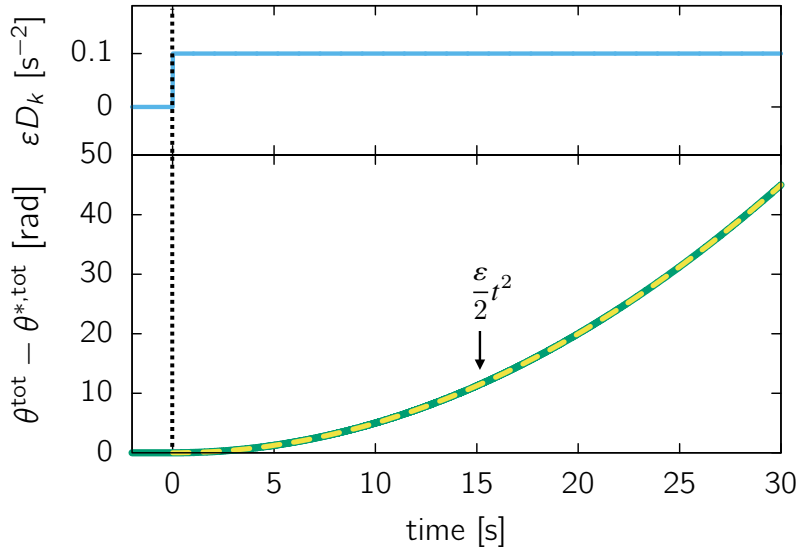


Fig. 6.5 **Network's total response to a sinusoidal driving signal at the low-damping limit.** An illustration for the total network response given in Eq. 6.31, which is essentially a parabolic drift. The step-function driving signal is plotted in the upper panel. The network setting is the same as in Fig. 4.1 except $\alpha = 0$.

which leads to the solution

$$\theta^{\text{tot}}(t) = \theta_0^{\text{tot}} + \dot{\theta}_0^{\text{tot}} t + \frac{\varepsilon}{2} t^2. \quad (6.30)$$

If the system is at a fixed point prior to perturbation,

$$\theta^{\text{tot}}(t) = \theta^{*,\text{tot}} + \frac{\varepsilon}{2} t^2. \quad (6.31)$$

The result suggests a parabolic drift away from the initial fixed point proportional to the perturbation strength ε (Fig. 6.5), thus no steady response pattern exist in this case either. As the nodal response to a sinusoidal signal, the nodal response to a step-function signal also has a more complicated form than parabolic drift. We discuss these cases in Chap. 10.

6.3 Conclusion

In this chapter we investigated the responses of the phase oscillator networks at the high- and low-damping limits. We computed the total network response and the nodal responses to a sinusoidal driving signal and to a step-function signal at the two limits, which are summarized in Tab. 6.1. Particularly, for the high-damping limit, we identified three frequency regimes of response patterns, two of which are similar as in the general

intermediate-damping case. An comparison between the frequency regimes in both cases is given in Tab. 6.2.

	driving signal ($t > 0$)	total response ($t > 0$)		nodal response ($t > 0$)	
		phase shift	particular response	phase shift	particular response
$\alpha = 1$ $\beta = 0$ high-damping limit	$\varepsilon e^{i(\omega t + \varphi)}$	$-\frac{\varepsilon}{i\omega} e^{i\varphi}$	$\frac{\varepsilon}{i\omega} e^{i(\omega t + \varphi)}$	$\frac{i\varepsilon e^{i\varphi}}{N\omega}$	$\sum_{\ell=0}^{N-1} \frac{\varepsilon e^{i(\omega t + \varphi)} v_k^{[\ell]}}{i\omega + \lambda^{[\ell]}} \mathbf{v}^{[\ell]}$
	ε		εt	$\sum_{\ell=1}^{N-1} \frac{\varepsilon}{\lambda^{[\ell]}} \left(v_k^{[\ell]} - \frac{1}{N} \sum_{i=1}^N v_i^{[\ell]} \right) v_i^{[\ell]} + \varepsilon \eta'^{(k)}$	$\frac{\varepsilon}{N} t$
$\alpha = 0$ $\beta = 1$ low-damping limit	$\varepsilon e^{i(\omega t + \varphi)}$	$\frac{\varepsilon}{\omega^2} e^{i\varphi}$	$\left(\dot{\theta}_0^{\text{tot}} + \frac{i\varepsilon}{\omega} e^{i\varphi} \right) t - \frac{\varepsilon}{\omega^2} e^{i(\omega t + \varphi)}$	see Part III	
	ε		$\frac{\varepsilon}{2} t^2$		

Table 6.1 Linear network responses at high- and low-damping limits.

At the high-damping limit ($\alpha = 1, \beta = 0$), the first-order derivatives of oscillators' phases dominate the system's dynamics, the network system becomes a network of Kuramoto oscillators. The total network responses still exhibit the same particular responses to driving signals: a sinusoidal oscillation with a complex amplitude for a sinusoidal signal, and a uniform drift to a step-function signal. However, unlike in the general second-order oscillator networks, the *particular responses* arise *instantaneously* in the first-order oscillator networks, i.e. no transient responses (Tab. 6.1). This can be understood as follows: the transient response in the general case, which is characterized by a time constant $\frac{\beta}{\alpha}$ shrinks to zero as $\beta = 0$. This means that the response patterns arise in Kuramoto oscillator networks immediately after the driving.

The nodal response of the networks of first-order oscillators has the same form as that of the networks of second-order oscillators with $\alpha = 1$ and $\beta = 0$ (Tab. 6.1, network topology-specific responses are shaded with orange, non-specific ones with blue). Based on the nodal responses, we again identified three frequency regimes of response patterns (Tab. 6.2). Different from the regimes for the general case, the three frequency regimes for the first-order oscillator networks are divided by the Laplacian eigenvalues instead of the eigenfrequencies, which are more wide-spreading. For first-order oscillator networks, no intrinsic oscillation frequency exists since all Jacobian eigenvalues are non-positive real numbers. Thus, no resonances can appear and the nodal response strengths exhibit smooth transitions in this regime. For lower frequencies $\omega \rightarrow 0$, the network responds to perturbations homogeneously as the second-order networks; for higher frequencies $\omega \rightarrow \infty$, the impact of the driving signal is localized. Remarkably, the distance-dependent power-law decay of the nodal response strength is slower than in second-order networks:

as $\sim \omega^{-1-d}$ instead of $\sim \omega^{-2-2d}$. Thus the spatial decay of the response strength is also two times slower, meaning the impact of the perturbation signal is *less* localized in Kuramoto oscillator networks. Additionally, for $\omega \rightarrow \infty$, the sinusoidal nodal response can appear as in phase and anti-phase with respect to the sinusoidal driving signal, in addition to the in quadrature responses in the second-order oscillator networks. That is, the phase delay can be $0, \pi, \pm\frac{\pi}{2}$ in first-order oscillator networks while it can only be $\pm\frac{\pi}{2}$ in first-order oscillator networks.

sinusoidal driving $\varepsilon e^{i\omega t+\varphi}$	Second-order oscillator networks			First-order (Kuramoto) oscillator networks		
	ω	$A_i^{*(k)}$	$\Delta_i^{*(k)} - \varphi$	ω	$A_i^{*(k)}$	$\Delta_i^{*(k)} - \varphi$
<i>bulk regime</i>	$\omega \rightarrow 0$	1	0	$\omega \rightarrow 0$	1	0
<i>resonance/ transition regime</i>	$\omega \sim \sqrt{\lambda^{[\ell]} - \frac{\alpha^2}{4}}$	topology-specific resonances		$\omega \sim \lambda^{[\ell]}$	transitions	
<i>localized regime</i>	$\omega \rightarrow \infty$	$\sim \omega^{-1-2d}$	$\pm\frac{\pi}{2}$	$\omega \rightarrow \infty$	$\sim \omega^{-d}$	$0, \pi, \pm\frac{\pi}{2}$

Table 6.2 Comparison of the frequency regimes for second- and first-order oscillator networks.

Especially, our results of the response patterns in sinusoidally driven Kuramoto oscillator networks are consistent with and goes beyond Zanette's results [39, 40]. We find the same dependence of the response strength on driving frequency and the topological distance between perturbation and response: (i) For large driving frequency, the response strength decreases exponentially with distance (Fig. 1 in [39]), and (ii) for small driving frequency and for nodes with large distance, the response strength A decrease with driving frequency ω as $A \sim \omega^{-1}$ (Fig. 2 in [39]). However, our work generalized Zanette's results in the sense of

1. For small frequency, we showed that the dependence $A \sim \omega^{-1}$ is valid for *all* nodes while Zanette only showed its validity for the nodes with large distance;
2. Although the adjacency matrix enters Zanette's analysis and different regimes of response pattern were observed, an explicit relation between network structure and regime-specific response pattern was missing. In comparison, our theory gives explicit definitions of the three frequency regimes in terms of the eigenvalues of the Laplacian matrix, which characterizes the underlying network topology.

3. Our results are valid for networks with *arbitrary* topologies while Zanette's results are derived only for regular graphs where each node has the same degree.

At the low-damping limit ($\alpha = 0, \beta = 1$), the second-order derivatives of oscillators' phases dominate the system's dynamics. The network system at this limit can be viewed as a network of ideal synchronous machines without dissipation of energy, that is, a Hamiltonian system. If without driving, the Hamiltonian of the system is time-independent; if driven by an external signal, the Hamiltonian becomes time-dependent. In comparison, in driven dissipative network systems ($\alpha \neq 0, \beta \neq 0$), the average energy dissipation must exactly compensate the average energy injection by the driving signal, so that a steady responding state can be maintained. The time-dependent Hamiltonian leads to completely different *particular responses* in the total network response: a sinusoidal oscillation and a uniform drift for a sinusoidal signal, and a parabolic drift for a step-function signal (Tab. 6.1). The drifts imply that there are no steady response pattern in network at the low-damping limit. Furthermore, the nodal response in this case has a more complicated form than the total network response, thus can not be determined following the same routine as in the previous analysis. The general solution of the nodal responses will be given in Part III of the thesis.

Chapter 7

Predicting Network Responses to Irregular and Distributed Signals

After the mathematical analysis of networks' dynamic responses presented in the previous chapters, in this chapter we move on to a more practical topic: the prediction of networks' responses to noisy signals, which can be irregular in time and distributed in space. That is, given the time series of arbitrary perturbation signals, how does a network with a specific topology respond?

We first propose an approach to predict the nodal response time series to irregular and distributed signals in a network based on the previously developed theory for linear network responses (Chap. 4 and Chap. 5). In Sec. 7.2, we apply the approach and make predictions for a sample power grid's nodal responses to two fluctuation time series recorded in real-world power supply from renewable energy sources. The sample power grid exhibits different responsive behaviors under the influence of a wind- and a solar-power fluctuation, due to the different frequency contents in the signals. In the last section, we discuss the error in the linear response prediction and explore the limit of validity of the linear response theory in challenging situations such as strong perturbations and heavily-loaded networks.

7.1 An approach to predict network responses

In Chap. 4 and Chap. 5 we discussed how a second-order phase oscillator network with a complex network topology responds to a single driving signal in its steady state, either to a sinusoidal signal with frequency $\omega > 0$ or to a step-function signal. However, in the real world, complex networks are usually exposed to noisy signals. Temporally, the signals can have irregular wave forms; and spatially, they can occur simultaneously at multiple site in a network. How does a complex network respond to such complex signals?

A short answer to this question is given by a simple generalization of our linear response theory. Recall that we build the entire theory on the linearization of the network system, meaning that the system under consideration can be viewed as a linear operator which satisfies two properties: additivity and homogeneity. That means, *the response to the sum is the sum of the responses*.

Fourier analysis provides a way to represent a general function in the time domain, i.e. a signal with an irregular waveform, as a sum of sinusoidal signals with different amplitudes and frequencies. Thus, given the trajectory of an irregular signal, a network's linear response equals to the sum of its linear responses to each frequency component of the irregular signal. Furthermore, if multiple nodes in a network are simultaneously and independently perturbed, the network response is simply the sum of the responses to each perturbation signal. Consequently, the linear frequency response of node i in a network driven by irregular and distributed signals can be expressed as a double sum over frequency components of one signal and over independent signals at different nodes:

$$\dot{\theta}_i^{(\kappa)}(t) = \sum_{k \in \kappa} \left(\frac{\varepsilon_{0_k}}{N\alpha} + \sum_{n_k} \iota \varepsilon_{n_k} \omega_{n_k} \sum_{\ell=0}^{N-1} \frac{v_k^{[\ell]} v_i^{[\ell]} e^{\iota(\omega_{n_k} t + \varphi_{n_k})}}{-\beta \omega_{n_k}^2 + \iota \alpha \omega_{n_k} + \lambda^{[\ell]}} \right). \quad (7.1)$$

Here κ is the set of the indices of the perturbed nodes, ω_{n_k} , ε_{n_k} and φ_{n_k} denote the frequency, the amplitude and the phase of the n -th frequency component of the perturbation signal at node k . Particularly, ε_{0_k} denotes the strength of the step-function signal at node k .

In practice, however, the longer the signal time series, the more frequency components it contains, and the longer the computation time is required to predict the network responses via formula (7.1). Specifically, a discrete time series with N data points corresponds to $\frac{N}{2}$ real frequency components via discrete Fourier transform. The number of frequency components increases linearly with the length of the time series, and so does the computation time. Therefore, given limited computation time or limited computational capacity, effective methods for frequency components selection are needed.

Information about how the power of a signal time series is distributed over frequency is given by the *power spectral density (PSD)*, $S(\omega)$, of the signal [119]. The PSD of frequency ω is given by the discrete Fourier transform of the signal time series $\mathcal{F}[F(t)](\omega)$ through $S(\omega) = \frac{1}{N_S} |\mathcal{F}[F(t)](\omega)|^2$ with N_S being the normalization factor. The frequency components with higher PSD values are stronger oscillatory modes of the signal. Therefore, PSD value serves as an index of the significance of a frequency component. For irregular signals with arbitrary power spectral distributions, selecting the frequency components with higher PSD values to represent the original signal yields smaller deviations from the original signal. For instance, to predict the network response to a recorded power

fluctuation signal (see Sec. 7.2), we select 50 frequency components with the top 50 PSD values. However, for noisy signals which are characterized by specific shapes of PSD function, e.g. pink noise with $S(\omega) \propto \omega^{-1}$, Brownian noise with $S(\omega) \propto \omega^{-2}$ and grey noise following an equal loudness curve¹, this naive frequency selection method has its drawbacks: wide bands of frequencies in the spectrum would be left unrepresented. This is undesired, especially when the excluded frequency block overlaps with the resonance regime where a certain frequency can cause a global resonant pattern across the network with strong responses at particular nodes.

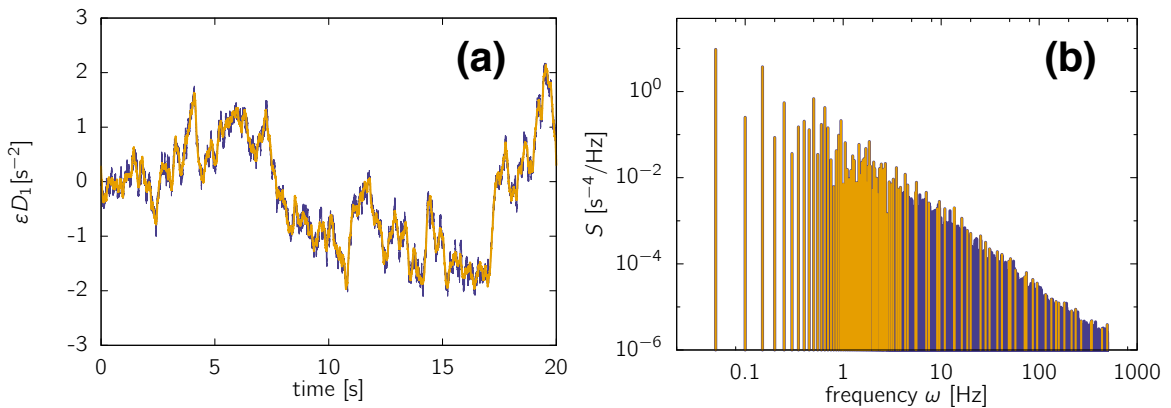


Fig. 7.1 An illustration of the frequency sampling method. A time series of Brownian noise (a) and its power spectral density (b) are plotted in purple. 100 selected frequencies out of 10^4 are highlighted in yellow in (b). The time series reconstructed by the 100 selected frequency components is shown with a yellow line in (a).

To avoid this, we propose a *frequency sampling method*: besides the strongest frequency components, we additionally select frequency components in the excluded block by binning the block and picking the strongest frequency component in each bin. An example of the method is illustrated in Fig. 7.1. We consider the artificial Brownian noise time series (Fig. 7.1a) with 20000 time steps in the example in Fig. 5.1. The PSD of the time series (Fig. 7.1b) contains 10000 frequencies up to 500Hz. We first select 50 frequency components with the top 50 PSD values, and the excluded frequencies form a band at the high-frequency end. Then we divide the frequency band into 50 bins and select the strongest one from each bin. In this way we select 100 frequency components in total out of 10000. As shown in Fig. 7.1a, the reconstruction of the signal time series containing only 1% of the frequency components is already very close to the original signal. It can be seen from the lower panels in Fig. 5.1b that predicted nodal responses based on the 100 selected frequency components (black lines) are also quite close to the responses to the original signal from numerical simulation (purple lines). How the performance of prediction depends on the number of Fourier modes used for prediction will be discussed in detail in Sec. 7.3. In general, the parameters in the

¹An equal loudness curve gives the sound pressure level of pure continuous tones with a specific frequency which are perceived as equally loud by human listeners [120].

frequency sampling method, such as the number of dominant frequencies to be selected, the number of bins in sampling the weaker frequencies, and the number of frequency to be selected in each bin, need to be tuned *ad hoc* for individual signals and for individual systems to deliver satisfying results.

In short, combining formula (7.1) and the frequency sampling method, we proposed an approach to predict the time-dependent network response to given time series of perturbation signals. Furthermore, for signals whose time series are unknown but the PSDs are given, our theory can still provide an upper bound of nodal frequency response, which is given by the sum of the frequency response strength for each frequency component:

$$|\dot{\theta}_i^{(\kappa)}(t)| = \sum_{k \in \kappa} \left(\frac{\varepsilon_{0_k}}{N\alpha} + \sum_{n_k} \left| i\varepsilon_{n_k} \omega_{n_k} \sum_{\ell=0}^{N-1} \frac{v_k^{[\ell]} v_i^{[\ell]}}{-\beta\omega_{n_k}^2 + i\alpha\omega_{n_k} + \lambda^{[\ell]}} \right| \right). \quad (7.2)$$

This bound can e.g. serve as a guideline in identifying “risky” nodes which exhibit strong responses to such signals.

7.2 Predicting dynamic responses of power grids to fluctuations

With an increasing share of renewable energy sources with intermittent nature in modern power grids, the fluctuations in power generation are stronger than ever before: For instance, in Germany the fraction of renewable energy sources was only 3.4% in 1990; it increased to 6.2% in 2000 and to 31.7% in 2016 [121]. Such fluctuations result in an imbalance between power generation and power consumption which endangers the stable operation of the power supply system. Thus it is essential to understand how a power grid network, as a collection of interacting units, would respond to potentially irregular and distributed power fluctuations. In this section, we apply the approach to predict network responses introduced in last section to make predictions for power grids’ nodal responses to power fluctuations from real-world recordings.

7.2.1 Modeling modern power grids with penetration of renewable energy sources

Units with and without inertia in modern power grids In Sec. 3.2 we introduced the oscillator model of power grids, where each unit in network is assumed to be synchronous machines and is modeled as a phase oscillator obeying the swing equation (Eq. 3.5). In practice, it is common to write the swing equation in per-unit form with

normalized parameters about the machine's technical features, such as the moment of inertia and the damping:

$$\frac{2H_i}{\Omega_0}\ddot{\theta}_i + \tilde{D}_i\dot{\theta}_i = \tilde{P}_i^{\text{mech}} - \tilde{P}_i^{\text{el}}. \quad (7.3)$$

Here $\tilde{P}_i^{\text{mech}}$ and \tilde{P}_i^{el} are respectively the net injected mechanical power and the transmitted electrical power in per unit form, i.e. P_i^{mech} and P_i^{el} divided by the machine rating P_i^{rated} . $\tilde{D}_i := \frac{D_i}{P_i^{\text{rated}}}$ is the normalized damping constant and H is the normalized *inertia constant* of the synchronous machine, proportional to the inertia of the rotor. It is defined as the stored kinetic energy stored at the synchronous speed Ω_0^m divided by the machine rating [114, 115]:

$$H_i := \frac{\frac{1}{2}I_i(\Omega_0^m)^2}{P_i^{\text{rated}}}. \quad (7.4)$$

In modern power grids with penetration of renewable energy sources, other types of units are integrated in the networks, i.e. the inertia-less power generators such as wind turbines and solar panels [122]. Usually there are two ways to model the impact of inertia-free generators: One is to consider the dynamics of the electronic devices connected to the renewable power generators, such as inverters and VISMAAs [123–125], the other is to model the power grids in a coarse grained perspective: The power grids are treated as a large-scale transmission network of coherent sub-grids, which can include both synchronous machines and inertia-less generators. As we are interested in the large-scale patterns in networks with complex topologies, we adopt the second approach in the thesis.

A coarse grained model of power grids In a coarse grained model, we assume that the power grid network consists of sub-grids, in which the units are strongly coupled, so that the inter-area dynamics is much slower than the intra-area dynamics. Thus all machines in a sub-grid can be condensed into one effective unit. The dynamics of the aggregated machines is then be described by the so-called *aggregated swing equation* [126]:

$$\frac{2\bar{H}}{\Omega_0}\ddot{\bar{\theta}} + \bar{D}\dot{\bar{\theta}} = \bar{P}^{\text{mech}} - \bar{P}^{\text{el}} \quad (7.5)$$

with $\dot{\bar{\theta}} := \frac{\sum_i H_i P_i^{\text{rated}} \dot{\theta}_i}{\sum_i H_i P_i^{\text{rated}}}$ being the center of inertia (COI) grid frequency, $\bar{H} := \frac{\sum_i H_i P_i^{\text{rated}}}{\sum_i P_i^{\text{rated}}}$ the aggregated inertia constant of the sub-grid, and \bar{D} the normalized damping constant assumed to be constant and uniform in the sub-grid. \bar{P}^{mech} is the total mechanical power injected in the sub-grid and \bar{P}^{el} is the total electrical power transmitted from the sub-grid. \bar{H} , \bar{D} , \bar{P}^{mech} and \bar{P}^{el} are all in per-unit form, i.e. normalized by the total rated power

of the sub-grid. The aggregated inertia \bar{H} can be smaller in sub-grids with a high penetration of renewables and changes on a larger time scale [126].

Modeling the fluctuating power input from renewables In conventional power grids relying on fossil fuels, the power generation is usually temporally constant in the time scale of seconds, i.e. $\tilde{P}^{\text{mech}} = 1$. However, it becomes highly fluctuating when power is generated from renewable energy sources. To investigate the impact of a single fluctuating power input from renewables, we assume all nodes (sub-grids) in the transmission network consist of only conventional synchronous machines, except one sub-grid is influenced by a fluctuating power input from the renewables. The effective inertia of the perturbed sub-grid is provided by the physical inertia of the synchronous machines and the virtual inertia of the electronic devices connected to the wind turbines or the solar panels. The total power injection $P_i^{\text{tot}}(t)$ in the sub-grid i is the sum of the constant mechanical power input from fossil fuels P_i^s and the fluctuating power input $P_i^r(t)$ from the renewables:

$$P_i^{\text{tot}}(t) = P_i^s + P_i^r(t). \quad (7.6)$$

The *penetration rate* p_i of fluctuating renewables in the sub-grid i is defined as

$$p_i := \frac{\langle P_i^r(t) \rangle_t}{\langle P_i^{\text{tot}} \rangle_t}. \quad (7.7)$$

To compare the impact of different power fluctuation recordings, we fix the penetration rate p_i and obtain per-unit power fluctuation time series by rescaling the recorded time series of power fluctuation $x_i(t)$ as

$$\begin{aligned} \bar{P}_i^{\text{mech}}(t) &= \frac{P_i^{\text{tot}}(t)}{\langle P_i^{\text{tot}}(t) \rangle_t} = \frac{P_i^s}{\langle P_i^{\text{tot}}(t) \rangle_t} + \frac{P_i^r(t)}{\langle P_i^{\text{tot}}(t) \rangle_t} = (1 - p_i) + \frac{x_i(t)}{\langle x_i(t) \rangle} p_i \\ \text{so that } \langle \bar{P}_i^{\text{mech}}(t) \rangle_t &= 1. \end{aligned} \quad (7.8)$$

Comparing the coarse grained model of power grids (Eq. 7.5) and the perturbed second-order Kuramoto-like oscillator model (Eq. 4.1), we arrive at the following relations:

$$\begin{aligned} \theta_i &= \bar{\theta}_i, \quad \beta_i = 1, \quad \alpha_i = \frac{\Omega_0 \bar{D}_i}{2 \bar{H}_i}, \quad P_i = \frac{\Omega_0}{2 \bar{H}_i}, \\ K_{ij} &= \frac{\Omega_0}{2 \bar{H}} \kappa_{ij}, \quad \varepsilon D_i(t) = \frac{\Omega_0}{2 \bar{H}} (\bar{P}_i^{\text{mech}}(t) - 1). \end{aligned} \quad (7.9)$$

Here $\kappa_{ij} := \frac{3U^2 B_{ij}}{2P_i^{\text{rated}}}$ denotes the *normalized* maximal transmission power between i and j in per-unit form (see Eq. 3.6). In this work, we assume identical node parameters and typical values for the rated grid frequency, the damping constant and the inertia constant:

$\Omega_0 = 2\pi \times 50 \text{ Hz}$, $\bar{D}_i = \bar{D} = 0.02 \text{ s}^2$, and $\bar{H}_i = \bar{H} = 4 \text{ s}$ [127]. The capacity of transmission lines is set to be twice of the rated power of generators: $\kappa_{ij} = \kappa = 2 \text{ p.u.}$. The penetration rate of renewables $p_i = 0.5\delta_{ik}$, i.e. is 50% for the node k which is exposed to a fluctuating power input, and is 0 for other nodes.

7.2.2 Grid responses to a real-world power fluctuation

As the first step of predicting power grid responses to given power fluctuations, we investigate the frequency response of a sample coarse-grained power grid network² to the time series of two real-world power fluctuation recordings, one of wind power and one of solar power. As we show below, the grid network exhibits prominently different responsive behavior to the two fluctuation signals due to their different PSDs. It will be an interesting future task to compute the response to time series generated by e.g. engineering inspired mathematical random processes to systematically investigate the impact of different types of power fluctuations with specific PSD characteristics.

For both fluctuation signals, we predict the impact via the approach introduced in Sec. 7.1, including select dominant frequency components according to the PSD of the signal and compute the response via linear response theory (Eq. 7.1). The predicted response is also compared to the results from direct numerical simulation.

Wind power fluctuation The time series of wind power fluctuations we use in this work is obtained from Ref. [20] of [129]. The data were provided by wpd windmanager GmbH, Bremen. The sampling rate of the data is 1 Hz, i.e. every data point in the time series is the time average of the instantaneous power over 1 second. We use a subset (100 second) of the time series labeled “power 1” in the data set and rescale the time series according to Eq. 7.2.1 (Fig. 7.2a). For computing the network’s response via numerical simulation with the 4-th order Runge–Kutta method (time step 0.01 s) we locally interpolate the time series as a polynomial of degree 2 and resample the interpolating function. However in the PSD of the signal all frequencies resulting from artificial interpolation, i.e. the ones larger than 1 Hz, are discarded. For predicting the network response, we select 50 frequency components with the largest PSD values as the dominant Fourier modes (Fig. 7.2d). The nodal frequency responses are computed as the sum of the responses to the 50 selected modes (Eq. 7.1).

The predicted nodal frequency responses are shown in Fig. 7.2b. After a transient stage of about 5 seconds, our approach well predicts the response time series (see Fig. 7.2c). Particularly, the slow-changing wind power fluctuation induces similar response time series at all units in the network. The reason for such a response pattern can be found by comparing the PSD of the fluctuation time series and the eigenfrequencies of the system

²The topology of the sample power grid is generated according to a random growth model of power grid networks proposed by P. Schultz et al. [128]. The cost-vs-redundancy trade-off parameter $r = 0$, meaning line redundancy is disregarded in the network growth.

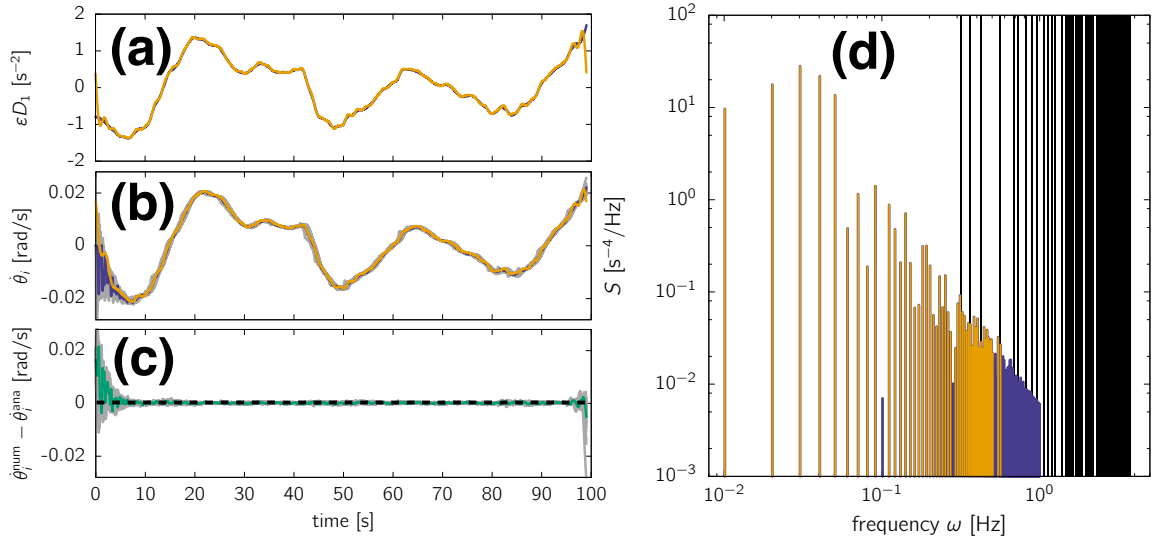


Fig. 7.2 Grid responses to a real-world wind power fluctuation recording. The wind power fluctuation time series obtained via (7.2.1) and (7.9) is shown in purple in (a). Its PSD is plotted with purple lines in (d) and 50 dominant frequency components are highlighted in yellow. The black vertical lines in (d) indicate the eigenfrequencies of the system. The reconstructed power fluctuation containing only the dominant Fourier modes is plotted in yellow in (a). The predicted frequency response time series of one node is plotted as the yellow line in (b), together with the result from numerical simulation (purple line). The responses of other nodes in the network are shown in light grey in (b). The difference between the numerical and the predicted response time series is shown in (c): green for the node highlighted in (b) and grey for other nodes. The network topology is the same as in Fig. 5.1.

(see Fig. 7.2d): the dominant frequencies are mostly lower than the lowest eigenfrequency, which means, they are in the bulk regime of perturbation frequencies and thus induce very similar responses at each node (see analysis in Sec. 5.3).

Solar power fluctuation The time series of a fluctuating solar power, i.e. the output power recording of a photovoltaic panel, is obtained from the same source (available under Ref. [20] of [129]). The measurement took place at a platform roof of the University Oldenburg, Germany (53.152°N , 8.164°E). The sampling rate of the recording is also 1 Hz as the wind power time series. The time series in the dataset are the dimensionless clear sky indices, which is the measured solar irradiance normalized by its theoretical prediction under clear sky at a given latitude and longitude. For simulations and analysis we use a part of the time series labeled “sensor 1” with a length of 100 seconds, locally interpolated as a polynomial of degree 2 and resample the interpolating function. The time series is also rescaled according to Eq. 7.2.1 (Fig. 7.3a). In the PSD of the time series (Fig. 7.3d) all interpolation-induced frequencies (> 1 Hz) are discarded.

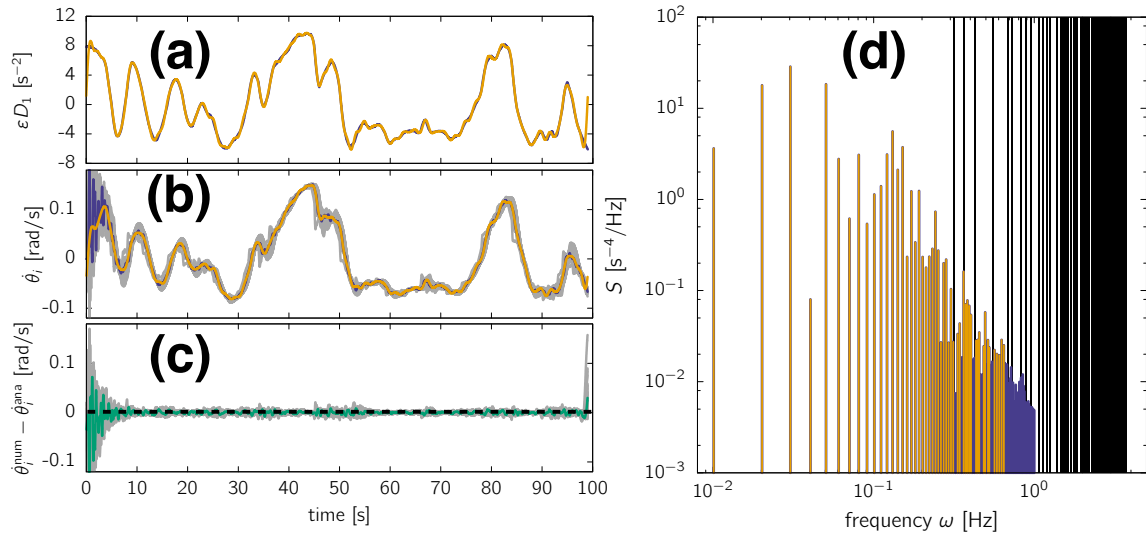


Fig. 7.3 Grid responses to a real-world solar power fluctuation recording. The color coding of the lines and the network settings except the power fluctuation fed into the network are the same as in Fig. 7.2.

The prediction for the frequency responses to the solar power fluctuation is shown in Fig. 7.3b. The larger deviation between the numerical and the predicted response time series than that for the wind power fluctuation comes from the larger perturbation magnitude (cf. Fig. 7.2a,c and Fig. 7.3a,c). Particularly, among the frequency responses of different nodes in the network, we observe a larger heterogeneity while they still share the same trend (cf. Fig. 7.2b). The low frequency components dominating the fluctuation time series (Fig. 7.2d) locate in the bulk regime, thus induce a common low-frequency response trend in the network. Meanwhile, the higher contribution of the frequencies larger than the smallest eigenfrequency, i.e. in the resonance regime (cf. Fig. 7.2d, Fig. 7.3d) leads to characteristic resonant response patterns in the power grid network, thus results in higher heterogeneity among the response time series.

7.3 Prediction error and limit of validity

In the last sections we propose an approach to predict dynamic network responses to irregular and distributed perturbations and present an example of its application on predicting the nodal frequency response of a sample power grid network to real-world power fluctuations. As shown in Fig. 7.2 and Fig. 7.3, the predicted responses are very close to the results from numerical simulation. However, how do our predictions based on the linearized dynamics deviate from the ones numerically determined from the nonlinear dynamics? How do the prediction error depend on variables in the prediction approach, in the perturbation signal and in the network prior to perturbation? In this

section we investigate the limit of validity of the linear response theory we developed for dynamic network responses by checking the prediction error in challenging situations, such as stronger perturbation signals, heavier network load prior to perturbations and less Fourier modes for prediction.

First we define the *prediction error* E as the root-mean-square deviations between the nodal frequency response time series from prediction $\dot{\theta}_i^{\text{LRT}}(t)$ (cf. Eq. 7.1) and from numerical simulation $\dot{\theta}_i^{\text{num}}(t)$:

$$E = \left\langle \left(\dot{\theta}_i^{\text{LRT}}(t) - \dot{\theta}_i^{\text{num}}(t) \right)^2 \right\rangle_{t,i}^{\frac{1}{2}}. \quad (7.10)$$

Here $\langle \cdot \rangle_{t,i}$ denotes the average taken over time and over all nodes in the network. Note that in time averaging we exclude the transient stage characterized by $e^{-\frac{\alpha}{\beta}t}$. The averaging starts when $e^{-\frac{\alpha}{\beta}t}$ is smaller than a threshold which we set as 10^{-3} . We compare the state variable $\dot{\theta}_i$ instead of θ_i , since for real-world power grids, the grid frequency $\dot{\theta}_i$ is measurable while the load angle θ_i is not. Additionally, the deviation in grid frequency is of greater practical significance in power grid operation.

Two sources of prediction error can be identified: the intrinsic limitation of the linear response theory and the artificial exclusion of weaker Fourier modes. First, since the analytical solution of the network response is derived based on the linearization of system's dynamics in the vicinity of the fixed point, the formula for prediction Eq. 7.1 is not exactly accurate per se. The neglected higher order terms result in the intrinsic error of prediction. In particular, the linearization of the nonlinear pair-wise interaction between node i and j , or what we call the *load* on edge (i, j) , L_{ij} , reads

$$\begin{aligned} L_{ij} := \sin(\theta_j - \theta_i) &\approx \sin(\theta_j^* - \theta_i^*) + \cos(\theta_j^* - \theta_i^*) (\theta_j - \theta_j^* - \theta_i + \theta_i^*) \\ &+ O\left((\theta_j - \theta_j^* - \theta_i + \theta_i^*)^2\right), \end{aligned} \quad (7.11)$$

where the nodal response $(\theta_i - \theta_i^*)$ is assumed to be small and proportional to the perturbation strength ε for each node $i = 1, \dots, N$. The leading term in the error of the linearization of L_{ij} :

$$\frac{1}{2} \sin(\theta_j^* - \theta_i^*) (\theta_j - \theta_j^* - \theta_i + \theta_i^*)^2 \quad (7.12)$$

depends on (i) the initial load on the edge (i, j) at the fixed point $\sin(\theta_j^* - \theta_i^*)$ and (ii) the perturbation strength which is proportional to the nodal response $\theta_i - \theta_i^*$.

The second source of error comes from the artificial selection of the Fourier modes in the signal. We compute the network responses for the dominant frequency components and neglect the influence of the weaker ones, which reduces the computational cost but

brings prediction error. Thus, we investigate how these three factors influence the overall prediction error in the following.

7.3.1 Prediction error vs. perturbation strength

We first test how the prediction error E changes with an increasing perturbation strength. We consider an 80-unit sample power grid as illustrated in Fig. 5.1 where every unit in the network is exposed under independent Brownian noises. To observe the system's critical behavior close to the bifurcation point, we set $\Omega_g = 3 \text{ s}^{-2}$ for the 20 generators, $\Omega_c = -1 \text{ s}^{-2}$ for the rest 60 consumers, and a smaller coupling strength $K_{ij} = 8 \text{ s}^{-2}$ for all links. The damping parameter $\alpha = 1$.

80 independent 20-second time series of Brownian noise are generated as baseline perturbations $D_i(t)$. The Brownian noises are produced by Wiener processes with normally distributed increments following $\mathcal{N}(0, 0.1)$. We first measure the prediction error via Eq. 7.10 for the baseline noise $D_i(t)$. In the prediction we select 50 dominant frequency components for each noise time series. Then we amplify the noises by multiplying the perturbation time series at each node with the same value ε . Every node is thus perturbed by $\varepsilon D_i(t)$ where ε is cranked up incrementally. We measure the prediction error E for increasing ε until the network is overloaded thus the stable fixed point is lost.

The result (Fig. 7.4) shows that, first, the prediction error E increases slowly for $\varepsilon \lesssim 3$, then faster for $3 \lesssim \varepsilon \lesssim 6$, and at the end almost explosively when ε reaches a threshold $\varepsilon \gtrsim 6$. This behavior can be understood as following. When the noises become stronger, they drive the system further away from the fixed point $\boldsymbol{\theta}^*$. The larger the deviation from the fixed point $|\boldsymbol{\theta} - \boldsymbol{\theta}^*|$, the larger the error in the linearization (7.12), hence the larger the prediction error. When $\varepsilon \gtrsim 6$, as the color coding in Fig. 7.4 indicates, the maximum load in the network reaches 1, meaning that the supply network is fully-loaded under such strong perturbation. Microscopically, the load linearization at the fixed point breaks down when a link goes beyond fully-loaded: the actual load $\sin(\theta_j - \theta_i)$ with $\theta_j - \theta_i \geq \frac{\pi}{2}$ and the linearization at the fixed point (7.11) with $\theta_j^* - \theta_i^* < \frac{\pi}{2}$ wildly diverge from each other (Fig. 7.5). Recall that we assumed $|\theta_i^* - \theta_j^*| \leq \pi/2$ for every edge (i, j) to ensure the stability of the fixed point. On the network level, when the perturbation is strong enough to overload at least one of the links, the flow pattern of the whole network is forced to change: both the direction and the amplitude of the flows can be significantly different from the fixed point. In fact, if the network dynamic system goes beyond the fully-loaded point, it reaches a bifurcation point where the stable fixed point annihilates with another unstable fixed point (see Sec. 3.2.2). The system thus enters an unstable regime which is rarely the case for real-world power grids.

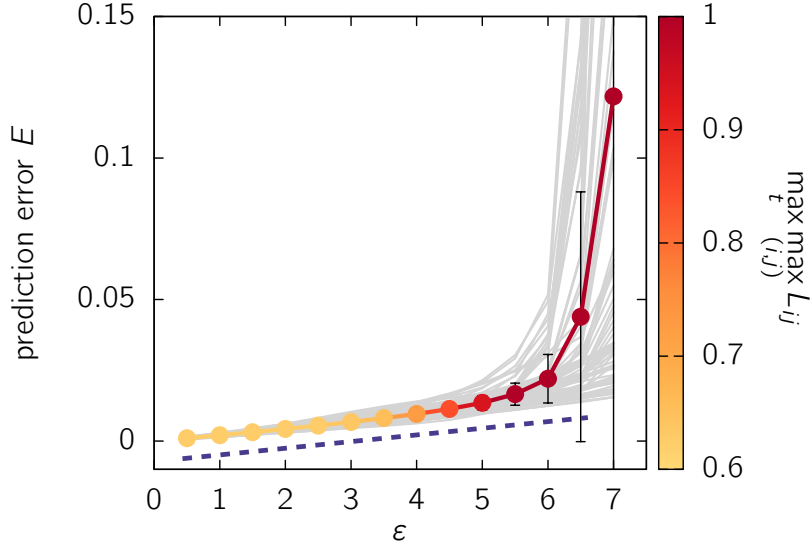


Fig. 7.4 Linear response theory's limit of validity for large noise strengths. The prediction error E (7.10) is plotted as a function of noise strength ε . The nodal prediction error, i.e. (7.10) without the average over nodes, is shown with light gray lines for all nodes. The error bar of E indicates the standard deviation of nodal error across the network. The prediction error is color coded with the maximum link load over time and over network at each ε . The purple dashed line helps to identify the increasingly faster growth of the prediction error. The network structure is the same as in Fig. 5.1. Parameters: $\Omega_g = 3 \text{ s}^{-2}$ for the 20 generators, $\Omega_c = -1 \text{ s}^{-2}$ for the rest 60 consumers, $K_{ij} = 8 \text{ s}^{-2}$, $\alpha = 1$. Every node is perturbed by an independent Brownian noise produced by Wiener processes with normally distributed increments following $\mathcal{N}(0, 0.1)$.

7.3.2 Prediction error vs. prior network load

Next we test the dependence of the prediction error on how heavily the network is initially loaded at the steady state prior to perturbations. We consider the same network as in Sec. 7.3.1 and perturb the network with the same Brownian noise $D_i(t)$. This time we crank up the power injections Ω_i by multiplying them with a ratio r : $\Omega_i \rightarrow r\Omega_i$, while fix the coupling strength, so that the network is more and more heavily loaded at the fixed point. We increase the ratio r incrementally until the steady-state maximum link load in the network $L_{ij}^* := \sin(\theta_j^* - \theta_i^*)$ reaches 1. For each r we measure the prediction error E .

The result (Fig. 7.6) reveals that the prediction error remains almost the same with an increasing prior network load until the maximum link load reaches about 0.9. Starting from this point, the error rises mildly at first, then drastically to about 300 times as before when the maximum load is close to 1. This behavior can also be explained in terms of the breakdown of the linearization of the load L_{ij} . When the network becomes more and

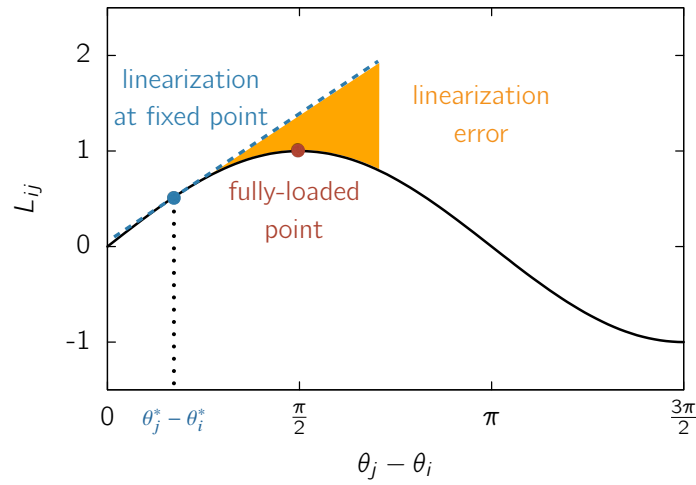


Fig. 7.5 Breakdown of linearization at full load. The linearization of the nonlinear coupling $L_{ij} := \sin(\theta_j - \theta_i)$ at the fixed point (blue disc) is indicated by a blue dashed line. The error of linearization (shaded in orange) diverges beyond the point where the link becomes fully-loaded (red disc).

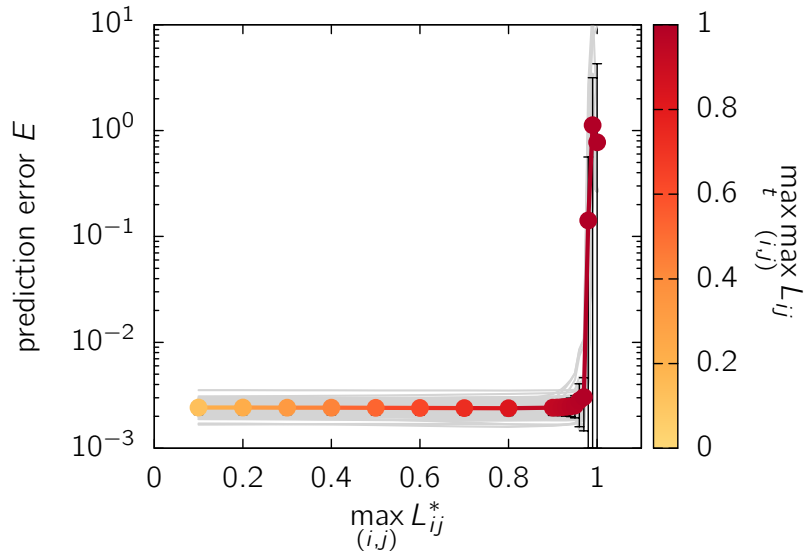


Fig. 7.6 Linear response theory's limit of validity for priorly heavily-load networks. The prediction error E (Eq. 7.10) is plotted as a function of network load at the fixed point, which is characterized by L_{ij}^* . The nodal prediction error, i.e. Eq. 7.10 minus the average over nodes, is shown with light gray lines for all nodes. The error bar of E indicates the standard deviation of nodal error across the network. The prediction error is color coded with the maximum link load over time and over network at each network load. Network settings are the same as in Fig. 7.4.

more heavily loaded at the fixed point, the fixed point moves closer and closer towards the fully loaded point (blue disc and red disc in Fig. 7.5). The error of linearization does not increase much since the slope of the linearization (blue dashed line in Fig. 7.5) also gets flatter. As long as the perturbation is not strong enough to drive the system beyond the fully-loaded point, the error stays relatively small. However, when the fixed point is so close to the fully-loaded point that the perturbation finally pushes the system over the fully-loaded point, the linearization and the actual load diverge and the prediction error increases explosively.

In the context of power grids, the typical load on transmission lines is about 0.3 [130], much lower than 0.9. In this regime, the prediction error of our approach is very low (Fig. 7.6). The error increases almost linearly with the perturbation strength (Fig. 7.4). Thus, we expect good performances of our approach in predicting the frequency response of power grids in a normal operation state (cf. Fig. 7.2, 7.3).

7.3.3 Prediction error vs. Fourier modes inclusion

At the end, we test how prediction error is influenced by the number of Fourier modes included in the prediction. The same network setting is considered as in the last subsections except the coupling strength is increased to $K_{ij} = 20 \text{ s}^{-2}$ so that the system stays lightly-loaded and does not exhibit a rapid increase of error due being close to the bifurcation point. We vary the number of included Fourier modes for prediction, and for each number of modes N_{mode} we measure the prediction error and the computation time. The dependence of the prediction error and the computation time on the number of modes is plotted in Fig. 7.7.

The result (Fig. 7.7) shows that the prediction error decreases exponentially with an increasing number of frequency modes included in prediction. Meanwhile, the computation time increases linearly as expected, since the time needed for computing the response for each Fourier mode should be the same. Thus there is a trade-off between prediction error and computation time in the decision of the number of frequency modes to be included for prediction. An “optimal” number of frequency modes is determined ad hoc depending on the tolerance of error and the available capacity of computation power. For Brownian noise with PSD $S \propto \omega^{-2}$, the prediction error decreases exponentially, thus accurate predictions can be made with relatively fewer Fourier modes thus shorter computation time. Of course, how fast the prediction error decays with the number of modes ultimately depends on the distribution of the signal’s power on frequency. The sharper the peaks in PSD, the faster the decay of the prediction error with increasing number of modes, thus the more efficient is our approach to predict the network responses.

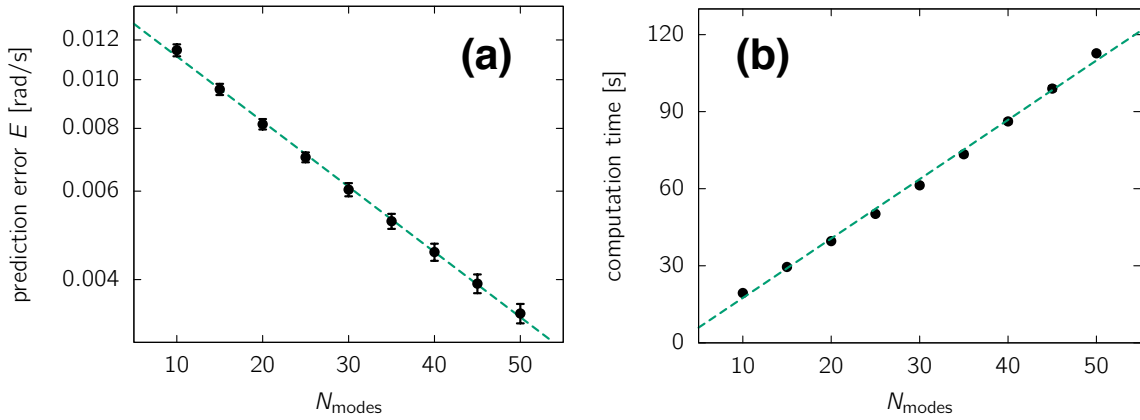


Fig. 7.7 **Trade-off between prediction error and computation time.** The prediction error is plotted over number of included Fourier modes in logarithmic scale in (a) and the time needed for computing the predictions is plotted in linear scale in (b). The linear shape of the functions in respective scale is indicated by a linear fit (green dashed lines). The error bars indicate the standard deviation across 70 realization of noise signals.

7.4 Conclusion

Based on the theory presented in Chap. 4 and Chap. 5, in this chapter, we proposed an approach to effectively predict the network responses to irregular and distributed signals, and examined the validity of our theory by testing the prediction errors in challenging situations. Specifically, our predictive approach employs (i) a Fourier analysis of the perturbation signals and (ii) a frequency sampling method to select the Fourier modes in the signals which would produce the strongest responses in the network. The application of the approach is demonstrated by predicting the response of a sample coarse-grained power grid network to two real-world power fluctuation recordings. Our approach accurately predicted the trajectory of the network response and revealed the significantly different network responsive behavior to the fluctuations in wind and solar power recordings: the response to the solar power fluctuation is more heterogeneous across the network, due to the signal's stronger frequency components in the resonant regime.

Furthermore, we showed that our theory is valid, in the sense of exhibiting a low level of prediction error (Fig. 7.4, 7.6), as long as the network system is far from the bifurcation point, which is associated with the annihilation of the fixed point and an overload in the context of power grids. At this point, the linearization of the nonlinear coupling function fails to provide a close approximation.

In short, in this chapter we showed that our theory can be applied to reliably predict the responses of normally-functioning networks to irregular and distributed signals. Interestingly, for signals characterized by specific power spectra, our theory can potentially serve

as a guideline in identifying risky nodes exhibiting strong responses by providing an upper bound of response amplitude (7.2), even the fluctuation time series is unknown. It would be an exciting future project to systematically investigate the correlation between the upper bound and the actual network responses induced by an ensemble of random time series with the same power spectral characteristics.

Part III. Transient Dynamics of Network Responses

In this part of the thesis, we study the transient response of the Kuramoto-like oscillator networks to external perturbations. To answer questions such as “How soon and how strongly does a perturbation influences other nodes in a complex network?”, we quantitatively characterize the transient perturbation spreading processes in terms of the finding the relation between the arrival time of the perturbation at each node and the distance the perturbation “travelled” in this time interval.

In Chap. 8, we start with solving for the full nodal response to an external driving signal, which includes the description of the transient responsive behavior of each node. Focusing on the transient nodal responses for small t , we derive a one-term approximation of the transient responses via Taylor expansion at $t = 0$, which is more mathematically tractable. The approximation provides insights into the analytical relation between the time when a node receives considerable influence from the perturbation and the topological features of the node.

Based on this approximation, we quantitatively characterize the perturbation spreading process in Chap. 9. We reveal the asymptotic behavior of perturbation spreading at large distance in homogeneous networks and propose an approach to predict the exact perturbation arrival time at each node.

In Chap. 10, we explore the possibility of extending the results to a theory on perturbation spreading in networks. We present the generalization of the previous results to similar scenarios and two conjectures on the bounds of the true asymptotic perturbation spreading speed in homogeneous networks of second-order dynamical systems.

Chapter 8

Transient Network Responses to Perturbations

As the starting point of studying the perturbation spreading behavior in networks, in this chapter, we present the analytical solution of the transient linear responses of Kuramoto-like oscillator networks to an external driving signal. In Sec. 8.1, we derive the solution of the full nodal response to an external driving near the fixed point, including the response to a sinusoidal signal and to a step-function signal. The solution describes the *full* time evolution of the linearized nodal response for $t > 0$. In Sec. 8.2, we focus on the first impact of the perturbation on the network, and derive an approximation of the transient nodal response via Taylor expansion at $t = 0$. The approximation is more mathematically tractable, thus allows us to gain insights into the perturbation spreading behavior in networks: two decisive factors in the nodal responsive behavior are identified (Sec. 8.3). In the last section we shortly summarize and discuss the results obtained in this chapter.

8.1 Full nodal response to external driving

In Part II of the thesis, we derived the solution of the steady nodal response to external driving signals for model class (4.1), and discussed the emerging steady response patterns based on the solution. However, to study the first impact of a perturbation on a network, or more specifically, to understand how a perturbation spreads in a network, we need the solution of the full time evolution of the nodal response, i.e. the one including the transient stage. Thus, in this section, we present the derivation of the *general* nodal response to a driving signal for the most general setting of the model class, i.e. for the second-order networks ($\alpha > 0, \beta > 0$).

In the spirit of linear response theory, we assume the full nodal response is linear with respect to the perturbation strength ε . However, unlike in Chap. 4, we do not make any assumptions on the form of the linear response, e.g. a sinusoidal response, a uniform

drift or a phase shift. We leave it undetermined to allow for more complicated forms of response. Thus, at the fixed point $\boldsymbol{\theta}^*$, the phase of oscillator i with a general linear response to the perturbation at oscillator k is written as

$$\theta_i^{(k)}(t) = \theta_i^* + \varepsilon \Theta_i^{(k)}(t). \quad (8.1)$$

In Part III of the thesis, $\Theta_i^{(k)}$ denotes the linear nodal response with a general form, not with a particular sinusoidal form as in Part II. Plugging (8.1) into the dynamics of the perturbed network (4.1), we obtain a matrix equation

$$\ddot{\Theta}^{(k)} + \alpha \dot{\Theta}^{(k)} = -\mathcal{L}\Theta^{(k)} + \mathbf{D}^{(k)} \quad (8.2)$$

describing the dynamics of the response vector $\Theta^{(k)}$. Here we assume identical system parameters $\beta_i \equiv \beta$ and $\alpha_i \equiv \alpha$ for all i . Furthermore, we assume $\beta = 1$ without loss of generality. In the following we solve for the linear response vector for two kinds of perturbations, a sinusoidal signal and a step-function signal.

8.1.1 Nodal response to a sinusoidal signal

To solve for the general linear response vector $\Theta^{(k)}(t)$, we again resort to the orthonormality of the Laplacian eigenvectors. However, the difference from before is, now we project the entire time-dependent response in the basis of Laplacian eigenvectors, not only the time-independent factors in it. Therefore, the projection coefficients $c^{[\ell]}$ are *time-dependent* for the general response vector:

$$\Theta^{(k)}(t) = \sum_{\ell=0}^{N-1} c^{[\ell]}(t) \mathbf{v}^{[\ell]}. \quad (8.3)$$

In this way, the dynamics of the response vector is decomposed into the dynamics of the projection coefficients $c^{[\ell]}(t)$ in the N eigenmodes of the Laplacian matrix.

If the network is driven by a single sinusoidal signal $\varepsilon e^{i(\omega t+\varphi)}$ at node k , the perturbation vector $\mathbf{D}^{(k)}$ is written as $D_i^{(k)} = \delta_{ik} e^{i(\omega t+\varphi)}$. The dynamics of $c^{[\ell]}(t)$ reads

$$\ddot{c}^{[\ell]} + \alpha \dot{c}^{[\ell]} - \lambda^{[\ell]} c^{[\ell]} = v_k^{[\ell]} e^{i(\omega t+\varphi)} \quad \text{for } \ell \in \{0, \dots, N-1\}. \quad (8.4)$$

Since the system is initially at the fixed point, the response vector $\Theta^{(k)}(t=0) = \mathbf{0}$. Thus for each projection coefficient we have initial conditions $c^{[\ell]}(0) = 0$ and $\dot{c}^{[\ell]}(0) = 0$,

which lead to the solution of the projection coefficients $c^{[\ell]}(t) =$

$$\begin{cases} \frac{v_k^{[0]} e^{i\varphi}}{-\omega^2 + i\omega\alpha} \left(-1 - \frac{i\omega}{\alpha} + \frac{i\omega}{\alpha} e^{-\alpha t} + e^{i\omega t} \right), & \ell = 0, \\ \frac{v_k^{[\ell]} e^{i\varphi}}{-\omega^2 + i\alpha\omega + \lambda^{[\ell]}} \left[\frac{\Delta_-^{[\ell]} - i\omega}{2i\gamma^{[\ell]}} e^{\Delta_+^{[\ell]} t} - \frac{\Delta_+^{[\ell]} - i\omega}{2i\gamma^{[\ell]}} e^{\Delta_-^{[\ell]} t} + e^{i\omega t} \right], & \ell \in \{1, \dots, N-1\}, \end{cases} \quad (8.5)$$

with

$$\gamma^{[\ell]} := \sqrt{\lambda^{[\ell]} - \frac{\alpha^2}{4}}, \quad \Delta_+^{[\ell]} := -\frac{\alpha}{2} + i\gamma^{[\ell]}, \quad \Delta_-^{[\ell]} := -\frac{\alpha}{2} - i\gamma^{[\ell]}. \quad (8.7)$$

Particularly, we notice that, although determined from a different ODE, the projection coefficient for $\ell = 0$ can be viewed as a special case of the projection coefficient for $\ell \in \{1, \dots, N-1\}$: replacing the $\lambda^{[\ell]}$ in (8.6) with 0 recovers the solution for $\ell = 0$ (8.5). Thus, the solution of the general linear nodal response to a sinusoidal driving is written as

$$\Theta^{(k)}(t) = \sum_{\ell=0}^{N-1} \frac{v_k^{[\ell]} e^{i\varphi}}{-\omega^2 + i\alpha\omega + \lambda^{[\ell]}} \left[\frac{\Delta_-^{[\ell]} - i\omega}{2i\gamma^{[\ell]}} e^{\Delta_+^{[\ell]} t} - \frac{\Delta_+^{[\ell]} - i\omega}{2i\gamma^{[\ell]}} e^{\Delta_-^{[\ell]} t} + e^{i\omega t} \right] \mathbf{v}^{[\ell]} \quad (8.8)$$

In the solution, we find the familiar response factor for the steady nodal responses again, but additional terms characterizing the transient response arise: the first two terms in the square bracket of (8.8) representing the oscillations with frequencies $\gamma^{[\ell]}$ and an amplitude decaying as $\sim e^{-\frac{\alpha}{2}t}$. It is notable that these frequencies equal the eigenfrequencies $\omega_{\text{eigen}}^{[\ell]}$ of the system (Eq. 5.4). This means, the transient response of every node in the network includes intrinsic oscillations at the system's eigenfrequencies, and the amplitudes of these oscillations decay with the same rate. Additionally, the general solution recovers the steady nodal response (4.17) for $t \rightarrow \infty$, as expected.

8.1.2 Nodal response to a step-function signal

How does the full nodal response to a step-function signal differ from the response to a sinusoidal signal in the transient stage? Intuitively, the transient impact of a step-function signal should be the same as that of a sinusoidal signal $\epsilon e^{i(\omega t + \varphi)}$ with $\varphi = 0$ and $\omega = 0$. Nevertheless, we verify this intuition by presenting the analytical solution of the full nodal response to a step-function signal.

Following the same idea as in last subsection, we express the response vector as a linear combination of the Laplacian eigenvectors with time-dependent coefficients. These coefficients obey the same dynamics as Eq. 8.4 if we replace $e^{i(\omega t + \varphi)}$ with 1. Solving for the coefficients separately for $\ell = 0$ and $\ell = 1, \dots, N - 1$ gives the solution of the full nodal response to a step-function signal

$$\Theta^{(k)} = \frac{1}{N} \left(-\frac{1}{\alpha^2} + \frac{1}{\alpha^2} e^{-\alpha t} + \frac{1}{\alpha} t \right) + \sum_{\ell=1}^{N-1} \frac{v_k^{[\ell]}}{\lambda^{[\ell]}} \left(\frac{\Delta_+^{[\ell]}}{2i\gamma^{[\ell]}} e^{\Delta_+^{[\ell]} t} - \frac{\Delta_-^{[\ell]}}{2i\gamma^{[\ell]}} e^{\Delta_-^{[\ell]} t} + 1 \right) \mathbf{v}^{[\ell]}. \quad (8.9)$$

As can be seen by compared to solution (8.8), except uniform drift $\frac{1}{N\alpha}t$ in the 0-th eigenmode, the full nodal response to a step-function signal has the same form as (8.8) with $\varphi = 0$ and $\omega = 0$. In fact, as we will see in the next section, the transient impact of a step-function signal and that of a sinusoidal signal are essentially identical.

8.2 Approximation of transient nodal response

In the last section, we derived the analytical solution (8.8) which describes the full time evolution of the nodal responses to a sinusoidal driving. As long as the network system is not close to the bifurcation point, the linear response solution exhibits good agreement with the numerically determined network response with high accuracy (see Sec. 7.3). However, it is not easy to gain valuable insights into the transient perturbation spreading behavior in networks directly from the solution (8.8), simply due to the nonlinear dependence on the Laplacian eigenvalue $\lambda^{[\ell]}$ in each eigenmode.

To obtain a more tractable form of the transient nodal response, we represent (8.8) by the leading term in the Taylor series of the function at $t = 0$. The n -th derivative of the full nodal response at $t = 0$ reads¹

$$D_t^n \Theta_i^{(k)}(0) = \sum_{\ell=0}^{N-1} \frac{v_i^{[\ell]} v_k^{[\ell]} e^{i\varphi}}{-\omega^2 + i\alpha\omega + \lambda^{[\ell]}} \left[\frac{\left(\Delta_+^{[\ell]}\right)^n \left(\Delta_-^{[\ell]} - i\omega\right)}{2i\gamma^{[\ell]}} - \frac{\left(\Delta_-^{[\ell]}\right)^n \left(\Delta_+^{[\ell]} - i\omega\right)}{2i\gamma^{[\ell]}} + (i\omega)^n \right], \quad (8.10)$$

where the summand from the ℓ -th eigenmode can be viewed as the division of two polynomials of the ℓ -th Laplacian eigenvalue². We thus focus on the division of the

¹Here we adopt Euler's notation for differential operator $D_t^n := \frac{d^n}{dt^n}$.

²It can be shown that the numerators are polynomials with non-negative integer exponents of $\lambda^{[\ell]}$ (Appx. B), although it includes $\Delta_+^{[\ell]}$, $\Delta_-^{[\ell]}$ and $\gamma^{[\ell]}$ which are not powers of $\lambda^{[\ell]}$.

polynomials

$$F_n(\lambda^{[\ell]}) := \frac{1}{-\omega^2 + i\alpha\omega + \lambda^{[\ell]}} \left[\frac{\left(\Delta_+^{[\ell]}\right)^n (\Delta_-^{[\ell]} - i\omega)}{2i\gamma^{[\ell]}} - \frac{\left(\Delta_-^{[\ell]}\right)^n (\Delta_+^{[\ell]} - i\omega)}{2i\gamma^{[\ell]}} + (i\omega)^n \right], \quad (8.11)$$

in the ℓ -th summand of the n -th derivative of the full nodal response at $t = 0$. For brevity, we denote the term with the highest order of variable x in an algebraic expression $P(x)$ as $LT[P](x)$ in the following.

Proposition 3. *The term with the highest order of $\lambda^{[\ell]}$ in $F_n(\lambda^{[\ell]})$ ($n \in \mathbb{N}, n \geq 2$)³ introduced in (8.11) is*

$$LT[F_n](\lambda^{[\ell]}) = \begin{cases} (-1)^{\frac{n-1}{2}} \left(-i\omega + \frac{n-1}{2}\alpha \right) (\lambda^{[\ell]})^{\frac{n-3}{2}} & \text{if } n \text{ is odd,} \\ (-1)^{\frac{n-2}{2}} (\lambda^{[\ell]})^{\frac{n-2}{2}} & \text{if } n \text{ is even.} \end{cases}$$

This result can be proved by e.g. observing the highest order of $\lambda^{[\ell]}$ in $\left(\Delta_+^{[\ell]}\right)^n$. A full proof is given in Appx. B.

Prop. 3 shows that the leading term of $F_n(\lambda^{[\ell]})$ always has an integer order, no matter n is odd or even. Therefore, it allow us to express the matrix composed of the leading term of $D_t^n \Theta(0)$, $LT[D_t^n \Theta(0)]$ with $(LT[D_t^n \Theta(0)])_{ki} = LT[D_t^n \Theta_i^{(k)}(0)]$, in terms of powers of the Laplacian matrix \mathcal{L} . Using the matrices $\mathbf{V} = (\mathbf{v}^{[0]}, \dots, \mathbf{v}^{[N-1]})$ and $\mathbf{\Lambda} = \text{diag}(\lambda^{[0]}, \dots, \lambda^{[N-1]})$ defined in Sec. 5.4, we have

$$LT[D_t^n \Theta(0)] = e^{i\varphi} \mathbf{V} LT[F_n](\mathbf{\Lambda}) \mathbf{V}^T = e^{i\varphi} LT[F_n](\mathcal{L}), \quad (8.12)$$

suggesting the n -th derivative of the nodal response at $t = 0$, $D_t^n \Theta_i^{(k)}(0)$, has a leading term involving $(\mathcal{L}^d)_{ki}$ with $d = \frac{n-3}{2}$ if n is odd and $d = \frac{n-2}{2}$ if n is even ($n \geq 2$). It is notable that the leading order d increases monotonically with the order of time derivative n : a higher-order time derivative of the nodal responses is leaded by an element of the Laplacian matrix to a higher power.

Now we use the result in Prop. 1, stating that $(\mathcal{L}^d)_{ki}$ is non-zero only for $d \geq d(k, i)$. Thus for node pair (k, i) with distance $d(k, i)$, the lowest power of \mathcal{L} with a non-zero ki -

³For $n = 0$ and $n = 1$, $F_n(\lambda^{[\ell]}) \equiv 0$ due to the initial condition. That is, the nodal response and its first time derivative are both zero at the time of perturbation: $t = 0$.

th element is $d(k, i)$ which corresponds to the lowest order of a non-zero time derivative $D_t^n \Theta_i^{(k)}(0)$ being $n = 2d(k, i) + 2$. Note that here the lowest order n is always even, since for every even n , the order of $LT [D_t^{n-1} \Theta(0)]$ is $d(k, i) - 1$ and the order of $LT [D_t^{n+1} \Theta(0)]$ is $d(k, i)$. The relation between the lowest order n of a non-zero time derivative $D_t^n \Theta_i^{(k)}(0)$ and the distance $d(k, i)$ for small distance $d(k, i) \in \{1, \dots, 5\}$ is shown in Tab. 8.1.

In fact, for node pair (k, i) , the lowest-order non-zero time derivative of the nodal response *equals* the leading term with the highest order of \mathcal{L} :

$$D_t^{2d(k,i)+2} \Theta_i^{(k)}(0) = e^{i\varphi} LT [F_{2d(k,i)+2}] (\mathcal{L})_{ki} = e^{i\varphi} (-1)^{d(k,i)} (\mathcal{L}^{d(k,i)})_{ki}, \quad (8.13)$$

since all other terms involve $(\mathcal{L}^d)_{ki}$ with $d < d(k, i)$ are zero. Hence, the series representation of the full nodal response $\Theta_i^{(k)}(0)$ can be written as

$$\begin{aligned} \Theta_i^{(k)}(t)|_{t=0} &= \sum_{n=0}^{\infty} \frac{D_t^n \Theta_i^{(k)}(0)}{n!} t^n = \sum_{n=2d(k,i)+2}^{\infty} \frac{D_t^n \Theta_i^{(k)}(0)}{n!} t^n \\ &= \frac{D_t^{2d(k,i)+2} \Theta_i^{(k)}(0)}{[2d(k, i) + 2]!} t^{2d(k,i)+2} + O(t^{2d(k,i)+3}). \end{aligned} \quad (8.14)$$

		order of time derivative n											
		2	3	4	5	6	7	8	9	10	11	12	13
distance $d(k, i)$	1	$-e^{i\varphi} \mathcal{L}_{ki}$											
	2	$e^{i\varphi} (\mathcal{L}^2)_{ki}$											
	3	$-e^{i\varphi} (\mathcal{L}^3)_{ki}$											
	4	$e^{i\varphi} (\mathcal{L}^4)_{ki}$											
	5	$-e^{i\varphi} (\mathcal{L}^5)_{ki}$											
	zero		non-zero										

Table 8.1 The distance dependence of the lowest-order non-zero time derivative of nodal response.

Combining (8.13) and (8.14), we thus obtain an approximation of the nodal responses for transient responses with small t as the first non-zero term with the lowest order of t

(i.e. the red boxes in Tab. 8.1):

$$\Theta_i^{(k)}(t) \approx \frac{e^{i\varphi}(-1)^{d(k,i)} (\mathcal{L}^{d(k,i)})_{ki}}{[2d(k,i) + 2]!} t^{2d(k,i)+2}. \quad (8.15)$$

An illustration of the transient linear nodal responses and the respective one-term approximations is given in Fig. 8.1.

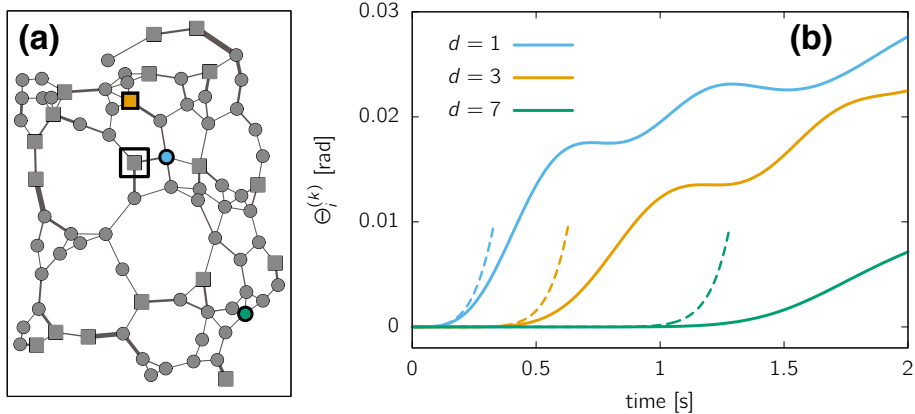


Fig. 8.1 One-term approximation of transient nodal responses. The transient responses of three representative nodes in a sample network (a) are plotted with solid lines in (b). The respective one-term approximation given by Eq. 8.15 are plotted with dashed lines. Parameters: $N = 80$, $K_{ij} \equiv K = 20 \text{ s}^{-2}$, $\alpha = 1 \text{ s}^{-1}$, $\Omega = 3 \text{ s}^{-2}$ for 20 nodes indicated by squares and $\Omega = -1 \text{ s}^{-2}$ for the rest 60 nodes indicated by discs in (a), $\varepsilon = 1$, $\omega = 0.01 \times 2\pi \text{ Hz}$, $\varphi = 0$.

In fact, same structures can be found in the series representation of the nodal responses to a step-function perturbation. The n -th time derivative of the nodal response (8.9) ($n \geq 2$) at $t = 0$ reads

$$D_t^n \Theta_i^{(k)}(0) = \sum_{\ell=0}^{N-1} v_i^{[\ell]} v_k^{[\ell]} \frac{\left(\Delta_+^{[\ell]}\right)^{n-1} - \left(\Delta_-^{[\ell]}\right)^{n-1}}{2i\gamma^{[\ell]}}, \quad (8.16)$$

which shares the same lowest-order non-zero terms for the same distance as (8.10) (cf. Appx. B). We thus arrive at the same one-term approximation for the transient nodal responses to a step-function perturbation.

8.3 First insights into perturbation spreading

The one-term approximation of the transient nodal response provides strong hints about the patterns in perturbation spreading behavior in networks. It exhibits explicit dependences on the distance between node pair $d(k, i)$, on the element of the Laplacian matrix to the power of $d(k, i)$, on the initial relative magnitude of the perturbation $e^{i\varphi}$, and on time t . It is true that neglecting higher-order terms of t in the transient nodal response causes error, nevertheless, the approximation captures some essential features of the perturbation spreading behavior in networks: e.g. the strong dependence of the nodal response on the topological distance and how the number of shortest paths influence the perturbation spreading process. In this section we present the two key factors in perturbation spreading qualitatively. Quantitative characterization of the perturbation spreading behavior in networks will be given and discussed in Chap. 9.

Topological distance Most notably, the one-term approximation of the transient linear nodal response (Eq. 8.15) reveals the strong dependence of the perturbation spreading behavior on the topological distance. The distance $d(k, i)$ between the perturbed node k and the responding node i appears in the factorial, in the power of t , and in the power of the Laplacian matrix. A strong dependence of transient nodal response on distance is also found in direct numerical simulations (see Fig. 8.2): the closer the nodes are, the more promptly they respond to perturbations, and the steeper the slopes of responses are (Fig. 8.2b). Additionally, the nodes with the same topological distance show similar transient responses (see the inset of Fig. 8.2b).

Number of shortest paths The dependence of the transient nodal response on the number of shortest paths between the perturbed node and the responding node is encoded in the ki -th element of the $d(k, i)$ -th power of the Laplacian matrix. As shown in Prop. 1, for a node pair (k, i) with distance $d(k, i)$, the element of Laplacian matrix power $(\mathcal{L}^{d(k,i)})_{ki}$ is in fact the product of the edge weights of (u, v) along a shortest path between (k, i) summed over all shortest paths:

$$(\mathcal{L}^{d(k,i)})_{ki} = \sum_{\mathcal{P}_{k \rightarrow i}^{d(k,i)}} \prod_{(u,v) \in \mathcal{P}_{k \rightarrow i}^{d(k,i)}} \mathcal{L}_{uv}. \quad (8.17)$$

Thus, the transient nodal response depends on the weighted sum of the shortest paths. Especially, we show that for lightly-loaded homogeneous networks, i.e. the coupling strength $K_{ij} \equiv K$ for all (i, j) , the weighted sum (8.17) is essentially the number of shortest paths: when the steady-state network system is far from the bifurcation point, i.e. lightly-loaded $L_{ij} = \sin(\theta_j^* - \theta_i^*) \ll 1$ for all edges (i, j) , all the Laplacian element becomes identical:

$$\mathcal{L}_{ij} := K_{ij} \cos(\theta_j^* - \theta_i^*) \approx K. \quad (8.18)$$

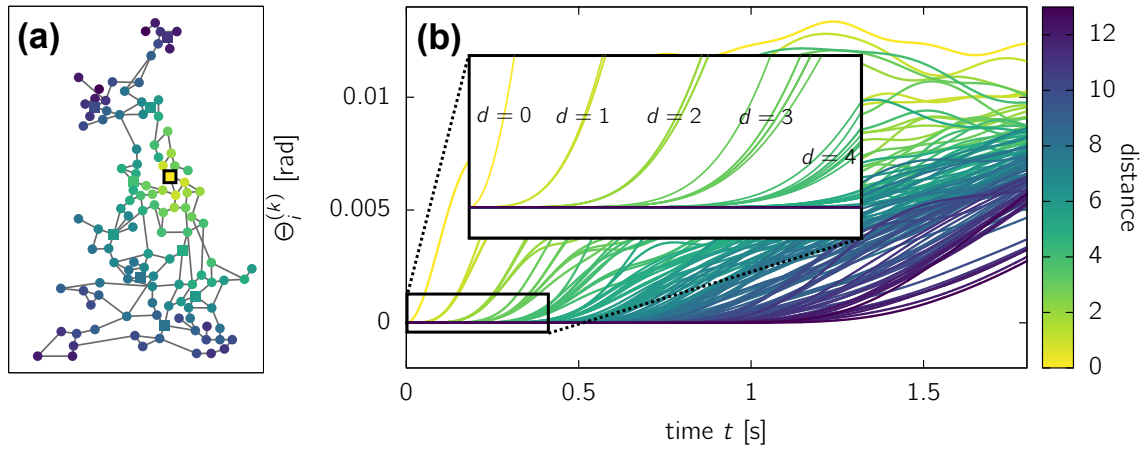


Fig. 8.2 Topological distance and transient network response. The transient nodal responses to a sinusoidal perturbation in British high-voltage power grid network (a) are shown in (b). Nodes in (a) and their responses in (b) are color-coded by the respective topological distance to the perturbed node, which is marked with a black square in (a). The inset in (b) is a zoom-in of the area in the black rectangular at the lower left corner of (b). Parameters: $N = 120$, $K_{ij} \equiv K = 100 \text{ s}^{-2}$, $\alpha = 1 \text{ s}^{-1}$, $\Omega = 11 \text{ s}^{-2}$ for 10 nodes (squares) and $\Omega = -1 \text{ s}^{-2}$ for the rest 110 nodes (discs) in (a), $\varepsilon = 1$, $\omega = 0.1 \times 2\pi \text{ Hz}$, $\varphi = 0$.

Hence we arrive at

$$(\mathcal{L}^{d(k,i)})_{ki} = \sum_{\mathcal{P}_{k \rightarrow i}^{d(k,i)}} \prod_{(u,v) \in \mathcal{P}_{k \rightarrow i}^{d(k,i)}} K \approx \#\mathcal{P}_{k \rightarrow i}^{d(k,i)} K^{d(k,i)}, \quad (8.19)$$

which reveals the approximately *linear* dependence of the transient nodal response (8.15) on the number of shortest paths $\#\mathcal{P}_{k \rightarrow i}^{d(k,i)}$ for a fixed distance and a fixed time.

This positively proportional relationship is confirmed by numerical simulations (see Fig. 8.3). Among the responses of all 11 nodes which have a distance 9 to the perturbed node, the red node with 12 shortest paths responds most rapidly, while the dark blue node with only 1 shortest path responds most slowly. Note that the one-term approximation is valid only for small t , thus it describes only the first impact of perturbations on the respective nodes, not the long-term time evolution of the nodal responses.

Specifically, if we divide the nodal responses of these 11 nodes by the respective number of shortest paths, we observe a collapse of transient responses (Fig. 8.4). However, the collapse is not exact, because of (i) we neglected the contribution of the higher order terms in the Taylor series, and (ii) the edge weights are not exactly identical, i.e. $\cos(\theta_j^* - \theta_i^*)$ is not exactly 1 for all (i, j) .

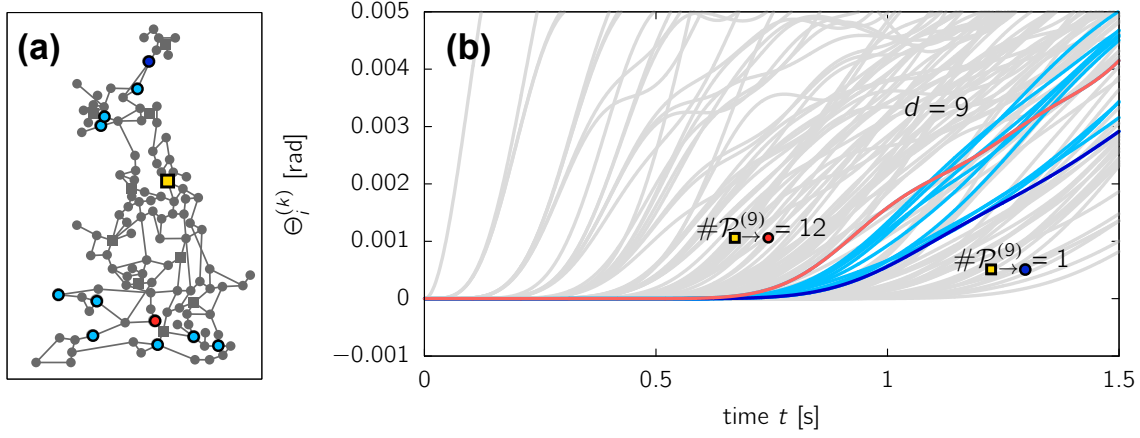


Fig. 8.3 Number of shortest paths and transient network response. The transient nodal response of the nodes with distance 9 (highlighted nodes in (a)) to the perturbed node (yellow square in (a)) are shown in (b). There are 12 shortest paths with distance 9 between the red node and the perturbed node, while there is only 1 between the dark blue node and the perturbed node. The parameter setting is the same as in Fig. 8.2.

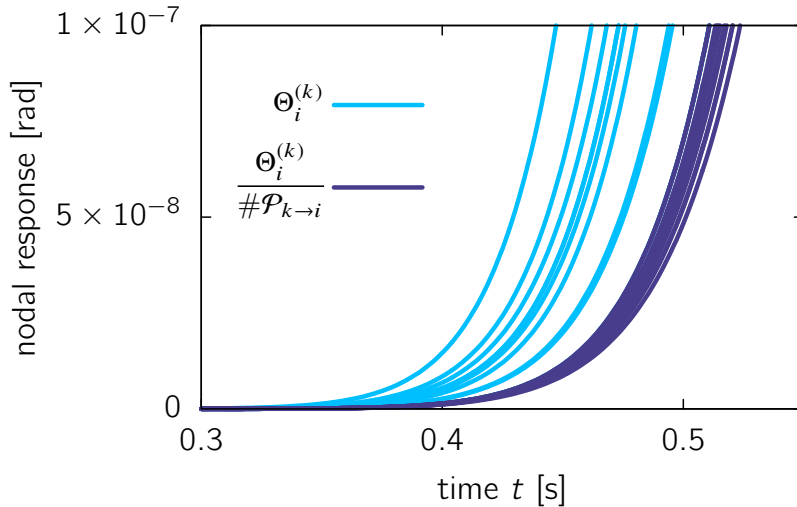


Fig. 8.4 Collapse of transient network response divided by number of shortest paths. The transient nodal responses of the nodes with distance 9 (blue lines) collapse if divided by the respective number of shortest paths (purple lines). The responding nodes and the perturbed node are illustrated in in Fig. 8.3a. The network setting is the same as in Fig. 8.2.

8.4 Conclusion

In this chapter we present the first steps in understanding the transient network responses to an external perturbation. First we derive the analytical solution of the general linear

nodal response to perturbations with different forms by generalizing the linear response theory developed in Part II and letting the projection coefficients of the response vector being time-dependent. The solution reveals that the exponentially decaying transient nodal response contains intrinsic sinusoidal oscillations at system's eigenfrequencies.

To better understand the transient network responses to a perturbation driving signal, we provide an approximation of the transient nodal response for small t , which is given by the first non-zero term in the Taylor series of the nodal response at $t = 0$. The approximation shows (i) a strong dependence on the distance between the perturbed node i and the responding node k , and (ii) an explicit relation to the ki -th element of the Laplacian matrix to the power of $d(k, i)$. It thus sheds lights on two key factors that determines the transient nodal response: the topological distance $d(k, i)$ and the weighted sum of the shortest paths between k and i . For networks with a homogeneous coupling, the latter is proportional to the number of shortest paths between node pair (k, i) . Thus, for nodes with same distance to the perturbation, the more shortest paths a node has, the stronger the first impact. Both findings are confirmed by numerical simulations.

Particularly, the one-term approximation of the transient nodal response (8.15) shows potential of generalization: both responses, the one to a sinusoidal signal and the one to a step-function signal, share the same form of one-term approximation. That means, both sinusoidal signal and step-function signal have the *identical* one-term transient spreading behavior. Since any perturbation signal with an arbitrary wave form can be expressed as a linear combination of such functions, we conclude that (8.15) reflects the *general* features of the one-term transient responsive behavior of networks under an arbitrary perturbation. Furthermore, we notice that the approximation (8.15) for the sinusoidal form of perturbation appears to be *independent* of the damping parameter α , which suggests a bigger room for generalization to related networks in the model class (4.1). We will further discuss the universality of the approximation in Chap. 10.

Chapter 9

Characterizing Perturbation Spreading in Networks

This chapter is devoted to a quantitative characterization of the perturbation spreading patterns in networks. Based on the one-term approximation of the transient nodal responses derived in Chap. 8, we estimate the arrival time of a perturbation at each node in a network by thresholding the nodal responses. Particularly, the one-term estimate of the perturbation arrival time implies an interesting asymptotic perturbation spreading behavior when the distance becomes large: the spreading speed decreases with distance and approaches a constant as distance goes to infinity (Sec. 9.1). In Sec. 9.2, we focus on the role of network topology in the spreading behavior. We define the *topological factor* to characterize the impact of network topology on the perturbation spreading process in networks. Based on the developed results, we propose an approach to predict the exact perturbation arrival time through a numerically determined *master curve* of perturbation spreading (Sec. 9.3). A short conclusion of the presented results is provided at the end of the chapter.

9.1 Asymptotic spreading behavior of perturbation

In last chapter we derived the one-term approximation of the transient nodal response to a perturbation of any form (Eq. 8.15). The approximation simplifies the analytical form of the transient nodal response (Eq. 8.8), and more importantly, it trims down its dependences on parameters, thus reveals the essential patterns in perturbation spreading. First insights provided by the one-term approximation has been discussed in Sec. 8.3.

In fact, more interesting patterns in perturbation spreading can be revealed by a more careful analysis of the one-term approximation. In this section, we first provide a quantitative characterization of the perturbation spreading processes in time and in topological

space based on the one-term approximation, followed by the discovery of an interesting asymptotic spreading behavior in homogeneous networks for large distances.

9.1.1 Estimating the perturbation arrival time

We start with characterizing the spreading of a perturbation in time, i.e. estimating the time when a perturbation arrives at a certain node in network. Usual definitions of the arrival time of a perturbation include (i) the time when the nodal response reaches its first peak after perturbation, and (ii) the time when it crosses a given threshold. The first definition makes sense for a delta-function perturbation, which occurs only at a certain time or lasts very shortly. Its impact on each node grows, reaches a peak at some point, and then fades in time. However, in our case where the network system is under a persistent perturbation of any form, this definition becomes pointless, since the impact of perturbation does not really fades in time. Therefore we adopt the second definition of arrival time in this thesis. On the verge of being perturbed, the system is at the fixed point thus all nodal responses are zero. After the time of perturbation ($t = 0$), the response grows at every node at its own pace. Once the nodal response reaches a specified threshold, which can be i.e. a measurable increase in the rotation speed of a synchronous machine, we say the impact of the perturbation has reached this node.

One-term approximation of arrival time We define the *arrival time* of a perturbation $\varepsilon e^{i(\omega t + \varphi)}$ starting from node k at node i , $\tau_i^{(k)}$, as the time when the absolute value of the response $\varepsilon \Theta_i^{(k)}$ reaches a threshold ϵ_{th} :

$$|\varepsilon \Theta_i^{(k)} (\tau_i^{(k)})| = \epsilon_{\text{th}}. \quad (9.1)$$

Adopting the one-term approximation of the transient linear response $\Theta_i^{(k)}$ for small t , we obtain an estimate of the arrival time by solving Eq. 9.1 for $\tau_i^{(k)}$ explicitly:

$$\tau_{i,\text{app}}^{(k)} = \left| \frac{\epsilon_{\text{th}} (2d + 2)!}{\varepsilon e^{i\varphi} (\mathcal{L}^d)_{ki}} \right|^{\frac{1}{2d+2}}. \quad (9.2)$$

From now on we denote the topological distance between the perturbed node k and the responding node i as d for simplicity. The one-term estimate of the arrival time $\tau_i^{(k)}$ (9.2) inherits the strong dependence on the topological distance from the one-term approximation (see Fig. 9.1). Moreover, it also depends on how the responding node is connected to the perturbed node, particularly the weighted sum of the shorted paths. This dependence is reflected by the explicit dependence of (9.2) on $(\mathcal{L}^d)_{ki}$, and causes the different arrival time for the nodes with the same d (Fig. 9.1d). Despite the deviation

between the estimates and the exact arrival times, apparently they both exhibit the same essential dependences on d and on $(\mathcal{L}^d)_{ki}$ (see Fig. 9.1b,d).

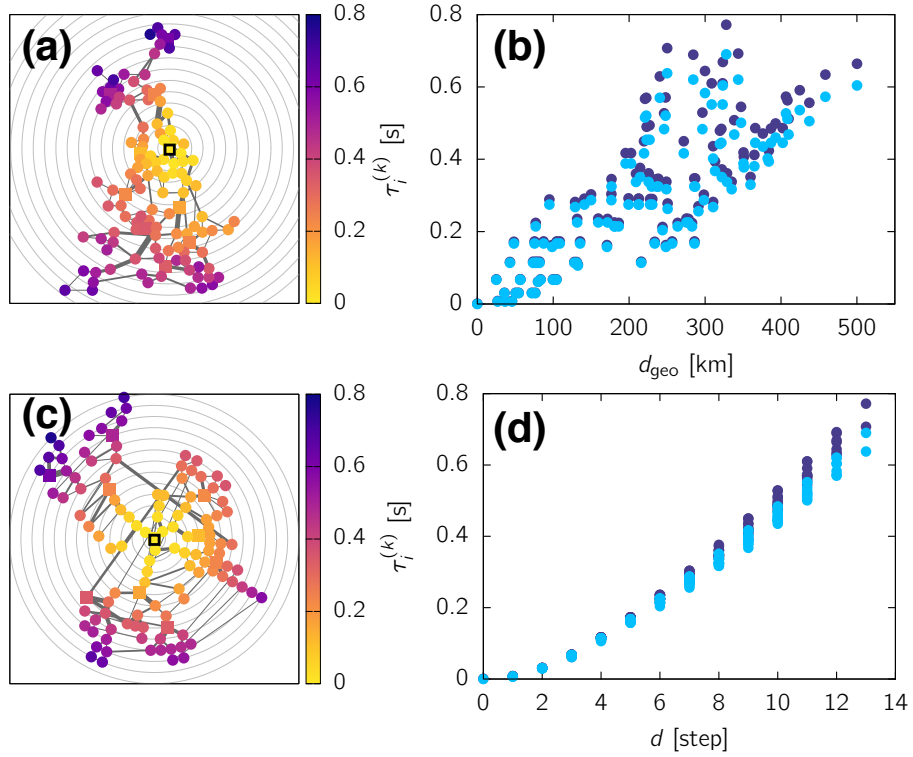


Fig. 9.1 Estimates of perturbation arrival time. The arrival time of a sinusoidal perturbation largely depends on the topological distance (d) rather than the geographical distance (b). In (b) and (d), the purple discs indicate the exact arrival time determined via numerical simulations and the blue discs indicate the one-term estimates given by (9.2). The British power grid network is embedded according to the geographical distance in (a) and according to the topological distance in (b). The concentric circles indicate the nodes with the same geographical or topological distance to the perturbed node. The network setting is the same as in Fig. 8.2, plus $\epsilon_{th} = 10^{-8}$.

Additionally, the estimate of arrival time also depends on the choice of the threshold value ϵ_{th} , or more specifically, on the ratio of ϵ_{th} to the initial magnitude of the perturbation, $\varepsilon e^{i\varphi}$. The higher the threshold value ϵ_{th} compared to perturbation magnitude, the later the perturbation arrives at the node. However, this difference of arrival time caused by the choice of ϵ_{th} decreases with distance and vanishes for nodes very far from the perturbation: the factor goes to 1 and becomes independent of the ratio $\frac{\epsilon_{th}}{\varepsilon e^{i\varphi}}$ as $d \rightarrow \infty$.

Error of estimation The error of the estimate (9.2) mainly comes from the neglected higher-order terms in the series representation of the nodal response (8.14). The estima-

tion error of the arrival time $\tau_i^{(k)}$ defined as

$$E_{\tau_i^{(k)}} := \frac{|\tau_{i,\text{app}}^{(k)} - \tau_{i,\text{num}}^{(k)}|}{\tau_{i,\text{num}}^{(k)}} \quad (9.3)$$

exhibits a clear dependence on the topological distance d (see Fig. 9.1d and Fig. 9.2a). It increases as the perturbation travels further. As we will see later, this divergence of both arrival times comes from their asymptotic behavior for large d . The apparently high error for small distance (Fig. 9.2a) comes from (i) the finite time step in numerical simulations and (ii) the very small absolute value of the arrival time for small distances. Furthermore, as the threshold ϵ_{th} being lowered, the deviation between the one-term estimate and the exact arrival time decreases. In particular, we find that the error averaged over the nodes with the largest distance d_{\max} decreases with the threshold as a power-law (Fig. 9.2b). This dependence is plausible since the leading term in the error has an order of $2d + 3$ with respect to t while the threshold has an order of $2d + 2$. Thus the logarithm of the error and the logarithm of the threshold has a linear dependence. As $t \rightarrow 0$, the higher-order terms in the series becomes much smaller than the first non-zero term, thus the estimation error approaches zero.

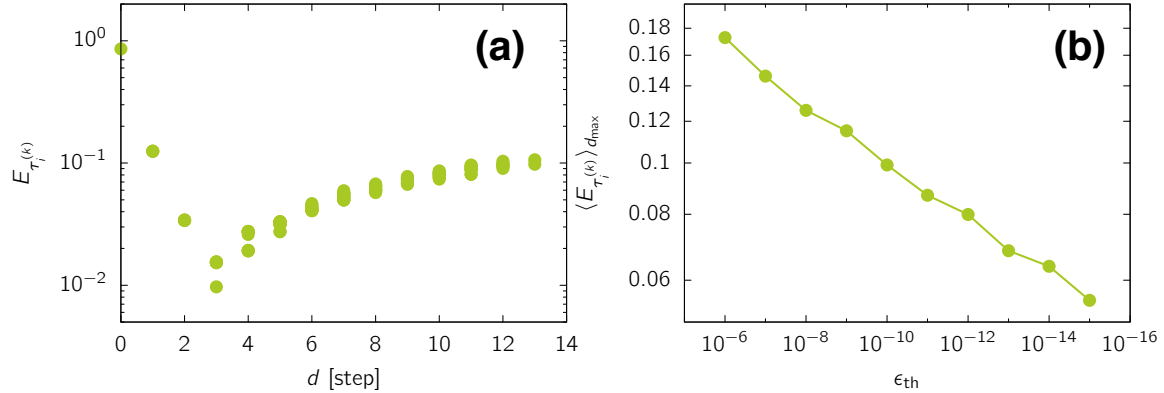


Fig. 9.2 The error of the one-term estimate of arrival time. (a) The estimation error defined in 9.3 is plotted over the topological distance ($\epsilon_{\text{th}} = 10^{-8}$). The averaged estimation error over the nodes with the largest distance in the network decreases with a lowered threshold as a power-law (b). The network setting is the same as in Fig. 9.1.

9.1.2 The asymptotic spreading speed

Observing the one-term estimate of the arrival time (9.3), one identifies two multiplying parts: one topology-dependent and one topology-independent:

$$\tau_{i,\text{app}}^{(k)} = \left| \frac{\epsilon_{\text{th}}(2d+2)!}{\varepsilon e^{i\varphi}} \right|^{\frac{1}{2d+2}} \left| (\mathcal{L}^d)_{ik} \right|^{-\frac{1}{2d+2}}. \quad (9.4)$$

As discussed in Sec. 8.3, the second part including $(\mathcal{L}^d)_{ik}$ is closely related to the shortest paths between the node pair (k, i) for homogeneous networks, thus reflects the nodal responding behavior for a specific network topology. Meanwhile, the first part depends only on topology-independent parameters: the ratio between the threshold and the perturbation magnitude, and the topological distance. Thus, the behavior of this part reflects the general pattern in perturbation spreading across networks. We call this part as the *general spreading function* $G(d)$ (9.4).

$$G(d) := \left| \frac{\epsilon_{\text{th}}(2d+2)!}{\varepsilon e^{i\varphi}} \right|^{\frac{1}{2d+2}} \quad (9.5)$$

As a function of distance d , the general spreading function $G(d)$ grows increasingly fast for small d and asymptotically approaches a linear function as d grows (Fig. 9.3a). This behavior implies a general spreading pattern: a perturbation travels very fast at the beginning, thus very small arrival times for nodes with small d , then the speed drops and converges to a constant as $d \rightarrow \infty$. To find out the asymptotic constant speed of perturbation spreading, we use Stirling's formula to rewrite the factorial and obtain

$$G(d) \xrightarrow{d \rightarrow \infty} \frac{2d}{e}. \quad (9.6)$$

It shows that as d goes to infinity, the slope of the linear increase of $G(d)$ with respect to d equals to $\frac{2}{e}$, which is independent of the choice of the threshold ϵ_{th} . However, the threshold does have influence on the speed of convergence to the linear function: the larger the threshold, the faster the convergence (Fig. 9.3b).

For perturbation spreading in networks with nontrivial topologies, the arrival time also depends on the second factor which involves the $(2d+2)$ -th root of the Laplacian power element. As shown in Sec. 8.3, for lightly-loaded homogeneous networks where $K_{ij} = K$ and $\sin(\theta_j^* - \theta_i^*)$ for all (i, j) , this factor is approximately the number of shortest paths $\#\mathcal{P}$ times K^d . In the following we denote $\#\mathcal{P}_{k \rightarrow i}^{d(k,i)}$ as $\#\mathcal{P}$ for simplicity. Therefore, the asymptotic behavior of this factor is essentially determined by how the number of shortest paths depends on the distance. Assuming an exponential growth, i.e. $\#\mathcal{P}(d) \propto \mu^d$ ($\mu > 1$)

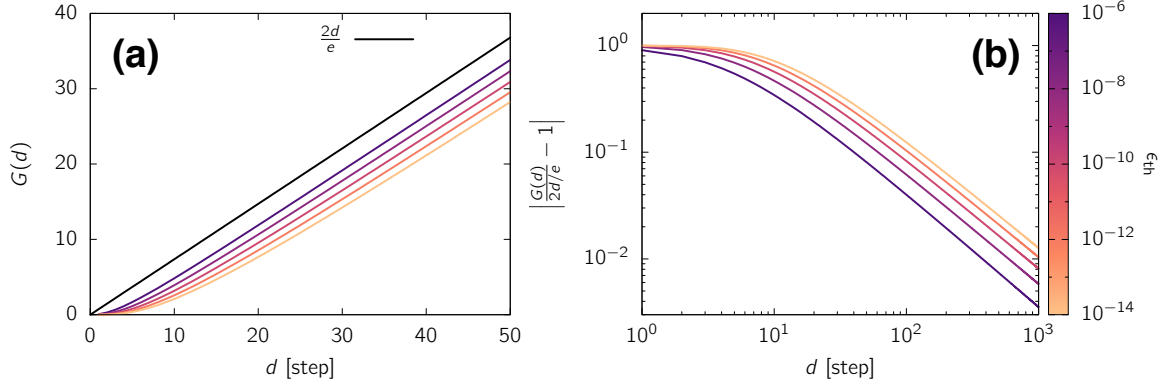


Fig. 9.3 The asymptotic behavior of the general spreading function $G(d)$. (a) As $d \rightarrow \infty$ the general spreading function $G(d)$ asymptotically approaches to a linear function with a slope of $2/e$. The deviation decreases with distance as a power law (b). The curves in (a) and (b) are color-coded by the threshold value ϵ_{th} .

for e.g. a μ -dimensional lattice, we have

$$\left|(\mathcal{L}^d)_{ik}\right|^{-\frac{1}{2d+2}} \approx (\#\mathcal{P}K^d)^{-\frac{1}{2d+2}} \propto (\mu^d K^d)^{-\frac{1}{2d+2}} \xrightarrow{d \rightarrow \infty} (\mu K)^{-\frac{1}{2}}. \quad (9.7)$$

Therefore, combining the results for the two factors in the arrival time, (9.6) and (9.7), we obtain asymptotic behavior of the arrival time as

$$\tau_{i,\text{app}}^{(k)} \xrightarrow{d \rightarrow \infty} \frac{2d}{e\sqrt{\mu K}}, \quad (9.8)$$

which suggests an *asymptotic spreading speed* in homogeneous networks with an exponential shortest path scaling:

$$C_\infty^{\text{exp}} = \frac{1}{2}e\sqrt{\mu K}. \quad (9.9)$$

In fact, an upper bound of $C_{d \rightarrow \infty}$ can be given in terms of the largest degree D_{\max} in the network. The number of shortest paths between two nodes is at most D_{\max}^d , thus the asymptotic spreading speed cannot surpass

$$C_\infty^{\text{upper}} = \frac{1}{2}e\sqrt{D_{\max}K}. \quad (9.10)$$

For more sparsely connected networks, where the number of shortest paths grows slower than exponentially with distance, e.g. as a power of the distance $\#\mathcal{P}(d) \propto d^\nu$ with ($\nu \geq 0$), the impact of the multiplicity of shortest paths disappear as $d \rightarrow \infty$, since

$\lim_{d \rightarrow \infty} (d^\nu)^{-\frac{1}{2d+2}} = 1$. Thus the asymptotic spreading speed becomes

$$C_\infty^{\text{sparse}} = \frac{1}{2}e\sqrt{K}. \quad (9.11)$$

This asymptotic behavior of the spreading speed is also observed numerically. For the British power grid network, we measure the *instantaneous spreading speed* of a perturbation from node k at distance d as the inverse of the difference between the average arrival time over nodes with distance d and the average arrival time over nodes with distance $d - 1$:

$$C^{(k)}(d) := \left(\langle \tau_i^{(k)} \rangle_d - \langle \tau_i^{(k)} \rangle_{d-1} \right)^{-1} \quad (9.12)$$

The instantaneous speeds computed based on the estimates and on the exact arrival time exhibit similar asymptotic behaviors to a constant spreading speed (Fig. 9.4). Since the British grid network is sparse, the estimated spreading speed converges to $C_\infty^{\text{sparse}} = \frac{1}{2}e\sqrt{K}$ as expected. The deviation between the instantaneous and the asymptotic spreading speed drops loosely as a power law with an increasing distance (Fig. 9.4b), such that it decreases to about 5% at only $d = 13$. However, this result has large fluctuations and errorbars at larger distance, due to the small number of nodes at these distances.

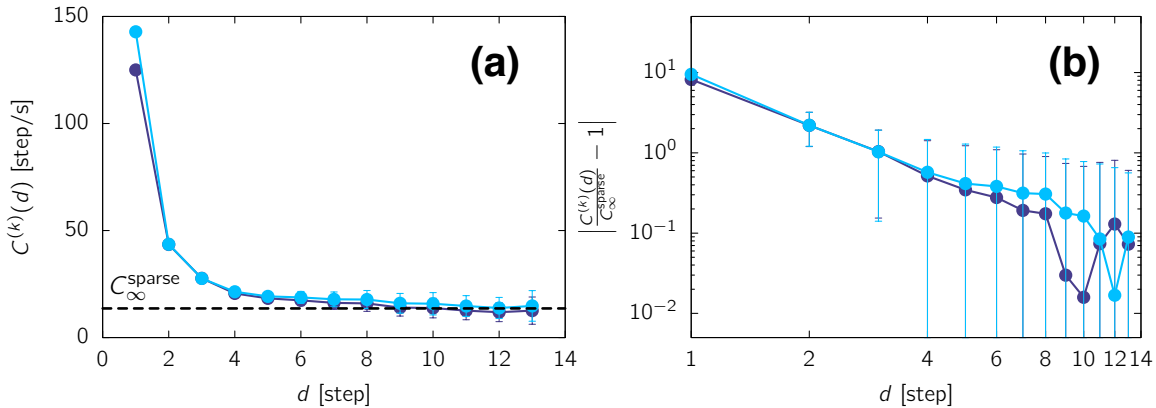


Fig. 9.4 **The asymptotic spreading speed for large distance.** The instantaneous speed defined in (9.12) asymptotically approaches a constant speed (black dashed line in (a)). The relative deviation between the two is plotted in (b). The instantaneous speed determined based on the estimated arrival time is shown in blue and the one based on exact arrival time in purple. The errorbars indicate the standard deviation among the nodes with the same distance. The network setting is the same as in Fig. 9.1.

9.2 The topological factor

In Sec. 9.1.2, we separate the one-term estimate of the arrival time (9.2) into two factors: the general spreading function $G(d)$ describing the general spreading pattern across networks, and one individualizes the nodal arrival times for specific network topologies through the element of the Laplacian matrix to the power of d . However, we notice that the one-term estimate show innegligible deviations to the exact arrival time which grows with distance (Fig. 9.1d, Fig. 9.3). Thus, how accurate is the topological dependence given by the one-term estimate for the exact arrival time? Does the weighted sum of the shortest paths between the perturbed node and the responding node (8.17) actually underlie the exact arrival time of a perturbation?

We name the topological-dependent factor in the one-term estimate of the arrival time (9.2) as the *general topological factor* of perturbation spreading:

$$\tilde{T}_i^{(k)} := \left| (\mathcal{L}^d)_{ik} \right|^{-\frac{1}{2d+2}}. \quad (9.13)$$

Particularly, for lightly-loaded homogeneous networks where the Laplacian element $\mathcal{L}_{ij} \approx -K$ for all edges (i, j) , the general topological factor is essentially determined by the number of shortest paths $\#\mathcal{P}$:

$$\tilde{T}_i^{(k)} \approx (\#\mathcal{P} K^d)^{-\frac{1}{2d+2}} = (\#\mathcal{P})^{-\frac{1}{2d+2}} K^{-\frac{d}{2d+2}}. \quad (9.14)$$

Thus, for such networks, we define the *topological factor* of a node pair (k, i) as

$T_i^{(k)} := (\#\mathcal{P})^{-\frac{1}{2d+2}}, \quad (9.15)$

which is a dimensionless quantity purely depending on the network structure. The topological factor is symmetric in the sense of $T_i^{(k)} = T_k^{(i)}$. For connected networks, there are at least one and at most D_{\max}^d paths between node pair (k, i) , thus the topological factor satisfies $(D_{\max})^{-\frac{d}{2d+2}} < T_i^{(k)} \leq 1$. The topological factor of the nodes in four example networks with various topological structures is shown in Fig. 9.5. In chain networks, there is only one shortest path between any pair of nodes, thus the topological factor is trivial: $T_i^{(k)}(d) = 1$ for all d . For square lattices, the topological factor is diverse: for node pairs which are strictly vertically or horizontally apart, $T_i^{(k)}(d) = 1$ as in chain networks; for node pairs which are diagonally apart, the number of shortest paths grows exponentially with the respective dimension as the base. Particularly, for node pairs

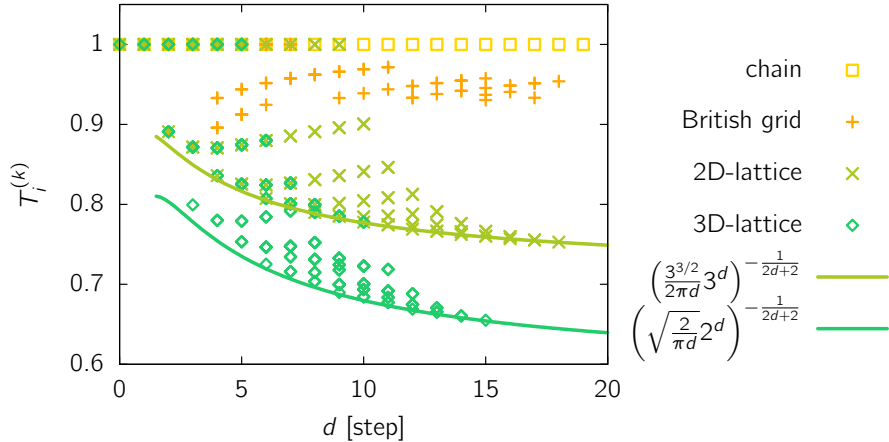


Fig. 9.5 Examples of topological factor. The topological factor of each node in example networks such as a chain network with $N = 20$, the British power grid network $N = 120$ (Fig. 9.1a), a 10×10 square lattice and a $6 \times 6 \times 6$ cubic lattice. The lines show the analytical results, (9.16) and (9.17), for diagonally positioned node pairs in square lattices.

diagonally apart in square lattice, the number of shortest paths grows with distance as

$$\#\mathcal{P}_{\text{square, diag}} = \binom{d}{d/2} = \frac{d!}{[(d/2)!]^2} \approx \sqrt{\frac{2}{\pi d}} 2^d. \quad (9.16)$$

For diagonal node pairs in cubic lattice, the number of shortest paths grows similarly

$$\#\mathcal{P}_{\text{cubic, diag}} = \binom{d}{d/3} \binom{2d/3}{d/3} = \frac{d!}{[(d/3)!]^3} \approx \frac{3^{3/2}}{2\pi d} 3^d. \quad (9.17)$$

The approximation in (9.16) and (9.17) results from the application of the Stirling's formula. Thus, for lattices the topological factor $T_i^{(k)}(d)$ ranges from 1 to significantly lower values (Fig. 9.5).

To test the dependence of the exact arrival time on the topological factor, we measure the nodal arrival time in the four example networks with diverse topologies but the same homogeneous coupling strength. As shown in Fig. 9.6a, the numerically determined exact arrival time differ across nodes and across networks. For nodes with distance 15, the arrival time in cubic lattice is about 35% smaller than the one in chain network. An intuitive picture of this result is, the more shortest paths there are between a node pair, the more routes the impact of the perturbation can be carried through between the two nodes, thus the faster the response at the responding node grows and the earlier it reaches the threshold. If normalized by the topological factor, the exact arrival times across nodes and across networks collapse nicely to the same curve (Fig. 9.6b). This result shows

that the topological factor accurately captures the impact of network topologies on the perturbation spreading process.

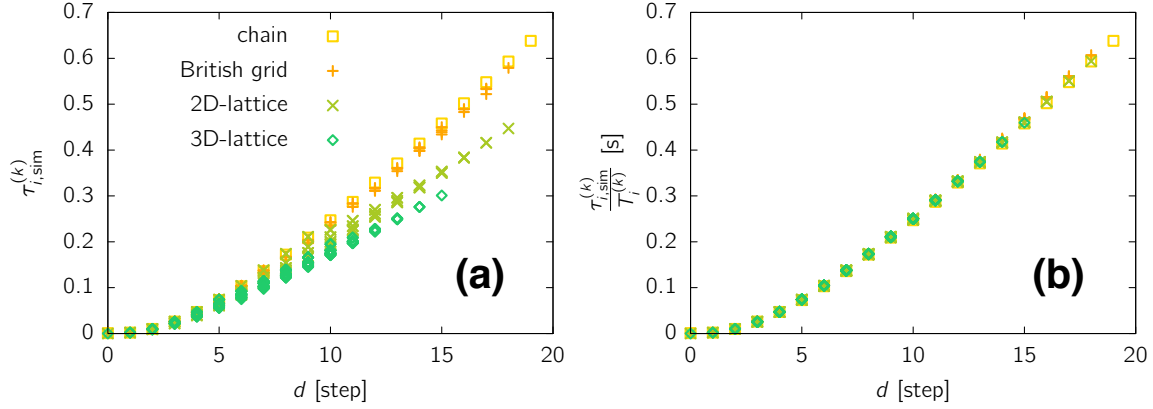


Fig. 9.6 The collapse of the exact arrival time normalized by the topological factor. The four example networks are the same as in Fig. 9.5. The numerically determined arrival time are shown in (a) and the ones normalized by the topological factor are shown in (b). Common parameters across networks: $K_{ij} \equiv K = 300 \text{ s}^{-2}$, $\alpha = 1 \text{ s}^{-1}$, $\varepsilon = 1$, $\omega = 0.01 \times 2\pi \text{ Hz}$, $\varphi = 0$, $\epsilon_{\text{th}} = 10^{-10}$.

9.3 Predicting perturbation arrival time

In this section we propose an approach to predict the exact perturbation arrival time at each node in a network with an arbitrary but given topology. As shown in last section, if normalized by the topological factor, the exact nodal arrival times measured in networks with different topologies collapse onto a universal curve characterizing the perturbation spreading pattern (Fig. 9.6). Based on this *master curve* of perturbation spreading, we are in a position to make predictions for nodal arrival times in networks with arbitrary network topologies.

The master curve is given by (i) numerically determine the exact nodal arrival times $\tau_i^{(k)}$ in a training data set of diverse network topologies, (ii) normalizing the recorded arrival times by the respective topological factor $T_i^{(k)}$, and (iii) averaging over the nodes with the same distance to the perturbation in the data set, i.e.

$$M(d) := \left\langle \frac{\tau_{i,\text{num}}^{(k)}}{T_i^{(k)}} \right\rangle_d. \quad (9.18)$$

The red line in Fig. 9.7b shows the master curve determined from the arrival time data collected in perturbing each node in 100 realizations of random Gabriel graph¹ with 100 nodes (see Fig. 9.7a for an example), i.e. 10^6 data points. Note that the master curve is not the same as the curve of the general spreading function $G(d)$. The general spreading function (9.4) is directly derived from the one-term approximation of the nodal response. Meanwhile, the master curve is determined based on the normalization of the *numerically* determined nodal arrival times, which includes also the higher-order terms in the nodal response. It is true that the contribution of the higher-order terms do not depend linearly on the topological factor, which is why the collapse of the arrival times is not exact (Fig. 9.6), however, the normalization significantly reduces the standard deviation of the arrival times among all nodes with the same distance across network (see inset of Fig. 9.7b).

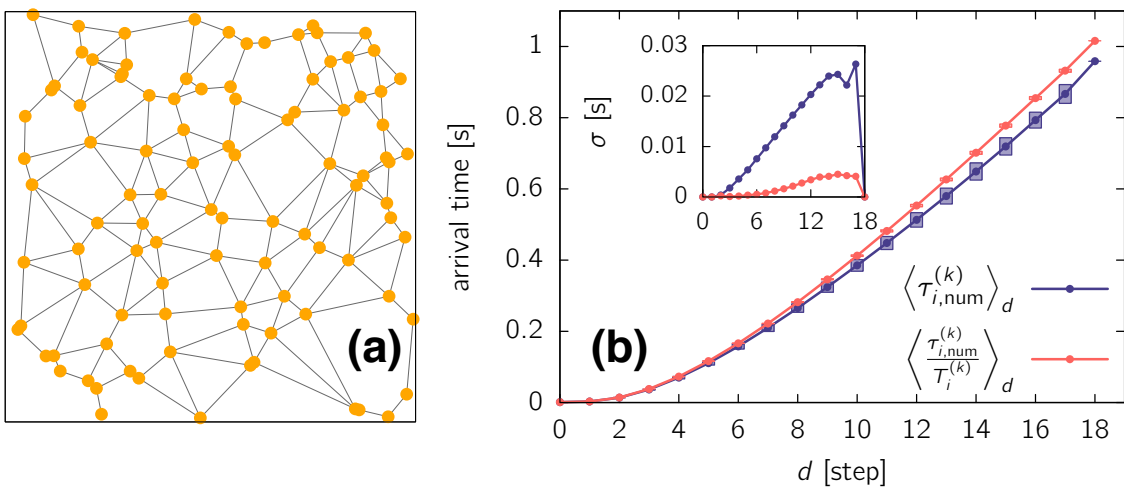


Fig. 9.7 The master curve of perturbation spreading. The arrival time averaged over nodes with the same distance is shown in purple, and the master curve determined based on the normalized arrival times (9.18) in red (b). The boxes around the data points indicate the standard deviation of data with the same distance. The standard deviation is additionally plotted in the inset. The data are collected from the perturbations of each node in 100 realizations of random Gabriel graph with 100 nodes. An example of a Gabriel graph is shown in (a). Parameters: $N = 100$, $K_{ij} \equiv K = 100 \text{ s}^{-2}$, $\alpha = 1 \text{ s}^{-1}$, $\Omega = 4 \text{ s}^{-2}$ for 20 nodes and $\Omega = -1 \text{ s}^{-2}$ for the rest 80 nodes, $\varepsilon = 1$, $\omega = 0.01 \times 2\pi \text{ Hz}$, $\varphi = 0$, $\epsilon_{\text{th}} = 10^{-10}$.

Based on the master curve, we are capable of making predictions for nodal arrival time for networks with arbitrary topologies. Given the network topology and the site of perturbation, it is computationally inexpensive to evaluate the topological factor. For

¹Gabriel graphs are planar graphs where two points p and q in the Euclidean plane are connected by an edge if and only if the circle with diameter pq does not contain any other nodes in its interior [131]. The random Gabriel graphs are generated by (i) producing 100 nodes with random coordinates in a unit square, and (ii) producing edges of the Gabriel graph via a variation of the Delaunay triangulation.

homogeneous networks, computing the topological factor is equivalent to counting the number of shortest paths, which can be carried out with a modified Breadth-first search (BFS) in linear time $O(|V|)$. The perturbation arrival time of a node i with distance d is given by:

$$\tau_{i,\text{pred}}^{(k)} = M(d)T_i^{(k)}. \quad (9.19)$$

The standard deviation σ for each d in the master curve, which rises from the finite training data set, gives the prediction interval of the nodal arrival time as $\pm\sigma(d)T_i^{(k)}$. Using the master curve shown in Fig. 9.7, we make predictions for nodal arrival times in a cubic lattice network and in another 100 realizations of random Gabriel graph. The results show that the prediction error defined as $|\tau_{i,\text{pred}}^{(k)}/\tau_{i,\text{num}}^{(k)} - 1|$ is almost always below 1% (Fig. 9.8b). The high errors for small distances come from the finite time step in numerical simulations. Notably, even for significantly different network topologies, e.g. for the cubic lattice network, our prediction approach yields good results with low prediction error. Compared to the prediction error for another 100 realizations of random Gabriel graph, the error for cubic lattice is even lower for some distances (Fig. 9.8b).

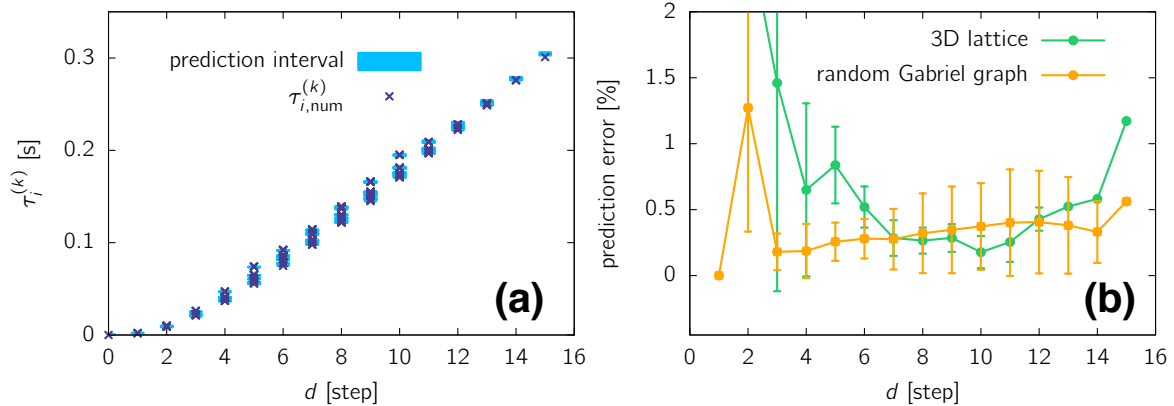


Fig. 9.8 Predictions for the exact arrival time. (a) The measured nodal arrival time in a $6 \times 6 \times 6$ cubic lattice (purple crosses) and the prediction interval (blue boxes) given by the master curve in Fig. 9.7b. (b) The prediction error for the nodal arrival times in the cubic lattice and another 100 realizations of random Gabriel graph. The errorbars indicate the standard deviation among the nodes with the same distance.

Although in the example of the prediction, the “task” networks, i.e. the networks in which the arrival times are to be predicted, and the “training” networks, i.e. the networks for determining the master curve, have the same relative threshold of the arrival time $\epsilon_{\text{th}}/\epsilon e^{\ell\varphi}$ and the same coupling strength K , the presented approach can be easily generalized to predict arrival times in “task” networks with a different threshold and a different coupling strength. The only extra work is to rescale the master curve by dividing it with the

factors $(\epsilon_{\text{th}}/\epsilon e^{i\varphi})^{1/(2d+2)}$ and $K^{-d/(2d+2)}$ for the training networks and to multiply the same factors with the new values of ϵ_{th} , $\epsilon e^{i\varphi}$ and K in the task networks. Furthermore, replacing the topological factor (9.15) in the approach with the general topological factor (9.13) allows predictions for task networks with inhomogeneous coupling strengths.

9.4 Conclusion

In this chapter we elaborate our study on the perturbation spreading processes in networks based on one-term approximation of the linear nodal response close to $t = 0$. Specifically, we investigate how the impact of a perturbation spreads in a network by looking into the relation between the first threshold-crossing time of nodal responses and the topological distance between the perturbation and the response. The one-term estimate of the perturbation arrival time suggests two patterns in perturbation spreading: (i) in homogeneous networks, the instantaneous spreading speed decreases with distance and converges to a topology-specific constant, and (ii) the (general) topological factor essentially underlies the nodal arrival times. Very similar patterns are observed for the numerically determined exact arrival times.

In particular, in homogeneous networks, the asymptotic spreading speed at large distance depends on how the number of shortest paths grows with distance, i.e. $\#\mathcal{P}(d)$. The asymptotic spreading speed is derived explicitly for networks with $\#\mathcal{P}(d)$ being an exponential growth and being an sub-exponential growth. However, we remind the readers that the results about the asymptotic spreading behavior and the asymptotic spreading speed is valid only for the one-term estimate of the arrival time. For the exact arrival time, a similar asymptotic behavior is observed, but a rigorous proof is still missing.

Nevertheless, the exact arrival time shows an accurate enough dependence on the topological factor suggested by the one-term estimate. The exact arrival times recorded in networks with the same homogeneous coupling but diverse topologies collapse nicely onto a universal *master curve* if normalized by the topological factor. Using the master curve of perturbation spreading, we develop an semi-numerical approach to accurately predict nodal arrival times in networks with arbitrary topologies. Remarkably, even if the training networks and the task networks have distinct network topologies, the prediction error is almost always below 1%.

In short, based on the analytical solution and approximation given in Chap. 8, in this chapter we quantitatively characterizes the perturbation spreading processes and unveil the asymptotic spreading behavior in homogeneous networks, which essentially depends on the network topology. Interestingly, this result is also largely valid for exact arrival times, which enables us to predict the exact perturbation arrival times for networks with arbitrary topologies. In fact, these results can be generalized to similar network systems

and perturbation scenarios to a large extent, which will be discussed in detail in the next chapter.

Chapter 10

Towards a Theory of Perturbation Spreading in Networks

In Chap. 9, we discussed the asymptotic spreading behavior in second-order dissipative oscillator networks based on the one-term approximation. However, how general are these results and how do we estimate the asymptotic spreading speed for the exact arrival time, which includes the higher order terms in the series?

In the final chapter of Part III, we present our attempts to develop the previously presented results to a theory of perturbation spreading in networks. Specifically, in Sec. 10.1, we generalize the results about the perturbation spreading behavior to similar network systems in the model class (3.1) by discussing the transient dynamics of perturbed networks in different scenarios. In Sec. 10.2, based on the observation of the perturbation spreading behavior in a chain network, we propose two conjectures on the bounds of the asymptotic spreading speed of the exact arrival time: a lower bound and an upper bound.

10.1 Universality of perturbation spreading behavior

In the last two chapters, we studied the perturbation spreading behavior in the most general setting of model class (4.1), i.e. $\alpha \neq 0$ and $\beta \neq 0$. Based on the solution of the linear nodal response and the one-term approximation at the time of perturbation, we discovered the strong distance-dependence of the threshold-crossing perturbation arrival time, the asymptotic behavior of the spreading speed, and the topological factor which characterizes the impact of network topology on perturbation spreading. However, how universal are these patterns in the perturbation spreading in networks?

Before generalizing the results, we first discuss the essential common properties of the systems to which the theory can be transferred. First, the underlying network should be connected so that there is at least one path that the perturbation can pass through and

reach every node in the network. Second, the system should be at a fixed point prior to perturbation. The very concept of “perturbation spreading” requires the media of perturbation spreading to be initially free of perturbation, i.e. to be resting at a steady state for dynamical systems or to be neutral/susceptible for populations in epidemics. Therefore, a necessary condition for the considered network systems is that it should have at least one fixed point, and it is at the fixed point for $t \leq 0$.

In the following, we consider if or how the discovered patterns in perturbation spreading change under varied circumstances, such as (i) at the limit of low- and high-damping, (ii) under the perturbation of different kinds of signals, (iii) with other forms of coupling functions, (iv) with a non-zero nodal relaxation in the dynamics and (v) if the responses in frequency instead of in phase are observed.

10.1.1 Impact of damping

Low-damping limit If the damping is very low, i.e. $\alpha \ll \beta$, we let $\alpha = 0$ and $\beta = 1$ without loss of generality. The response vector $\Theta^{(k)}(t)$ to a driving at node k thus follows the dynamics

$$\ddot{\Theta}^{(k)} = -\mathcal{L}\Theta^{(k)} + \mathbf{D}^{(k)}, \quad (10.1)$$

which yields the solution in the basis of Laplacian eigenvectors as

$$\begin{aligned} \Theta^{(k)}(t) = & \frac{e^{i\varphi}}{N\omega^2} \left(-1 - i\omega t + e^{i(\omega t + \varphi)} \right) \mathbf{1} \\ & + \sum_{\ell=1}^{N-1} \frac{v_k^{[\ell]} e^{i\varphi}}{-\omega^2 + \lambda^{[\ell]}} \left[\left(1 + \frac{\omega}{\sqrt{\lambda^{[\ell]}}} \right) \cos \left(\sqrt{\lambda^{[\ell]}} t \right) + e^{i\omega t} \right] \mathbf{v}^{[\ell]}. \end{aligned} \quad (10.2)$$

Analyzing the n -th time derivative of the linear response in a similar way as in Sec. 8.2, we arrive at the same result: the contribution of each eigenmode in the n -th time derivative is a polynomial of the respective eigenvalue with degree $\frac{n-2}{2}$. Thus, the one-term approximation of the linear response at the low damping limit is exactly the same as for the networks with finite damping, and the same perturbation spreading patterns follow.

In fact, as the damping parameter decreases, the exponential decay of the transient response in the dissipative second-order phase oscillator network (8.8) slows down and finally ceases to decay at all. Once triggered by the perturbation, the intrinsic oscillations keep going with system’s eigenfrequencies. However, the change in the long-term behavior of the oscillations does not affect the perturbation spreading process close to $t = 0$. Interestingly, at the low-damping limit, stronger resonances occur: the response amplitude of the ℓ -th eigenmode is not only maximized as a finite value, but approaches

infinity when the perturbation frequency equals the eigenfrequency/resonance frequency: $\omega = \omega_{\text{eigen}}^{[\ell]} = \sqrt{\lambda^{[\ell]}}$.

High-damping limit With a very high damping parameter $\alpha \gg \beta$, the system becomes a network of first-order oscillators and thus loses the oscillatory behavior. In this case the response vector obeys

$$\dot{\Theta}^{(k)} = -\mathcal{L}\Theta^{(k)} + \mathbf{D}^{(k)}, \quad (10.3)$$

if we let $\alpha = 1$ and $\beta = 0$. The linear solution in the basis of Laplacian eigenvectors reads

$$\Theta^{(k)}(t) = \sum_{\ell=0}^{N-1} \frac{v_k^{[\ell]} e^{i\varphi}}{i\omega + \lambda^{[\ell]}} \left(-e^{i\lambda^{[\ell]} t} + e^{i\omega t} \right) \mathbf{v}^{[\ell]}. \quad (10.4)$$

It is possible to carry out the same procedure as before and determine the one-term approximation of the linear response, which gives the estimate of the arrival time

$$\tau_{i,\text{app}}^{(k)} = \left| \frac{\epsilon_{\text{th}}(d+2)!}{\epsilon e^{i\varphi} (\mathcal{L}^d)_{ki}} \right|^{\frac{1}{d+2}}. \quad (10.5)$$

However, although the distance-dependence and the asymptotic behavior still exist for the networks at the high damping limit (Fig. 10.1), the error of the one-term estimate is large. This means that the higher order terms have considerable contributions to the transient response, much more significant than the higher-order terms in the responses of the second-order oscillators.

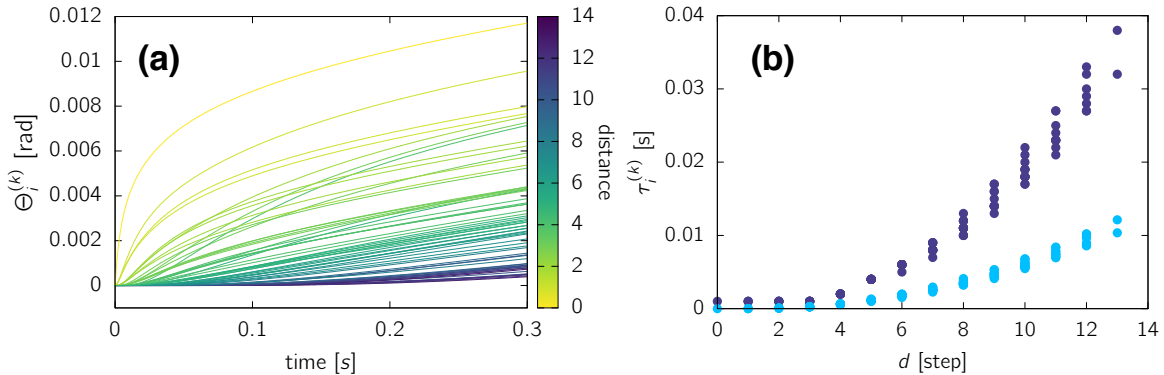


Fig. 10.1 **Perturbation spreading in Kuramoto networks.** (a) Transient nodal responses of a network of first-order Kuramato oscillators, color-coded with the distance to the perturbation. (b) The numerically measured nodal arrival times (purple) and the one-term estimates (blue). The underlying network topology is the British power grid network as illustrated in Fig. 8.2a. Parameters are also set as the same plus $\epsilon_{\text{th}} = 10^{-8}$.

The large error is a consequence of the changed relation between the order of the time derivative of the nodal response and the highest order of the Laplacian matrix it includes. We have seen in Sec. 8.2 that, in the series representation of the response of second-order oscillator networks, the order of the first non-zero term n depends on distance d as $n = 2d + 2$, and the first non-zero term includes elements of \mathcal{L}^d (see Tab. 8.1). In the time derivatives of the response, the highest order of Laplacian matrix steps up by 1 as the order of time derivative steps up by 2, meaning that the elements of \mathcal{L}^{d+1} appears in time derivatives with order $\geq 2d + 4$. However, in the time derivatives of the responses of first-order oscillator networks, the highest order of Laplacian matrix steps up by 1 as the order of time derivative steps up by 1. Therefore the elements of \mathcal{L}^{d+1} appears in the time derivatives with order $\geq d + 1$, so that the error from \mathcal{L}^{d+1} is significantly less penalized by the factorial and thus plays a bigger role in the response.

10.1.2 Impact of the form of perturbation

Perturbation as driving In last two chapters we have been focusing on the transient impact a perturbation on the dynamics of an oscillator. That is, the transient response of a network system at a steady state to an external driving. We derived the linear network response to a sinusoidal signal and to a step-function signal in Sec. 8.1 and arrived at the same transient response pattern.

In fact, we notice that the one-term approximation of the response to a sinusoidal driving signal is independent of the driving frequency ω and the damping parameter α , and is linear to the initial magnitude of impact $e^{i\varphi}$. This result is plausible since both ω and α describe system's longer-term behavior: the driven oscillation frequency and the rate of the exponential decay of the transient response. Therefore, we arrive at the conclusion that for driving signals with any form and for any damping parameter α not much larger than β in the network, the transient network response exhibits the same essential pattern. The influence of ω and α comes into play only in a larger time scale, or in higher-order terms in the series representation of the nodal response.

Perturbation on state variables If the network is not driven, but is only perturbed by a deviation at the state variable θ_k or $\dot{\theta}_k$, do the patterns in transient response change? The answer is yes, but they change only slightly.

The linear network response $\Theta(t)$ to a small deviation

$$\Theta_0 = \sum_{\ell=0}^{N-1} c_0^{[\ell]} \mathbf{v}^{[\ell]} \quad \text{and} \quad \dot{\Theta}_0 = \sum_{\ell=0}^{N-1} \dot{c}_0^{[\ell]} \mathbf{v}^{[\ell]}$$

at $t = 0$ follows

$$\ddot{\Theta} + \alpha \dot{\Theta} + \mathcal{L}\Theta = \mathbf{0}, \quad (10.6)$$

which yields the solution

$$\Theta(t) = \frac{1}{\sqrt{N}} \left(c_0^{[0]} + \frac{\dot{c}_0^{[0]}}{\alpha} - \frac{\dot{c}_0^{[0]}}{\alpha} e^{-\alpha t} \right) \mathbf{1} + \sum_{\ell=1}^{N-1} \left(\frac{-\Delta_-^{[\ell]} c_0^{[\ell]} + \dot{c}_0^{[\ell]}}{2i\gamma^{[\ell]}} e^{\Delta_+^{[\ell]} t} + \frac{\Delta_+^{[\ell]} c_0^{[\ell]} - \dot{c}_0^{[\ell]}}{2i\gamma^{[\ell]}} e^{\Delta_-^{[\ell]} t} \right) \mathbf{v}^{[\ell]}. \quad (10.7)$$

Here $\Delta_+^{[\ell]}$, $\Delta_-^{[\ell]}$ and $\gamma^{[\ell]}$ are defined as in Eq. 8.7. Focusing on the impact of a signal initial perturbation $\theta_i = \theta_i^* + \delta_{ik}$, we have the linear nodal response

$$\Theta^{(k)}(t) = \frac{1}{N} \mathbf{1} + \sum_{\ell=1}^{N-1} \frac{v_k^{[\ell]}}{2i\gamma^{[\ell]}} \left(-\Delta_-^{[\ell]} e^{\Delta_+^{[\ell]} t} + \Delta_-^{[\ell]} e^{\Delta_-^{[\ell]} t} \right) \mathbf{v}^{[\ell]}. \quad (10.8)$$

Following a similar procedure as in Sec. 8.2, we obtain the result that the lowest-order non-zero term in the series representation of the nodal response at $t = 0$ has order $n = 2d$. Thus the one-term approximation of nodal response is given as

$$\tau_{i,\text{app}}^{(k)} = \left| \frac{\epsilon_{\text{th}}(2d)!}{\epsilon e^{i\varphi} (\mathcal{L}^{2d})_{ki}} \right|^{\frac{1}{2d}}. \quad (10.9)$$

Thus, we can see that the transient response pattern for a perturbation on the phase is very similar to the one for a perturbation on the dynamics. The only difference is that the one-term estimates depend on distance as $2d$ instead of as $2d + 2$. This can be understood as an *earlier* arrival of a perturbation: the perturbed phase transfers the impact *immediately* to the neighboring nodes, while a perturbation on the second-order time derivative of the phase needs a bit extra time to affect the phase of the perturbed oscillator.

10.1.3 Impact of the form of coupling

In the previous analysis we assume the form of the coupling function as $g(\cdot) = \sin(\cdot)$, which yields the dynamics of the classical Kuramoto model ($\alpha = 1, \beta = 0$) and the oscillator model of AC power grids ($\alpha > 0, \beta = 1$). However, the choice of the specific form of coupling function does not affect the patterns in perturbation spreading in networks. As long as (i) the nodes are pairwise *diffusively* coupled, i.e. the coupling depends on the difference of the state variable of the neighboring nodes, and (ii) the coupling function is differentiable, the Laplacian matrix arises in the dynamics of the linear response vector Θ thus the same results follow. The only difference is that the Laplacian element is then given by

$$\mathcal{L}_{ij} = K_{ij} g'(\theta_j^* - \theta_i^*), \quad (10.10)$$

where $g'(\theta_j^* - \theta_i^*)$ denotes the derivative of the coupling function g with respect to the state difference at the fixed point. However, a network-wide asymptotic spreading speed requires a same weight of all edges. Otherwise, the spreading speed is heterogeneous across network. Therefore the coupling function $g(\cdot)$ must satisfy $g'(\theta_j^* - \theta_i^*) \equiv g^*$ for all edges (i, j) .

10.1.4 Impact of relaxation

If each node has a non-zero relaxation in the dynamics, i.e.

$$\beta \ddot{\theta}_i = -\alpha \dot{\theta}_i - \xi \theta_i + \sum_{j=1}^N K_{ij} \sin(\theta_j - \theta_i), \quad (10.11)$$

how does the perturbation spreading behavior change? With relaxation, the dynamics of the linear response vector reads

$$\ddot{\Theta} = -\alpha \dot{\Theta} - \xi \Theta - \mathcal{L} \Theta, \quad (10.12)$$

which resembles the dynamics without relaxation (10.6) if we absorb the relaxation term into the Laplacian term. Thus it is easy to see that the solution of the linear response with relaxation has exactly the same form as before if we replace $\lambda^{[\ell]}$ with $\lambda^{[\ell]} + \xi$. Since ξ is simply a constant, so it has no influence on the results of the one-term estimates and thus does not affect the perturbation spreading behavior in networks.

10.1.5 Behavior of frequency response

Sometimes the behavior of the frequency responses is more relevant than the behavior of the phase response, e.g. in the context of the AC power grid dynamics. The magnitude of the frequency responses is crucial for the safety operation of the synchronous machines and other components in the grid. Does the frequency response share the same patterns in perturbation spreading as the phase response?

The solution of the linear frequency response is simply the first time derivative of the linear phase response (Eq. 8.8). Hence, the lowest-order non-zero term in the Taylor expansion at $t = 0$ which includes $(\mathcal{L}^d)_{ki}$ has the same form as the one for the phase response, but just one order lower. The estimated arrival time is thus

$$\tau_{i,\text{app}}^{(k)} = \left| \frac{\epsilon_{\text{th}} [2d+1]!}{\epsilon e^{i\varphi} (\mathcal{L}^d)_{ki}} \right|^{\frac{1}{2d+1}}. \quad (10.13)$$

This can be interpreted as a very similar perturbation spreading pattern with a little *earlier* arrival of the perturbation at the frequency than at the phase: driven by the perturbation on the second-order derivative of node k , the phase velocity of node k reaches the threshold first, then the phase of node k .

10.2 Two conjectures on bounds of asymptotic spreading speed

Previously in Chap. 9, we revealed the asymptotic behavior of the one-term estimate of the arrival time at large distance: regardless of the network topology, the estimated arrival time approaches a linear function of the topological distance, which suggests a constant asymptotic perturbation spreading speed C_∞ . Furthermore, the asymptotic spreading speed with respect to the one-term estimate does depends on the network topology, in particular, on how the number of shortest paths between the perturbed node and the responding node grows with distance: $\#\mathcal{P}(d)$. A similar asymptotic behavior is observed for the numerically determined exact arrival time (Fig. 9.4). However, does the true spreading speed converge to the same constant as we derived from the one-term estimate? Although rigorous proofs are still absent, we propose two conjectures on the bounds of the true asymptotic spreading speed in this section.

Conjecture on a lower bound

Let us first consider an elementary example: perturbation spreading in a chain network of second-order oscillators, i.e. (4.1) with $\alpha > 0$ and $\beta > 0$. We perturb the phase of the node at one end of the chain with a small deviation $\theta_0(t = 0) = \theta_0^* + \varepsilon$, and let the perturbation spread through the chain. We measure the exact arrival time of the perturbation through numerical simulation, and compute the one-term estimate of the arrival time via Eq. 10.9. Additionally, we measure the time when the nodal response reaches its first peak. Since there is only one shortest path in the chain network, the first peak can be considered as the initial and the major impact of the perturbation. We also computed the instantaneous spreading speed C for the three arrival times.

We obtain intriguing results about the asymptotic spreading behaviors of the estimated and the exact arrival time (Fig. 10.2). Both arrival times exhibit convergence to a linear function of d , but the linear functions have different slopes (Fig. 10.2a). Both of the deviations of the arrival time to the respective linear function of d drop with d as a power-law (Fig. 10.2b). That means, the true perturbation spreading *does* approach a constant spreading speed as expected, but the value of the speed is *different* from the one derived from the one-term estimate. The asymptotic spreading speed with respect to the one-term estimate is $\frac{1}{2}e\sqrt{K}$, as expected: there is only one shortest path between

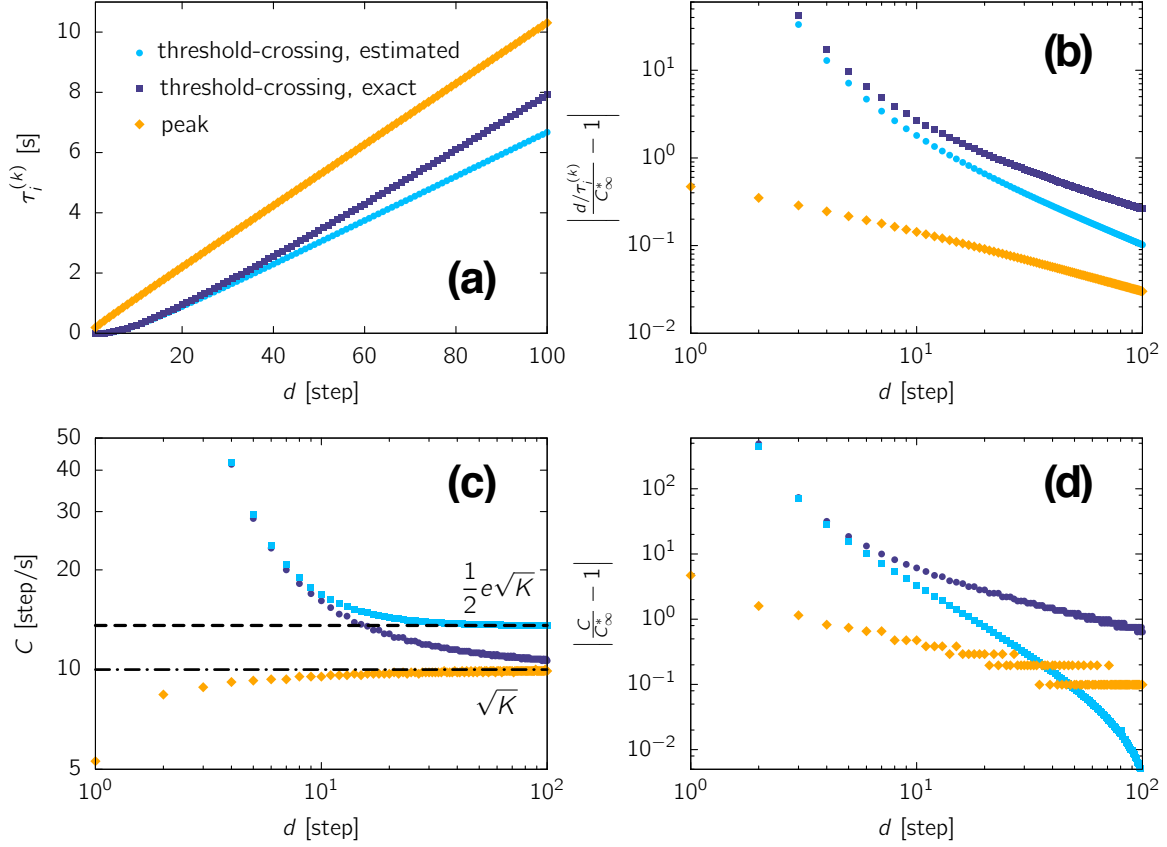


Fig. 10.2 The asymptotic spreading behavior in a chain network. (a) Three arrival times, the exact, the estimated, and the peak, asymptotically approach linear functions of d at large distance, with the respective relative deviations dropping as a power-law (b). (c) The instantaneous spreading speed computed based on the one-term estimate approaches $\frac{1}{2}e\sqrt{K}$ while the ones computed based on the exact and the peak arrival times approaches \sqrt{K} . The relative deviations of the instantaneous speed drops at least as fast as a power-law (d). Parameter: $N = 120$, $K_{ij} \equiv K = 100 \text{ s}^{-2}$, $\alpha = 1 \text{ s}^{-1}$, $\Omega = 1 \text{ s}^{-2}$ for 60 nodes alternatively arranged with the rest nodes with $\Omega = -1 \text{ s}^{-2}$, $\varepsilon = 1$, $\epsilon_{\text{th}} = 10^{-8}$.

any node pair in a chain network, $\#\mathcal{P}(d) = 1$, so the asymptotic spreading speed in sparse networks (9.11) fits. Meanwhile, the true asymptotic spreading speed appears to be smaller than $\frac{1}{2}e\sqrt{K}$. In fact, it approaches \sqrt{K} , which is the asymptotic spreading speed with respect to the peak time of nodal response (Fig. 10.2c). The deviations of the instantaneous spreading speed to the respective speed limit C_∞^* all drops as a power-law, if not faster (Fig. 10.2d). The steps in the deviations are the consequence of the finite time step in numerical simulation.

In fact, we notice that if without damping and external driving, the dynamics of the response vector of a second-order oscillator networks, Eq. 10.1, resembles a discrete version the standard wave equation. For homogeneously coupled networks, the dynamics

of the response vector can be written as

$$\ddot{\Theta} = -K \tilde{\mathcal{L}} \Theta. \quad (10.14)$$

Here $\tilde{\mathcal{L}}$ denotes the unweighted Laplacian matrix, whose negative is equivalent to the discrete Laplace operator. For chain networks, Eq. 10.14 is the discrete version of the wave equation in classical continuous media, thus suggests a “natural speed of wave propagation” of \sqrt{K} , which fits the asymptotic spreading speed we observe for the peak arrival time and the true threshold-crossing arrival time. Thus, the transient linear response of a second-order phase oscillator network at a fixed point can be compared to wave propagation in N -dimensional space. Especially, we notice that the instantaneous spreading speed with respect to the exact threshold-crossing arrival time and with respect to the peak arrival time approach to the same constant speed differently: one from above and one from below. The decrease of the spreading speed with respect to the threshold-crossing arrival time is due to the broadening of the first peak, while the increase of the spreading speed with respect to the peak arrival time is artificial: for small t the first peak has a very sharp shape while the time step of simulation is finite.

As concluded in Chap. 9, the asymptotic spreading speed is closely related to the topological factor. For homogeneous networks, it is essentially the inverse of the number of shortest paths between the perturbed node and the responding node. The more shortest paths are there, the faster the spreading. Thus, for networks with any other topologies, the true asymptotic spreading speed should only be larger than the one for chain networks: \sqrt{K} . We hence propose an lower bound of the true asymptotic spreading speed.

Conjecture 1. *Let $G(V, E)$ be a network of second-order dynamical systems $\Theta(t) \in \mathbb{R}^{|V|}$ with a diffusive coupling function $g(\theta_j - \theta_i)$ and a homogeneous coupling strength $K_{ij} = K$ for all $(i, j) \in E$. Given a fixed point $\Theta^* \in \mathbb{R}^{|V|}$, if $g'(\theta_j^* - \theta_i^*) = g^*$ for all $(i, j) \in E$, then the asymptotic spreading speed of a perturbation at the fixed point has a lower bound $\sqrt{g^* K}$.*

Conjecture on an upper bound

To find an upper bound for the true asymptotic spreading speed, we first review the one-term approximation of the nodal response. Observing (8.15), we notice that, as a positive function of t to the power of $2d + 2$, it goes rapidly to infinity as t grows. Although not yet proven mathematically, the one-term approximation appears to be always greater than the actual nodal response in all of our observations (see Fig. 8.1). Thus, the threshold-crossing arrival time determined from the one-term approximation is always smaller than the true threshold-crossing arrival time. As a consequence, the asymptotic spreading speed derived from the one-term estimate of the arrival time is

always larger than the true asymptotic spreading speed. We therefore propose an upper bound of the true asymptotic spreading speed.

Conjecture 2. *Let $G(V, E)$ be a network of second-order dynamical systems $\boldsymbol{\theta}(t) \in \mathbb{R}^{|V|}$ with a diffusive coupling function $g(\theta_j - \theta_i)$ and a homogeneous coupling strength $K_{ij} = K$ for all $(i, j) \in E$. Given a fixed point $\boldsymbol{\theta}^* \in \mathbb{R}^{|V|}$, if $g'(\theta_j^* - \theta_i^*) = g^*$ for all $(i, j) \in E$, then the asymptotic spreading speed of a perturbation at the fixed point has an upper bound $\frac{1}{2}e\sqrt{\mu g^* K}$ with $\mu \geq 1$. The factor μ is determined by the dependence of the number of shortest paths $\#\mathcal{P}$ with the distance d :*

$$\mu = \lim_{d \rightarrow \infty} [\#\mathcal{P}(d)]^{\frac{1}{d}}. \quad (10.15)$$

10.3 Conclusion

In the last chapter, we explored the possibility to generalize our previous results to a theory of perturbation spreading in networks. First, we discussed the universality of the discovered patterns in perturbation spreading, essentially the one-term estimate of the arrival time. The results are summarized as follows:

- At the low-damping limit, our results still holds. However, at the high-damping limit, the one-term approximation exhibits large error, due to the much less penalized higher order contribution from $(\mathcal{L}^{d+1})_{ki}$.
- The perturbation spreading behavior does *not* depend on the specific form of the perturbation, but only on the ratio between the threshold and the initial magnitude of the perturbation. The impact of a perturbation on the state variable of a node arrives two steps *earlier* than the impact of a perturbation on the dynamics: the one-term estimate of the arrival time depends on $2d$ instead of $2d + 2$.
- A general diffusive coupling function g is allowed, as long as it is differentiable so that the system's dynamics can be linearized. However, a network-wide asymptotic spreading speed exist only when its first derivative at the fixed point g^* for all edges.
- If the dynamics includes a relaxation term $-\xi\theta_i$, the spreading pattern remains the same.
- If observing the frequency response, the impact of the perturbation arrives one step earlier: the one-term estimate of the arrival time depends on $2d + 1$ instead of $2d + 2$.

In short, the one-term estimate of the threshold-crossing arrival time in second-order networks (3.1) can be unifiedly expressed as

$$\tau_{i,\text{app}}^{(k)} \approx \left| \frac{\epsilon_{\text{th}}^* \delta!}{(\mathcal{L}^d)_{ki}} \right|^{\frac{1}{\delta}}. \quad (10.16)$$

Here ϵ_{th}^* denotes the ratio between the threshold ϵ_{th} and the initial magnitude of the perturbation, ϵ for a step-function signal and $\epsilon e^{i\varphi}$ for a sinusoidal signal. Additionally, δ depends on which variable is perturbed: $\delta = 2d$ if the state variable is perturbed and $\delta = 2d + 2$ if the dynamics is perturbed. If one observes the frequency response, δ should be subtracted by 1. However, no matter how we choose ϵ_{th}^* and δ , the asymptotic spreading speed remains the same as discussed in Chap. 9. It solely depends on the topology of the network.

Moreover, we propose two conjectures on the true asymptotic spreading speed. Inspired by the observations of the asymptotic perturbation spreading behavior in a chain network, we propose $\sqrt{g^* K}$ as a lower bound, which can be seen as the discrete version of the wave propagation speed. Conjecturing the one-term approximation of the nodal response is always larger than the actual response, we propose the topology-dependent asymptotic spreading speed derived from the one-term estimate $\tau_{i,\text{app}}^{(k)}$ as an upper bound of the true asymptotic spreading speed.

As shown in this chapter, our findings in Chap. 9 reveal general patterns in the perturbation spreading processes in diffusively coupled networks of second-order dynamical systems. Thus, our work serves as a contribution to the study of transient network dynamics under perturbation and may shed light on the understanding of perturbation spreading processes in biological and chemical networks with diffusive coupling such as [79, 83]. Especially, the proposed conjectures on the bounds of the asymptotic spreading speed may stimulate proofs (or falsifications), which would hopefully bring deeper insight into the topic, e.g. establishing the relation between the perturbation spreading dynamics in networks and in continuous media.

Conclusions

In this thesis we studied how networks of diffusively coupled dynamical systems close to a normal operation state dynamically respond to spatiotemporal perturbation signals. Based on the well-established methods in mathematics and physics such as linear response theory and asymptotic analysis, we discovered a way to systematically link the second-order network dynamics to the network topology, thus obtained analytical insights in the patterns rising in the dynamic network responses. We analyzed the response patterns in two timescales: (i) the long-term steady pattern driven by the external signals, and (ii) the short-term transient pattern in the spreading impact of a single signal. Furthermore, we explored the boundary of the validity and the generality of our theory. We also proposed practical schemes to predict network responses in different timescales.

In Part I of the thesis (Chap. 1–3), we reviewed the standard approach to solve for the response of a high-dimensional dynamical system to a perturbation at its fixed point and showed its limitations: As soon as the Jacobian matrix of the system is asymmetric, which is typical for a dynamical system with an order larger than one, an explicit solution for dynamic response becomes impossible through a conventional approach. Moreover, we introduced a model class of diffusively coupled phase oscillators (3.1). In particular, we focused on the most general case in the model class, the second-order Kuramoto-like oscillator model (3.8), demonstrated its relation to the dynamics of the AC power grids and its several dynamical features.

In Part II of the thesis (Chap. 4–7), we developed a theory of the steady patterns rising in normally-operating networks as a response to external driving signals. Inspired by linear response theory, we derived an analytical solution of the long-term network responses characterized by the underlying network topology. The solution opens up paths to a theoretical understanding of dynamic network responses, rendering distinct spatiotemporal responsive behaviors in three frequency regimes. At the low-damping limit, our theory appears as a generalization of Zanette’s findings for network of Kuramoto oscillators [39, 40]. Based on our theory, we proposed an approach to efficiently and accurately predict the long-term network response to irregular and distributed noises. Finally, we showed that our theory, which is based on the linearization of system’s dynamics at a fixed point, holds validity with high accuracy as long as the system does not reach a bifurcation point where the fixed point annihilates.

In Part III of the thesis (Chap. 8–10), we investigated the patterns in the transient response of a network to a single perturbation. We derived the analytical solution of the full time evolution of network responses to a driving signal, and provided a more tractable one-term approximation of the transient response. Based on the approximation, we discovered an asymptotic spreading pattern of perturbations in homogeneous networks: the instantaneous spreading speed decreases with the topological distance and approaches a constant speed. We revealed that the network topology, specifically, the number of shortest paths between perturbation and response, is the decisive factor in the asymptotic perturbation spreading behavior. Based on these results, we proposed an approach to accurately predict the perturbation arrival times in a given yet arbitrary network. Finally, we explored the generality of our results and proposed two conjectures on the bounds of the exact asymptotic spreading speed, which suggests the potential extension of our results towards a complete theory of perturbation spreading in networks.

The achievement of the thesis can be condensed into three aspects. In the following, we discuss each of the three in combination with an outlook to future research.

Analytical solution of dynamic network responses

In contrast to previous studies which rarely provide explicit, deterministic results for dynamic network responses to a fluctuating signal [31, 58], for the first time, we provided an analytical formulation describing the full time evolution of the network responses to irregular and distributed driving signals close to a fixed point (Chap. 4 and Chap. 8). Although the solutions are derived for phase oscillator networks with a Kuramoto-type coupling function, they can be easily generalized to other undirected, diffusively-coupled networks [79, 83] which have a symmetric Laplacian matrix (Chap. 10).

Especially, in the investigation of the transient responsive behavior, we derived an one-term approximation of the nodal response, which significantly improves the tractability of the analytical solution, and allows analytical insights into the transient perturbation spreading process in networks (Chap. 8).

The derived analytical solutions and approximations, as well as the methodology in the derivation, can be valuable for physicists, complex network researchers and will hopefully stimulate novel theoretical insights in study of dynamic network responses and other related fields.

Response patterns in long and short timescale

Based on the analytical solutions of the network responses, we revealed novel response patterns in both long and short timescales for networks driven by time-dependent perturbation signals. In comparison to previous studies which focus on *instability*-induced

long-term patterns [17–19, 30–36], we discovered nontrivial spatiotemporal patterns in complex networks rising from the dynamic interaction between the time-dependent driving signal and the intrinsic dissipative network dynamics (Chap. 5). Particularly, at the high-damping limit, our theory not only shows consistency with Zanette’s findings [39, 40], but provide a generalization of the results to networks with non-identical nodes and arbitrary topologies. Furthermore, our theory reveals the relation between the regime shift of the response patterns and the topological features of the underlying network structure, which is missing in Zanette’s work (Chap. 6).

Our theory opens novel perspectives on dynamic network responses and imply suggestions on regime- and topology-specific principles on the planning and optimization of real-world networks. For instance, for modern power grids which are exposed to fluctuating power generation from the renewable energy sources, our theory suggests a high risk from the fluctuations containing strong frequency components in the homogeneous and resonance regimes.

In short timescale, we revealed the asymptotic spreading behavior of a single perturbation (Chap. 9), which can be naturally compared to the information propagation process in various systems. For instance, it would be an interesting interdisciplinary research topic to relate the asymptotic spreading speed with the Lieb–Robinson bound in non-relativistic quantum systems [132]. Additionally, it would be exciting to find the connection between our theory and the theory of effective distance established for stochastic systems [43, 44]. Furthermore, the proposed conjectures on the asymptotic spreading speed would hopefully stimulate creative proofs (or falsifications) and bring deeper insight into the topic, e.g. establishing the relation between the perturbation spreading dynamics in networks and in continuous media.

Predicting networks responses

Another important aspect of this thesis is the approaches to predict the dynamic network responses (Chap. 7 and Chap. 9). In principle, for given perturbation time series, the analytical solutions of the linear network responses, i.e. linear combinations of (8.8) and (8.9), provide accurate predictions for the trajectory of network response within the range of validity. However, our predictive approach for steady responses (Sec. 7.1) exhibits its efficiency through the frequency sampling scheme: computing responses only for dominant frequencies with high amplitudes in signal’s power spectrum and close to the resonance frequencies yields reduced computation time and high accuracy.

Particularly, for perturbation signals with a characteristic power spectrum, such as the real-world wind power fluctuation [129], our theory provides an upper bound of the nodal response (7.2) without knowing the specific perturbation time series. This bound provides a guideline in identifying the nodes which are “in danger” under such specific type of perturbations, in the sense of potentially exhibiting strong responses.

In the field of perturbation spreading, the prediction of the arrival time is of greater practical relevance than the prediction of the full time-dependent response [44, 59, 61, 62]. Thus, we developed a fast and straightforward approach to directly predict the perturbation arrival time in a network with a given yet arbitrary topology. We expect that this approach can be used to predict perturbation arrival times in other diffusively-coupled networks in biological and chemical systems such as [79, 83]. Although real-world networks such as power grids involve more complex sub-structures and local dynamics, our prediction can serve as a fundamental guideline regarding the behavior of perturbation spreading in high-voltage transmission grids, whose dynamics is essentially captured by the oscillator model (3.8) [26, 107].

Despite of the low error ($< 1\%$) of this approach, we believe that its accuracy can be largely improved if a stronger mathematical tool can be found to include the contribution of the higher-order terms in the transient response, i.e. to provide a reasonable correction of the one-term approximation. Furthermore, if extended to stochastic systems such as epidemic spreading, our prediction may provide comparison or even theoretical insights into the puzzling spreading patterns revealed by the data-driven microsimulation models, such as [60].

How complex networks dynamically respond to external disturbances has been, and will continue to be a fascinating research topic in foreseeable future, due to its ubiquity and fundamental significance in understanding the rise of complexity in complex networks. This thesis represents our efforts in the analytical interpretation and the quantitative prediction of the dynamic responses of networks with diffusive coupling. It might be a tiny step in a long journey, nevertheless, we hope it contributes to the collective knowledge about complex network dynamics and stimulate more brilliant future work in this field.

Appendix A

Proof of Proposition 2

Proposition 2. *The product $Q(\omega)$ defined in (5.14), i.e.*

$$Q(\omega) := \prod_{\substack{\ell'=0, \\ \ell' \neq \ell}}^{N-1} \left[(-\omega^2 + \lambda^{[\ell']})^2 + \alpha^2 \omega^2 \right],$$

with $\omega > 0, \alpha > 0, \lambda^{[\ell]} \geq 0, \ell \in \{0, \dots, N-1\}$ (A.1)

satisfies

$$Q(\omega) = \sum_{j=0}^{2N-2} C_\ell^{[j]} \omega^{4N-4-2j},$$

where the coefficients $C_\ell^{[j]}$ can be expressed as a polynomial of $\lambda^{[\ell]}$ with degree j .

Proof. We first show that the product $Q(\omega)$ can be written as the following polynomial

$$Q(\omega) = \sum_{j=0}^{2N-2} C_\ell^{[j]} \omega^{4N-4-2j}, (A.2)$$

where the coefficient $C_\ell^{[j]}$ involves a multiplication of j Laplacian eigenvalues.

In the expansion of the product

$$Q(\omega) = \prod_{\substack{\ell'=0, \\ (\ell' \neq \ell)}}^{N-1} \left[\omega^4 + (\alpha^2 - 2\lambda^{[\ell']}) \omega^2 + (\lambda^{[\ell']})^2 \right],$$

each term is a product of, say, a times ω^4 , b times $(\alpha^2 - 2\lambda^{[\ell']})\omega^2$, and c times $(\lambda^{[\ell']})^2$, with $a + b + c = N - 1$. In each term involves ω to the power of $x = 4a + 2b$, and a multiplication of $j = b + 2c$ Laplacian eigenvalues. Thus, for each term, the number of multiplied Laplacian eigenvalues is related to the order of ω as $x = 4N - 4 - 2j$, which leads to the formulation (A.2).

Then we prove that the coefficient $C_\ell^{[j]}$ can be expressed as a polynomial of $\lambda^{[\ell]}$ with degree j . By definition, $\lambda^{[\ell]}$ should be the sum of products of a times 1, b times $(\alpha^2 - 2\lambda^{[\ell']})$, and c times $(\lambda^{[\ell']})^2$, over all possible choices of (a, b, c) with constraints $a + b + c = N - 1$ and $b + 2c = j$:

$$C_j^{[\ell]} = \sum_{\substack{a+b+c=N-1 \\ b+2c=j}} \sum_{P_\ell(a,b,c)} \prod_{p \in s_b} (\alpha^2 - 2\lambda^{[p]}) \prod_{q \in s_c} (\lambda^{[q]})^2. \quad (\text{A.3})$$

Here the second sum goes through all possible partitions $P_\ell(a, b, c)$ of the $N-1$ eigenmodes with indices $S_\ell := \{0, \dots, N-1\} \setminus \{\ell\}$ into three subsets s_a , s_b and s_c with a , b and c elements respectively. In the following, we show the coefficient (A.3) can be expressed as a polynomial of $\lambda^{[\ell]}$ in three steps.

1. First, we prove that

$$\sum_{s_b \in \binom{S_\ell}{b}} \prod_{p \in s_b} (\alpha^2 - 2\lambda^{[p]})$$

can be expressed by a polynomial of $\lambda^{[\ell]}$ with degree b . Here $\binom{S_\ell}{b}$ denotes the set of all possible b -subset of S_ℓ . We show this result via mathematical induction.

- 1.a For $b = 1$, we have

$$\sum_{s_1 \in \binom{S_\ell}{1}} \prod_{p \in s_1} (\alpha^2 - 2\lambda^{[p]}) = \sum_{p \in S} (\alpha^2 - 2\lambda^{[p]}) - (\alpha^2 - 2\lambda^{[\ell]}),$$

which is a polynomial of $\lambda^{[\ell]}$ with degree 1 since the first term is a sum over $S := \{0, \dots, N-1\}$, thus it is a constant independent of $\lambda^{[\ell]}$.

- 1.b If the statement holds for $b = n - 1$, i.e.

$$\sum_{s_{n-1} \in \binom{S_\ell}{n-1}} \prod_{p \in s_{n-1}} (\alpha^2 - 2\lambda^{[p]})$$

is a polynomial of $\lambda^{[\ell]}$ with degree $n - 1$, then for $b = n$ we have

$$\begin{aligned} \sum_{\substack{s_n \in \binom{S_\ell}{n}} \prod_{p \in s_n} (\alpha^2 - 2\lambda^{[p]}) &= \sum_{\substack{s_n \in \binom{S}{n}} \prod_{p \in s_n} (\alpha^2 - 2\lambda^{[p]}) \\ &\quad - (\alpha^2 - 2\lambda^{[\ell]}) \cdot \sum_{\substack{s_{n-1} \in \binom{S_\ell}{n-1}} \prod_{p \in s_{n-1}} (\alpha^2 - 2\lambda^{[p]}), \end{aligned}$$

which is a polynomial of $\lambda^{[\ell]}$ with degree n . The first term goes through all n -subset in S so is a constant independent of $\lambda^{[\ell]}$, and the second term is a polynomial of $\lambda^{[\ell]}$ with degree n . Thus the statement holds for $b = n$.

2. Similarly, we prove

$$\sum_{\substack{s_c \in \binom{S_\ell}{c}} \prod_{q \in s_c} (\lambda^{[q]})^2$$

is a polynomial of $\lambda^{[\ell]}$ with degree $2c$ by mathematical induction.

2.a For $c = 1$,

$$\sum_{\substack{s_1 \in \binom{S_\ell}{1}} \prod_{q \in s_1} (\lambda^{[q]})^2 = \sum_{q \in S} (\lambda^{[q]})^2 - (\lambda^{[\ell]})^2$$

is a polynomial of $\lambda^{[\ell]}$ with degree 2 since the first term is a constant.

2.b If the statement holds for $c = n - 1$, i.e.

$$\sum_{\substack{s_{n-1} \in \binom{S_\ell}{n-1}} \prod_{q \in s_{n-1}} (\lambda^{[q]})^2,$$

is a polynomial of $\lambda^{[\ell]}$ with degree $2n - 2$, then for $c = n$ we have

$$\sum_{\substack{s_n \in \binom{S_\ell}{n}} \prod_{q \in s_n} (\lambda^{[q]})^2 = \sum_{\substack{s_n \in \binom{S}{n}} \prod_{q \in s_n} (\lambda^{[q]})^2 - (\lambda^{[\ell]})^2 \cdot \sum_{\substack{s_{n-1} \in \binom{S_\ell}{n-1}} \prod_{q \in s_{n-1}} (\lambda^{[q]})^2,$$

which is a polynomial of $\lambda^{[\ell]}$ with degree $2n$ with similar arguments as in the last step.

3. As the final step we prove that

$$\sum_{\substack{s_b \in \binom{S_\ell}{b} \\ s_c \in \binom{S_\ell \setminus \{s_b\}}{c}}} \prod_{p \in s_b} (\alpha^2 - 2\lambda^{[p]}) \prod_{q \in s_c} (\lambda^{[q]})^2$$

is a polynomial of $\lambda^{[\ell]}$ with degree $b + 2c$. If either b or c is zero, the statement becomes equivalent to statement proved in former steps 1 or step 2, thus it still holds. In the following we again use mathematical induction to prove this result with $b, c \in \mathbb{N}$.

3.a For $b = 1$ and $c = 1$, we have:

$$\begin{aligned} \sum_{\substack{s_1 \in \binom{S_\ell}{1} \\ s_1 \in \binom{S_\ell \setminus s_1}{1}}} \prod_{p \in s_1} (\alpha^2 - 2\lambda^{[p]}) \prod_{q \in s_1} (\lambda^{[q]})^2 &= \sum_{\{p,q\} \in \binom{S}{2}} (\alpha^2 - 2\lambda^{[p]}) \cdot (\lambda^{[q]})^2 \\ &\quad - (\alpha^2 - 2\lambda^{[\ell]}) \cdot \sum_{q \in \binom{S_\ell}{1}} (\lambda^{[q]})^2 \\ &\quad - (\lambda^{[\ell]})^2 \cdot \sum_{p \in \binom{S_\ell}{1}} (\alpha^2 - 2\lambda^{[p]}), \end{aligned}$$

which is a polynomial of $\lambda^{[\ell]}$ with degree 3 since the first term is a $\lambda^{[\ell]}$ -independent constant, the second and the third term are polynomials of $\lambda^{[\ell]}$ with degree 3. Here we use the results from step 1 and step 2.

3.b Then we prove that the statement is true for $b = m, c = n$ if it is for $b = m - 1$ and $c = n - 1$. With the following notations

$$\begin{aligned} Y_{(b,c)} &:= \sum_{\substack{s_b \in \binom{S}{b} \\ s_c \in \binom{S \setminus s_b}{c}}} \prod_{p \in s_b} (\alpha^2 - 2\lambda^{[p]}) \prod_{q \in s_c} (\lambda^{[q]})^2 \\ Y_{(b,c)}^{[\ell]} &:= \sum_{\substack{s_b \in \binom{S_\ell}{b} \\ s_c \in \binom{S_\ell \setminus \{s_b\}}{c}}} \prod_{p \in s_b} (\alpha^2 - 2\lambda^{[p]}) \prod_{q \in s_c} (\lambda^{[q]})^2, \end{aligned}$$

the statement can be reformulated as: $Y_{(m,n)}^{[\ell]}$ is a polynomial of $\lambda^{[\ell]}$ with degree of $m + 2n$ if $Y_{(m-1,n-1)}^{[\ell]}$ is a polynomial of $\lambda^{[\ell]}$ with degree $m + 2n - 3$. Similar to the previous proofs, we write $Y_{(m,n)}^{[\ell]}$ as

$$\begin{aligned} Y_{(m,n)}^{[\ell]} &= Y_{(m,n)} - (\alpha^2 - 2\lambda^{[\ell]}) Y_{(m-1,n)}^{[\ell]} - (\lambda^{[\ell]})^2 Y_{(m,n-1)}^{[\ell]} \\ &= Y_{(m,n)} - (\alpha^2 - 2\lambda^{[\ell]}) \left(Y_{(m-1,n)} - (\lambda^{[\ell]})^2 Y_{(m-1,n-1)}^{[\ell]} \right) \\ &\quad - (\lambda^{[\ell]})^2 \left(Y_{(m,n-1)} - (\alpha^2 - 2\lambda^{[\ell]}) Y_{(m-1,n-1)}^{[\ell]} \right). \end{aligned}$$

Since $Y_{m,n}$, $Y_{m-1,n}$ and $Y_{m,n-1}$ are all $\lambda^{[\ell]}$ -independent constants, it is easy to see that $Y_{(m,n)}^{[\ell]}$ is a polynomial of $\lambda^{[\ell]}$ with degree $m + 2n - 1$, given that $Y_{(m-1,n-1)}^{[\ell]}$ is a polynomial of $\lambda^{[\ell]}$ with degree $m + 2n - 3$.

In fact, $Y_{(b,c)}^{[\ell]}$ is equivalent to the sum over $P_\ell(a, b, c)$ in the expression of $C_\ell^{[j]}$ (A.3), as $s_a = S_\ell \setminus (s_b \cup s_c)$ by definition. Therefore, the sum in (A.3) is also a polynomial of $\lambda^{[\ell]}$ with degree $b + 2c$. Finally, the coefficient $C_\ell^{[j]}$, as the sum of $Y_{(b,c)}^{[\ell]}$ over all the possible combinations of (a, b, c) under constraints $a + b + c = N - 1$ and $b + 2c = j$, is also a polynomial of $\lambda^{[\ell]}$ with degree $j = b + 2c$.

□

Appendix B

Proof of Proposition 3

Proposition 3. *The term with the highest order of $\lambda^{[\ell]}$ in $F_n(\lambda^{[\ell]})$ ($n \in \mathbb{N}, n \geq 2$)¹ introduced in (8.11)*

$$F_n(\lambda^{[\ell]}) = \frac{1}{-\omega^2 + i\alpha\omega + \lambda^{[\ell]}} \left[\frac{\left(\Delta_+^{[\ell]}\right)^n (\Delta_-^{[\ell]} - i\omega)}{2i\gamma^{[\ell]}} - \frac{\left(\Delta_-^{[\ell]}\right)^n (\Delta_+^{[\ell]} - i\omega)}{2i\gamma^{[\ell]}} + (\iota\omega)^n \right]$$

with $\gamma^{[\ell]} = \sqrt{\lambda^{[\ell]} - \frac{\alpha^2}{4}}$, $\Delta_+^{[\ell]} = -\frac{\alpha}{2} + i\gamma^{[\ell]}$, $\Delta_-^{[\ell]} = -\frac{\alpha}{2} - i\gamma^{[\ell]}$
 and $\omega > 0, \alpha > 0, \lambda^{[\ell]} \geq 0, \ell \in \{0, \dots, N-1\}$ (B.1)

is

$$LT[F_n](\lambda^{[\ell]}) = \begin{cases} (-1)^{\frac{n-1}{2}} \left(-i\omega + \frac{n-1}{2}\alpha\right) (\lambda^{[\ell]})^{\frac{n-3}{2}} & \text{if } n \text{ is odd,} \\ (-1)^{\frac{n-2}{2}} (\lambda^{[\ell]})^{\frac{n-2}{2}} & \text{if } n \text{ is even.} \end{cases}$$

Proof. To prove Prop. 3, we first define

$$f_n(\lambda^{[\ell]}) := \frac{\left(\Delta_+^{[\ell]}\right)^n - \left(\Delta_-^{[\ell]}\right)^n}{2i\gamma^{[\ell]}}, \quad (\text{B.2})$$

¹For $n = 0$ and $n = 1$, $F_n(\lambda^{[\ell]}) \equiv 0$ due to the initial condition. That is, the nodal response and its first time derivative are both zero at the time of perturbation: $t = 0$.

so that $F_n(\lambda^{[\ell]})$ can be simplified as

$$F_n(\lambda^{[\ell]}) = \frac{\lambda^{[\ell]} f_{n-1}(\lambda^{[\ell]}) - \iota\omega f_n(\lambda^{[\ell]}) + (\iota\omega)^n}{-\omega^2 + \iota\alpha\omega + \lambda^{[\ell]}}. \quad (\text{B.3})$$

To determine the leading term in $F_n(\lambda^{[\ell]})$, which is essentially one order lower than the leading term in $\lambda^{[\ell]} f_{n-1}(\lambda^{[\ell]}) - \iota\omega f_n(\lambda^{[\ell]})$, we first observe the leading term in $(\Delta_+^{[\ell]})^n$ which is easier to obtain.

In the following we prove the leading term with respect to $\lambda^{[\ell]}$ in $(\Delta_+^{[\ell]})^n$ is

$$LT \left[\operatorname{Re} (\Delta_+^{[\ell]})^n \right] = \begin{cases} (-1)^{\frac{n+1}{2}} \frac{n\alpha}{2} (\lambda^{[\ell]})^{\frac{n-1}{2}} & \text{if } n \text{ is odd,} \\ (-\lambda^{[\ell]})^{\frac{n}{2}} & \text{if } n \text{ is even;} \end{cases} \quad (\text{B.4})$$

$$LT \left[\operatorname{Im} (\Delta_+^{[\ell]})^n \right] = \begin{cases} (-1)^{\frac{n-1}{2}} (\lambda^{[\ell]})^{\frac{n}{2}} & \text{if } n \text{ is odd,} \\ (-1)^{\frac{n}{2}} \frac{n\alpha}{2} (\lambda^{[\ell]})^{\frac{n-1}{2}} & \text{if } n \text{ is even.} \end{cases} \quad (\text{B.5})$$

via mathematical induction.

1. First, by simply inserting the definition

$$\Delta_+^{[\ell]} := -\frac{\alpha}{2} + \iota\sqrt{\lambda^{[\ell]} - \frac{\alpha^2}{4}} \quad (\text{B.6})$$

in to the first and second power of $\Delta_+^{[\ell]}$, we easily verify that the statement (B.4) and (B.5) is true for $n = 1$ and $n = 2$. Note that here we assume low dissipation, i.e. $\sqrt{\lambda^{[\ell]} - \frac{\alpha^2}{4}} \approx (\lambda^{[\ell]})^{\frac{1}{2}}$ (for the argumentation of a low damping parameter α see Sec. 5.2).

2. Then we show the statement is true for $n + 1$ given it is true for n with n being odd.

$$\begin{aligned}
LT \left[\operatorname{Re} \left(\Delta_+^{[\ell]} \right)^{n+1} \right] &= LT \left[LT \left[\operatorname{Re} \left(\Delta_+^{[\ell]} \right)^n \right] \left(-\frac{\alpha}{2} \right) - LT \left[\operatorname{Im} \left(\Delta_+^{[\ell]} \right)^n \right] \left(\lambda^{[\ell]} \right)^{\frac{1}{2}} \right] \\
&= LT \left[(-1)^{\frac{n+3}{2}} \frac{n\alpha^2}{4} \left(\lambda^{[\ell]} \right)^{\frac{n-1}{2}} - (-1)^{\frac{n-1}{2}} \left(\lambda^{[\ell]} \right)^{\frac{n+1}{2}} \right] \\
&= (-1)^{\frac{n+1}{2}} \left(\lambda^{[\ell]} \right)^{\frac{n+1}{2}}, \\
LT \left[\operatorname{Im} \left(\Delta_+^{[\ell]} \right)^{n+1} \right] &= LT \left[LT \left[\operatorname{Re} \left(\Delta_+^{[\ell]} \right)^n \right] \left(\lambda^{[\ell]} \right)^{\frac{1}{2}} + LT \left[\operatorname{Im} \left(\Delta_+^{[\ell]} \right)^n \right] \left(-\frac{\alpha}{2} \right) \right] \\
&= (-1)^{\frac{n+1}{2}} \frac{\alpha}{2} \left(\lambda^{[\ell]} \right)^{\frac{n}{2}} + (-1)^{\frac{n+1}{2}} \frac{n\alpha}{2} \left(\lambda^{[\ell]} \right)^{\frac{n}{2}} \\
&= (-1)^{\frac{n+1}{2}} \frac{(n+1)\alpha}{2} \left(\lambda^{[\ell]} \right)^{\frac{n}{2}}, \tag{B.7}
\end{aligned}$$

which agree with the statement since $n + 1$ is even.

3. At the end we show the statement is true for $n + 1$ given it is true for n with n being even. Similarly,

$$\begin{aligned}
LT \left[\operatorname{Re} \left(\Delta_+^{[\ell]} \right)^{n+1} \right] &= \left(-\lambda^{[\ell]} \right)^{\frac{n}{2}} \left(-\frac{\alpha}{2} \right) - (-1)^{\frac{n}{2}} \frac{n\alpha}{2} \left(-\lambda^{[\ell]} \right)^{\frac{n-1}{2}} \left(-\lambda^{[\ell]} \right)^{\frac{1}{2}} \\
&= (-1)^{\frac{n+2}{2}} \frac{(n+1)\alpha}{2} \left(\lambda^{[\ell]} \right)^{\frac{n}{2}}, \\
LT \left[\operatorname{Im} \left(\Delta_+^{[\ell]} \right)^{n+1} \right] &= LT \left[(-1)^{\frac{n+2}{2}} \frac{n\alpha^2}{4} \left(\lambda^{[\ell]} \right)^{\frac{n-1}{2}} + (-1)^{\frac{n}{2}} \left(\lambda^{[\ell]} \right)^{\frac{n+1}{2}} \right] \\
&= (-1)^{\frac{n}{2}} \left(\lambda^{[\ell]} \right)^{\frac{n+1}{2}}, \tag{B.8}
\end{aligned}$$

which agree with the statement since $n + 1$ is odd.

With the result (B.4) and (B.5) it is easy to find the leading term of $f_n(\lambda^{[\ell]})$. Since $\Delta_+^{[\ell]}$ and $\Delta_-^{[\ell]}$ are a complex conjugate pair, we have $\left(\Delta_-^{[\ell]} \right)^n = \overline{\left(\Delta_+^{[\ell]} \right)^n}$. Therefore

$$f_n(\lambda^{[\ell]}) = \frac{\operatorname{Im} \left(\Delta_+^{[\ell]} \right)^n}{\gamma^{[\ell]}}, \tag{B.9}$$

from which we obtain the leading term of $f_n(\lambda^{[\ell]})$

$$LT [f_n](\lambda^{[\ell]}) = \begin{cases} (-1)^{\frac{n-1}{2}} \left(\lambda^{[\ell]} \right)^{\frac{n-1}{2}} & \text{if } n \text{ is odd,} \\ (-1)^{\frac{n}{2}} \frac{n\alpha}{2} \left(\lambda^{[\ell]} \right)^{\frac{n-2}{2}} & \text{if } n \text{ is even.} \end{cases} \tag{B.10}$$

and the leading term of $F_n(\lambda^{[\ell]})$

$$\begin{cases} (-1)^{\frac{n-1}{2}} \left(-\iota\omega + \frac{n-1}{2}\alpha \right) (\lambda^{[\ell]})^{\frac{n-3}{2}} & \text{if } n \text{ is odd,} \\ (-1)^{\frac{n-2}{2}} (\lambda^{[\ell]})^{\frac{n-2}{2}} & \text{if } n \text{ is even.} \end{cases} \quad (\text{B.11})$$

□

References

- [1] René Descartes. *A Discourse on the Method*. Oxford University Press, 1637/2006.
- [2] D. R. Hofstadter. *Gödel, Escher, Bach: An Eternal Golden Braid*. Basic Books, 1979.
- [3] Melanie Mitchell. *Complexity: A guided tour*. Oxford University Press, 2009.
- [4] M. E. J. Newman. *Networks: an introduction*. Oxford University Press, 2010.
- [5] Robin J. Wilson. *An introduction to graph theory (5th Edition)*. Pearson Education Limited, 2010.
- [6] Frederico A. C. Azevedo, Ludmila R. B. Carvalho, Lea T. Grinberg, José Marcelo Farfel, Renata E. L. Ferretti, Renata E. P. Leite, Roberto Lent, Suzana Herculano-Houzel, et al. Equal numbers of neuronal and nonneuronal cells make the human brain an isometrically scaled-up primate brain. *Journal of Comparative Neurology*, 513(5):532–541, 2009.
- [7] Suzana Herculano-Houzel. The human brain in numbers: a linearly scaled-up primate brain. *Frontiers in Human Neuroscience*, 3, 2009.
- [8] Eugene P. Odum and Gary W. Barrett. *Fundamentals of ecology (third ed.)*, volume 3. Saunders, 1971.
- [9] Michael Zeilik and Stephen A. Gregory. *Introductory Astronomy Astrophysics (4th ed.)*. Saunders College Publishing, 1998.
- [10] Complex networks. <https://www.nature.com/subjects/complex-networks>. Accessed: 2017-10-18.
- [11] Steven H. Strogatz. Exploring complex networks. *Nature*, 410(6825):268–276, March 2001.
- [12] Renato E. Mirollo and Steven H. Strogatz. Synchronization of pulse-coupled biological oscillators. *SIAM Journal on Applied Mathematics*, 50(6):1645–1662, 1990.
- [13] Louis M. Pecora, Thomas L. Carroll, Gregg A. Johnson, Douglas J. Mar, and James F. Heagy. Fundamentals of synchronization in chaotic systems, concepts, and applications. *Chaos: An Interdisciplinary Journal of Nonlinear Science*, 7(4):520–543, 1997.

- [14] Adilson E. Motter, Seth A. Myers, Marian Anghel, and Takashi Nishikawa. Spontaneous synchrony in power-grid networks. *Nature Physics*, 9(3):191–197, 2013.
- [15] Martin Rohden, Andreas Sorge, Dirk Witthaut, and Marc Timme. Impact of network topology on synchrony of oscillatory power grids. *Chaos*, 24(1):013123–013123, February 2014.
- [16] Daniel M. Abrams and Steven H. Strogatz. Chimera states for coupled oscillators. *Physical Review Letters*, 93(17):174102, October 2004.
- [17] Peter K. Moore and Werner Horsthemke. Localized patterns in homogeneous networks of diffusively coupled reactors. *Physica D: Nonlinear Phenomena*, 206(1–2):121–144, June 2005.
- [18] Hans G. Othmer and L. E. Scriven. Instability and dynamic pattern in cellular networks. *Journal of Theoretical Biology*, 32(3):507–537, 1971.
- [19] Hans G. Othmer and L. E. Scriven. Non-linear aspects of dynamic pattern in cellular networks. *Journal of Theoretical Biology*, 43(1):83–112, 1974.
- [20] Kunihiko Fukushima and Sei Miyake. Neocognitron: A self-organizing neural network model for a mechanism of visual pattern recognition. In *Competition and cooperation in neural nets*, pages 267–285. Springer, 1982.
- [21] R. C. Mureşan, O. F. Jurjuţ, V. V. Moca, W. Singer, and D. Nikolic. The oscillation score: An efficient method for estimating oscillation strength in neuronal activity. *Journal of Neurophysiology*, 99(3):1333–1353, January 2008.
- [22] Sven Jahnke, Raoul-Martin Memmesheimer, and Marc Timme. Oscillation-induced signal transmission and gating in neural circuits. *PLoS Computational Biology*, 10(12):e1003940, December 2014.
- [23] E. Karzbrun, A. M. Tayar, V. Noireaux, and R. H. Bar-Ziv. Programmable on-chip dna compartments as artificial cells. *Science*, 345(6198):829–832, 2014.
- [24] Katayoun Sohrabi, Jay Gao, Vishal Ailawadhi, and Gregory J. Pottie. Protocols for self-organization of a wireless sensor network. *IEEE Personal communications*, 7(5):16–27, 2000.
- [25] Christian Prehofer and Christian Bettstetter. Self-organization in communication networks: principles and design paradigms. *IEEE Communications Magazine*, 43(7):78–85, 2005.
- [26] G. Filatrella, A. H. Nielsen, and N. F. Pedersen. Analysis of a power grid using a kuramoto-like model. *The European Physical Journal B*, 61(4):485–491, February 2008.

- [27] Stefano Ciliberti, Olivier C. Martin, and Andreas Wagner. Robustness can evolve gradually in complex regulatory gene networks with varying topology. *PLoS Computational Biology*, 3(2):e15, 2007.
- [28] Arun Krishnan, Masaru Tomita, and Alessandro Giuliani. Evolution of gene regulatory networks: Robustness as an emergent property of evolution. *Physica A: Statistical Mechanics and its Applications*, 387(8):2170–2186, 2008.
- [29] Maximino Aldana, Enrique Balleza, Stuart Kauffman, and Osbaldo Resendiz. Robustness and evolvability in genetic regulatory networks. *Journal of Theoretical Biology*, 245(3):433–448, 2007.
- [30] Ehud Meron. Pattern formation in excitable media. *Physics Reports*, 218(1):1–66, 1992.
- [31] M. C. Cross and P. C. Hohenberg. Pattern formation outside of equilibrium. *Reviews of Modern Physics*, 65(3):851–1112, July 1993.
- [32] Alan C. Newell and John A. Whitehead. Finite bandwidth, finite amplitude convection. *Journal of Fluid Mechanics*, 38(2):279–303, 1969.
- [33] Alan C. Newell. Envelope equations. *Lectures in Applied Mathematics*, 15(157):4, 1974.
- [34] Hiroya Nakao and Alexander S. Mikhailov. Turing patterns in network-organized activator-inhibitor systems. *Nature Physics*, 6(7):544–550, July 2010.
- [35] Malbor Asllani, Joseph D. Challenger, Francesco Saverio Pavone, Leonardo Sacconi, and Duccio Fanelli. The theory of pattern formation on directed networks. *Nature Communications*, 5:4517–4517, July 2014.
- [36] Nikos E. Kouvaris, Shigefumi Hata, and Albert Díaz-Guilera. Pattern formation in multiplex networks. *Scientific Reports*, 5:10840, June 2015.
- [37] Kunihiko Kaneko. Chaotic but regular posi-nega switch among coded attractors by cluster-size variation. *Physical Review Letters*, 63(3):219, 1989.
- [38] Pierre Coullet and Kjartan Emilsson. Strong resonances of spatially distributed oscillators: a laboratory to study patterns and defects. *Physica D: Nonlinear Phenomena*, 61(1-4):119–131, 1992.
- [39] D. H. Zanette. Propagation of small perturbations in synchronized oscillator networks. *Europhysics Letters*, 68(3):356–362, November 2004.
- [40] D. H. Zanette. Disturbing synchronization: Propagation of perturbations in networks of coupled oscillators. *The European Physical Journal B-Condensed Matter and Complex Systems*, 43(1):97–108, 2005.

- [41] Mark E. J. Newman. Spread of epidemic disease on networks. *Physical review E*, 66(1):016128, 2002.
- [42] Lars Hufnagel, Dirk Brockmann, and Theo Geisel. Forecast and control of epidemics in a globalized world. *Proceedings of the National Academy of Sciences of the United States of America*, 101(42):15124–15129, 2004.
- [43] Dirk Brockmann and Dirk Helbing. The hidden geometry of complex, network-driven contagion phenomena. *Science*, 342(6164):1337–1342, 2013.
- [44] Flavio Iannelli, Andreas Koher, Dirk Brockmann, Philipp Hövel, and Igor M. Sokolov. Effective distances for epidemics spreading on complex networks. *Physical Review E*, 95(1):012313, 2017.
- [45] Henri Degueldre, Jakob J. Metzger, Theo Geisel, and Ragnar Fleischmann. Random focusing of tsunami waves. *Nature Physics*, 12(3):259, 2016.
- [46] Van Jacobson. Congestion avoidance and control. In *ACM SIGCOMM computer communication review*, volume 18, pages 314–329. ACM, 1988.
- [47] Peter J. Menck, Jobst Heitzig, Jürgen Kurths, and Hans Joachim Schellnhuber. How dead ends undermine power grid stability. *Nature Communications*, 5:3969, 2014.
- [48] Dirk Witthaut, Martin Rohden, Xiaozhu Zhang, Sarah Hallerberg, and Marc Timme. Critical links and nonlocal rerouting in complex supply networks. *Physical Review Letters*, 116(13):138701, 2016.
- [49] Dirk Witthaut and Marc Timme. Nonlocal effects and countermeasures in cascading failures. *Physical Review E*, 92(3):032809, 2015.
- [50] UCTE. [Final report: System disturbance on 4 November 2006](#), 2007.
- [51] Debsankha Manik, Martin Rohden, Henrik Ronellenfitsch, Xiaozhu Zhang, Sarah Hallerberg, Dirk Witthaut, and Marc Timme. Network susceptibilities: Theory and applications. *Physical Review E*, 95(1):012319, 2017.
- [52] Daniel Jung and Stefan Kettemann. Long-range response in ac electricity grids. *Physical Review E*, 94(1):012307, 2016.
- [53] Adilson E. Motter and Ying-Cheng Lai. Cascade-based attacks on complex networks. *Physical Review E*, 66(6):065102, 2002.
- [54] Paolo Crucitti, Vito Latora, and Massimo Marchiori. Model for cascading failures in complex networks. *Physical Review E*, 69(4):045104, 2004.
- [55] Martin Rohden, Daniel Jung, Samyak Tamrakar, and Stefan Kettemann. Cascading failures in ac electricity grids. *Physical Review E*, 94(3):032209, 2016.

- [56] Benjamin Schäfer, Dirk Witthaut, Marc Timme, and Vito Latora. Dynamically induced cascading failures in supply networks. *arXiv preprint arXiv:1707.08018*, 2017.
- [57] Yang Yang, Takashi Nishikawa, and Adilson E. Motter. Vulnerability and co-susceptibility determine the size of network cascades. *Physical Review Letters*, 118(4):048301, 2017.
- [58] Romualdo Pastor-Satorras, Claudio Castellano, Piet Van Mieghem, and Alessandro Vespignani. Epidemic processes in complex networks. *Reviews of Modern Physics*, 87(3):925–979, AUG 31 2015.
- [59] Aurélien Gautreau, Alain Barrat, and Marc Barthélémy. Arrival time statistics in global disease spread. *Journal of Statistical Mechanics: Theory and Experiment*, 2007(09):L09001, 2007.
- [60] Hiroshi Nishiura. Prediction of pandemic influenza. *European Journal of Epidemiology*, 26(7):583–584, Jul 2011.
- [61] Lidia A. Braunstein, Sergey V. Buldyrev, Reuven Cohen, Shlomo Havlin, and H. Eugene Stanley. Optimal paths in disordered complex networks. *Physical Review Letters*, 91(16):168701, 2003.
- [62] Mohammad Roosta. Routing through a network with maximum reliability. *Journal of Mathematical Analysis and Applications*, 88(2):341–347, 1982.
- [63] Stefan Kettemann. Delocalization of disturbances and the stability of ac electricity grids. *Physical Review E*, 94(6):062311, 2016.
- [64] Justine Wolter, Benedict Lünsmann, Xiaozhu Zhang, Malte Schröder, and Marc Timme. Quantifying transient spreading dynamics on networks. *ArXiv e-prints*, October 2017.
- [65] Yoshiki Kuramoto. Self-entrainment of a population of coupled non-linear oscillators. In *International symposium on mathematical problems in theoretical physics*, pages 420–422. Springer, 1975.
- [66] Richard A. Brualdi and Herbert J. Ryser. *Combinatorial Matrix Theory*. Cambridge University Press, 2014.
- [67] Marco Giunti and Claudio Mazzola. Dynamical systems on monoids: Toward a general theory of deterministic systems and motion. *Methods, Models, Simulations and Approaches towards a General Theory of Change*, pages 173–185, 2012.
- [68] John Guckenheimer and Philip J. Holmes. *Nonlinear oscillations, dynamical systems, and bifurcations of vector fields*, volume 42. Springer Science & Business Media, 2013.

- [69] D. K. Arrowsmith and C. M. Place. *An Introduction to Dynamical Systems*. Cambridge University Press, 1990.
- [70] Steven H. Strogatz. *Nonlinear Dynamics and Chaos*. Perseus Books Publishing, LLC, 1994.
- [71] Lawrence Perko. *Differential Equations and Dynamical Systems*. Springer-Verlag New York, 1991.
- [72] Nicholas Loehr. *Advanced Linear Algebra*. CRC Press, 2014.
- [73] Tomasz Kapitaniak and Steven R. Bishop. *The Illustrated Dictionary of Nonlinear Dynamics and Chaos*. Wiley, 1999.
- [74] Mason A. Porter and James P. Gleeson. *Dynamical Systems on Networks: A Tutorial*. Springer, 2016.
- [75] M. E. Starzak. *Mathematical Methods in Chemistry and Physics*. Springer, Boston, MA, 1989.
- [76] Han Ying-Duo, Min Yong, and Hong Shao-Bin. A co-frequency dynamic equivalence method for power-frequency dynamics simulation in multi-machine power systems. In *1991 International Conference on Advances in Power System Control, Operation and Management, APSCOM-91.*, pages 877–882. IET, 1991.
- [77] Jack K. Hale. Diffusive coupling, dissipation, and synchronization. *Journal of Dynamics and Differential Equations*, 9(1):1–52, January 1997.
- [78] T. Stankovski, T. Pereira, P. V. E. McClintock, and A. Stefanovska. Coupling functions: Universal insights into dynamical interaction mechanisms. *ArXiv e-prints*, June 2017.
- [79] Cynthia L. Stokes and John Rinzel. Diffusion of extracellular K⁺ can synchronize bursting oscillations in a model islet of langerhans. *Biophysical Journal*, 65(2):597–607, 1993.
- [80] Raima Larter, Brent Speelman, and Robert M. Worth. A coupled ordinary differential equation lattice model for the simulation of epileptic seizures. *Chaos: An Interdisciplinary Journal of Nonlinear Science*, 9(3):795–804, 1999.
- [81] Dmitry E. Postnov, Ludmila S. Ryazanova, Erik Mosekilde, and Olga V. Sosnovtseva. Neural synchronization via potassium signaling. *International Journal of Neural Systems*, 16(02):99–109, 2006.
- [82] H. Hong, Hyunggyu Park, and M. Y. Choi. Collective synchronization in spatially extended systems of coupled oscillators with random frequencies. *Physical Review E*, 72(3):036217, 2005.

- [83] Vanessa Casagrande. *Synchronization, waves, and turbulence in systems of interacting chemical oscillators*. PhD thesis, Institute for Theoretical Physics of the Technical University of Berlin, February 2006.
- [84] Yoshiki Kuramoto. *Chemical oscillations, waves, and turbulence*, volume 19. Springer Science & Business Media, 2012.
- [85] Juan A. Acebrón, Luis L. Bonilla, Conrad J. Pérez Vicente, Félix Ritort, and Renato Spigler. The kuramoto model: A simple paradigm for synchronization phenomena. *Reviews of Modern Physics*, 77(1):137, 2005.
- [86] Bernd Blasius and Ralf Tönjes. Quasiregular concentric waves in heterogeneous lattices of coupled oscillators. *Physical Review Letters*, 95(8):084101, 2005.
- [87] Spase Petkoski and Aneta Stefanovska. Kuramoto model with time-varying parameters. *Physical Review E*, 86(4):046212, 2012.
- [88] Thomas S. Shores. Applied linear algebra and matrix analysis, 2007.
- [89] Ryogo Kubo. Statistical-mechanical theory of irreversible processes. i. general theory and simple applications to magnetic and conduction problems. *Journal of the Physical Society of Japan*, 12(6):570–586, 1957.
- [90] David Ruelle. A review of linear response theory for general differentiable dynamical systems. *Nonlinearity*, 22(4):855, 2009.
- [91] Arkady Pikovsky, Michael Rosenblum, and Jürgen Kurths. *Synchronization: a universal concept in nonlinear sciences*. Cambridge University Press, 2003.
- [92] Grigory V. Osipov, Jürgen Kurths, and Changsong Zhou. *Synchronization in oscillatory networks*. Springer, 2007.
- [93] Louis Lapicque. Recherches quantitatives sur l'excitation électrique des nerfs traitée comme polarisation. *J. Physiol. Pathol. Gen.*, 9:620–635, 1907.
- [94] H. C. Tuckwell. Introduction to theoretical neurobiology: Volume 1, linear cable theory and dendritic structure (cambridge studies in mathematical biology), 1988.
- [95] Balth Van Der Pol and Jan Van Der Mark. Lxxii. the heartbeat considered as a relaxation oscillation, and an electrical model of the heart. *The London, Edinburgh, and Dublin Philosophical Magazine and Journal of Science*, 6(38):763–775, 1928.
- [96] Ali R. Yehia, Dominique Jeandupeux, Francisco Alonso, and Michael R. Guevara. Hysteresis and bistability in the direct transition from 1: 1 to 2: 1 rhythm in periodically driven single ventricular cells. *Chaos: An Interdisciplinary Journal of Nonlinear Science*, 9(4):916–931, 1999.

- [97] Arthur T. Winfree. Biological rhythms and the behavior of populations of coupled oscillators. *Journal of Theoretical Biology*, 16(1):15–42, 1967.
- [98] Hidetsugu Sakaguchi and Yoshiki Kuramoto. A soluble active rotater model showing phase transitions via mutual entertainment. *Progress of Theoretical Physics*, 76(3):576–581, September 1986.
- [99] Shinya Watanabe and Steven H. Strogatz. Integrability of a globally coupled oscillator array. *Physical Review Letters*, 70(16):2391–2394, April 1993.
- [100] Steven H. Strogatz. From kuramoto to crawford: exploring the onset of synchronization in populations of coupled oscillators. *Physica D: Nonlinear Phenomena*, 143(1-4):1–20, September 2000.
- [101] David Cumin and C. P. Unsworth. Generalising the kuramoto model for the study of neuronal synchronisation in the brain. *Physica D: Nonlinear Phenomena*, 226(2):181–196, 2007.
- [102] Michael Breakspear, Stewart Heitmann, and Andreas Daffertshofer. Generative models of cortical oscillations: neurobiological implications of the kuramoto model. *Frontiers in Human Neuroscience*, 4, 2010.
- [103] Kurt Wiesenfeld. New results on frequency-locking dynamics of disordered josephson arrays. *Physica B: Condensed Matter*, 222(4):315–319, 1996.
- [104] Steven H. Strogatz, Charles M. Marcus, Robert M. Westervelt, and Renato E. Mirollo. Simple model of collective transport with phase slippage. *Physical Review Letters*, 61(20):2380, 1988.
- [105] Steven H. Strogatz, Charles M. Marcus, Robert M. Westervelt, and Renato E. Mirollo. Collective dynamics of coupled oscillators with random pinning. *Physica D: Nonlinear Phenomena*, 36(1-2):23–50, 1989.
- [106] Debsankha Manik, Dirk Witthaut, Benjamin Schäfer, Moritz Matthiae, Andreas Sorge, Martin Rohden, Eleni Katifori, and Marc Timme. Supply networks: Instabilities without overload. *The European Physical Journal Special Topics*, 223(12):2527–2547, September 2014.
- [107] Martin Rohden, Andreas Sorge, Marc Timme, and Dirk Witthaut. Self-organized synchronization in decentralized power grids. *Physical Review Letters*, 109(6):064101, 2012.
- [108] European Network of Transmission System Operators for Electricity. <https://www.entsoe.eu/>. Accessed: 2017-08-27.
- [109] Christian Schaffner and Rafael Mihalic. Economic evaluation of controllable devices in the slovenian electric power system—a case study. In *Proc. of 2005 Power Systems Computation Conference (PSCC'05), Liege, Belgium*, 2005.

- [110] J. O. G. Tande, M. Korpås, L. Warland, K. Uhlen, and F. Van Hulle. Impact of tradewind offshore wind power capacity scenarios on power flows in the european hv network. In *Proc. 7th International Workshop on Large-Scale Integration of Wind Power and on Transmission Networks for Offshore Wind Farms, Madrid, Spain, May.*, 2008.
- [111] Siemens AG. PSS®E - Power Transmission System Planning Software. <http://w3.siemens.com/smartergrid/global/en/products-systems-solutions/software-solutions/planning-data-management-software/planning-simulation/Pages/PSS-E.aspx>. Accessed: 2017-08-27.
- [112] Dirk Withaut and Marc Timme. Braess's paradox in oscillator networks, desynchronization and power outage. *New Journal of Physics*, 14(8):083036, 2012.
- [113] Florian Dörfler and Francesco Bullo. Synchronization and transient stability in power networks and nonuniform kuramoto oscillators. *SIAM Journal on Control and Optimization*, 50(3):1616–1642, 2012.
- [114] P. Kundur, N. J. Balu, and M. G. Lauby. *Power System Stability and Control*, volume 7. McGraw-Hill, 1994.
- [115] Jan Machowski, Janusz Bialek, and Jim Bumby. *Power System Dynamics: Stability and Control*. John Wiley & Sons, 2011.
- [116] Martin Rohden. *Synchronization and Stability in Dynamical Models of Power Supply Networks*. PhD thesis, Georg-August-Universität Göttingen, 2013.
- [117] Debsankha Manik, Marc Timme, and Dirk Witthaut. Cycle flows and multistability in oscillatory networks. *Chaos: An Interdisciplinary Journal of Nonlinear Science*, 27(8):083123, 2017.
- [118] John R. Taylor. *Classical Mechanics*. University Science Books, 2005.
- [119] Marcelo S. Alencar and Valdemar C. Da Rocha. *Communication systems*. Springer Science & Business Media, 2005.
- [120] International Organization for Standardization. Acoustics – normal equal-loudness-level contours. <https://www.iso.org/standard/34222.html>. Accessed: 2017-10-30.
- [121] Bundesministerium für Wirtschaft und Energie. Zeitreihen zur entwicklung der erneuerbaren energien in deutschland. http://wwwerneuerbare-energien.de/EE/Navigation/DE/Service/Erneuerbare_Energien_in_Zahlen/Zeitreihen/zeitreihen August 2017. Accessed: 2017-10-30.
- [122] Pieter Tielen and Dirk Van Hertem. Grid inertia and frequency control in power systems with high penetration of renewables. In *Young Researchers Symposium in Electrical Power Engineering, edition:6*, apr 2012.

- [123] Ralf Hesse, Dirk Turschner, and Hans-Peter Beck. Micro grid stabilization using the virtual synchronous machine (visma). In *Proceedings of the International Conference on Renewable Energies and Power Quality, ICREPQ'09*, page 6, 2009.
- [124] Salvatore D'Arco and Jon Are Suul. Virtual synchronous machines – classification of implementations and analysis of equivalence to droop controllers for microgrids. In *PowerTech (POWERTECH), 2013 IEEE Grenoble*, pages 1–7. IEEE, 2013.
- [125] Johannes Schiffer, Darina Goldin, Jorg Raisch, and Tevfik Sezi. Synchronization of droop-controlled microgrids with distributed rotational and electronic generation. In *Decision and Control (CDC), 2013 IEEE 52nd Annual Conference on*, pages 2334–2339. IEEE, 2013.
- [126] Andreas Ulbig, Theodor S. Borsche, and Göran Andersson. Impact of low rotational inertia on power system stability and operation. *IFAC Proceedings Volumes*, 47(3):7290–7297, 2014.
- [127] Göran Andersson. Modelling and analysis of electric power systems. *EEH-Power Systems Laboratory, Swiss Federal Institute of Technology (ETH), Zürich, Switzerland*, 2008.
- [128] Paul Schultz, Jobst Heitzig, and Jürgen Kurths. A random growth model for power grids and other spatially embedded infrastructure networks. *The European Physical Journal Special*, 223(12):2593–2610, September 2014.
- [129] M. Anvari, G. Lohmann, M. Wächter, P. Milan, E. Lorenz, D. Heinemann, M. Reza Rahimi Tabar, and Joachim Peinke. Short term fluctuations of wind and solar power systems. *New Journal of Physics*, 18(6):063027, jun 2016.
- [130] T. Pesch, H. J. Allelein, and J. F. Hake. Impacts of the transformation of the german energy system on the transmission grid. *The European Physical Journal Special Topics*, 223(12):2561–2575, Oct 2014.
- [131] M. de Berg. *Computational Geometry: Algorithms and Applications*. Springer, 1997.
- [132] Elliott H. Lieb and Derek W. Robinson. The finite group velocity of quantum spin systems. *Communications in Mathematical Physics*, 28(3):251–257, 1972.

Acknowledgements

This thesis means so much more than a collection of scientific work for me. A substantial stage of my life, 2008–2018, is concentrated in the 185 pages. About 10 years ago, I stepped on a strange land without knowing a single soul in the continent, pursuing a deeper understanding of the complex world in Europe, where modern science came into existence. Today I have almost finished my PhD study and will soon start my career in scientific research. I could never have come this far without the countless help of so many teachers, friends in Göttingen and also, the understanding and support of my dear family in China.

First of all, I would like to thank my supervisor, Prof. Dr. Marc Timme for making this thesis possible. Thank you, Marc, for your immeasurable help in science, in scientific communication, in fighting for my funding and your constant trust and encouragement in challenging times. Especially, thank you for making me realize I am capable of doing more than I thought, just like riding a bike.

I would like to thank the members of my thesis committee, Prof. Dr. Reiner Kree and Prof. Dr. Ulrich Parlitz, for attending my TAC meetings and providing me valuable suggestions.

And my dear colleagues (and former colleagues) in the Network Dynamics group of the Max Planck Institute for Dynamics and Self-organization, Sarah, Jose, Diemut, Nora, Debsankha, Benjamin, Malte, Florencia, Andreas, Nahal and Martin, thank you so much, for your warm friendship which makes Göttingen feel like second home for me. We shared so many happy and memorable times together in the aged building at Bunsenstrasse. I learned a lot from you, scientifically and culturally. Special thanks are due to Malte, Debsankha and Benjamin. I benefited a lot from the discussions with you and your brilliant ideas.

I would like to thank Barbara, Ayse and Monika. Your constant and thoughtful support made my work and conference trips so much easier. Thank you.

I would also like to thank Antje and Frauke at the PBCS office. Thank you for answering my many questions and for your attentive reminders about extensions, deadlines, and submission issues. I can't be graduating so smoothly without your help.

Special thanks to my friends, Chenchang, Manli, Chenyu, Bee-Zen, Chi, Zhiyi and Deqing. Many thanks for your constant caring and encouragement during the final stage of my thesis. Thank you for allowing me delay all the lunch- and dinner-plans with you until the submission of my thesis. I'll make up to you. Especially, thank you Chenchang, for reading my thesis and providing valuable suggestions from a mathematician's perspective.

Last but not least, I thank all my family in China for your unconditional understanding, love and support. There is not a single moment in the almost 10 years I don't think about coming back to China, to you. Thank you mother, for remotely accompanying me throughout the journey. And thank you grandma, for your daily prayer for my safety and wellness over the years I have been a continent away from home. This thesis is dedicated to you.

Xiaozhu Zhang 张潇竹



PhD student

Network Dynamics

Max Planck Institute for Dynamics and Self-organization

Born: March 20, 1985 – Shanghai, China

Citizenship: Chinese

Research Experiences

2014 - present PhD in Physics, Network Dynamics, Max Planck Institute for Dynamics and Self-organization, Germany

Thesis: *Dynamic Responses of Networks under Perturbations*

2009 - 2011 Scientific assistant, Dynamics of Complex Fluids, Max Planck Institute for Dynamics and Self-organization, Germany

Education

2011 - 2013 M.Sc. in Physics *with distinction*, Georg-August-University Göttingen, Germany

Thesis: *Statistics, Predictability and Dynamics of Critical Transitions*

2008 - 2011 B.Sc. in Physics, Georg-August-University Göttingen, Germany

Thesis: *Impact of Stochastic Delays in Extremal Evolutionary Dynamics*

2003 - 2007 B.Sc. in Optical Science and Engineering, Fudan University, China

Thesis: *The Dynamical Behavior of a Single Ad-atom in the Self-Diffusion on Ag(001) Surfaces*

Language Skills

NATURAL Chinese (native), English (fluent, IELTS score: 7.0), German (reading knowledge)

ARTIFICIAL C/C++ (good), Mathematica (basic), Matlab (basic)

Teaching

at Georg-August-University Göttingen, Germany:

2014 - 2015 lecture *Network Dynamics*, winter term, Teaching assistant

2015a *Practical Course on Network Science*, summer term, Organizer

2015b *Seminar on Network Science*, summer term, Organizer

Scholarships

2014 MPG-stipend of the International Max Planck Research Schools (IMPRS) for Physics of Biological and Complex Systems

2016 Fellowship of the IMPRS for Physics of Biological and Complex Systems

Publications

- 2017a **X. Zhang**, D. Witthaut, and M. Timme.
Transient Responses in Oscillatory Networks
(in preparation)
- 2017b J. Casadiego, **X. Zhang**, and M. Timme.
Locating Perturbation Sources and Monitoring Unmeasured Units from Collective Dynamics
(in preparation)
- 2017c Zhiyi Lv, Jan Rosenbaum, **X. Zhang**, Timo Aspelmeier, Jörg Groshans
Collective Dynamics in Drosophila Embryo
(in preparation)
- 2017d **X. Zhang**, S. Hallerberg, M. Matthiae, D. Witthaut, and M. Timme.
Dynamic Response Patterns of Complex Oscillator Networks
(submitted)
- 2017e D. Manik, M. Rohden, H. Ronellenfitsch, **X. Zhang**, S. Hallerberg, D. Witthaut, and M. Timme.
Network Susceptibilities: Theory and Applications.
Phys. Rev. E 95, 012319.
- 2016a D. Witthaut, M. Rohden, **X. Zhang**, S. Hallerberg, and M. Timme.
Critical Links and Nonlocal Rerouting in Complex Supply Networks.
Phys. Rev. Lett. 116(13):138701.
- 2016b M. Matthiae, B. Schäfer, **X. Zhang**, M. Rohden, M. Timme, and D. Witthaut.
Escape Routes, Weak Links, and Desynchronization in Fluctuation-driven Networks.
Phys. Rev. E 95, 060203(R).
- 2015 **X. Zhang**, C. Kuehn, and S. Hallerberg.
Predictability of Critical Transitions.
Phys. Rev. E 92(5):052905.
- 2012 **X. Zhang**, K. Hantke, C. Fischer, and M. Schröter.
Performance of Polarization-based Stereoscopy Screens.
3D Research, 3(4), 1-5.

Conferences

- 2017a DPG Spring Meeting, Dresden, Germany
talk “*Response Patterns for Fluctuations in Complex Oscillator Networks*”
- 2017b Conference “Dynamics in Power Systems – from Science to Industry”, Potsdam, Germany
poster “*Perturbation Spreading in Oscillatory Networks and Power Grids*”
- 2016a Lake Como School of Advanced Studies in Complex Systems “Complex Networks: Theory, Methods and Applications (2nd edition)”, Como, Italy

- 2016b Conference “Complex Networks: from Theory to Interdisciplinary Applications”, Marseille, France
poster “*Dynamic Response Pattern in Oscillatory Networks and Power Grids*”
- 2015a DPG Spring Meeting, Berlin, Germany
talk “*Predicting Critical Links in Complex Supply Networks*”
- 2015b Workshop “Energy Scenario and Secure Electricity Supply - Role of Electricity Grid”, Jülich, Germany
talk “*Steady Response Patterns to Perturbations in Power Grids*”
- 2014 Symposium “Future Energy Systems: Collective Dynamics and Self-Organization of Power Grids”, Göttingen, Germany
talk “*From Perturbations to Instabilities in Power Grids*”
- 2013 DPG Spring Meeting, Regensburg, Germany
talk “*Statistics, Predictability and Dynamics of Critical Transitions*”